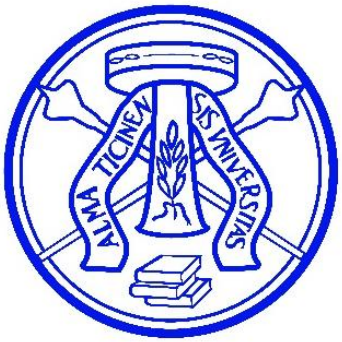

UNIVERSITÀ DEGLI STUDI DI PAVIA

DOTTORATO IN SCIENZE CHIMICHE E FARMACEUTICHE E INNOVAZIONE INDUSTRIALE (XXXIII Ciclo)

Coordinatore: Chiar.mo Prof. Giorgio Colombo

NANOCOMPOSITE SCAFFOLDS FOR TISSUE ENGINEERING

Tutor
Chiar.ma Prof.ssa Giuseppina Sandri

Tesi di Dottorato di
Angela Faccendini

AA 2019/2020

Aim and Summary of the thesis.

The electrospinning technique, used to create ultra-thin polymeric nanofibers with controlled topography for biomedical application, started around thirty years ago and still remains an emerging and unexplored method in many aspects. The tissue engineering, started in the last century, using tissue grafts directly from humans or animals to be transplanted in the wounds, and it has continued to evolve over centuries, until to use 3D-scaffolds in conjunction with living cells for remaking many types of tissues.

Electrospun nanofibers become one type of scaffold amply studied in tissue engineering approach. Thanks to their numerous properties (i.e. high surface-to-volume ratio, anisotropy, bio-mimicking structure, biodegradability). The ultimate goal of the tissue regeneration treatments, is to generate a fully functional tissue, without disorganised scar tissue, which is structurally and biomechanically inferior to the native one. However it's difficult to mimic all the tissue micro-environment, in only one feasible platform.

The major chances of electrospinning technique is the possibility to create nano/micro fibers in continuous manufacturing without interruption, and the excellent capability to be loaded with different kind of active molecules, in order to obtain advanced systems. Moreover, electrospun nano/microfibers can be made by different biocompatible or biodegradable materials. They can be further designed and assembled in order to create ulterior shape and nano-structured scaffolds, showing their enormous versatility.

There is a constant need of developing new scaffolds more personalised, which request better biocompatibility, less immune response, and longevity, for this reasons, the tissue engineering method is in continuous evolution.

Recently hybrid electrospun scaffolds have been explored , in particular in biomedical area. This includes systems able to control drug delivery and engineered tissues. The versatility of hybrid electrospun scaffolds grew thanks to the optimization of innovative strategies for the loading of functional proteins, colloidal nano-carriers or inorganic nanoparticles in the fibrous matrix, or by building structures able to act in situ in response to the environment, or to support stem cells.

Given this premise, the aim of this thesis was the development of electrospun scaffold based on polysaccharide polymers, hybridized with clays, nanocomposite or

hydroxyapatite in the nanofibrous matrix. The scaffolds have been designed for two types of applications, with appropriate shape and topography:

1) soft membranes intended for dermal application;

2) flexible tubes, designed as a surgical support in bone-tendon surgery.

The selected polymers belong to polysaccharides, as biocompatible and natural materials and among them, glycosaminoglycans were considered for their bio-mimetic properties of extracellular matrix.

Both dermal or bone-tendon scaffolds, as medical devices, were hybridized with inorganic components and clays or hydroxyapatite were taken into account. Moreover a drug-clay nanocomposite was loaded in dermal scaffold, to treat infections or to prevent them, in the healing process of difficult to heal wounds.

The inorganic components were added in the scaffolds at critical concentration, for increasing the system mechanical properties and for reaching the scaffold stiffness suitable for their application. Additionally, the hybrid scaffolds strongly affect the cell biological signals, and this should be beneficial to cell proliferation and tissue reparation.

The thesis is divided in five chapters and hereafter a brief description of each is reported.

Chapter 1 focuses on specific overview of the art state of the electrospun hybrid nanofibers loading inorganic particles and their uses in regenerative medicine. In particular, the dermal and osteo-tendineous tissues were considered. This opening chapter leads to a general evaluation of the potentiality and the critical issues existing in such systems.

In the chapter 2, the design and development of hybrid electrospun scaffold loading two types of clays (phyllosilicates: montmorillonite and halloysite), is reported. The electrospun scaffolds were proposed for dermal reparation. The study had the objective to correlate the 3D structures obtained by the clays embedded in the fibers, with the derived mechanical properties, human fibroblast spreading and immune response. Considering what has been reported in literature (Solon J. et al 2007), the scaffolds were prepared with elastic values under 20kPa (= 2000 mN/cm^2), at which fibroblasts spreading did not reach a saturation level of F-actin contraction.

The scaffolds were based on pullulan, chitosan and chondroitin sulfate. The polymer aqueous solutions prepared were blended with clays before electrospinning, in order to incorporate the clays in the fibrous structures. The amount of clay strongly affected fiber diameter and porosity, especially in hydrated state, as well as the mechanical properties of

the systems. Scaffolds loading 2% of clay suggested higher capability to sustain fibroblast spreading and proliferation in the scaffolds. Finally, it was confirmed that the presence of both the clays in the scaffold was biocompatible without pro-inflammatory activity (collaboration with the Trinity College of Dublin and University of Granada).

Chapter 3 focuses on the development of hybrid electrospun scaffolds loaded with a nanocomposite previously prepared in collaboration with the University of Granada. The nanocomposite was prepared by intercalation of norfloxacin into the interlayer spaces of the clay. The nanocomposite development was published in *García-Villén F, Faccendini A, et al. Int J Nanomedicine. (2019).*The study had the objective to examine the potential drug release profile from the nano-structured system, with particular attention to the influence of glycosaminoglycans in the scaffold biodegradation and drug delivery, in correlation with the scaffold capability to support cell growth and antimicrobial activity.

Two scaffolds were compared: the hybrid scaffolds loading norfloxacin as nanocomposite, and the same scaffolds loading norfloxacin as free drug. Three kinds of hybrid scaffolds were prepared: the first based on chitosan, the other two scaffolds were based on chitosan/chondroitin sulfate, or chitosan/hyaluronic acid. The norfloxacin as nanocomposite or as free drug were loaded at 1 or 2% w/w, in the scaffolds. The electrospun scaffolds were characterized by fibers having smooth surface when free drug was loaded or havingknots in presence of nanocomposite.

The drug release profiles were studied in physiological solution and in presence of lysozyme, an enzyme produced by macrophages during the inflammatory phase of healing. In all cases, the drug released from the nanocomposite-loaded scaffolds was lower than that released from the free drug loaded scaffolds. Meanwhile the presence of glycosaminoglycans strongly influenced norfloxacin release. Particularly in physiological solution, the free drug loaded-scaffold based on glycosaminoglycans lead to a higher norfloxacin release. However, the presence of glycosaminoglycans hindered the interaction with the lysozyme, interfering with the enzymatic activity. Anyway, the degradation activity of the lysozyme, strongly increased the drug release, suggesting the scaffold biodegradation and the concurrent drug release. Finally chondroitin sulfate and montmorillonite in the nanocomposite-scaffold showed a synergic effect in enhancing fibroblast proliferation and their spreading, without impairing norfloxacin antimicrobial activity on Gram positive and negative bacteria.

Based on the knowledge acquired from the development of the dermal scaffolds descript in the chapter 3, scaffolds intended for surgical support in the orthopaedic treatment were developed, and chapter 4 focuses on the design and development of tubular nanofibrous scaffold, to mimic the fibrocartilage existing in the tendon/ligament matrix. The tubular scaffold was based on pullulan and chitosan polymers and was made of electrospun nanofibers. The nanofibers were oriented along the main length of the tube, to mimic the tendon fascicle direction. The electrospun fibers were reinforced with hydroxyapatite in low concentration. Platelet lysate was loaded inside the tubular scaffold to have *in situ* release of growth factors after implant. The mineral part was found to affect the scaffold hydrophilicity, porosity and alignment as well as the mechanical properties, in dry and wet state. The platelet lysate loaded in the tubular scaffold constituted a growth factor reservoir, which crossed the scaffold wall with controlled release up to14 days. The growth factors strongly supported SAOS-2 and tenocytes adhesion and proliferation and stimulated the production of specific extracellular matrix.

Chapter 5 focuses on the development of a tubular scaffold, with the same composition as that of the scaffold, as previously described in chapter 4, but with a mineral and topographical gradient. This approach was carried out for mimicking the tendon-to-bone interface in vivo, where a gradual fibrocartilage mineralization exists (in collaboration with the 3Bs institute in Braga, University of Minho).

The bone part of the tubular scaffold consisted of randomly collected nanofibers loading hydroxypapatite (HP), while the tendon part was made of aligned fibers without hydroxypapatite (blank). The alizarin red distribution confirmed the HP gradient along the scaffold. While the Micro CT suggested a unique continuous structure, with a gradient in porosity and fiber alignment. The biological response of the scaffold was evaluated using human adipose stem cell. Initial stem cell differentiations towards bone or tendon like cells were observed, as function of the hydroxyapatite concentration in the scaffolds.

CHAPTER 1

Hybrid electrospunfiber in tissue engineering

Abstract:. The use of inorganic components as components in hybrid scaffolds, have been obtained a greater interest in tissue engineering applications, thanks to their important technological properties, as well as their capability to induce biological responses. However, some issues have still to be faced for improving their efficacy. This chapter will focus on the use of electrospinning as an emerging technique to obtain more versatile hybrid scaffolds. In particular the most effective inorganic components used in tissue engineering, and the most common hybrid electrospun scaffolds based on those, will be reviewed. The critical technological parameters for the development of suitable hybrid electrospun nanofibers, will be discussed: fiber diameter/porosity, system conductivity, homogeneity and mechanical properties. Finally, the most recent advance to understand the interactions between scaffolds and cells, and in detail how the hybrid nanofibers activate specific intracellular pathways, will be described. In addition, the use of inorganic components, as innovative drug delivery systems, will be also considered.

1. INTRODUCTION

In tissue engineering, the use of inorganic component to enrich different polymeric scaffolds, allows to mimic the native tissue composition (in particular those of mineralized tissues), to improve the tissue conduction, to support cell regeneration, and finally this allows to load drugs (in nanocomposites, colloidal particles) or to guide magnetic or thermal pulses.

Inorganics are employed in tissue engineering in amorphous or crystal state and basically in nanosize, because the particles in nanometric dimension, are more biologically active. The most commonly inorganic materials used in tissue engineering could be grouped in few huge categories: the bioceramics, the bioglass, the phyllosilicate, the carbonanotubes, the metal oxide and the metal nanoparticles.

However, there are some issues in their use when combined with polymers. It is hard to produce homogeneous hybrid scaffolds, because of the separation of organic/inorganic phase or their incompatibility. Moreover, the presence of inorganic part in the scaffold

could affect 3D structure, and this has an impact on the control the scaffold nano-topography, an essential feature to promote cell adhesion or differentiation. Lastly, the large mechanical difference between organic and inorganic phase, creates fractures or problem in system homogeneity. In order to overcome all these problems, efforts have been made to develop biomimetic scaffolds possessing well integrated structure, based on organic and inorganic phases. In this context, the electrospinning represents an emerging easy technique to obtain more homogenous and flexible hybrid scaffolds. (Andric T et al 2012; Bramhill J et al 2017;Das et al 2011; Gorain B et al 2018; Joshi M.K et al 2015;Krishna L et al 2016;Ozdemir T et al 2013; Savelyeva M S et al 2017; Rahaman MN et al 2011; Lvov Y et al 2016; Contreras-Cáceres R et al 2019)

In this chapter, the most recent literature studying electrospun scaffolds enriched with inorganic components, for tissue engineering, will be reviewed. In particular, two thematic areas will be considered: one focused on the dermal application, the other concerning the tendon and bone reparation.

All the challenges remaining in the development of homogeneous inorganic dispersion, fabrication of continuous fibrous structures, in the control of cell conduction, will be taken into consideration. All the critical issues will be analyzed in connection with the cellular biological responses. Firstly, the most important classes of inorganic component employed in tissue engineering, will be shortly listed and secondly electrospun fibers based on those will be illustrate in tables.

Bioceramics

Bioceramics includes different materials. Basically the bioceramics which have received the most attention for the hard tissue reparations, are calcium phosphate-based bioceramics, among them the hydroxyapatite (HP) [$Ca_{10}(PO_4)_6$-$(OH)_2$], the β-tricalcium phosphate ($Ca_3(PO_4)_2$, β-TCP), the dicalcium phosphate ($CaHPO_4$, DCP), and the biphasic calcium phosphate (BCP), which is a combination of constant ratios of HA with β-TCP. The selection of the type, mostly depends on their chemical physical properties and biological response, depending on the site of application and formulation process to be subjected. For mentioning some example, an hydrousdicalcium phosphate ($CaH_1(PO_4)$, DCPA, monetite) and dicalcium phosphate dehydrate ($CaH(PO_4)\cdot 2H_2O$; DCPD) are the very stable calcium phosphate types at 37°C, and they resist even in the physiological fluid

under acidic conditions (pH <4.8). On the contrary HP is soluble at pH values lower than 4.5.

In order to overcome the solubility at low pH, some authors propose the mixture between HP and β-TCP, to obtain BCP composite with different HA ratios for controlling the degradation rate (Rahaman M. et al 2011; Souza D.C et al 2019). The β/α-tri-calcium phosphate ($Ca_3(PO_4)_2$; β-TCP) and tetracalcium phosphate ($Ca_4(PO_4)_2O$; TTCP) are the hardest solids and crystals stable at temperatures higher than 37°C.

Calcium carbonate($CaCO_3$) is another significant bioceramic used in biomedicine. Different crystal forms exist such as vaterite (hexagonal), calcite (trigonal) and aragonite (orthorhombic) lattices characterized by needle-shape structure. Their crystal properties lead to different solubility properties and thermal stability. However, at physiological temperature, transition from vaterite to calcite could occur. For this reason, this type of crystal isnot optional in a spinning process, where the temperature easily affects their polymorphic behaviour (Savelyeva et al 2017).

In general, all of them are no toxic, they possess bioresorbability and osteoinduction. Their biological activity consists in the hydrolysis mechanism, by generating hydroxyapatite phase in the implant site.

Bioglass

Bioglass are in many cases mixed with bioceramics, to form a unique nanocomposite. However, pure Bioglass are structurally different from bioceramics, having silica atoms and amorphous state.

The glass–ceramic composite are crystalline glasses, where a crystalline phase is blended with a residual glassy phase. They interact *in vivo* as bioceramics, by promoting the formation of apatite-like crystals *in situ.* The *in situ* hydroxyapatite nucleation, is due to the calcium and silica hydration. However, if one type of bioglass generated apatite-nucleation after submersion in simulated biological fluids *in vitro*, the same solid would not be able to bond the tissue *in vivo* at the implant site in the same way.

Generally, the high Ca:P ratio in the bioglass composition is reported to be more effective for enhance the tissue reparation *in vivo*, but how the conversion product forms hydroxyapatite,still remains unclear (Rahaman M. et al 2011; Song et al 2012; Shankhwar N et al 2016).

The silicate bioactive glasses most frequently used in biomedicine application, is 45S5 composition. The 45S5 code means glass with 45 weight % of SiO_2, and 5:1 molar ratio of calcium to phosphorus. Thanks to its optimal composition, the bioglass 45S5 has been frequently used in regenerative medicine. It possesses favourable chemical-physical properties for the technological management, also optimal biocompatibility, and active interaction *in vivo*, by producing hydroxyapatite interface layer. Moreover, the flexibility of composition of glass allows to obtain new solid glass-composite with other minor mineral elements, well known to support tissue growth such as Zn, Cu, F, Mn, Sr and B (borate bioactive glass) (Savelyeva M.S. et al 2017).

The use of bioglass as well as bioceramics, has been in general recognized extremely effective for repairing bone or dental defect, because they guide the osteo-inductive tissue response, through the hydroxyapatite gel-layer. But the deposition of such mineralized layer has been also proven to help even the soft tissue regeneration. In particular, bioactive glass 45S5 has been referred as enhancer to promote angiogenesis, which is a crucial step for the tissue engineering application and the healing process in wounds (Day R.M et al 2004; Keshaw et al 2005; Rahaman M. et al 2011) .

Magnetic nanoparticles

The magnetic components recognized as non toxic in medical field, thanks to their oxidative stability, are magnetite (Fe_3O_4) and maghemite (γ-Fe_2O_3). When the iron oxide particles arrive to nano-size lower than 200nm, they become superparamagnetic iron oxide nanoparticles (SPIONs), which exhibit their magnetic behaviour if an external magnetic field is applied. Among them the bioactive magnetic glass-ceramic nanocomposites have been recently developed, in order to improve their magnetic reactivity and biocompatibility. Magnetic bioactive nanocomposites have been used in biomedical applications with different purpose: as magnetic resonance imaging (MRI) diagnosis, as drug delivery control and cell/tissue targeting (Tomas A. R et al 2019).

Recently the inclusion of magnetic nanoparticles into electrospun scaffolds results in unique properties to control cell signalling. In particularly the most efficient effect of magnetic electrospun fiber is the mechano-stimulation. The cells act in response to mechanical stimulation, by four major biochemical pathways: ion channels activation, ATP release, contraction of the cytoplasmatic actin and alteration of protein expression (Matos AM et al 2020). These mechanisms are the basis of biochemical signals that stimulate cells

to increase the remodelling and differentiation. In this context, the magnetic electrospun fibers can guide the mechano-trasduction signals, along the fibrous structure by allowing deeper tissue reparation.

Phyllosilicate

Clays are natural crystals presenting layered structure in nanoscale size. They possess good biocompatibility and low cost. They are made of stratified sheets of tetrahedral silica oxide, and octahedral Al, Fe, or Mg oxide, condensed in different ratio or conformation. Their typical feature is the high ion-exchange capacity inside of the interlayer spaces, which is promising for different bio-application. Clayscan be classified in different groups, based on their layered structure and chemical composition. The major clay groups employed in pharmaceutical or cosmetic products are Serpentine (e.i.Kaolins and Halloysites), Pyrophyllites (e.i. Talc), Chlorites, Smectites (e.i. Montmorillonites), Vermiculites, Illites, Sepiolites (e.i.Palygorskites) (Marras SI et al 2008; Garcia – Villèn F. et al 2019).

Despite their countless employments (such as anti-acids, gastrointestinal protectors, dermatological medication ingredients, anti-inflammatories, local anaesthetics, lubricants, diluents, emulsifying, flavour correctors and so on), recently they have been explored also in the field of tissue engineering as regenerative agent or even as innovative drug carriers (Xue J. et al 2015). Thanks to their versatility, they are employed in both the hard and soft tissue applications (Lvov Y et al 2016; Qi R. et al 2012).

Carbonanotubes

Carbon Nanotubes (CNs) were discovered 3 decades ago and currently they are widely studied in many biomedical fields in tissue engineering, diagnostic imaging, and drug delivery .

CNs are basically a cylindrical nanotube having few nanometres in diameter and some micrometers in length. The tubular size depends on the walls since they can be single-walled CNT (SWCNTs with 0.8 to 2 nm diameter) or multi-walled CNT (MWCNTs with 2 nm to 200 nm diameter). They exhibit electrical, optical, thermal properties and biocompatibility, which depend to their nanosize, and shape. They are totally made of carbon atoms, which form hexagonal lattices rolled without interruptions. The SWCNT exist in some different conformation depending on the arrangement of the atoms in the

lattice: the zigzag and armchair configurations are the most studied especially for their electrical properties (Ohlendorf P. et al 2017; Sharma Y. Et al 2012).
In the field of tissue engineering, they are incorporated in different types of scaffolds and strongly affect their chemical physical performance, as well as their biological response. The major areas of applications are in cardiac, nerve, and bone tissue engineering for their electrical conductivity and osteogenic assets. But more recently they gained interest in the application in dermal tissue engineering (Gorain B et al 2018; Eivazi Zadeh Z et al 2021; Franca E. Et al 2016; Gorain B et al 2018; Liao H. et al 2011; Liu et al 2010; Luo F et al 2010).

Metal Oxide

Metal oxide nanoparticles (NPs) exhibit unique physic-chemical properties derived by the early metal transition state, including their use in many reactions: oxidation, dehydration, photocatalysis, and electrocatalysis. Other remarkable variety of properties are their high surface area to volume ratio (larger particle sizes of these metal oxides do not have the same distinctive properties), good mechanical stability, biodegradation and biocompatibility. For these reasons, metal oxide nanoparticles have been the base of a wide variety of new biomedical materials.
The most important examples of metal oxide NPs employed in biomedicine are titania (TiO_2), zinc oxide (ZnO), magnetic iron oxides (Fe_2O_3 and Fe_3O_4), and ceria (CeO_2) (Thakore R et al 2018; Nasari – Nosar M et al 2017;). They found application in numerous biomedical purposes: diagnosis, drug delivery, medical implants, and biosensing. In particular, the superparamagnetic iron oxide NPs are biodegradable diagnostic agents, widely used for magnetic resonance imaging. $TiO_2$is the material of choice in medical implants following by ZrO_2, and Al_2O_3. ZnO NPs (recognized safe by the FDA) and CuO, have been proven to possess good antimicrobial properties. Moreover, CeO_2NPs, have recently received a great interest for their redox, and antioxidant, free radical scavenging properties particularly in the neuro-science field. For instance, medical diseases related to reactive oxygen species, such as spinal cord injury, lesion and degenerative retinal disorders, have been successfully treated with CeO_2 based systems.
However further advantages, limitations, and toxicity of these compounds are still waiting for being fully explored (Ahmad F et al 2020).

Electrospun hybrid scaffolds in biomedicine

In biomedicine, the general term *hybrid* sometime is used to describe electrospunfiber made of different polymer types. However, the term *hybrid scaffold* in tissue engineering, is referred to scaffolds structurally made of the combination of polymeric materials and inorganic mats.

Electrospun hybrid scaffolds are systems build by the deposition of fibers as basic building blocks. The technique allows to form ultrathin nano/micro polymeric fibers, starting from a polymeric blend.

By adding inorganic material before electrospinning, the solid fibers are hybridized presenting inorganic particles incorporated in the polymeric matrix.

The electrospinning process could be divided in 3 steps. In the first one a liquid droplet at the spinneret tip, is charged by the voltage applied. In this phase the electrostatic repulsion occurs until to surpass the surface tension of the liquid. (Figure 1).

In the second step, the resulted repulsion phenomena cause a drop stretching at a critical point, where the liquid jet emerges from the drop surface. This emerging point is named Taylor cone (Figure 2). During the final step, the fiber solidification and collection occur. This is possible only if the polymeric chain entanglement in liquid, is strong and elastic enough to resist the elongation during the whipping phase. In the whipping phase the liquid jet become solid, by flying under convective flow caused by the electrical field. This step finishes with the deposition of solid fiber onto the collector (Zong H. Et al 2018; Wei J. Et al 2019).

In electrospinning of polymer and mineral blends, the mineral phase takes part and influences the whole electrospinning process. At the beginning of the process, the mineral particle size can influence the drop shape, as well as the surface tension and conductivity equilibrium of the drop. The mineral part often affects the solution viscosity and conductivity, in these cases, it could be useful to change the spinneret diameter in order to control the amount of electrostatic charges in the droplet surface. In the subsequent process, the interface stability, between the polymer and mineral phase, plays an important role for resisting against the jet elongation and whipping (Reyes CG et al 2020).

In many cases, it is difficult to develop homogeneous distribution of mineral particles in each solid fibers, due to the great numbers of variables which should be satisfied for creating the ideal mineral dispersion.

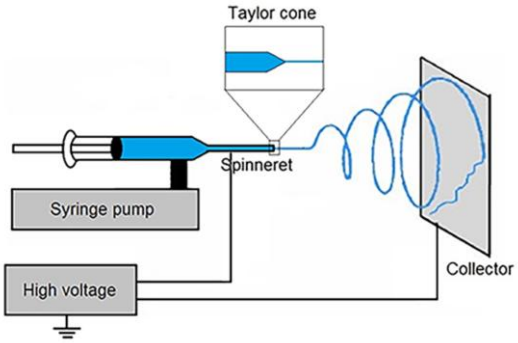

Figure 1 *Schematic representation of the electrospinning equipment*

(a) Stable (b) Unstable

Figure 2 *Screenshots of Taylor cone with a) stable shape and b)warped unstable jet (Reyes CG et al 2020)*

The major chances of these techniques are the excellent capability to load drugs, the possibility to be based on different biocompatible or biodegradable polymer types, the flexibility to be designed in different forms as structured system.

On the other hands, the topography of fiber is another important parameter having influence on material interface. The hybrid electrospun fibers obtained, can be structurally combined in different way because the technique can control the 3D conformation, as well as the formation of interconnected nano-pores, knots and meshes. It results on a management of scaffold topography, that can be translated into intracellular signalling activity (Ozdemir T. et al 2013; Liu F et al 2010; Solon et al 2007). In fact, the scaffold geometry is crucial towards the sensing mechanisms of the cells in adhesion on the material, even when the fibers are pure or without hybridization, and the ultra high surface-to-volume ratio of the electrospun fiber permits homogeneous ion exchange *in situ.*

The application of hybrid electrospun-fiber in the biomedical field, is promising for a clinical evaluation. Moreover new strategies are considered in the electrospinning technique to incorporate colloidal inorganic nano-carriers as well as magnetic nanoparticles, or by building up fibers sensitive to *in situ* environment (Figure 3) (Ren K et al 2017; Joshi M.K. et al 2015; Contreras-Caceres R et al 2019; Krishna L et al 2016 ;

Faccendini et al 2017). Unfortunately, the processing efficiency and their reproducibility are still on development for a commercial applications (Zong H. et al 2018).

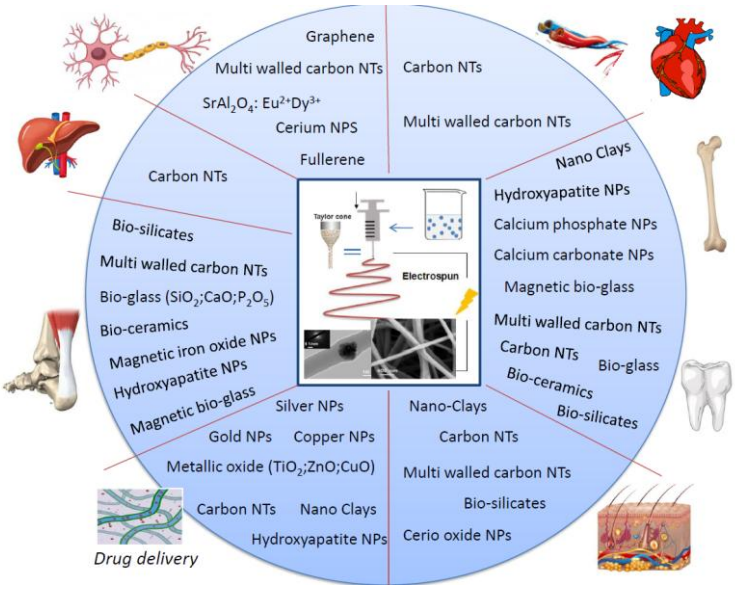

Figure 3. *Schematic representation of currently used hybrid electrospun nanofibers. Inorganic components incorporated in fiber matrix for different tissue engineering applications.*

The major hybrid electrospunfibers which were tested *in vitro* for tissue engineering applications, were reviewed schematically in tables 1, 2, and 3. They were classified on the basis of their polymer and inorganic compositions, and for their effects on the specific cellular response.

Each table divides the hybrid electrospunfibers between different tissues of application: The table 1 summarized the dermal applications. These studies confirmed the increase of fibroblast proliferation by increasing nanofibers stiffness (as tensile stress values), inter-porosity, and by including specific amounts of inorganic fillers in their structures. However few results examined enough, the local immunological response induced, as well as the entity of cell penetration and matrix production. Also the hybrid scaffold biodegradation mechanisms were poorly highlighted, especially in the case of synthetic polymers.

Subsequently table 2 lists the hybrid scaffold in musculoskeletal and bone tissues application. Finally,table3 recaps the drug delivery fiber systems.

Table 1. *Hybrid electrospunfibers for skin applications*

ElectrospunFibers	Inorganic component	Results	In vitro test	In vivo test	Development Method	Ref
Silk fibroin/PEO	NaCl crystals	Higher porosity , water uptake ability, more cell infiltration	Fibroblast keratinocytes		NaCl released on the drum collector	Park Y.R. et al 2016
PLGA	Halloysite (HNT 1, 3, 5%)	Increase cell adhesion, proliferation and protein absorption	Mouse Fibroblast		Incorporated into the fiber structured	Qi R et al 2013
Polyaniline/poly(N-isopropyl acrylamide-co-methacrylic acid)	CNTs	Excellent fibroblast adhesion, proliferation	L929 fibroblast	/	Polyaniline-CNT covalent bound	Sharma et al 2012
Silk or Collagen	CNT (0.5-0.05% wt)	Fibroblast adhesion and proliferation. Collagen 1 and 3 stimulation under electrical field	Vaginal fibroblast		Incorporated into the fiber structured	Chi N et al 2019
PVA/Chitosan	MWCNT 1%	Significant protein absorption (FBS), cell attachment polygonal shape and proliferation	L929 fibroblasts		Incorporated into the fiber structured	Liao H. et al 2011
PU	MWCNT (3% wt)	Fibroblast adhesion, migration proliferation, aggregation, release of collagen	3T3-L1 mouse fibroblasts		Incorporated into the fiber structured	Meng J. et al 2009
PU	MWCNT	Cell proliferation and orientation, collagen secretion anticoagulant	HUVECs		Incorporated into the	Meng J. et al 2010

		function, Rho, GTPases and the MAPKs pathway attivation			fiberstructured	
PCL-Gelatin	CeO_2 (1,5,3,6% wt)	Cell proliferation decrease increasing CeO2 content. Wound treated closure after2 weeks, in treated wound histology	L929 fibroblast cells	Full-thickness wound in adult male Wistar rats	Incorporated into the fiber structured	Naseri-Nosar et al 2017
PCL-Gelatin	CeO_2nanoparticle	Normal ROS intracellular level. Cell viability. Cytoprotective effect	3T3-L1 embryo fibroblast cell		Incorporated into the fiber structured	Rather HA et 2018

Table 2. *Hybrid electrospunfiber with muscoloskeletal, and bony applications*

ElectrospunFibers	Inorganic component	Results	In vitro test	In vivo test	Development Method	Ref
poly glycerol sebacate (PGS)/polycaprolactone (PCL)	10% (w/w) β-tri-calcium phosphate (β-TCP)	Higher mechanical properties and fiber diameter at critical concentration. Osteoconductivity	Human embryo osteoblast (hFOS)		Incorporated into the fiber structured	MasoudiRad M et al 2017
PVA	bioglass 45S5 (BG) and magnetic (Fe_2O_3) bioglass45S5 (MBG)	Higher mechanical properties, higher viscosity and conductivity, slow degradation in SBF. Osteogenic differentiation	Bone derived MG-63		Incorporated into the fiber structured	Shankhwar N et al 2016

PCL/gelatin	Hap gradient	cell anisotropic alignment, proliferation, mineral deposition, collagen and non collagen proteins deposition in gradient	hASCs		Incorporated into the fiber structured	Claejo et al 2019).
PCL	Cellulose nanocrystal coated with polydopamina/magnetic iron oxide (MNPs)	Tenogenic differentiation (collagen, tenomodulin and scleraxin protein) and osteocalcin (OCN) inhibition under magnetic field	Adipose stem cell (hASCs)		Incorporated into the fiber structured	Tomas et al
PLLA	Hydroxyapatite (200nm particle size HP)	In situ bio-mineralization. BFM significantly increased glycosaminoglycans formation and improved collagen organization compared with SFM.		Rotator cuff New Zealand White rabbits	Incorporated into the fiber structured	Li X. et al 2017
Chitosan / genipin	Nano Hydroxyapatite (0,8%-1%-2%)	Improve mechanical properties with HP cell adhesion and differentiation	mouse 7F2 osteoblasts		HP linked to chitosan	Frohbergh ME et al 2012
PLLA	Octacalcium phosphate and hydroxyapatite (OCP/HA) functionalized withlauroylchlorid	Improve mechanical properties, high bioactivity, neo-vascularisation	Pre-osteoblasticcells (MC3T3-E1)	Intra-dermal implantation in mice	Incorporated into the fiber structured	Souza D.C. et al 2019

	e					
Poly(butylene-adipate-co-terephthalate) (PBAT)	Hydroxyapatite 2-5% w/w	high cell proliferation; formation of mineralized nodules; osteogenesis, bone neoformation, suitable mechanical properties	osteoblast-like MG63 cells	tibia defect model in male rats	Incorporated into the fiber structured	Santana-Melo GF et al 2017
Poly (butylene adipate-co-terephthalate (PBAT)	CNT 0.1-0,5%	Strongly affect mechanical properties; cell proliferation; osteogenesis, formation of mineralized nodules	osteoblast-like MG63 cells		Incorporated into the fiber structured	Rodrigues BVM et al 2016
Tussah silk fibroin	Hydroxyapatite (5% w/w)	Strongly affect mechanical properties; cell proliferation; osteogenesis, mineral deposition	osteoblast-like MG63 cells		Coaxial electrospunfiber: core mineralized	Shao W. et al 2016
PCL/chondrotinsulfate in hydrogel	Bio glass (SiO_2;CaO;P_2O)	Secretion: hyaline like matrix (sGAG; Col II; aggrecan) and mineralized matrix (Calciumdeposition;hypertrophic protein; Col X; osteocalcin)	Goat chondrocytes		Chondroitin sulfate and mineral gradient incorporated. Coating with agar-gelatin hydrogel	Mohan N et al 2015
Chitosan hexamethylene-1,6-diaminocarboxysulfonate (HDACS) or genipin,	nano Hydroxyapatite (1-10% w/w)	Cell adhesion, proliferation, biocompatibility, not significant ALP expression	Pre-osteocyte cell line (MLO-A5)		Incorporated into the fiber structured	Kiechel MA et al 2015
PCL	Nanoclay (0.1%,	Scaffold degradation rate	hMSCs		Incorporated into	Gaharwar

	1% 10%)	improvement; *in vitro* biomineralization; cell attachment and proliferation; osteogenic differentiation by ALP activity and mineralized matrix production			the fiber structured	A. et al 2014
PCL-gelatin B	Mineralized surface linked FN-OCN	Cell adhesion, gene expression and spreading. Osteogenic differentiation, in vivo bone formation	hMSCs	Implantation in parietal bone of the male rats cranium	Mineralized surface by SBF soaking	Lee JH et al 2014
PLGA	MWCNTs (0,1-0,5-1%wt)	Adhesion, viability, mature myotube formation (myosin havy chain)	Murine skeletal muscle cell line C2C12 cells		Incorporated into the fiber structured	Xu et al 2014.
PCL	COOH-MWCNT (0,5-1-2-3% wt)	Cell proliferation adhesion, matrix mineralization, osteogenic expression of alkaline phosphatase (ALP), runt-related transcription factor 2 (RUNX-2), osteocalcin (OCN), osteopontin (OPN), collagen type 1 and bone morphogenetic protein 2 (BMP-2).	Human mesenchymal stem cells (MSCs) from bone marrow		Incorporated into the fiber structured	Jahanmard F et al 2020

Table 3. *Hybrid electrospunfiber as drug delivery system*

ElectrospunFibers	Inorganic component	Results	In vitro test	In vivo test	Development Method	Ref
PCL/gelatin	halloysite/metronidazolo blended with free metronidazolo (25%)	3-week sustained drug release(75%) Antibacterial activity for *Fusobacterium nucleatum*; Cell adhesion and proliferation.	L929 Fibroblast		Incorporation of nanocomposite with free drug	Xue J. e al 2015
PLGA	Halloysite/tetracycline hydrochloride	28 days prolonged release rate (32%), improve mechanical properties; positive cell viability and morphology	Rat fibroblasts		Incorporated into the fiber structured	Qi R et al 2010
PLGA	Laponite/ amoxicillin	Drug release after 2 weeks 63%; effective antibacterial activity, positive cell viability and morphology	porcine iliac endothelial (PIEC) cells		Incorporated into the fiber structured	Wang S. et al 2012
PLGA	Nano-hydroxyapatite/amoxicillin	Drug plateau for 18days at 35%. Improved mechanical properties, cell viability and adhesion	L929 fibroblast		Incorporated into the fiber structured	Zheng et al 2013
PLA/PVP	MWCNTs/TCH 0,1-0,3-0,5%wt	Drug plateau for 2 days from 27 to 41%. Improved fiber diameter, mechanical properties, cell viability	HUVEC		Incorporated into the fiber structured	Bulbul YE et al 2019

PCL	Functionalized MWCNTs/ green tea polyphenols (GTP) 5-10%wt	Lower drug release for lower MWCNT content, osteoblasts proliferation, Inhibition of sarcoma A549 and Hep G2 cells	osteoblasts, sarcoma A549 and Hep G2 cell	Incorporated into the fiber structured	Shao S. et al 2011
Chitosan oligosaccharide/poly(vinyl alcohol	AgNPs	Cell proliferation and adhesion, TGF-β1/Smad signal transduction pathway, collagen synthesis,	Human skin fibroblast (HSF)	One step AgNPs incorporation	Zi-Wei L et al 2017

2. SKIN APPLICATIONS

Skin anatomy

The skin is a multilayer tissue consisting of epidermis, dermis, and the inner subcutaneous (or hypodermis) stratum.

The epidermis is the outer and thinner layer of skin. It is a stratified epithelium lacking blood supply. It is divided in 4 layers made of type keratinocytes at different stage of differentiation. The deepest layer is the basal stratum (populated by basal cells), then the stratum spinosum (prickle cells), the granulosum (granular cells) and the outer stratum corneum. This is a hydrophobic layer, made of stratified a-nucleated dead cells – corneocytes – that are filled and enveloped with keratin filaments, constantly derived from the underlying basal cells. Stratum corneum has 10–15 μm of thick, and the keratin molecules constitute 85% of the total dry weight of the corneum layer.

The melanocytes, Langerhans' cells and Merkel cells, are also present in epidermis layer, for mediating the local immunologic responses and they are formed from the bone marrow. Melanocytes are generated from neural crest and populate basal layer. These cells produce melanin, which protects the deeper stratum of the skin and the nuclei of the keratinocytes from ultraviolet radiation and gives pigmentation to the skin.

The mechanical properties of the skin in terms of strength and elasticity can be affected by hydration state of corneum stratus. The water is primarily captured by the corneocytes, which can control the viscoelastic properties of corneum sheet, through the swelling of the keratin macromolecules.

Dermis is the stratum of the skin under the epidermis basal layer. It is based on a connective tissue which includes hair follicles, sweat glands, sebaceous glands, apocrine glands, lymphatic vessels and capillaries. Also, this region is multilayered, having the upper papillarzone and the deeper reticularzone. The top region is made of loose areolar connective tissue. The under-layered zone is thicker, with dense connective tissue based on high levels of collagen, elastin, glycosaminoglycans and reticular fibers. These macromolecules are responsible for the dermis strength and elasticity. All the connective matrix in dermis is totally produced by the fibroblasts, which play an important role in remodelling the tissue, especially in the wound healing.

The deepest subcutaneous tissue, or hypodermis, is in connection up, with the dermis and down, with the bone or muscle. It is formed by loose connective matrix enriched by adipocytes (50% of body fat), nerves and blood vessels. (Figure 4).

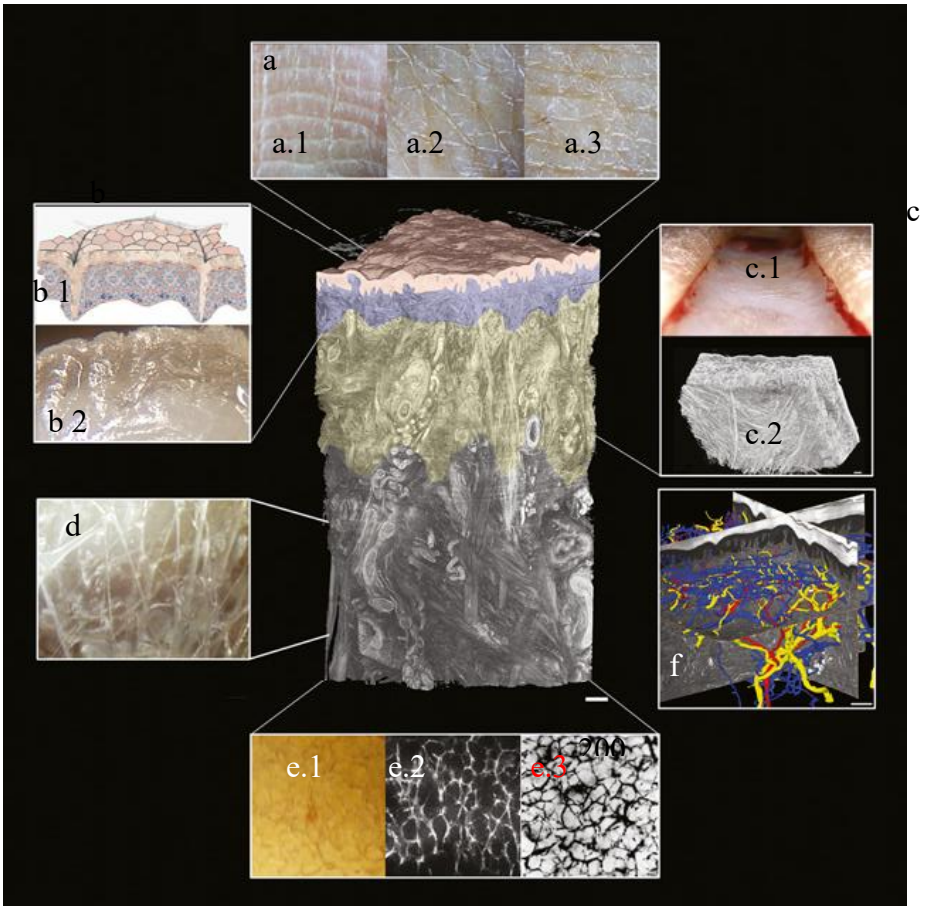

Figure 4*. 3D render skin anatomy of the episcopic imaging. Epidermis in pink; Papillar Dermis in blue; Reticular Dermis in yellow; Hypodermis in white. (a) Surface morphology of Epidermis at different body part: a.1 finger surface with stacked pattern; larger triangular subunits in a.2 hand dorsum and a.3 abdomen. (b)b.1 Epidermis layer from basal epithelium to the upper corneocyte layer hexagonally shaped; b.2 epidermis is visible above (enriched with lucid ceramide) and dermis appear white due to high collagen content. c.1 Skin cut to the Reticular Dermis layer. c.2 Rendered image of Dermis showing collagen fibre network. (200 µm scale). (d) The loose collagenous strata in Dermis. (e) histology of the Hypodermal fat in different imaging type. e.1. endoscopy of fat globules; e.2 fluorescence images of hypodermal fibroelastic fibres;e.3 lymphatics system in hypodermal fat layer. (f) 3D rendering of the skin vascularity and innervation in all the skin thickness; arterial tree configuration (Red), venous plexuses (Blue); nerve endings (Yellow)(Figures adapted with permission from Wong et al 2016; Copyright 2021)*

Hybrid electrospun scaffolds intended for skin reparation

In comparison with the conventional wound dressings, electrospinning technique allowed to create innovative scaffolds, that aim to regenerate skin injuries through tissue

engineering approach. This type of scaffolds was designed to induce a local biological response and provide a tissue replacement by mimicking components and structures of the skin and by coordinating scaffold desorption with new tissue formation.

At this purpose the scaffold in tissue engineering, should meet the following essential requirements: biocompatibility, biodegradability, suitable mechanical properties, bio-mimicking structures and feasibility.

The electrospun nanofiber showed many exceptional properties which make them attractive for the treatment of chronic skin wounds. Firstly the electrospun nanofibers possess a surface-to-volume ratio typically very high. This intrinsic feature causes other consequent and essential properties, such as inter/intra-connected porosity, mechanical anisotropy, and nano-vehiculation.

Beyond their unique features, they exhibited all the usual characteristics, that are common to the conventional wound dressing, such as: to isolate the wound from microbial infection, to be haemostatic, to absorb exudates, to exchange gas and to control moisture and temperature. Moreoversince skin injuries are often subjected to microbial infections, electrospun scaffolds were amply employed, very effective, also as local drug delivery systems.

The tissue engineering capability of electrospun nanofibers, lied precisely in their own fibrous structure, which mimic the extracellular matrix morphology of the dipper dermis layer. The scaffold mechanical properties, biocompatibility and bio-adsorption, are tightly dependent on the polymers used to make up the system. Because electrospinning is a very versatile and relative easy technique, numerous type of polymers can be employed: natural or synthetic or a blend of them. Also the electrospinning process works “in continuous manufacturing” giving the possibility to create fiber hybridized with functional molecules, as inorganic components, that adding to the scaffold superior properties. This technique can even work in aseptic condition, appearing one of the few method scalable for the industrial production.

The material used should confer to the scaffold the stiffness required for clinical application, not only in order to be well integrated in the host tissue, but more specifically for supporting fibroblast adhesion, migration and remodelling with a final scaffold degradation.

. .

Some studies carried on by Atomic Force Microscopy, suggested that fibroblasts achieve maximal spreading and F-actin stimulation at substrate stiffness (elastic Young modulus) not higher than 20 kPa, above which the cellular cytoskeleton reached a saturated level of contraction (Solon et al 2007).

In this way, the electrospun scaffold can support every healing step, by engineering the initial haemostasis and inflammation phases, to the last wound closure, preventing the chronic scar formation.

Clay based electrospunfibers

Thanks to their interesting properties, many studies have been focused on clay-based electrospun scaffold for biomedical application. In general, when the clay/silica are added into polymeric solution, they increase the solution viscosity, as a consequence, the jet becomes more resistant to extensional force during electrospinning. These factors allow to obtain bead-less fibers and cause change in fiber diameters. Thus the employment of clay in electrospinning is used in tissue engineering, with different aims: to control the degradation properties of the resulting electrospun fiber, to obtained bead-less fiber and, to improve the physical chemical properties of the clay-enriched constructs, such as thermal stability, porosity, wet -ability and mechanical properties, by exploiting the specific interaction between clay and polymers (Ji Y et al 2006; Marras S. et al 2008) .

The presence of clays in the electrospunfibers was found to promote better fibroblast adhesion and migration in many works. This result was reported by Qi et al 2012 ,due to the capability of clay based fibers to absorb more proteins than those without clay. The absorbed proteins onto the individual nanofiber surface, clearly provide nutrition for cell growth and proliferation. However, increasing the amount of clay (halloysite up to 5%) the beneficial effect is lost probably, due to the clay aggregation in the fiber matrix (Qi et al 2012).

To conclude the clay can be generally considered suitable in soft and hard tissue engineering application. However additional attention can be devoted to study their biodegradation in the implant site.

Hybrid electrospunfibers as innovative drug delivery in infected skin wound

The inorganic components loaded into the electrospunfiber have been proved also as effective innovative drug-delivery vehicle, for encapsulation and release of drug. When the

drugs bond the inorganic compound, and the nanocomposite obtained is included inside the fiber, the initial burst release of drug, that often occurs from the high surface area of the fibers, was significantly avoided. Coaxial or emulsion electrospinning are two furthertechniques which are able to reduce the burst effect.

Clay as a drug carrier

The clay based nanocomposite are easily incorporated in electrospun nanofibers. The absorption capacity of the clay leads to an easy drug loading. Then clay nanocomposites are mixed in a suitable polymeric mat, and the mineral polymeric solution obtained is electrospun. Many works confirmed that encapsulation of drug in nanocomposite could positively affect fiber mechanical properties, porosity, biocompatibility, drug efficacy and cellular response, by having a synergic effect with the drug release control (García-Villén F et al 2019; Song B. et al 2012 ; Zeng F. et al 2013; Wang S. et al 2012; Qi R. et al 2010). Despite the total drug loaded in a nanocomposite system is lower than this obtained in the free drug mixing, the nanocomposites provide stronger effect for the infection, because also the clay can take part into the antibacterial activity synergically with the drug release, as demonstrated by many authors (García-Villén F et al 2019; Gao Y. et al 2014; Xue J. e al 2015) .

In particular, numerous authors demonstrated the various potentialities in the use halloysite as vehicle of drug (Xue J. e al 2015; Qi R. et al 2010; Lvov Y. et al 2016). Halloysite belongs to Kaolinites groups, is a rolled 1:1 phyllosilicate type, with an external layer negatively charged and an inner layer positively charged. Thanks to its unique shape, halloysite can be filled in the lumen with bioactive molecules or outside on the surface, improving the drug loading capacity. Thus a sequential adsorption of polycations and polyanions polymers on charged clay nanotubes, could be obtained to have a more slow release controlled by the polymeric diffusion layer(Qi R. et al 2010; Lvov Y. et al 2016). Lvov Y. et al. demonstrated that, the end of halloysite tube can be stopped for allowing a more sustained release of a drug for many hours, at percentage lower than 10%. Moreover, the thermal stability of the clay protected the drug degradation at high temperature, and the tube orientation causes an anisotropic gradient inside the scaffold (Figure 5; Lvov Y. et al 2016).

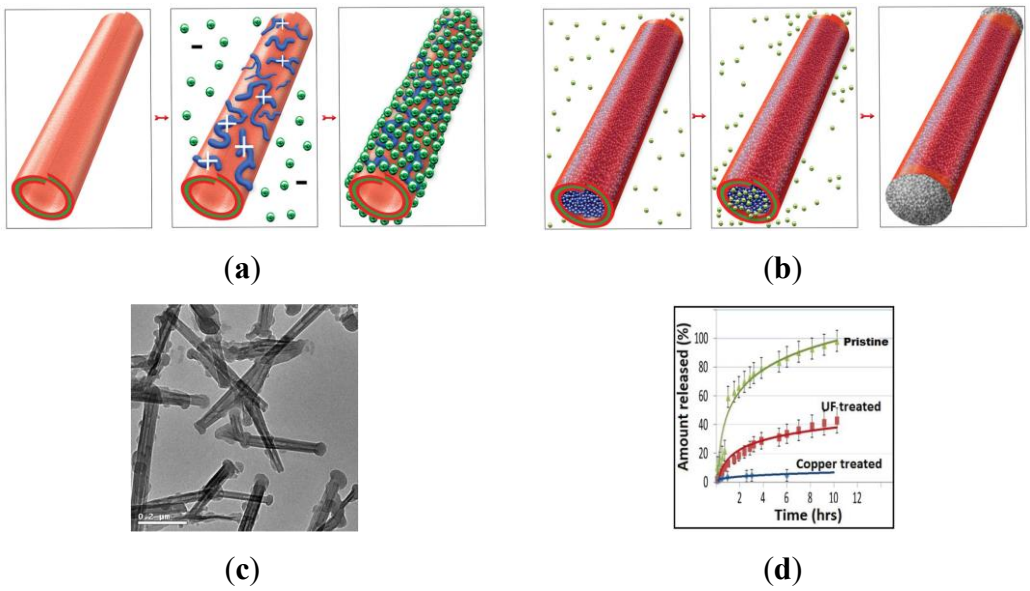

Figure 5. *(**a**) Scheme of polycations/polyanions sequential absorption layer by layer on the halloysite tube and formation of the tube-end stops. (**b**)TEM images of tube opening clogged with glycogen stoppers. (**c**) Comparison of drug release curve from particle, when incapsulated, and when loaded in end-tube stopped (Figures adapted with permission from Lvov Y. et al 2016); Copyright (2021)*

Another form of phyllosilicates is the 2:1 type. Montmorillonite and Laponite, belonging to this 2:1 group, named Smectite group. This type of phyllosilicate is normally used in pharmaceutical applications. Their crystal structure is a sandwich-like system with expanding layer, where cation exchange can take place. Despite a lower drug loading efficiency, in this type of clay / drug interaction, the intercalation occurs between the drug and the clay. This intercalation resulted in a stable and high retention capacity, depending by the pH and ion exchange in release media. (Jung H. et al 2008; Wang S. et al 2012). The "de-intercalation" mechanism, by which drug is released from the clay interlayer space, was studied in the past by Jung H et al (Jung H. et al 2008). They confirmed that simple cations such as Na^+, K^+, Ca^{++}, have a poor ion exchange capability in comparison to H^+, or even to other organic ions with larger charge and molecular size, because they are more capable to facilitate the exchange reaction between clay and biological fluids (i.e. cationic surfactants). This effect is also more evident for hydrophobic or poorly water soluble drugs such as itraconazole (Jung H. et al 2008).

In this context Wang et al obtained a sustained control of the amoxicillin release by intercalating the antibiotic in Laponite clay. The nanocomposite obtained was loaded in

PLGA nanofibers to achieve a reservoir release of 65% of antibiotic in2 weeks (Figure 6; Wang S. et al 2012).

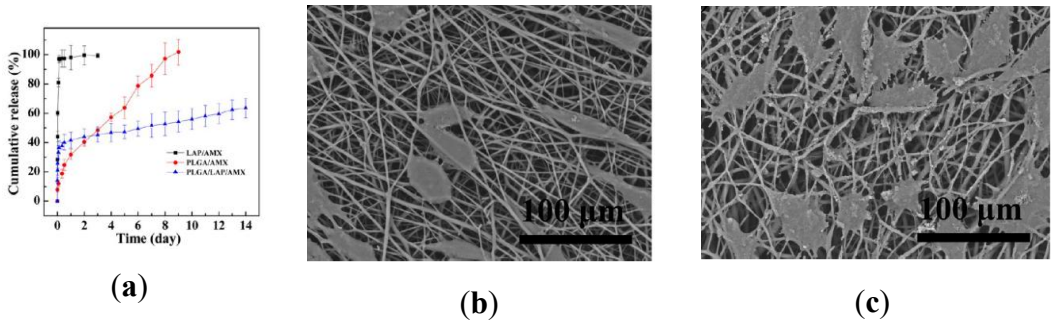

(a) (b) (c)

Figure 6. *(**a**) Amoxicillin (AMX) release in vitro from laponite nano-disks (LAP), PLGA/LAP and PLGA/LAP/AMX nanocomposite. Fibroblasts grown for 3days onto the electrospun scaffold (**b**) PLGA and (**c**) PLGA/LAP/AMX (Figures adapted with permission from Wang Y., et al. 2012; Copyright (2021) American Chemical Society.)*

Hydroxyapatite as drug carrier

Hydroxyapatite well known for its biocompatibility, non-size particles, good spinnability and strong ability to absorb a variety of chemical, is another suitable component for developing active nanocomposite.

However, the weak interaction between drug and n- hydroxyapatite crystals often leads to an initial burst release. The absorption site is positioned between the planar space of the crystal, this bond happens without changing the crystal structure and morphology. The weak bond between drug and hydroxyapatite could be also easy destroy by the pH. However, the burst effect can be limited by including the nanocomposite in the fibers as demonstrated by Zheng F. et al (2013). They developed hybrid electrospun PLGA based nanofibers, loading nano-hydroxyapatite (n-HA) particles absorbed with amoxicillin (AMX). The antibiotic released from HP/PLGA fibers, was characterized by an initial burst release at 16%, and subsequently around 35% for 18 days. The first step was the result of a rapid release of AMX from the PLGA, followed by a second slower release of drug from the HP particles. The double incorporation of AMX, in fiber and in HP, was proven as an efficient strategy to slow down the total release of drug. Moreover, they confirmed cytocompatibility giving additional potentiality of this hybrid system in tissue regeneration (Figure 7, Zheng et al 2013).

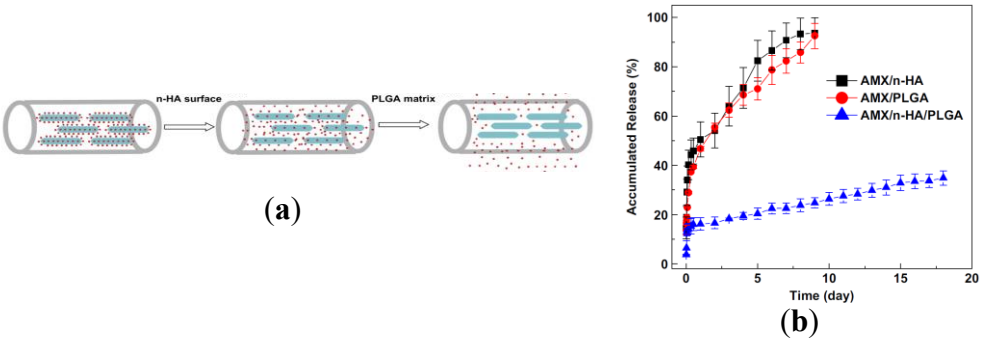

Figure 7 *Schematic representation of the release pathways* ***(a)*** *of amoxicillin (AMX) loaded n-HA inside PLGA nanofibers.****(b)*** *AMX release curves from n-HA particles, from PLGA fibers and n-HA/PLGA hybrid fibers. (Figures adapted with permission from Zheng et al 2013); Copyright (2021) .*

Antimicrobial application of hybrid electrospunfibers in infected skin wounds

Because of high specific surface area, tenable pore size and versatility, the hybrid electrospun nanofibrous have been found suitable delivery systems for the local application of inorganic antibacterial components in the treatment of infected skin wounds.

In order to avoid the burst effect of the antimicrobials released from the fiber surfaces, many strategies have been employed for loading antibacterial components in fibrous membranes. Many inorganic antibacterial components generally are very easily oxidized in air, and they are normally coated with nanostructure or used as precursor that can be converted into the active form for post-treatment; finally, they can be confined in the fiber core (by coaxial electrospinning), or can be absorbed onto the fiber surface (by attachment).The strategies chosen depends on the biocides type used, and their bio-availability, and evaluated on the base of polymer selected for the targeting application, in particularly their degradation rate affecting the particle delivery in the wounds (Gao Y. et al 2014).

Silver based electrospunfibers

The blending approach for incorporating pure AgNP in the polymer matrix is the simplest method commonly used. The most important advantages of this method are the one-step approach to obtain the final product and the possibility to load larger quantities of particles. However, the high loading of AgNP may cause the nanoparticle aggregation, due to their high superficial area (Bramhill J et al 2017). With this method the colloidal solution obtained, can enrich up to 5% AgNPs of the polymer mass. Thanks to the AgNP compatibility with many solvents, many types of synthetic polymers have been blended

with AgNP for electrospinning such as PVDF, PVA, PVA/PU, Nylon6, PLGA, polyacrylonitrile (PAN) and PVP (Yuan J et al 2010; Park J et al 2011; Li W et al 2012; Park S.-W. et al 2009; Hong H. F et al 2011; Xing Z.-C et al 2011; Shi Q. et al 2011; Pant B et al 2012; Hwang S. et al 2011; Yang Q et al 2003) However few studies have been still carried out in the use of natural polymers (Zi-Wei L et al 2017; Sandri et al 2019).

An interesting study of this year was conducted by Zi-Wei L et al. to clarify the specific biological mechanisms promoted by AgNPs-nanofiber for the wound healing. They incorporated chitosan oligosaccharides (COS)/Ag nanoparticles in PVA polymer for electrospinning. The human skin fibroblast response was studied treating the cell with the supernatant derived by the nanofiber at different concentrations. They proved that PVA/COS-AgNP nanofibers promoted the secretion of fibroblast transforming growth factor TGF-β1, within improving their adhesion and proliferation, by inducing the S and G2/M cycles in cells. Moreover, the nanofiber treatment significantly up-regulated the collagen and fibronectin synthesis in a dose-dependent manner. Finally, they confirmed that PVA/COS-AgNP nanofibers activated the key signal TGF-β1/Smad transduction, that is an important pathway affecting the early stages of wound healing (Zi-Wei L et al 2017).

Despite of the promising outcomes obtained by Zi-Wei L et al, further studies must be performed to evaluate the cellular response of AgNPs/nanofiber onto the dermal cellular growth, especially in function of the metal concentrations. (Destaye et al 2013; Zienkiewicz-Strzałka M et al 2019; Li W. et al 2012; Pan B. et al 2012)

3. BONE APPLICATIONS

Bone anatomy

The bone is a dense connective tissue composed by two different zone: the corticaland the spongy-like part. It is populated by osteoblasts and osteocytes involved in the matrix production, and osteoclasts involved in the bio-adsorption of the tissue. The extracellular matrix consists of 70% of mineral phase, mainly hydroxyapatite, and 30% of ossein, mainly collagen fibers.

The bone cortical zone is the outer and harder compact area, the 80% of the total bone mass. It is constituted by osteon functional units, which are micro-tube having a central hole for blood vessels passage. Each osteon includes concentrically oriented lamellae of

matrix forming lacunae, where the cells live. Normally after bone fractures the cells are unable to recreate the native aligned lamellae, but rather a woven tissue with more fibrous compositions and weaker. This cortical part is covered by a bi-layered membrane: the periosteum and the vascular endosteum sheets.

The sponge –like part, or trabecular bone, is the internal centre of the bone. It is a porous tissue, with randomly spread empty areas. It is greatly vascularised, because often contains the red bone marrow, where hematopoiesis takes place. This central zone is crucial for the calcium ions exchange. In fact bone tissue during all human life, is constantly under remodelling, for regulating the calcium homeostasis (Figure 8).

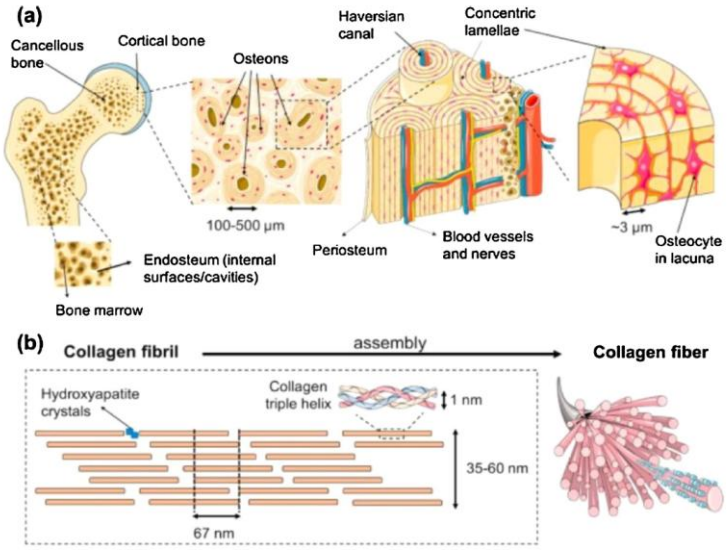

Figure 8 *Bone histology images (a-b). a) Bone structure from macro to micro scale size. b)Bone ECM constituted collagen fiber nucleated by hydroxyapatite crystals. (Figures adapted with permission from Shuai C et al 2020); Copyright (2021)*

Large experiments recorded the compressive force and young modulus of cortical bone, in the range of 100-150 MPa, and 5-15 GPa respectively in the direction of the osteon major axis. The same parameters in the perpendicular direction are 2 times lower. The trabecular bone possesses the respective parameters an order of magnitude 10 times lower.

Hybrid electrospun scaffolds intended for bone application

In tissue engineering, electrospun scaffolds are an emerging tool studied for obtained biomimetic scaffolds having the suitable features for a bone insertion. Electrospunfibers could be developed for being easily integrated in the hard bone, but mechanically strong.

The fibrous structures could mimic the lamellar alignment of the matrix in the cortical area, or the randomly orientation of the trabecular part. They could be composed by high concentrations of mineral phase, or loaded with drugs, magnetite or biomolecules. The fibrous arrangement also supplies a controlled porosity for cell migration.
Bones posse a high compressive force around 150-200 MPa, tensile force around 100-120 MPa and poor resistance to shear stress (50 MPa), however the constant turnover of the bone, makes this tissue particularly ductile. For this reason the use of bio-resorbable materials for designing scaffold, is currently a challenge.

Clay based electrospunfibers

The clay possesses unique physical-chemical features such as high specific surface area, adsorption capacity, ion exchange capacity. These properties conveyed to use clays as promising bioactive materials in tissue engineering, especially in mineralized tissue application (Bramhill J et al 2017). The nano-clay bioactivity is even increased especially when nano-clay are loaded in suitable electrospun nanofibers. In fact the resulted hybrid electrospunfibers show superior physical and mechanical properties. This is due by their high surface area of interaction.
Their great chemical physical stability also favours their employment in electrospinning technique, where few amounts of clay added, are needed to reach the required scaffold properties, and at these low concentrations, the clays are not toxic in vivo. At a suitable concentration, clays can promote cell spreading, for both soft and hard tissues, and were found to be osteo-inductive in stem cell culture. Gaharwar A. et al showed that the PCL/clay based scaffold promoted osteogenic differentiation on stem cell (MSCs) by increasing alkaline phosphatise activity, along with the production of mineralized matrix (Figure 9, Gaharwar A. et al 2014). The osteogenic effect increased in a concentration dependent manner with the clay concentration at 10%w/w. The tensile modulus appropriate for stem cell growing, was recorded between 1-5 MPa.

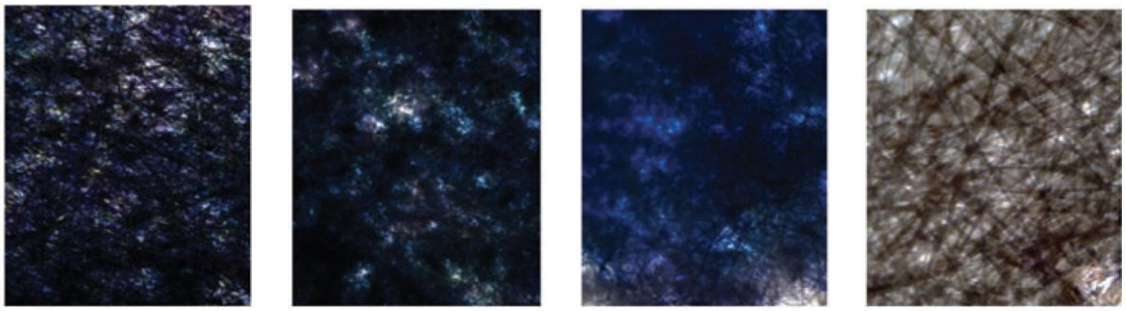

Figure 9. *Effect of nanoclay loaded at* ***(a)*** *10% (b) 1% (****c****) 0.1% in* ***(d)*** *PCL fibers on osteogenic differentiation of hMSCs (purple staining) (Gaharwar A. et al 2014).*

Nitya et al 2012 also proved the osteogenic effect derived by Halloysite nanoclay loaded in fiber. The authors suggested that the silicon, existing normally in the clay, participates in cell metabolism, and produces ions which are able to activate the bone related gene expression.

Other recent studies verified how curvature of the substrate influenced osteogenesis. Ozdemir T et al demonstrated that increased stem cell differentiation growing on fibrous rough topography, was due to the acto-myosin contractility and intracellular stiffness via GTPase-RhoA activation. The study was carried on osteoprogenitor cell line, and demonstrated that Myosin IIa was the key protein promoting the early osteogenic differentiation (Figure 10).

This study lets speculate that, also the rough fiber surface induced by the clay incorporation, can act on the cytoskeleton contractility by activating specific proteins.

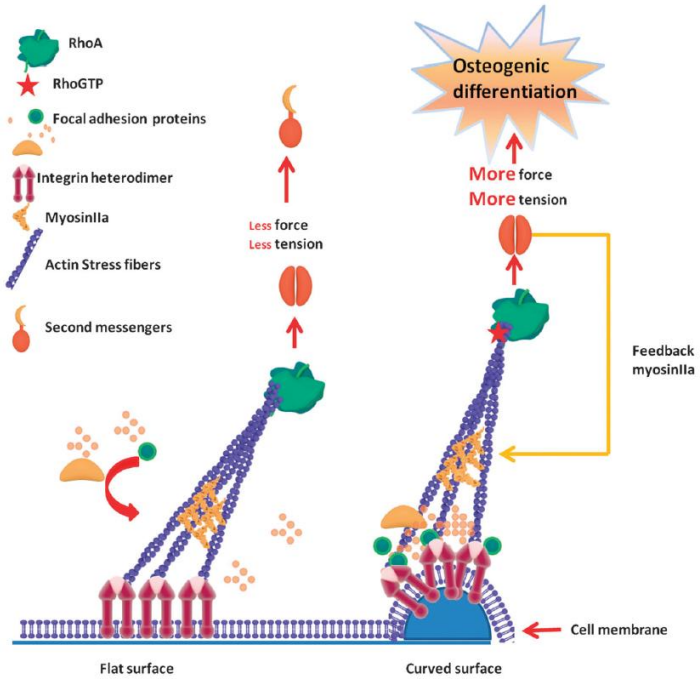

Figure 10 *Schematic images of GTPase-RhoA pathway mediating cell osteogenesis. The focal adhesion proteins group generates different actin stress onto the curved topography in comparison with the flat surface (Figures adapted with permission from Ozdemir T et al 2013); Copyright (2021)*

4. TENDON-LIGAMENT APPLICATION

Tendon and ligament anatomy

The ligaments and tendons are dense regular fibrous connective tissues, made of hierarchical arrangement of collagen bundles. This architecture includes tendon units, which run parallel to the geometrical axis and are responsible for the tendon tensile strength. Each tendon unit includes fascicles, which are covered by the endotenon sheet, enriched with nerves and blood vessels. Each fascicle contains fibril bundles (or sub fascicle), with 15-50 mm of diameter. The bundles in turn, are made of fibrils with around 1 µm of diameters. The collagen (type I) fibers with 50-500 nm of diameters, are the constitutive molecules of fibrils. Outside the tendon is localized the epitenon membrane, which is surrounded by the paratenon, the outersheet. Fluid can be found between the paratenon and the epitenon,preventing friction.

Tenocytes and tenoblasts populate the tendon. The cells amount is relatively low, and the cell turnover is minimum, for this reason the healing process in tendon-ligament is really

long and painful. The tenocytes are involved in the production of the extracellular matrix, they secrete vesicles of tropocollagen which spontaneously assemble into insoluble fibrils. The total dry weight of the extracellular matrix is constituted by 85% of aligned collagen fibers type I, 5% of proteoglycans (PGs), 2% of elastin, 0.2% of inorganic components (copper, magnesium and calcium) and the residual part of minor collagen types such as II, III, IV, V, VI, IX and X, which are anyway really essential for tendon functionality.

The PGs are macromolecules consisting of protein linked with glycosaminoglycans (GAGs) polysaccharides. These macro-molecules are interwoven with the collagen fibers, throughout the GAGs side chains, which establish reversible cross-linking between fibrils. Moreover, thanks to their hydrophilicity, GAGs are able to absorb water conferring resistance to compression/elongation. The water homeostasis influences tissue mechanical properties, in terms of tensile stress, compressive and elastic forces. However, since tendon and ligament are involved cyclically in energy storage and transmission, the matrix constantly undergoes to continuous reversible reorganization. Especially the GAGs, which establish non-covalent bound with fibrils, frequently break and reform bridges between fibrils. (Figure 11). The matrix re-arrangement is cyclically influenced by external mechanical loading, which transmits signals to the cells for changing even their genetic expression. This phenomenon pass through the cellular cytoskeleton deformation, which mediates in cascade: the focal adhesion sites, the integrins cell- cell junctions, and the ion channels activation, until arriving to the intracellular G-protein involved in the nuclear signalling. The resulted cell-matrix dynamic interaction confers viscoelastic property to the tissue.

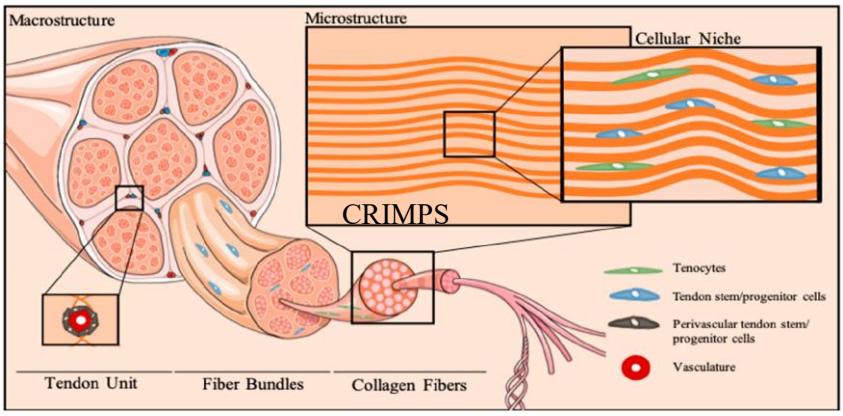

Figure 11 *Schematic representation of the tendon tissue organization. From the macro to nano-structure architecture(Costa-Almeida R et al 2019).*

All the studies about the mechanical behaviour of the tendon, are in agree to define the tissue as an imperfect elastomer, with time-dependent viscoelastic behaviour. Its viscoelasticity is not linear and is defined by low Young's Modulus values at small strains and high values at higher strains.

The tendon under tensile stress exhibits the typical sigmoid stress-strain curve (Figure 12), when the load is in line with the fiber direction. In fact, tendon tissue, for its hierarchical arrangement, is highly anisotropic. In the very low stiffness region (toe region) of the stress-strain curve, the crimp structures are stretched. 0-1% is the strain range where the tendons are completely elastic. Above this point, the strain applied requires the sliding of the collagen fibers (heel region), showing high slope until 2% of extension. In this region the tendon shows plastic behaviour. The final phase is the linear region, where the deformation is irreversible and proportional to the strain applied up to the break of the collagen fibres. Here the tissue possesses viscous property (Figure 12).

Tendons typically arrive to the ultimate stress of broken in the 50-100 MPa range at 4-10% of strain, with Young Modulus of 1-2 GPa, but it can change a lot depending on the tendon type and shape (Morais et al 2015).

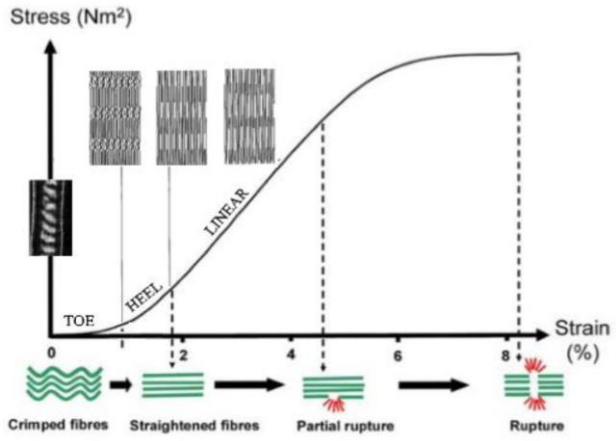

Figure 12 *stress- strain curve of the tendon (Figures adapted with permission from Fratzl P et al.1997); Copyright (2021)*

Tendon to bone interface tissue

The tendon to bone insertion is a region highly specific named enthesis. It acts as a shock-absorber of the mechanical load transmitted from tendon/ligament to the bone in joint movement. Two types of enthesis exist: the direct and the indirect insertion. The direct

type is characterized by fibrous dense connective tissue attached to the bone trough the periosteum sheet. For this reason, this type of attachment is more vascularised.

In the indirect enthesis, the tendon – ligament is directly connected with the bone, where the periosteum membrane is discontinuous. The indirect enthesis, exhibits 4 zones in gradient: the first is the tendon with aligned collagen fiber (type I). The second is a fibro-cartilagineous tissue, with higher level of collagen type II and III. The third is a hybrid tissue of mineralized fibro-cartilagineous tissue, where hydroxyapatite and collagen type II are gradually combined. The last zone is the bone having low amount of collagen I e mineral.

The tidemark between the mineralized fibrocartilagen (zone 3) and the not mineralized fibro-collagineous tissue (zone 2) is frequently involved in damage between the soft and hard tissues. This is due to the localization of this type of insertion, that is found in the anatomical site more subjected to cyclically mechanical loading, such as Anterior Cruciate ligament, Rotator cuff and Achille's tendon (Figure 13).

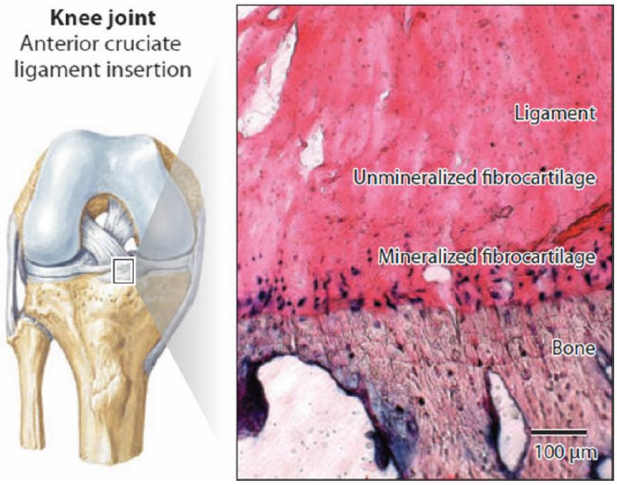

Figure 13*Anterior Cruciate ligament insertion to the bone. Direct enthesis tissue with gradual mineralization. (Figures adapted with permission from Atesok K et al 2016); Copyright (2021)*

Electrospun hybrid scaffold intended for tendon/ligament reparation

Tendon-ligament healing processes can be divided in three phases. The first phase is the inflammation, in which the macrophages remove necrotic cells, and where the hematoma occurs in the site of injury. The second phase is the cellular phase, where tenocytes start the synthesis of collagen and all the proteins required for extracellular matrix reorganization. In this phase neoangiogenesis occurs. The last phase is the remodelling

one, when the newly synthesized collagen fibres align their self with the tendon axis. During this last phase GAGs play important role in ECM regulation and bonding with growth factors.

The common surgical treatments of tendon-ligament full lacerations consist in arthroscopically rerouting of the injured ligament across drill holes in the bone, in order to imitate the original attachment. However, in all the cases, these treatments cause the formation of a scar tissue, with minor functionality. The full recovery of the surgical treatments should be supported by optimal scaffolds able to assist all the healing phases.

Moreover, the ideal scaffold should be relatively simple, involve minimal tendon handling, should contain both a core and peripheral structure.

The history of the surgical scaffolds for ligament reconstruction included many types of grafts, that led to the recent tissue engineering approach. The first types of grafts were allo/xenograft or aoutogenous tissue grafts, subsequently the artificial ligaments were explored, which entered in trials until the1950s; lastly the “decellularized” tendons were invented, which enhanced to explore a new tissue engineering approach. Decellularization procedures were explored for avoiding the negative immune response observed in human after implantation of allo or xenografts. However, the immune reaction was not the only problem faced using tissue grafts, in fact they also needed to be organized in tissue banks and sterilized adequately for maintaining cell viability and tissue strength.

Thanks to their capability to be more available and strength, and to be equipped with suitable sutures, the artificial ligaments acquired much more emerging interest, in order to covering that drawbacks noted using animal or human tissue grafts. However the artificial ligaments, early observed in clinical studies, showed considerable lack of biocompatibility and biodegradation, in many cases.

At the turn of 20th century, the tissue engineering method started to explore the combination of endogenous cells or proteins, conjugated with functional biomimetic and biodegradable scaffolds, in the effort of improving the scaffold integration in the host, and the intrinsic personalised treatment.

The tissue engineering research have considered the biodegradable and bio-mimicking materials, the ultimate challenge for tendon/ligament reconstruction, because they allowed the initial cell adhesion, the consequent cell-cell interaction and their last differentiation. These passages imply that the scaffold guides a new functional tissue by mimicking the native tissue structure, with simultaneous absorption.

In this context, the electrospun nano/micro fibers found tremendous matching in tendon surgical reconstruction.

Firstly because the tendon and ligament are essentially composed by hierarchical aligned collagen fibers, with few fibroblast population, the electrospun nanofibers showed the ideal morphology for better resemble the native tendon extracellular matrix, also due to the possibility to be typically designed with fiber aligned in direction with the collagen fascicles. In particular the most interesting feature of the electrospun nanofibers, was found in their anisotropic mechanical property, which was extremely important for designing a musculoskeletal system: not only because it offered a support for modelling the cells in alignment with the structural axes, but even because it could drive the cellto build viscoelastic fully functional matrix, by reproducing the same mechanical properties of the native tendon, without causing damaging frictions.

Secondarily electrospinning technique can use very different type of polymers, allowing to creates biodegradable and biocompatible fibrous structures. For this reasons electrospun nanofibers become suitable scaffold to be loaded with biological modulator, such as growth factor or stem cells, or hybridized with further functional nano-components (such as inorganic particle, nanoparticles and drugs), which could influence more locally the cell pathway.

Lastly electrospinning presented some advantages compared with the other previous methods: it is cheaper, scalable, and easier to be sterilized, thanks to its typical assessment in continuous manufacturing.

However before developing electrospun scaffolds for muskoloskeleton reparation, special observations should to be considered about the desired mechanical properties. They should match the time dependent-viscoelastic and anisotropic mechanical behaviour of the in vivo tendon, exhibiting non linear profile in a stress-strain curve. The in vivo tendons mechanical values, can change a lot depending from type, thickness and patient gender or age. However it was possible estimate a range of numeric values where the bio-mechanical characteristics of the native tendon have been generally expressed, and where the developed scaffold can referred. They are: the Ultimate Stress values (or maximum force before break), that express the scaffold stiffness, normally expected between 5-100 MPa; the Ultimate Strain values, (or elongation maximum at the break), which show the irreversible deformability of the tissue, generally among 4-10%;the Young’s Modulus, (the slope value of the tangent line to the stress-strain curve), which gives an idea of the

viscoelastic properties and significant for the ligaments loaded cyclically, reported between 20-1200 MPa. (Laranjeira Met al 2017; Youngstrom D.W. et al 2015; Morais D.S. et al 2015; Walsh W.R. 2007)

The developed scaffold after implantation, should assisted all the mechanical load required by the host tissue, in order to supporting the mechano-transduction signals between the cell and cell-matrix. They seems a key factors for controlling cell phenotype, proteins synthesis and eventually change in matrix arrangement. Therefore the long-term success of the implantation also depend by effective post-surgery rehabilitation protocols which could dramatically influence the final healing process.

5. FINAL REMARKS

Extensive studies were devoted to the development of electrospun hybrid scaffold enriched with inorganic components. They have been proposed as medical device in regenerative medicine and tissue engineering, in both soft and hard tissue applications. They are explored also in drug delivery system, with significant results for clay and hydroxyapatite as drug carriers, when they are nanocomposite crystals loaded in electrospun nanofibers. In this case, the drug delivery can be strongly controlled from the nanocomposite, as well as the nanofibrous structures.

In the development of hybrid electrospun scaffold, relevant criticalities emerged in the quantity of inorganic fillers that can be loaded. Too high metal content can destroy the fiber structure or induce thick mineral layer onto the fiber surface, which impairs the cellular interaction. In every case, a suitable mineral concentration exists for supporting the fibrous texture, with the appropriate stiffness for the cellular response.

The type of inorganic fillers selected must be compatible with the polymer forming the fibers, also must be stable towards temperature, pH, oxidation level and solvent used in the development process. Finally, they should be biocompatible, possibly able to induce positive cellular responses and to be bioresorbable. Numerous studies focused hard tissues as the favourite site for the application of hybrid mineral scaffolds, however emerging results have showed that the same inorganic components, are promising also for the soft tissue application, in particular the angiogenesis and nerve stimulations.

The mechanisms of interaction between the hybrid fibers and the cells are still partially unknown. But the major of them have been identified in actin activation, via mechano-transduction signals, in the extracellular matrix deposition, via biomimetic cues, and lastly in the alteration of the gene expression, throughout control of ROS level, or link with proteins (fibronectin or albumin), or via ATPase protein activation.

In conclusion in this multifaceted scenario, big steps have been made for employing different inorganic filler with different polymers, but few studies highlighted the new potentiality of these systems in controlling the specific tissue functionality.

REFERENCES

1. Ahmad F., Al-Douri Y., .Kumar D., Ahmad S. Metal-oxide powder technology in biomedicine. Metal Oxide Powder Technologies (2020). pp 121-168
2. Andric T.; Wright LD.; Taylor BL.; Freeman JW. Fabrication and characterization of three-dimensional electrospun scaffolds for bone tissue engineering. J. Biomed. Mater. Res. A. (2012) 8: 2097-105
3. Atesok K, Doral MN, Karlsson J, Egol KA, Jazrawi LM, Coelho PG, Martinez A, Matsumoto T, Owens BD, Ochi M, Hurwitz SR, Atala A, Fu FH, Lu HH, Rodeo SA. Multilayer scaffolds in orthopaedic tissue engineering. Knee Surg Sports TraumatolArthrosc. (2016);24(7):2365-73
4. Bramhill J, Ross S, Ross. Bioactive Nanocomposites for Tissue Repair and Regeneration: A Review. Int. J. Environ. Res. Public Health (2017), 14: 66;
5. Bulbul YE, Eskitoros-Togay ŞM, Demirtas-Korkmaz F, Dilsiz N. Multi-walled carbon nanotube-incorporating electrospun composite fibrous mats for controlled drug release profileInt J Pharm.(2019)
6. Calejo I, Costa-Almeida R, Reis RL, Gomes ME. A Textile Platform Using Continuous Aligned and Textured Composite Microfibers to Engineer Tendon-to-Bone Interface Gradient Scaffolds. Adv Healthc Mater. (2019);8(15):e1900200
7. Chae T. Yang H, Ko F, Troczynski T. Bio-inspired dicalcium phosphate anhydrate/poly(lactic acid) nanocomposite fibrous scaffolds for hard tissue regeneration: in situ synthesis and electrospinning. J Biomed Mater Res A. (2014) 102(2): 514-22

8. Chi N, Wang R. Electrospun protein-CNT composite fibers and the application in fibroblast stimulation. BiochemBiophys Res Commun. (2019) 504(1):211-217
9. Contreras-Cáceres R, Cabeza L, Perazzoli G, Díaz A, López-Romero JM, Melguizo C, Prados J. Electrospun Nanofibers: Recent Applications in Drug Delivery and Cancer Therapy. Nanomaterials (Basel). (2019) 24;9(4):656
10. Costa-Almeida R, Calejo I, Gomes ME. Mesenchymal Stem Cells Empowering Tendon Regenerative Therapies. Int J Mol Sci. 20 (2019) : 3002
11. Cui W,. Li X,. Zhou S,.Weng J, Degradation patterns and surface wettability of electrospun fibrous mats, Polym. Degrad. Stab. 93 (2008) 731–738.
12. Cui W., Li X., Xie C., Zhuang H., Zhou S., Weng J. Hydroxyapatite nucleation and growth mechanism on electrospun fibers functionalized with different chemical groups and their combinations. Biomaterials (2010) 31: 4620-29
13. Das S. K.,.Marsili E. Bioinspired Metal Nanoparticle: Synthesis, Properties and Application. Nanomaterials (2011) pp 254-278
14. Day RM, Boccaccini AR, Shurey S, Roether JA, Forbes A, Hench LL, et al. Assessment of poly(glycolic acid) mesh and bioactive glass for soft tissue engineering scaffolds. Biomaterials. (2004). 25:5857–5866.
15. Destaye A.G, Lin C.-K.,. Lee C.-K, Glutaraldehyde vapor cross-linked nanofibrous PVA mat with in situ formed silver nanoparticles, ACS Appl. Mater. Interfaces 5 (2013) 4745–4752.
16. Eivazi Zadeh Z, Solouk A, Shafieian M, HaghbinNazarpak M. Electrospun polyurethane/carbon nanotube composites with different amounts of carbon nanotubes and almost the same fiber diameter for biomedical applications. Mater Sci Eng C Mater Biol Appl. (2021) 118:111403
17. Faccendini A, Ruggeri M, Miele D, et al. Norfloxacin-Loaded Electrospun Scaffolds: Montmorillonite Nanocomposite vs. Free Drug. Pharmaceutics. (2020)12:1-25
18. Faccendini A, Vigani B, Rossi S, et al. Nanofiber Scaffolds as Drug Delivery Systems to Bridge Spinal Cord Injury. Pharmaceuticals (Basel). (2017);10(3):63
19. Franca E, Jao PF, Fang SP, et al. Scale of Carbon Nanomaterials Affects Neural Outgrowth and Adhesion. IEEE Trans Nanobioscience. 2016;15(1):11-18
20. Fratzl P., Misof K., and Zizak I. Fibrillar Structure and Mechanical Properties of Collagen. J. Struc. Bio. (1997) 122: 119-122,

21. Frohbergh ME; Katsam A.; Botta GP; Lazarovici P.; Schauer CL; Wegst UG.; Lelkes PI.; Electrospun hydroxyapatite-containing chitosan nanofibers crosslinked with genipin for bone tissue engineering. Biomaterials (2012) 33: 9167-78
22. Fu-Chen Kung, Chi-Chang Lin, Wen-Fu T Lai. Osteogenesis of Human Adipose-Derived Stem Cells on Hydroxyapatite-Mineralized Poly(lactic Acid) Nanofiber Sheet. Mater Sci Eng C Mater Biol Appl.(2014) 45: 578-88
23. Gaharwar AK, Mukundan S, Karaca E, Dolatshahi-Pirouz A, Patel A, Rangarajan K, Mihaila SM, Iviglia G, Zhang H, Khademhosseini A. Nanoclay-enriched poly(ε-Caprolactone) electrospun scaffolds for osteogenic differentiation of human mesenchymal stem cells. Tissue Eng Part A, 20: 2088-101 (2014)
24. Gao Y., Bach Truong Y., Zhu Y., Louis Kyratzis I. Electrospun antibacterial nanofibers: production, activity, and in vivo applications. Journal of Appl. Polym. Science, (2014). 131: 18.
25. García-Villén F, Faccendini A, Aguzzi C, et al. Montmorillonite-norfloxacin nanocomposite intended for healing of infected wounds. Int J Nanomedicine. (2019)14:5051-5060.
26. Gorain B, Choudhury H, Pandey M, Kesharwani P, Abeer MM, Tekade RK, Hussain Z. Carbon nanotube scaffolds as emerging nanoplatform for myocardial tissue regeneration: A review of recent developments and therapeutic implications. Biomed Pharmacother. (2018) 104: 496-508.
27. Hong, H. F.; Jeong, S. J. Nanosci. Nanotechnol. Effect of Nano Sized Silver on Electrospun Nylon-6 Fiber (2011) 11: 372-376
28. Hong, K. H.; Park, J. L.; Sul, I. H.; Youk, J. H.; Kang, T. J. J. Polym. Sci., Part B: Polym. Phys. 2006, 44, 2468−2474.
29. Hwang, S.; Jeong, S. J. Electrospun Nano Composites of Poly(vinyl pyrrolidone)/Nano-Silver for Antibacterial Materials. Nanosci. Nanotechnol. (2011) 11, 610
30. Jahanmard F, BaghbanEslaminejad M, Amani-Tehran M, et al. Incorporation of F-MWCNTs into electrospun nanofibers regulates osteogenesis through stiffness and nanotopography. Mater Sci Eng C Mater Biol Appl. (2020) 106:110163.
31. Jeong J.S., Moon J.S., Jeon S.Y., Park J.H., Alegaonkar P.S., YooJ.B.. Mechanical properties of electrospun PVA/MWNTs composite nanofibers. Thin Solid Films. (2007). 515: 5136-41.

32. Jeong J.S., Moon J.S., Jeon S.Y., Park J.H., Alegaonkar P.S., YooJ.B.. (2007). Mechanical properties of electrospun PVA/MWNTs composite nanofibers. Thin Solid Films. 515 (2007) 5136-5141
33. Ji Y, Li B, Ge S,. Sokolov J C,.Rafailovich M H. Structure and Nanomechanical Characterization of Electrospun PS/Clay Nanocomposite Fibers.Langmuir (2006) 22: 1321-1328
34. Joshi M.K, Tiwari A.P.,. Pant H.R,. Shrestha B.K, Kim H.J.,. Park C.H,. Kim C.S, In situ generation of cellulose nanocrystals in polycaprolactone nanofibers: effects on crystallinity, mechanical strength, biocompatibility, and biomimetic mineralization, ACS Appl. Mater. Interfaces 7 (2015) 19672–19683.
35. Joshi M.K,. Tiwari A.P, Pant H.R., Shrestha B.K.,. Kim H.J. Park, C.H, Kim C.S., In situ generation of cellulose nanocrystals in polycaprolactone nanofibers: effects on crystallinity, mechanical strength, biocompatibility, and biomimetic mineralization, ACS Appl. Mater. Interfaces 7 (2015) 19672–19683.
36. Jung, H.; Kim, H. M.; Choy, Y. B.; Hwang, S. J.; Choy, J. H. Int. Laponite-based nanohybrid for enhanced solubility and controlled release of itraconazole Int. J. Pharm. (2008) 349: 283−290.
37. Jung, H.; Kim, H. M.; Choy, Y. B.; Hwang, S. J.; Choy, J. H. Itraconazole–Laponite: Kinetics and mechanism of drug release Appl. Clay Sci. (2008) 40: 99−107.
38. Keshaw H, Forbes A, Day RM. Release of angiogenic growth factors from cells encapsulated in alginate beads with bioactive glass. Biomaterials. (2005); 26:4171–4179.
39. Kiechel MA, Beringer LT, Donius AE, Komiya Y, Habas R, Wegst UG, Schauer CL. Osteoblast biocompatibility of premineralized, hexamethylene-1,6-diaminocarboxysulfonate crosslinked chitosan fibers. J Biomed Mater Res A. (2015) 103 : 3201-11.
40. Kim GM, AsranASh, Michler GH, Simon P, Kim JS. Electrospun PVA/HAp nanocomposite nanofibers: biomimetics of mineralized hard tissues at a lower level of complexity. BioinspirBiomim.(2008) 3: 046003.
41. Krishna L, Dhamodaran K, Jayadev C, Chatterjee K, Shetty R, Khora SS, Das D. Nanostructured scaffold as a determinant of stem cell fate. Stem Cell Res Ther. (2016), 7(1):188.

42. Lee JH, Park JH, El-Fiqi A, Kim JH, Yun YR1, Jang JH, Han CM, Lee EJ, Kim HW .Biointerface control of electrospun fiber scaffolds for bone regeneration: engineered protein link to mineralized surface. Acta Biomater. 10:2750-61 (2014)
43. Li -YuanX.,Xia Y.,Coating electrospun poly(epsilon-caprolactone) fibers with gelatin and calcium phosphate and their use as bio-mimetic scaffolds for bone tissue engineering.Langmuir. (2008) 24:14145-50.
44. Li X,. Cheng R,.SunZ,.SuW,. Pan G,. Zhao S, Zhao J.,. Cui W, Flexible bipolar nanofibrous membranes for improving gradient microstructure in tendon-to-bone healing, Acta Biomater. 61 (2017) 204–216.
45. Li, W.; Wang, J.; Chi, H.; Wei, G.; Zhang, J.; Dai, L. Preparation and antibacterial activity of polyvinyl alcohol/regenerated silk fibroin composite fibers containing Ag Nanoparticles. J. Appl. Polym. Sci. (2012) 123: 20-25
46. Liao H, Qi R, Shen M, et al. Improved cellular response on multiwalled carbon nanotube-incorporated electrospun polyvinyl alcohol/chitosan nanofibrous scaffolds. Colloids Surf B Biointerfaces. (2011) 84(2):528-53
47. Liao JL, Zhong S, Wang SH, et al. Preparation and properties of a novel carbon nanotubes/poly(vinyl alcohol)/epidermal growth factor composite biological dressing. Exp Ther Med. 2017;14(3):2341-2348
48. Lipner J., Boyle J.J , Xia Y, Birman V,. Genin G M, Thomopoulos S. Toughening of fibrous scaffolds by mobile mineral deposits. Acta Biomater. (2017) 58: 492-501
49. Liu Y,. Lu J,. Xu G,. Wei J,. Zhang Z,. Li X, Tuning the conductivity and inner structure of electrospun fibers to promote cardiomyocyte elongation and synchronous beating, Mater. Sci. Eng. C 69 (2016) 865–874.
50. Liu, F., Guo, R., Shen, M., Cao, X., Mo, X., Wang, S. H., et al. Effect of the porous microstructures of poly (lactic-co-glycolic acid)/carbon nanotube composites on the growth of fibroblast cells. Soft Materials (2010). 8(3), 239–253.
51. Luo Y, Wang S, Shen M, et al. Carbon nanotube-incorporated multilayered cellulose acetate nanofibers for tissue engineering applications. CarbohydrPolym. (2013) ; 91:419-427
52. Lvov Y., Wang W., Zhang L., Fakhrullin R. Halloysite clay nanotubes for loading and sustained release of functional compounds. Expert Opin. Drug Deliv, (2016) 28: 1227–1250.

53. Laranjeira M., Domingues R.M.A., Costa–Almeida R., Reis R., Gomes E. 3D mimicry of native-tissue-fiber architecture guidestendon-derived cells and adipose stem cells intoartificial tendon constructs. Small (2017), 13: 1-13
54. Marino, A.; Tonda-Turo, C.; De Pasquale, D.; Ruini, F.; Genchi, G.; Nitti, S.; Cappello, V.; Gemmi, M.; Mattoli, V.; Ciardelli, G.; et al. Gelatin/nanoceria nanocomposite fibers as antioxidant scaffolds for neuronal regeneration. Biochim. Biophys. Acta (BBA)—Gen. Subj. (2016) 1861: 386–395.
55. Marras SI,.Kladi KP, Tsivintzelis I., Zuburtikudis I., Panayiotou C. Biodegradable polymer nanocomposites: The role of nanoclays on the thermomechanical characteristics and the electrospun fibrous structure. Acta Biomaterialia (2008), 4:756–765
56. Masoudi Rad M, Nouri Khorasani S, Ghasemi-Mobarakeh L, et al. Fabrication and characterization of two-layered nanofibrous membrane for guided bone and tissue regeneration application. Mater Sci Eng C Mater Biol Appl. (2017). 80:75-87
57. MasoudiRad M, NouriKhorasaniS.,.Ghasemi-MobarakehL,.Prabhakaran M.P,. Foroughi M.R,.KharazihaM,.Saadatkish N, Ramakrishna S., Fabrication and characterization of two-layered nanofibrous membrane for guided bone and tissue regeneration application, Mater. Sci. Eng. C 80 (2017) 75–87
58. Matos A M, Gonçalves A I., Hajd A J. El, Gomes M. E. Magnetic biomaterials and nano-instructive tools as mediators of tendon mechanotransduction. Nanoscale Adv., (2020) 2: 140-48
59. Meng J, Han Z, Kong H, et al. Electrospun aligned nanofibrous composite of MWCNT/polyurethane to enhance vascular endothelium cells proliferation and function. J Biomed Mater Res A. 2010;95(1):312-320
60. Meng J, Kong H, Han Z, et al. Enhancement of nanofibrous scaffold of multiwalled carbon nanotubes/polyurethane composite to the fibroblasts growth and biosynthesis. J Biomed Mater Res A. (2009) 88(1):105-116
61. Mohan N, Wilson J, Joseph D, Vaikkath D, Nair PD. Biomimetic fiber assembled gradient hydrogel to engineer glycosaminoglycan enriched and mineralized cartilage: An in vitro study.J Biomed Mater Res A. (2015) 103: 3896-906.
62. Morais DS, Torres J, Guedes RM, Lopes MA. Current Approaches and Future Trends to Promote Tendon Repair. Ann Biomed Eng. (2015) 43(9):2025-35.

63. Naseri-Nosar M, Farzamfar S, Sahrapeyma H, et al. Cerium oxide nanoparticle-containing poly (ε-caprolactone)/gelatin electrospun film as a potential wound dressing material: In vitro and in vivo evaluation. Mater Sci Eng C Mater Biol Appl. (2017) 81:366-372
64. Nitya, G., Nair, G.T., Mony, U., Chennazhi, K.P., and Nair, S.V. In vitro evaluation of electrospun PCL/nanoclay composite scaffold for bone tissue engineering. J Mater Sci Mater Med (2012) 23: 1749,
65. Ohlendorf P, Ruyack A., Leonardi A, Shi C., Cuppoletti C., Bruce I., Lal A., K. Ober C. Transient fiber mats of electrospunpoly(propylene carbonate) composites with remarkable mechanical strength. ACS Appl. Mater. Interfaces (2017) 9: 25495−25505
66. Ozdemir T, Xu LC, Siedlecki C, Brown JL. Substrate curvature sensing through Myosin IIa upregulates early osteogenesis. Integr Biol (Camb). (2013) 11:1407-16.
67. Pant, B.; Pant, H. R.; Pandeya, D. R.; Panthi, G.; Nam, K.T.; Hong, S. T.; Kim, C. S.; Kim, H. Y. Characterization and antibacterial properties of Ag NPs loaded nylon-6 nanocomposite prepared by one-step electrospinning process. Colloids Surfaces A-Physicochem. Eng. Aspects 2012, 395, 94.
68. Park Y.R,. Ju H.W,. Lee J.M,. Kim D.-K,. Lee O.J,. Moon B.M, H.J. Park, J.Y. Jeong, Y.K. Yeon, C.H. Park, Three-dimensional electrospun silk-fibroin nanofiber for skin tissue engineering, Int. J. Biol. Macromol. 93 (2016) 1567–
69. Park, J. H.; Kim, I. K.; Choi, J. Y.; Karim, M. R.; Cheong, I. W.; Oh, W.; Yeum, J. H. Electrospinning fabrication of poly(vinyl alcohol)/waterborne polyurethane/silver composite nanofibre mats in aqueous solution for anti-bacterial exploits Polym. Polym. Compos. (2011). 19: 753.
70. Park, S.-W.; Bae, H.-S.; Xing, Z.-C.; Kwon, O. H.; Huh, M.-W.; Kang, I.-K. J. Appl. Preparation and properties of silver-containing nylon nanofibers formed by electrospinning. Polym. Sci. 2009, 112: 2320.
71. Pereira IH; Ayres E, Averous L, Schlatter G, Hebraud A, de Paula AC, Viana PH, Goes AM, Oréfice RL. Differentiation of human adipose-derived stem cells seeded on mineralized electrospun co-axial poly(ε-caprolactone) (PCL)/gelatin nanofibers. J Mater Sci Mater Med. (2014) 25: 1137-4
72. Qi R., Cao X., Shen M., Guo R., Yu J., Shi X. Biocompatibility of electrospun halloysite nanotube-doped poly(lactic-co-glycolic acid) composite nanofibers. Journal of Biomaterials Science, Polymer Edition, (2012). 23:299–313.

73. Qi R., Guo R., Zheng F., Liu H., Yu J., Shi X. Controlled release and antibacterial activity of antibiotic-loaded electrospun halloysite/poly(lactic-co-glycolic acid) composite nanofibers. Colloids Surfaces B-Biointerfaces, (2013). 110: 148-155.
74. Qi, R.; Guo, R.; Shen, M.; Cao, X.; Zhang, L.; Xu, J.; Yu, J.; Shi, Electrospun poly(lactic-co-glycolic acid)/halloysite nanotube composite nanofibers for drug encapsulation and sustained release X. J. Mater. Chem. (2010) 20: 10622−10629.
75. Rahaman MN, Day DE, Bal BS, Fu Q, Jung SB, Bonewald LF, Tomsia AP. Bioactive glass in tissue engineering. Acta Biomater. (2011). 7 (6) :2355-73.
76. Ren K., Y. Wang, T. Sun, W. Yue, H. Zhang, Electrospun PCL/gelatin composite nanofiber structures for effective guided bone regeneration membranes, Mater. Sci. Eng. C 78 (2017) 324–332.
77. Reyes CG, Lagerwall JPF. Disruption of electrospinning due to water condensation into the taylor cone. ACS Appl Mater Interfaces. (2020) 12:26566-26576.
78. Rodrigues BVM, Silva AS, Melo GFS, Vasconscellos LMR, Marciano FR, Lobo AO. Influence of low contents of superhydrophilic MWCNT on the properties and cell viability of electrospun poly (butylene adipate-co-terephthalate) fibers.Mater Sci Eng C Mater Biol Appl.(2016) 59:782-791.
79. Sandri G, Faccendini A, Longo M, et al. Halloysite and Montmorillonite-Loaded Scaffolds as Enhancers of Chronic Wound Healing. Pharmaceutics. (2020) 12(2):179
80. Sandri G, Miele D, Faccendini A, et al. Chitosan/glycosaminoglycan scaffolds: The role of silver nanoparticles to control microbial infections in wound healing. Polymers (Basel). (2019). 11(7):1207
81. Santana-Melo G.F., Rodrigues B.V.M., Da Silva E., Ricci R., Marciano F.R., Webster T.J., Vasconcellos L.M.R., Lobo A.O.,Electrospun ultrathin PBAT/nHAp fibers influenced the in vitro and in vivo osteogenesis and improved the mechanical properties of neoformed bone. (2017) 155: 544-552
82. Savelyeva M S,Abalymov A A, Lyubun G P, Vidyasheva I V,YashchenokAM, Douglas T.E.L , Gorin D A,Parakhonskiy B V. Vaterite Coatings on electrospun polymeric fibers for biomedical applicationsJ Biomed Mater Res A (2017) 105: 94-103
83. Sepahvandi A, Eskandari M, Moztarzadeh F. Fabrication and characterization of $SrAl_2O_4$: $Eu^{2+}Dy^{3+}$/CS-PCL electrospun nanocomposite scaffold for retinal tissue regeneration. Materials Science and Engineering C (2016) 66: 306–314

84. Shankhwar N, Kumar M, Mandal BB, Srinivasan A. Novel polyvinyl alcohol-bioglass 45S5 based composite nanofibrous membranes as bone scaffolds. Mater Sci Eng C Mater Biol Appl. (2016) 69:1167-1174.
85. Shao W, He J, Sang F, Ding B, Chen L, Cui S, Li K, Han Q, Tan W. Coaxial electrospun aligned tussah silk fibroin nanostructured fiber scaffolds embedded with hydroxyapatite-tussah silk fibroin nanoparticles for bone tissue engineering. Mater Sci Eng C Mater Biol Appl. (2016) 58:342-51
86. Sharma Y, Tiwari A, Hattori S, Terada D, Sharma AK, Ramalingam M, Kobayashi H. Fabrication of conducting electrospun nanofibers scaffold for three-dimensional cells culture.Int J Biol Macromol.(2012) 51:627-31.
87. Sheikh FA, Macossay J, Cantu T, et al. Imaging, spectroscopy, mechanical, alignment and biocompatibility studies of electrospun medical grade polyurethane (Carbothane™ 3575A) nanofibers and composite nanofibers containing multiwalled carbon nanotubes. J Mech Behav Biomed Mater. 2015;41:189-198
88. Shi, Q.; Vitchuli, N.; Nowak, J.; Noar, J.; Caldwell, J. M.; Breidt, F.; Bourham, M.; McCord, M.; Zhang, X. J. One-step synthesis of silver nanoparticle-filled nylon 6 nanofibers and their antibacterial properties Mater. Chem. (2011) 21: 10330-10335
89. Shrestha S, Shrestha BK, Lee J, et al. A conducting neural interface of polyurethane/silk-functionalized multiwall carbon nanotubes with enhanced mechanical strength for neuroregeneration. Mater Sci Eng C Mater Biol Appl. (2019), 102:511-523
90. Shuai C, Yu L, Feng P, Gao C, Peng S. Interfacial reinforcement in bioceramic/biopolymer composite bone scaffold: The role of coupling agent. Colloids Surf B Biointerfaces. 193 (2020):111083.
91. Si J, Cui Z, Wang Q, Liu Q, Liu C.Biomimetic composite scaffolds based on mineralization of hydroxyapatite on electrospun poly(ε-caprolactone)/nanocellulose fibers.CarbohydrPolym.(2016) 143:270-8
92. Solon J, Levental I, Sengupta K, Georges PC, Janmey PA. Fibroblast adaptation and stiffness matching to soft elastic substrates. Biophys J. (2007) 93(12):4453-61
93. Song B., Wu C., Chang J.J. Controllable delivery of hydrophilic and hydrophobic drugs from electrospunpoly(lactic-co-glycolic acid)/mesoporous silica nanoparticles composite mats. J. Biomed. Mater. Res. Part B - Appl. Biomater. (2012). 100: 2178-2186.

94. Souza DC, Abreua HLV, Oliveira PV, Capelo LP, Passos-Bueno MR, Catalani LH. A fast degrading PLLA composite with a high content of functionalized octacalcium phosphate mineral phase induces stem cells differentiation. J. Mech Behav. Biomed Mater (2019) 93: 93-104
95. Srikanth M, Asmatulu R, Cluff K, Yao L. Material Characterization and Bioanalysis of Hybrid Scaffolds of Carbon Nanomaterial and Polymer Nanofibers. ACS Omega. (2019). 4(3):5044-5051
96. Thakore R, Singh R, Jhala D, Singh S, Vasita R. Antioxidative study of Cerium Oxide nanoparticle functionalised PCL-Gelatin electrospun fibers for wound healing application. Bioact Mater. (2018). 3(2):201-211.
97. Tomas A. R,. Goncalves AI. Paz E., Freitas P,. Domingues R. M A,. Gomes M E, Magneto-mechanical actuation of magnetic responsive fibrous scaffolds boosts tenogenesis of human adipose stem cells. Nanoscale (2019) 11: 18255–18271.
98. WalshWR. Repair and regeneration of ligaments, tendons, and joint capsule. Orthopedic Biology and Medicine. (2007) pp 1-324
99. Wang Y., Gao R., Wang P.P., Jian J.; Jiang X-L, Yan C., Lin X., Wua L., Chen G-Q., Wu Q ;The differential effects of aligned electrospunPHBHHx fibers on adipogenic and osteogenic potential of MSCs through the regulation of PPARg signaling. Biomaterils(2012) 33:485-493.
100. Wang, S.; Zheng, F.; Huang, Y.; Fang, Y.; Shen, M.; Zhu,M.; Shi, X. Encapsulation of Amoxicillin within Laponite-Doped Poly(lactic-coglycolic acid) Nanofibers: Preparation, Characterization, and Antibacterial Activity. Acs Appl. Mater. Interfaces (2012) 4: 6393.
101. Wei J, Lu J, Chen M, Xie S, Wang T, Li X. 3D spheroids generated on carbon nanotube-functionalized fibrous scaffolds for drug metabolism and toxicity screening.Biomater Sci. (2019)
102. Wei K., Kim BS., Kim IS.; Fabrication and biocompatibility of electrospun silk biocomposites. Membranes (2011) 1: 275-98
103. Wesełucha-Birczyńska A, Morajka K, Stodolak-Zych E, et al. Raman studies of the interactions of fibrous carbon nanomaterials with albumin. Spectrochim Acta A Mol BiomolSpectrosc. (2018), 196:262-267.
104. Wong R, Geyer S, Weninger W, Guimberteau JC, Wong JK. The dynamic anatomy and patterning of skin. Exp Dermatol. (2016) 25(2):92-8.

105. Xie J; Zhong S; Ma B.; Shuler F.D.; Lim C.T. Controlled biomineralization of electrospun poly(e-caprolactone) fibers to enhance their mechanical properties Acta Biomater (2013) 9:5698-5707

106. Xing, Z.-C.; Chae, W.-P.; Huh, M.-W.; Park, L.-S.; Park, S.-Y.; Kwak, G.; Yoon, K.-B.; Kang, I.-K. J. In Vitroanti-bacterial and cytotoxic properties of silver-containing poly(l-lactide-co-glycolide) nanofibrous scaffolds. Nanosci. Nanotechnol. (2011) 11: 61-65

107. Xu J, Xie Y, Zhang H, Ye Z, Zhang W. Fabrication of PLGA/MWNTs composite electrospun fibrous scaffolds for improved myogenic differentiation of C2C12 cells. Colloids Surf B Biointerfaces. (2014)123:907-915

108. Xue J., Niu Y., Gong M., Shi R., Chen D., Zhang L..Electrospunmicrofiber membranes embedded with drug-loaded clay nanotubes for sustained antimicrobial. Engineering B.T. (2015). 2: 1600–1612.

109. Yang, Q. B.; Li, D. M.; Hong, Y. L.; Li, Z. Y.; Wang, C.; Qiu, S. L.; Wei, Y. Preparation and characterization of a PAN nanofibre containing Ag nanoparticles via electrospinning. Synth. Met (2003)137. 973-974

110. Youngstrom DW, Barrett JG. Engineering tendon: scaffolds, bioreactors, and models of regeneration. Stem Cells Int. (2016) ;2016:3919030

111. Yuan, J.; Geng, J.; Xing, Z.; Shen, J.; Kang, I.-K.; Byun, H.J. Electrospinning of antibacterial poly(vinylidene fluoride) nanofibers containing silver nanoparticles. Appl. Polym. Sci. (2010) 116: 668-672

112. Zheng, F.; Wang, S.; Wen, S.; Shen, M.; Zhu, M.; Shi, X. Characterization and antibacterial activity of amoxicillin-loaded electrospun nano-hydroxyapatite/poly(lactic-co-glycolic acid) composite nanofibers.Biomaterials (2013) 34: 1402

113. Zienkiewicz-Strzałka M, Deryło-Marczewska A, Skorik YA, Petrova VA, Choma A, Komaniecka I. Silver nanoparticles on chitosan/silica nanofibers: Characterization and antibacterial activity. Int J Mol Sci. (2019);21(1):166

114. Zi-Wei L, Li CW, Wang Q, et al. The cellular and molecular mechanisms underlying silver nanoparticle/chitosan oligosaccharide/poly(vinyl alcohol) nanofiber-mediated Wound Healing. J Biomed Nanotechnol. (2017).13(1):17-34

115. Zong H, X Xia, Y Liang, S Dai, A. Alsaedi, T. Hayat, F. Kong, J. H. Pan, Designing function-oriented artificial nanomaterials and membranes via electrospinning and electrospraying techniques Mater. Sci. Eng. C (2018) 92 1075–91

CHAPTER 2

Halloysite and Montmorillonite loaded scaffolds as enhancers of chronic wound healing

Giuseppina Sandri [1],*, Angela Faccendini [1], Marysol Longo [1,2], Marco Ruggeri [1], Silvia Rossi [1], Maria Cristina Bonferoni [1], Dalila Miele [1], Adriele Prina-Mello [2], Carola Aguzzi [3], Cesar Viseras [3] and Franca Ferrari [1]

[1] *Department of Drug Sciences, University of Pavia, Viale Taramelli 12, 27100 Pavia, Italy;*
[2] *Trinity Translational Medicine Institute, Trinity College Dublin, Dublin 8, Dublin, Ireland;*
[3] *Department of Pharmacy and Pharmaceutical Technology, Faculty of Pharmacy, University of Granada, Campus of Cartuja s/n, 18071 Granada, Spain;*
***** *Corresponding author*
Received: 31 December 2019; Accepted: 15 February 2020; Published: 20 February 2020

Abstract

The increase in life expectancy and the increasing prevalence of diabetic disease and venous insufficiency lead to the increase of chronic wounds. The prevalence of ulcers ranges from 1% in the adult population to 3–5% in the over 65 years population, with 3–5.5% of the total healthcare expenditure, as recently estimated. The aim of this work was the design and the development of electrospun scaffolds, entirely based on biopolymers, loaded with montmorillonite (MMT) or halloysite (HNT) and intended for skin reparation and regeneration, as a 3D substrate mimicking the dermal ECM. The scaffolds were manufactured by means of electrospinning and were characterized for their chemico-physical and preclinical properties. The scaffolds proved to possess the capability to enhance fibroblast cells attachment and proliferation with negligible proinflammatory activity. The capability to facilitate the cell adhesion is probably due to their unique 3D structure which are assisting cell homing and would facilitate wound healing in vivo.

1. INTRODUCTION

The skin is the largest organ of the body and plays a pivotal role in maintaining physiological homeostasis against fluid imbalance, thermal dysregulation, and infections. It is formed by the epidermis, consisting of keratinocytes, and by the dermis, mainly based

on the extracellular matrix (ECM) (collagen, elastin, glycosaminoglycans) and sparse fibroblasts. Damage or loss of integrity of the skin caused by a wound, may impair skin functions, exposing the body to potentially challenging situations. Wound healing is a complex event based on overlapping but well-orchestrated cellular and molecular processes to repair damaged tissue and restore skin function. Healing is divided in different phases (hemostasis, inflammatory, proliferative, and remodeling) and is accomplished by ECM molecules, soluble mediators, as cytokines and growth factors, various resident cells, and infiltrating leucocytes [1].

Acute wounds are mainly traumatic or surgical and generally heal within few weeks without any significant interventions, whereas in chronic wounds, the healing process remains frozen in the inflammatory state. These, commonly defined as wounds that fail to proceed through an orderly and timely process to restore skin anatomical and functional integrity. These include venous leg ulcers, arterial ulcers, diabetic ulcers, and pressure ulcers, such as bed sores. The increase in life expectancy and the increasing prevalence of diabetic disease and venous insufficiency lead to an increase in chronic wounds. Although assessing the prevalence of chronic wounds is problematic because of the disparities in study design and their evaluation, they have become a major challenge to healthcare systems worldwide. It is estimated that the prevalence of ulcers ranges from 1% in the adult population to 3–5% in the over 65 years population; whereas globally it accounts for the 3–5.5% of the total healthcare expenditure as recently estimated [2,3].

Recently, clay minerals have been proposed in the biomedical field in tissue engineering as enhancers of cell attachment, proliferation and differentiation [4,5], and also as antimicrobials [6]. In particular, montmorillonite (MMT, M_x (Al_2-yMg_y) Si_4O_{10} $(OH)_2$ nH_2O) and halloysite (HNT, Al_2O_3 $2SiO_2$ $2H_2O$) have been recently described as biocompatible and as proliferation enhancers [7]. Both MMT and HNT are phyllosilicates, having a planar and rolled structure, respectively. Nanocomposites, based on these biomaterials, have been developed to tune cell adhesion and their biocompatibility [8–11]. The cell interaction with clays remain unclear and not fully understood, and only a few recent studies have attempted to shed light on this interaction [7,12].

However, there are many evidences in literature related to the combination of nanostructured materials with nanoscale fabrication processes, to achieve high levels of morphological control, surface and mechanical properties [13–15]. In light of these, layered silicates are characterized by a high aspect ratio with the ability to confer high

strength to 3D structures. Moreover, unlike most inorganic fillers, layered silicates are hydrophilic, and capable to interact with the polymer matrix, by changing surface tension, conductivity, and shear viscosity. Thus, the combination of clay minerals and nanofibrous scaffolds should lead to 3D architectures which facilitate cell homing, but also enhance the cell attachment and proliferation thanks to the enhancing properties provided by biopolymers. In particular, chitosan and chondroitin sulfate are polysaccharides capable to aid cell proliferation, and moreover, the latter is also providing protection against growth factor degradation by electrostatic interaction [16]. Having previously assessed the scaffold composition in the basic biopolymers [16]; these made of pullulan, chitosan, and chondroitin sulfate; the manufacturing processing was then addressed by means of electrospinning in a one-pot process to obtain a nanofibrous scaffold which proved to enhance the mechanical properties of the scaffold.

Given the advances achieved on these materials and their manufacturing processes, the aim of this work was the design, development and characterization of electrospun 3D scaffolds, entirely based on biopolymers, loaded with MMT or HNT, as a dermal substitute for skin reparation and regeneration tested in a preclinical model, leading to tissue reparation towards a complete skin restore.

2. MATERIALS AND METHODS

2.1. Materials and reagents

The following polysaccharides were used: chitosan (CH) (β-(1-4)-linked D-glucosamine and N- acetyl-D-glucosamine) low MW 251 kDa, deacetylation degree 98%, (ChitoClear, Iceland); chondroitin sodium sulfate (CS) (β-1,4-linked D-glucuronic acid and β-1,3-linked N-acetyl galactosamine) bovine 100 EP, low MW 14 kDa, and a mixture of chondroitin A (chondroitin 4 sulfate) and chondroitin C (chondroitin 6 sulfate) (Bioiberica, Italy); pullulan (P) (based on maltotriose repeating units, linear α 1–4 and α 1–6 glucan, produced by *Aureobasidium pullulans*) low MW ~200– 300 kDa (food grade, Hayashibara, Giusto Faravelli, Italy). Citric Acid (CA) (monohydrated citric acid, EP grade, Carlo Erba, I) was used as the crosslinking agent. Pharmaceutical grade clay minerals were considered: montmorillonite (MMT) (particle size: 1352 nm (±17); polydispersity index: 0.696 (±0.184)) (Veegum® HS, Vanderbilt, Nashville, TN, USA) or halloysite (particle size: 563

nm (±70); polydispersity index: 0.647 (±0.077); internal diameter = 28 ± 5.1 nm and external diameter = 70 ± 8.3 nm) (Halloysite Nanotubes—HTNs) (Sigma-Aldrich, St. Louis, MO, USA).

2.2. Preparation of polymeric blends

P and CS were solubilized in water while the CH solution was prepared in 90% v/v acetic acid and CA was added. A polymeric blend was prepared by mixing P and CS with a CH solution at a 1:1 weight ratio. The preparation schematic is reported in Figure 1.

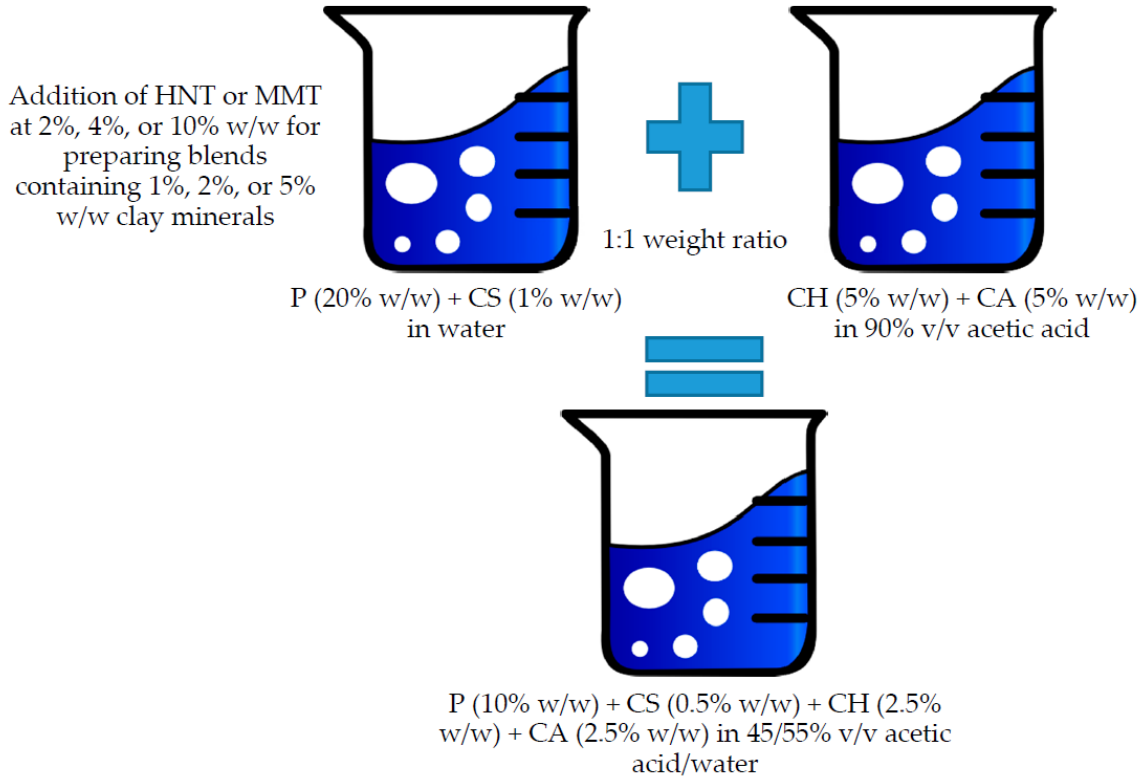

Figure 1 *:Schematic of the blend preparation.*

The hybrid blends were then prepared by the addition of MMT or HNT to the polymeric blend, prepared as previously described [16]. For this purpose, clay minerals were grounded in a mortar and sieved with a 75 μm sieve. Either MMT or HNT were added to the P and CS blend at different concentrations. All the blends prepared had the same composition in polysaccharides while they were based on different concentrations of clay minerals. The composition of all the systems prepared is reported in Table 1.

***Table 1**. Composition (% w/w) of the polymeric blends.*

% w/w	MMT	HNT	P	CH	CA	CS	H_2O/CH_3COOH
Blank	-	-	10	2.5	2.5	0.5	55/45
MMT1	1	-	10	2.5	2.5	0.5	55/45
MMT2	2	-	10	2.5	2.5	0.5	55/45
MMT5	5	-	10	2.5	2.5	0.5	55/45
HNT1	-	1	10	2.5	2.5	0.5	55/45
HNT2	-	2	10	2.5	2.5	0.5	55/45
HNT5	-	5	10	2.5	2.5	0.5	55/45

2.3. Characterization of polymeric blends

The surface tension of the blends was measured at T = 30 °C with a tensiometer (DY-300, Kyowa, Japan) (measurement range 0–300 mN/m) equipped with a platinum plate of 2.5 cm × 1 cm.

The electrical conductivity was determined by a conductometer (FiveGoTM-Mettler Toledo, Italy) equipped with the LE703-IP67 sensor.

The penetrometry was measured using the Texture Analyzer TA-XT plus (ENCO, Italy), equipped with an A/TG measuring system and a 5 kg load cell. The analysis was performed employing a Perspex 20 mm cylinder probe (P/20P; Batch N° 11434). The measuring probe was lowered at a 0.50 mm/s speed up to a 3 mm penetration distance. The penetration force was recorded as a function of probe displacement

2.4. Preparation of electrospun scaffolds

Scaffolds were obtained using an electrospinning apparatus (STKIT-40, Linari Engineering, Italy), equipped with a high-voltage power supply (40 kV), a volumetric pump (Razel R99-E), a 10 mL syringe, and a conductive static collector, covered by aluminum foil. The following parameters were used: ΔV (voltage) = 22 kV, collector spinneret distance = 24 cm, polymeric solution flow = 0.4 mL/h, spinning time = 1.30 h, temperature = 30 °C, relative humidity = 30%; and needle dimensions:

0.5 × 20 mm for MMT and 0.4 × 20 mm for HNT. The obtained scaffolds were then crosslinked by heating at 150 °C for 1 h, to prevent their solubilization in aqueous media and to allow cell homing. The heating process is also reported as able to dry sterilize the products [17].

2.5. Scaffold characterizations: chemico-physical characterization

Scaffold morphology was assessed by means of SEM (Tescan, Mira3XMU, CISRIC, University of Pavia) after graphite sputtering. The scaffolds were analyzed before and after the crosslinking procedure and after 6 days of hydration in distilled water. Nanofiber diameters and pores sizes were measured by image analysis software (DiameterJ plugin, Image J, NIH).

X-ray powder diffraction (XRPD) analysis was carried out using a diffractometer (X-Pert Pro model, Malven Panalytical, Italy) equipped with a solid-state detector (X-Celerator) and a spinning sample holder. The diffractogram patterns were recorded using random oriented mounts with CuKα radiation, operating at 45 kV and 40 mA, in the range 4–60° 2θ. The diffraction data were analyzed using the XPOWDER® software (www.xpowder.com).

Fourier-transform infrared spectroscopy (FT-IR) spectra were recorded using spectrophotometer (JASCO 6200) with a Ge ATR. All samples were analyzed from 400 to 4000 cm−1 with a resolution of 0.25 cm−1 and the results were processed with Spectra Manager v2 software.

Thermogravimetric analysis (TGA) (TGA-50H, Shimadzu, Kyoto, Japan) was performed using a vertical oven and a precision of 0.001 mg. Approximately 40 mg of each sample were placed in aluminum pans. The experiments were performed at the 30–950 °C range and using a 10 °C/min heating rate. Additionally, differential scanning calorimetry (DSC) analyses were performed (Mettler Toledo, Columbus, OH, USA) using aluminum crucibles, a 30–400 °C temperature range, at a heating rate of 10 °C/min. All the analyses were performed in atmospheric air.

High-resolution Transmission Electron Microscopy (TEM) was performed by means of an analytical electron microscope (AEM) (Titan G2 60–300, FEI Company, Thermo Fisher Scientific, Waltham, MA, USA) with a SUPER-X silicon-drift windowless energy dispersive X-ray spectroscopy detector. X-ray chemical element maps were also collected. The samples were directly deposited onto copper grids (300 mesh coated by formvar/carbon film, Agar Scientific, Italy).

2.6. Scaffold characterizations: mechanical properties

Mechanical properties of nanofibrous scaffolds were measured using a TA-XT plus Texture Analyzer (Stable Microsystems, ENCO, Italy) equipped with a 5.0 kg load cell.

Before testing, nanofibrous scaffolds were cut 30 × 10 mm and the strips (thickness ranging from 150 to 200 □m, thickness gauge apparatus, Mitutoyo) were clamped between two tensile grips (A/TG probe) setting an initial distance between the grips of 10.0 mm. Mechanical properties were evaluated in the dry and hydrated state. The hydration was performed by dipping the scaffolds in water up to complete hydration (1 h). Then, the upper grip was moved forward at a constant speed of 5.0 mm/s up to break.

The force at break was recorded (force at break) (TS, N/mm2) and the elongation (%) was calculated as follows (Eq 1):

$$E\% = 100 \times (L_{break} - L_0)/L_{break} \qquad (Eq1)$$

where L_{break} is the distance of the two grips at scaffold breaking and L_0 is the initial distance of the two grips.

Moreover, Young's Modulus (mN/cm^2) was calculated as the slope of the initial linear portion of force vs. grip displacement [10,18,19].

2.7. Fibroblasts biocompatibility and adhesion

NHDFs (normal human dermal fibroblasts from juvenile foreskin, Promocell WVR, Italy) were grown with Dulbecco's Modified Eagle Medium (Sigma, I) supplemented with 10% fetal bovine serum (FBS, Sigma, Italy) and with 200 IU/mL penicillin/0.2 mg/mL streptomycin (Sigma-Aldrich, Italy), kept at 37 °C in a 5% CO_2 atmosphere with 95% relative humidity (RH).

Preliminarily, the cytocompatibility and proliferation in the presence of pure components were assessed. Fibroblasts were seeded with a seeding density of 25 × 103 cells/well in 96-well plates. After 24 h of growth (at sub-confluence), the following samples (in growth medium, GM) were considered: CS (0.08 mg/mL), P (1.5 mg/mL), CA (0.4 mg/mL), CH (0.4 mg/mL), MMT (MMT1: 0.2 mg/mL; MMT2: 0.8 mg/mL; MMT5: 1.2 mg/mL), and HNT (HNT1: 0.2 mg/mL; HNT2: 0.8 mg/mL; HNT5: 1.2 mg/mL). Valinomycin (Val, Fisher Scientific, Ireland) (final concentration 120 μM) was used as the cytotoxic control and GM (growth medium) as the biocompatible control.

After 24 or 72 h of contact, the MTT test was performed. Briefly, the MTT test evaluates the activity of mitochondrial dehydrogenase of vital cells that convert MTT into formazan salts. The MTT was solubilized in PBS at a concentration of 5 mg/mL per well. A total of 50 μL of the MTT solution and 100 μL of the DMEM (DMEM w/o phenol red, Sigma, Italy) were dispensed into each well and subsequently the plates were placed in an

incubator at 37 °C for 3 h. The reagent was then removed from each well and the cells were washed with 150 µL of PBS to remove the samples and the un- reacted MTT solution. After PBS removal, 100 µL of DMSO were added to each well and the absorbance was detected with an ELISA plate reader (ELISA plate reader, Biorad, Italy; Epoch, Microplate Spectrophotometer, BioTek, Ireland) at a wavelength of 570 nm with a wavelength of reference of 690 nm.

Subsequently the scaffold cytocompatibility was assessed. For this purpose, scaffolds were cut to have an area of 0.36 cm^2 to cover the bottom of a well in a 96 well-plate and fibroblasts were seeded onto each scaffold with 35 × 103 cells/well and grown for 3, 6, and 10 days. An MTT assay was performed, as previously described. In addition, SEM and CLSM analysis were performed to visualize the fibroblasts adhered and proliferated to each scaffold.

Fibroblasts grown onto the scaffolds were fixed with a 3% glutaraldehyde solution for 1 h at 4°C (glutaraldehyde 50%—Sigma Aldrich, Italy), and washed twice with PBS. As for SEM, scaffolds were dehydrated in increasing concentrations of ethanol, placed onto stub and sputtered with graphite. The images were acquired at a high voltage of 8 kV, in high vacuum, at room temperature and different magnifications (5.00 kX; 10.00 kX; 20.00 kX) (SEM: Tescan, Mira3XMU, CISRIC, University of Pavia).

As for CLSM the fixed scaffolds were stained by dipping the scaffolds in contact with 50 µL of phalloidin Atto 488 (50 µg/mL in PBS) (Sigma Aldrich, Italy) for 40 min. Cell nuclei were subsequently stained by dipping the scaffolds in 100 µL of Hoechst 33258 solution (0.5 µg/mL in PBS) (Sigma Aldrich, Italy) for 10 min. Subsequently, the samples were washed twice for 10 min with PBS and placed on microscope slide and analyzed by using a CLSM (Leica TCS SP2, Leica Microsystems, Italy) using λ_{ex} = 346 nm and λ_{em} = 460 nm for Hoechst 33342 (Sigma, Italy) and λ_{ex} = 501 nm and λ_{em} = 523 nm for phalloidin Atto 488 (Sigma, Italy).

2.8. Cytocompatibility of macrophages and pro-inflammatory immune response

Human monocytic cell line THP-1 (American Type Culture Collection, Manassas, VA, USA) was cultured in RPMI-1640 medium (Gibco, Thermo Fisher, Ireland) supplemented with 10% fetal bovine serum (FBS, Sigma, Ireland), and with 200 IU/mL penicillin/0.2 mg/mL streptomycin kept at 37 °C in a 5% CO_2 atmosphere with 95% relative humidity (RH). A total of 1 × 105 cells/mL were treated with 100 nM phorbol-12-myristate-13-

acetate (PMA, Sigma Aldrich, Germany) for 48 h. After 48 h the cells were differentiated into macrophages and let to rest for 24 h before being treated.

Preliminarily, the cytocompatibility of the pure components was assessed considering sample concentrations as previously described in Section "Fibroblasts Biocompatibility and Adhesion" paragraph. Valinomycin (Val, Fisher Scientific, Ireland) or cysplatinum (Cys, Sigma Aldrich, Ireland) (final concentration 120 μM) was used as the cytotoxic control and GM (growth medium) as the biocompatible control.

THP-1 was differentiated using PMA and 20 × 103 cells were seeded in each well of the 96-well plates. After 24 h rest, the components were added to each well and the biocompatibility was assessed after 24 or 72 h of contact time, using MTT test, as previously described.

Subsequently, the scaffold cytocompatibility was assessed. Scaffolds were cut to have an area of 7.65 cm^2 (diameters of 1.5 cm) and placed on a cell crown (Sigma, Italy). THP-1 cells were differentiated by seeding 200 × 103 cells on the bottom of each well of the 24-well plates. After 24 h rest, the scaffold placed on the cell crown was inserted in the well. The cytocompatibility was assessed using an MTT assay (Sigma Aldrich, Ireland) after 24 or 72 h of contact time, as previously described. TNF-α, pro-inflammatory cytokine, was assayed to evaluate the pro-inflammatory immune response using the commercially available ELISA kit (BioLegend, Medical Supply Co. Ltd., Ireland). Supernatants were collected from the cultures at 24 or 72 h after the treatment with the components or the scaffolds.

The cytokine secretion by macrophages was assayed at 450 nm with 570 nm as the reference wavelength (Epoch microplate reader, Biotek, Mason Technologies, Ireland). The method was linear in the concentration range from 7.8 to 500 pg/mL with the R^2 always higher than 0.995. Lipopolysaccharide (LPS, 100 ng/mL for 24 h) was used as the positive control.

2.9. Statistical analysis

Statistical differences were evaluated using a non-parametric test: the Mann–Whitney (Wilcoxon) W-test, (Statgraphics Centurion XV, Statistical Graphics Corporation, MD, USA). Differences were considered significant at $p < 0.05$.

3. RESULTS AND DISCUSSION

3.1. Polymeric blend characterization

The characterization of the polymers in terms of conductivity (μS/cm), surface tension (N/m), and consistency (mN × mm) of all the polymeric blends is reported in Table 2.

Sample	Conductivity (μS/cm)	Surface Tension (N/m)	Consistency (mN × mm)
Blank	1363 ± 11	36.6 ± 0.2	188 ± 2
HNT1s	1271 ± 3	37.7 ± 0.2	155 ± 3
HNT2s	1303 ± 4	38.1 ± 0.1	175 ± 2
HNT5s	1352 ± 9	38.6 ± 0.2	203 ± 5
MMT1s	1255 ± 23	38.7 ± 0.4	171 ± 2
MMT2s	1527 ± 17	40.8 ± 0.2	308 ± 8
MMT5s	1663 ± 9	41.3 ± 0.1	338 ± 4

Table 2. *Conductivity, surface tension, and consistency of the polymer blends (blank) and polymer blends containing MMT or HNT at 1%, 2%, or 5% w/w (mean values ± SD; n = 3).*

The increase in clay mineral concentration caused an increase in conductivity, surface tension, and consistency. In particular, MMT at concentrations higher than 1% increased conductivity, surface tension, and consistency to values greater than those of the blank (blend without MMT). This behavior was less evident when HNT was blended with the polymeric mixture, probably due to the different particle sizes of the two clays. It is conceivable that the addition of HNT or MMT to the polymer blend caused a partial immobilization of the polymer chains due to charge–charge or hydrophobic interaction. In case of a lower amount of clay minerals added (1%), this determined a decrease in consistency and conductivity, while higher amounts (2% or 5%) had the opposite behavior probably due to an excess of charges from MMT or HNT not counterbalanced from the polymers in the solution [14].

3.2. Scaffold characterization: chemico-physical characterization

Advanced images such as SEM microphotographs of MMT- or HNT-based scaffolds and a blank scaffold in the dry or hydrated state are presented in Figure 2. The pore size

evaluated for each scaffold is reported in an inset. Furthermore, in each image, the fiber diameter is reported.

In the dry state, the blank scaffold was characterized by fibers with a smooth surface, and fiber diameters with a coarse distribution around 1500 nm. HNT scaffolds were therefore characterized by the nanofibers' regular structure and smooth surface, where the addition of the clay minerals in the scaffolds provided a significant decrease in the fiber dimensions. The scaffolds containing 2% and 5% HNT had halved the diameter size compared to the blank scaffolds. Moreover, HNT determined a much more regular structure compared to the blank scaffolds. This was probably due to the unique structure of HNT, which are nanotubes with a high aspect ratio of 10 [9,20], thus capable of aligning along the fiber length and providing increasing surface tension. This allowed to obtain a more regular polymer solution jet during the electrospinning process. MMT scaffolds were characterized by nanofiber portions with a regular, smooth surface spaced out in a broaden interwoven, resembling knots, and with a wider structure organization. These conceivably could be related to montmorillonite [9,21]. The increase of MMT concentration, especially in the 5% MMT scaffold, caused an increase in the surface roughness of the fibers, while the fiber diameters were significantly lower than those of the blank scaffold, although this was not influenced from the clay concentration. It is reported that clay minerals could act as a compatibilizer and this could positively affect the electrospinning of a polymer blend, containing positively and negatively charged polymers, as chitosan and chondroitin sulfate. Therefore, MMT or HNT could conceivably reduce the interfacial tension in the polymer blend, thus facilitating electrospinning, to obtain finer and more homogeneous nanofibers with respect to the blank [22]. Moreover, it is reported that the conductivity of the solution, influenced by the clay content, could increase the charge on the surface of the droplet to form a Taylor cone, and consequently could cause the decrease in the fiber diameter [23].

The presence of HNT or MMT in the scaffolds increased the systems porosity, and although there were not significant differences, the increase of clay mineral concentration increased the pore dimensions: this seems inversely related to the decrease of fiber dimensions. Porosity and fiber dimensions seem to have a crucial role for facilitating cell adhesion in the scaffold: The porosity could convert the scaffold from a surface to a fiber network, which could act as a sieve to the home cells.

The hydration significantly increased the fiber dimension, however no solubilization of the scaffold occurred thanks to the cross-linking by heating: The structural analysis (FTIR and

SAXS) and the water holding capacity suggested that no new chemical bond was formed upon heating treatment while a polymer chain felting occurred when water was released due to thermal treatment, resulting in local physical multi-entanglement between the fibers, which could not be released by simple hydration. When HNT or MMT were at lower concentrations, up to 2%, the hydration did not alter the fibrous structure of the scaffolds, while when HNT or MMT were at a 5% concentration, the fibers were fused although the morphology was preserved. The higher content of hydrophilic clay minerals could weaken the overall scaffold structure, since the polymer chains in the matrix loosened their tightness causing a higher fiber swelling.

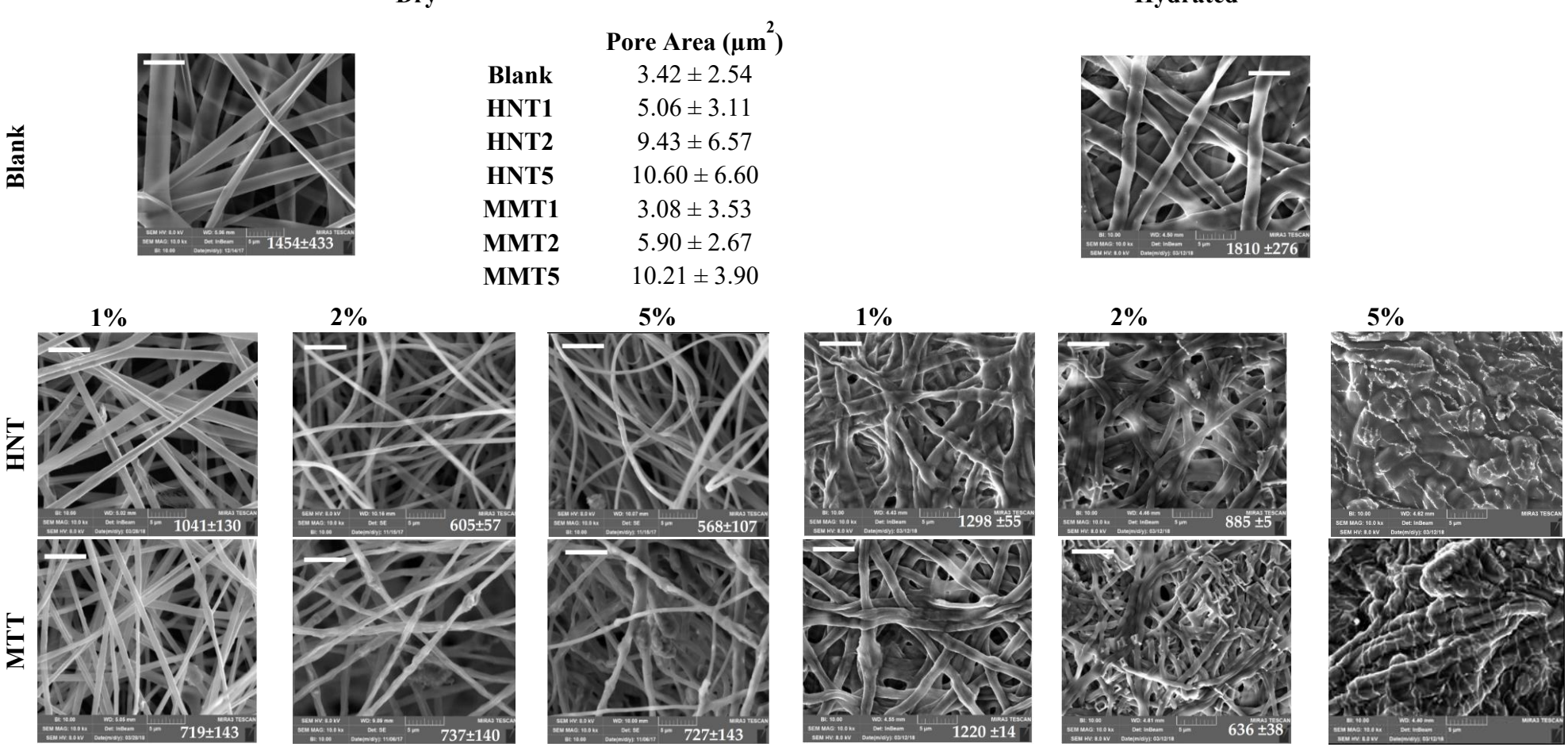

Figure 2. *SEM images of the scaffolds: blank (scaffold without clay) and montmorillonite (MMT) or halloysite (HNT) scaffolds containing 1%, 2%, or 5% of the clay mineral in the dry and hydrated state (the bar in each image is 5 μm). In the inset the fiber diameters (nm) are reported (mean values ± SD; n = 100).*

XRPD of all the scaffolds developed is presented as comparison to the pristine HNT and MMT, in Figure 3. A blank scaffold was characterized by an amorphous pattern and no crystalline or paracrystalline behavior could be detected. Pristine HNT was characterized by a peak at 12.25° 2θ corresponding to 7.24 Å, a typical height of the dehydrated HNT interlaminar spaces (Figure 3, peak labelled as #). The peaks at 20.14° 2θ and at 25.03° 2θ confirmed the HNT tubular structure and its phyllosilicate nature (Figure 3, peak labelled as ##) [24]. HNT-loaded scaffolds were characterized by patterns more similar to that of the blank scaffold rather than those of pristine HNT: In these patterns, only the peaks attributable to the phyllosilicate nature of HNT (peaks at 25.03° 2θ) were present and there was a signal increase directly related to HNT concentration. Since the diffraction angle remained constant in all the patterns and it was the same as in the pristine HNT, it could be argued that no enlargement of the interlaminar space of the rolled structure occurred.

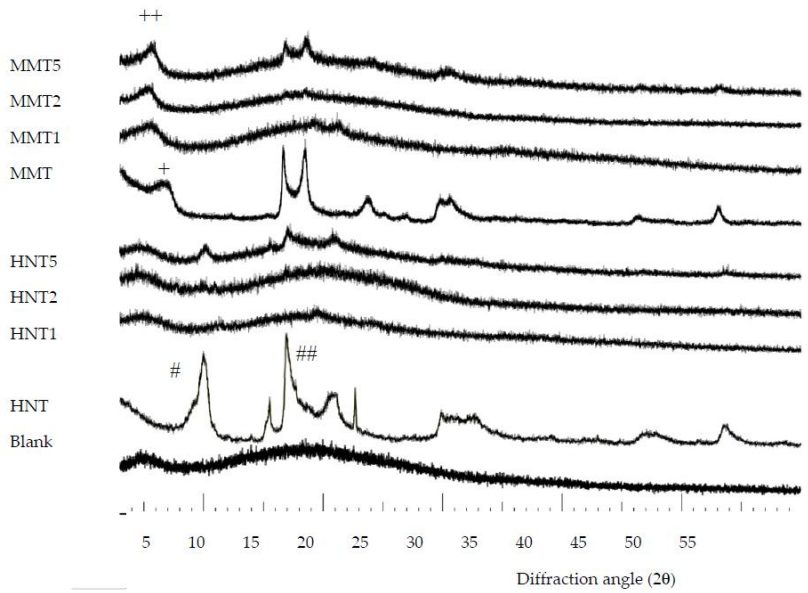

Figure 3. *Comparison of XRPD patterns of all the scaffolds developed against pristine HNT and MMT.*

The pattern of pristine MMT was characterized by a peak at 7° 2θ due to the distance of the d001 basal reflection, corresponding to 12.2 Å, characteristic of predominantly Na+ smectites (Figure 3 peak labelled as +).

In the MMT scaffolds, the d001 basal reflection was shifted to approximately 6° 2θ. This corresponded to a distance of 14.0 Å, suggesting that there was an enlargement of the interlayer space (Figure 3, peak labelled as ++). This was associated with the intercalation

of the biopolymer into MMT layers, probably as monolayer between the silicate layers [10,25].

FTIR spectra of all the scaffolds developed is presented as comparison to the pristine HNT and MMT in Figure 4. In the spectrum of the blank scaffold, the signals related to pullulan (P) and citric acid (CA) are marked. These characteristic signals were present also in all the scaffolds containing either MMT or HNT

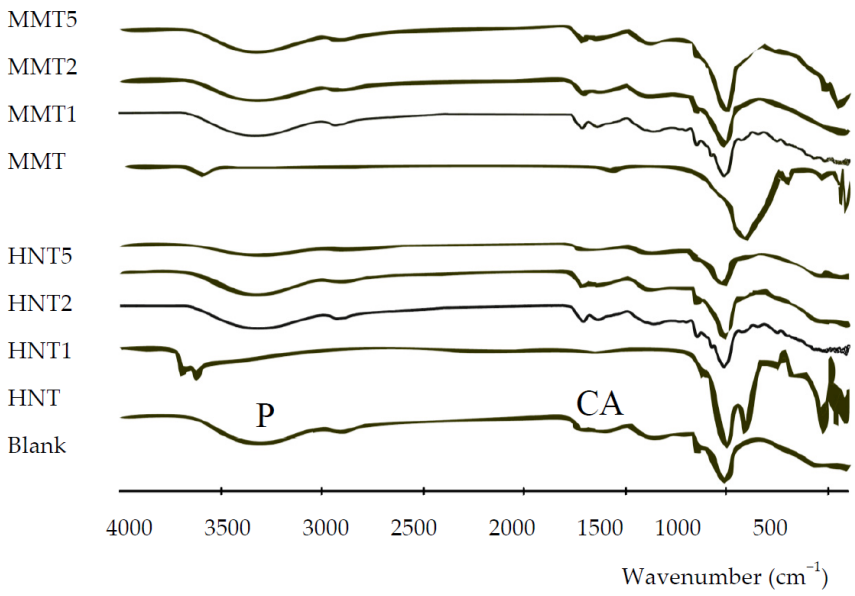

Figure 4. *Comparison of the FTIR spectra of all the scaffolds developed against to the pristine HNT and MMT. In the blank spectrum the signals related to P (pullulan) and CA (citric acid) are marked*

HNT spectrum was characterized by two signals at 3696 cm−1 and 3622 cm−1, due to OH inner and outer stretching, respectively, while the MMT spectrum was characterized by a signal at 3624 cm−1 caused by the Al–OH stretching. The characteristic peaks of both the clay minerals were hidden by a broad band due to a typical polysaccharide signal (hydrogen bonds of –OH and –NH_2 groups). (pullulan: 3331 cm−1 and chitosan: 3355 cm−1). Moreover, the vibrational band of NH_3+ groups of chitosan could be identified at 1550 cm−1, as a shoulder [26,27].

TGA (a,b) and DSC (c) profiles of all the scaffolds, compared to pristine HNT and MMT is reported in Figure 5. Thermal analysis was performed to characterize the role of the clay minerals in the scaffold structure. TGA and DCS profiles suggested than both HNT and MMT had high thermal stability.

TGA analysis suggested that all the scaffolds, independently of the clay mineral loaded and its concentration, were subjected to a slight weight loss corresponding to the evaporation of hydration water. This accounted for about 7% of the scaffolds weight (30–101 °C) (Figure 5a). DSC analysis (Figure 5b,c) showed a slight endothermic event between 30 and 110°C, confirming the TGA results.

Additionally, characterization showed that all the scaffolds reported a more prominent weight loss (onset: about 230 °C; offset: about 400 °C) with greater mass loss to reach 26%, 12%, and 7% of residual weight for the MMT 5, MMT2, and MMT1, respectively. These coincided with two endothermic events in the DSC thermograms and these could be conceivably caused by the decomposition [28,29].

The clay minerals loaded into the scaffolds, independently from the types and concentrations used, maintained their thermal stability and were able to slightly stabilize the scaffolds towards thermal degradation, increasing the onset temperatures of each thermal event; this is particularly evident in the TGA profiles (Figure 5a,b).

The residual mass was related to the clay mineral concentration in each scaffold: HNT: 5.56% for 1% loading; 11.40% for 2%, and 21.02% for 5%; MMT: 5.46% for 1% loading; 11.02% for 2%, and 22.36% for 5%

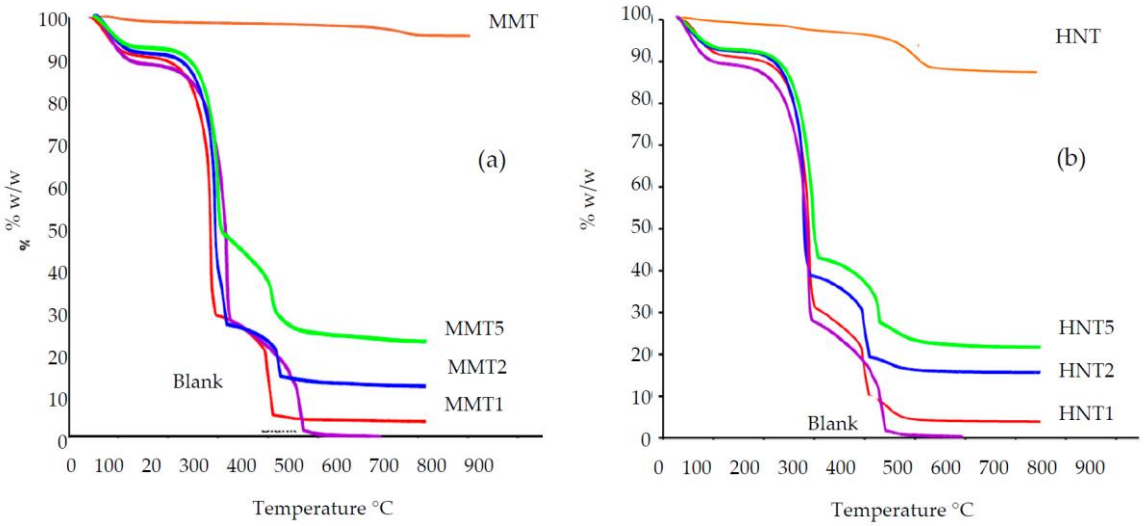

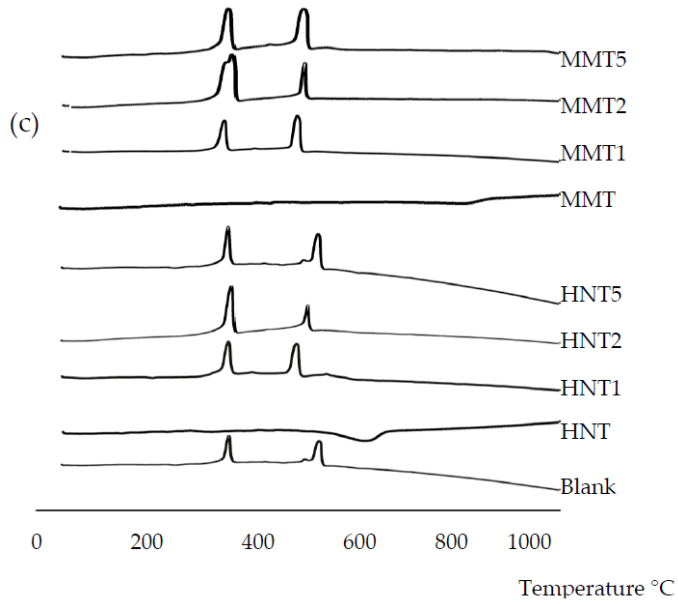

Figure 5. *Comparison of TGA (**a**,**b**) and DSC (**c**) profiles of all the scaffolds against pristine HNT and MMT.*

HRTEM microphotographs of the broadened parts of the fibers is presented in Figure 6, and Figure 7 reports their EDX spectra.

The HRTEM and EDX analysis evidenced that the broadened parts were based on clay mineral particles: The tubular structure of HNT and laminar one of MMT could be identified. Moreover, the elemental analysis showed the presence of Al and Si typical in the case of HNT and the presence of Al, Si, and Mg in the case of MMT, but also of S and C, to indicate that the inorganic material was embedded into the organic component.

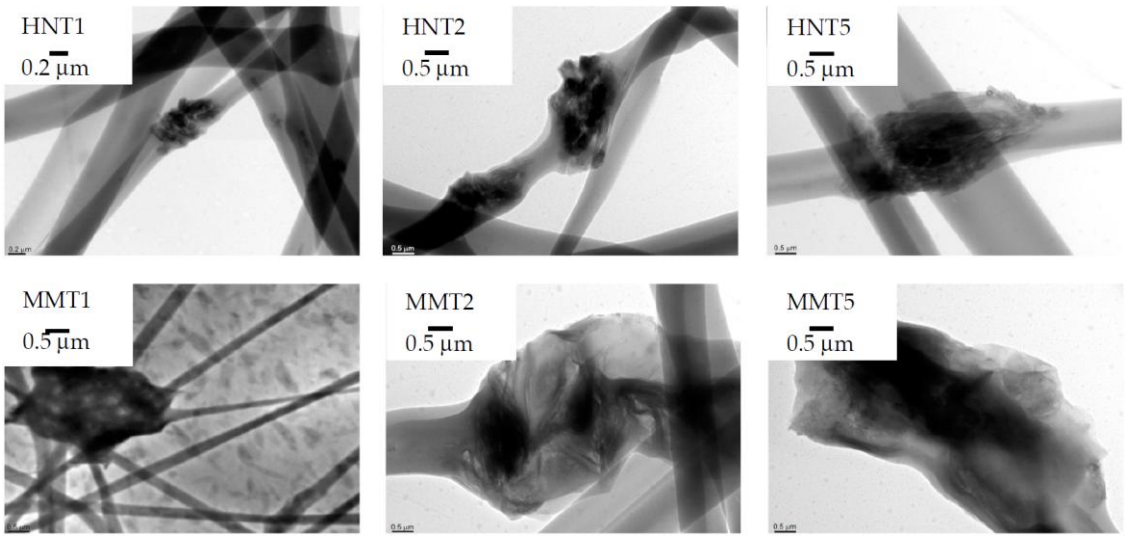

Figure 6. *HRTEM microphotographs of the broadened parts of the fibers.*

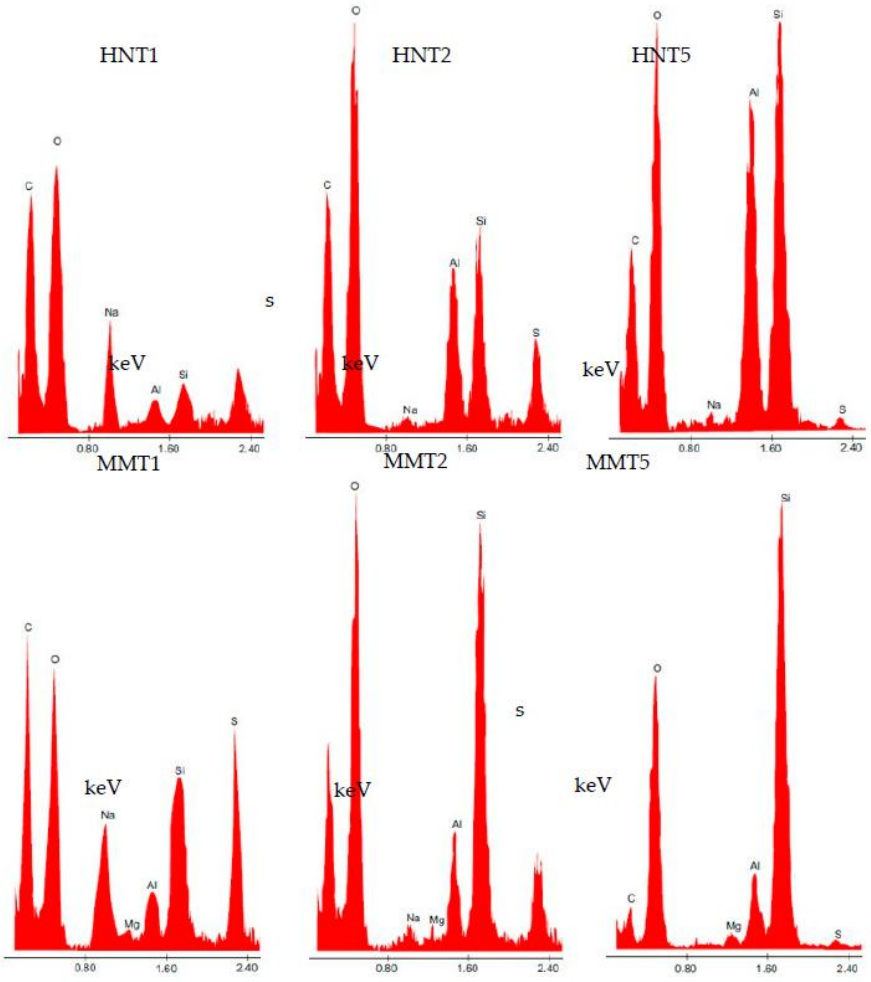

Figure 7. *EDX spectra of the broadened parts of the fibers.*

3.3. Scaffold characterizations: mechanical properties

The mechanical properties (force at break mN, a,b; elongation %, c,d; Young's Modulus mN/cm^2, e,f) of scaffolds loaded with HNT or MMT, in dry (a,c,e) or wet (b,d,f) conditions are presented in Figure 8.

In the dry state, the increase of HNT caused a decrease of force at break (Figure 8a) and of system elasticity (Figure 8c), while MMT reinforced the scaffold structure increasing the resistance to break (Figure 8a) and the system elasticity (Figure 8c) up to the 2% concentration; a further increase weakened the scaffold. The scaffolds were characterized by moderate deformability higher than that of the blank scaffolds (Figure 8b). The hydration caused a remarkable decrease in resistance to break, an increase of deformability, and a loss of elasticity (Figure 8d–f). Clay minerals seem to reinforce the scaffold structure; however, if their concentration exceeded a certain threshold, the

presence of particles embedded into the polymeric matrix could disrupt the polymer chain entanglements, weakening the scaffolds.

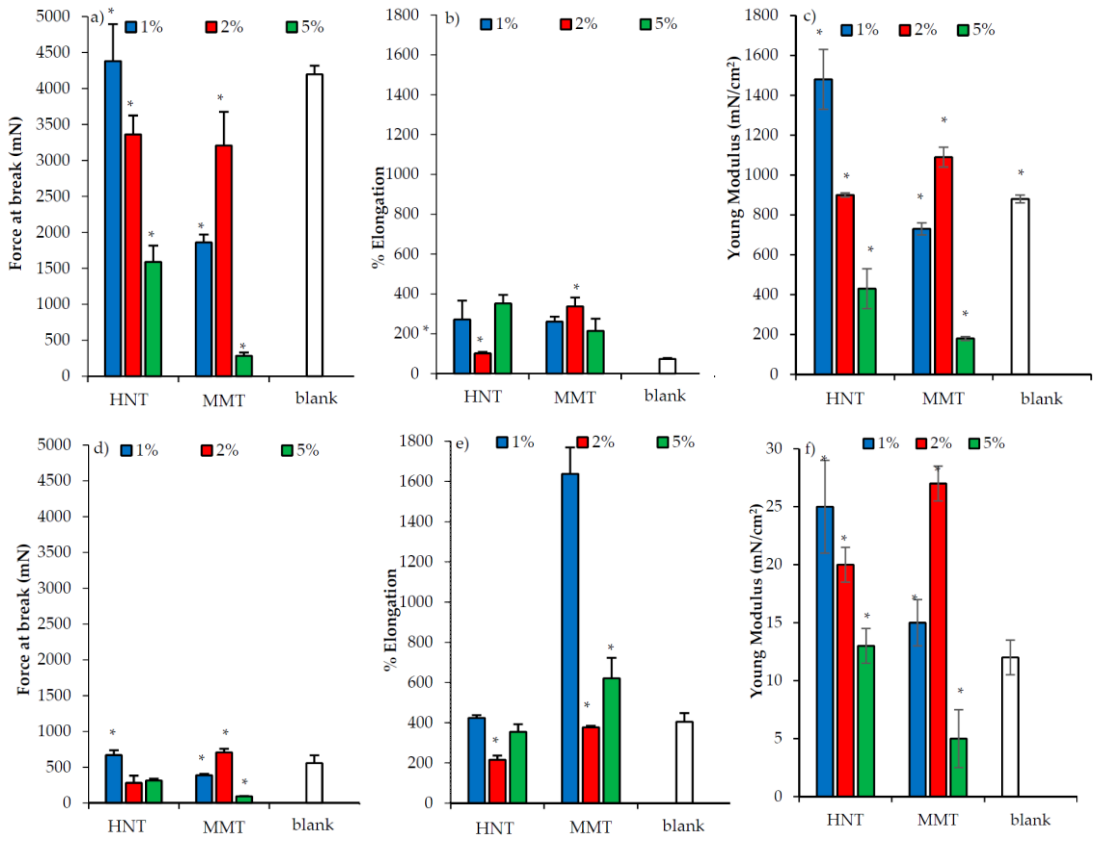

Figure 8. *Mechanical properties (force at break mN,* ***a–c****; elongation %,* ***b–e****; Young's Modulus mN/cm2,* ***c–f)*** *for dry (****a–c****) and wet (****d–f****) scaffolds loaded with HNT or MMT at different concentrations (mean values ± SD; n = 3). Statistics: * = Mann–Whitney (Wilcoxon) W test p < 0.05*

3.4. Fibroblasts biocompatibility and adhesion

Assessment for the cytocompatibility (OD, optical density) towards fibroblasts of (a) the scaffold components after 3 and 6 days of growth, and (b) the scaffolds after 3, 6, and 10 days of growth is summarized and presented in Figure 9. All the scaffold components (solubilized or dispersed in growth medium, GM) were characterized by similar biocompatibility considering 3 or 6 days of interaction, attachment and exposure with the fibroblasts (Figure 9a). Both HNT and MMT showed good biocompatibility. Of note, the fibroblast cytocompatibility decreased with their concentrations: in these conditions, clay minerals as powders (not soluble in GM) could negatively influence cell viability due to their sedimentation

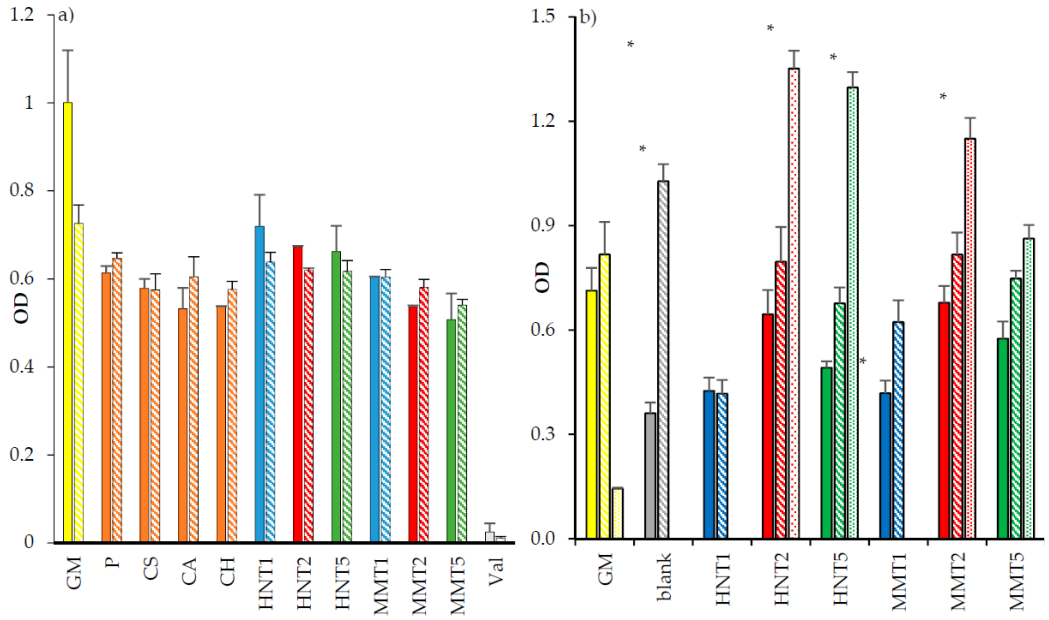

Figure 9. *Cytocompatibility (OD, optical density) towards fibroblasts of (**a**) the scaffold components (GM: growth medium; P: pullulan; CS: chondroitin sulfate; CA: citric acid; CH: chitosan; Val: valinomycin) after 3 days (plain color) and 6 days (oblique line) of growth, and (**b**) of the scaffolds loaded with HNT or MMT after 3 days (plain colors), 6 days (oblique lines), and 10 days (spotted) of growth (**b**) (mean values ± SD; n = 8). Statistics: * = Mann–Whitney (Wilcoxon) W test p < 0.05.*

Fibroblast cells showed to grow onto the scaffolds, and these were compared to those of the control (GM, cell growth in standard conditions) (Figure 9b). After 3 days of cell growth onto the scaffolds loaded with either 2% HNT or 2% MMT, these were able to proliferate similarly to that seen when in simple substrate exposed to growth medium (as reference control). Conversely, all the other compositions caused a significant decrease in cell viability, as shown in Figure 9a,b. After 6 days, the blank scaffold and the scaffolds loaded with MMT (at all the concentrations) and HNT (at 2% and 5%) enhanced cell proliferation similarly to control samples, and only the scaffolds loaded with HNT at 1% was not able to show any proliferation as the control. After 10 days, the GM was unable to progress into further cell growth due to the extensive cytotoxicity issues. Nonetheless, the scaffolds loaded with both the clay minerals at 2% and 5% showed increased cell proliferation, and HNT and MMT at 2% showed the best proliferative responses. A possible explanation could be due to the specific properties of halloysite and montmorillonite which showed the enhancing fibroblast proliferation [9,10].

These results are in agreement with the analysis carried out on the observed CLSM and the SEM images (Figure 10). In particular, from the SEM and CLSM analysis it could be suggested that the loading of clay minerals in the scaffolds allowed homogeneous fibroblast attachment, spreading and growth all over the scaffolds. Interestingly, only the scaffold containing MMT at 5% caused cell growth in clusters and this could be associated with the irregular surface and morphology of the scaffold fibers, which prevented cell attachment and surface adhesion. However, the scaffolds loaded with HNT or MMT at 2% allowed the fibroblasts to maintain their fusiform structure and aligned and elongated the cytoskeleton filaments, enhancing cell confluency.

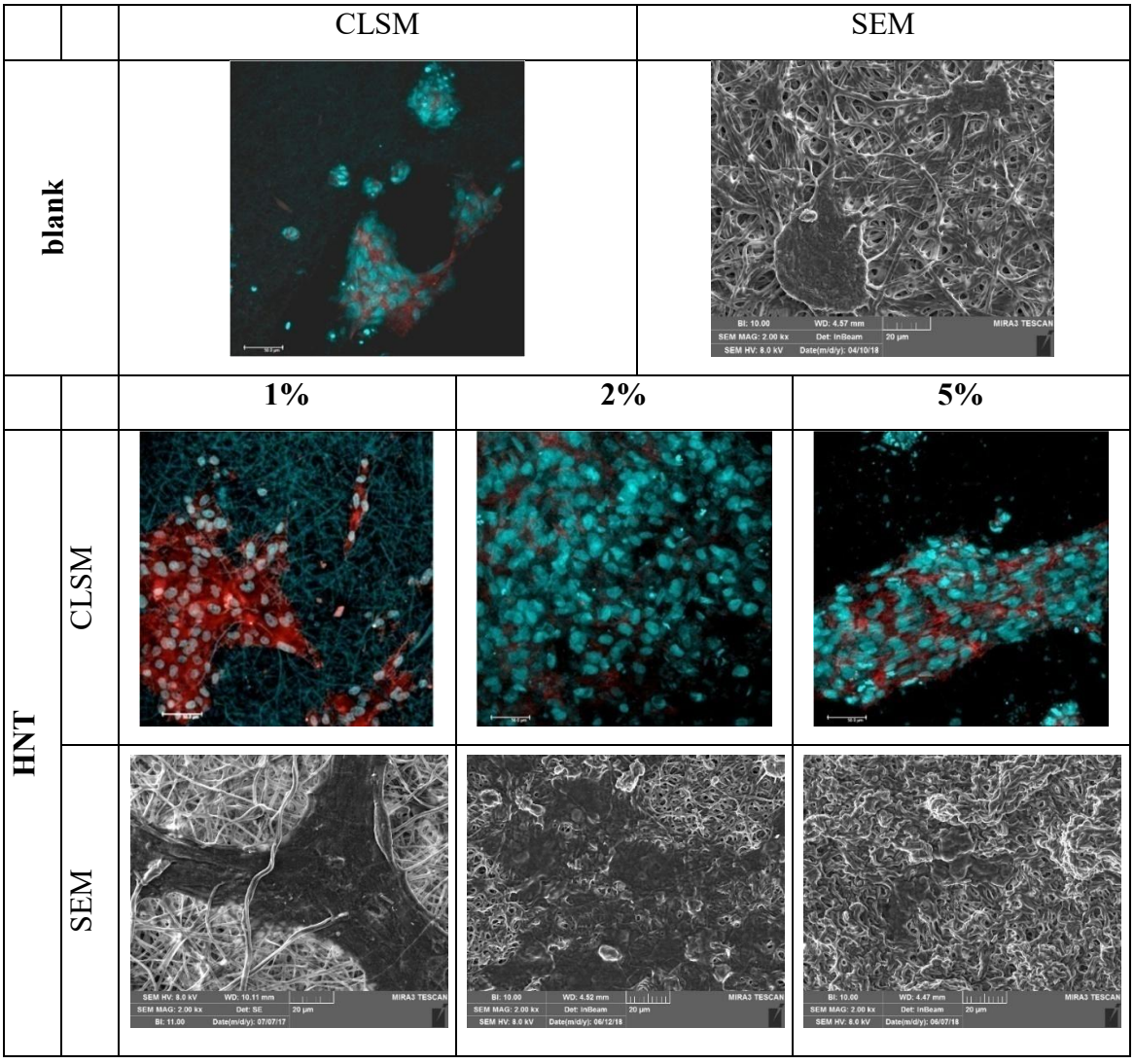

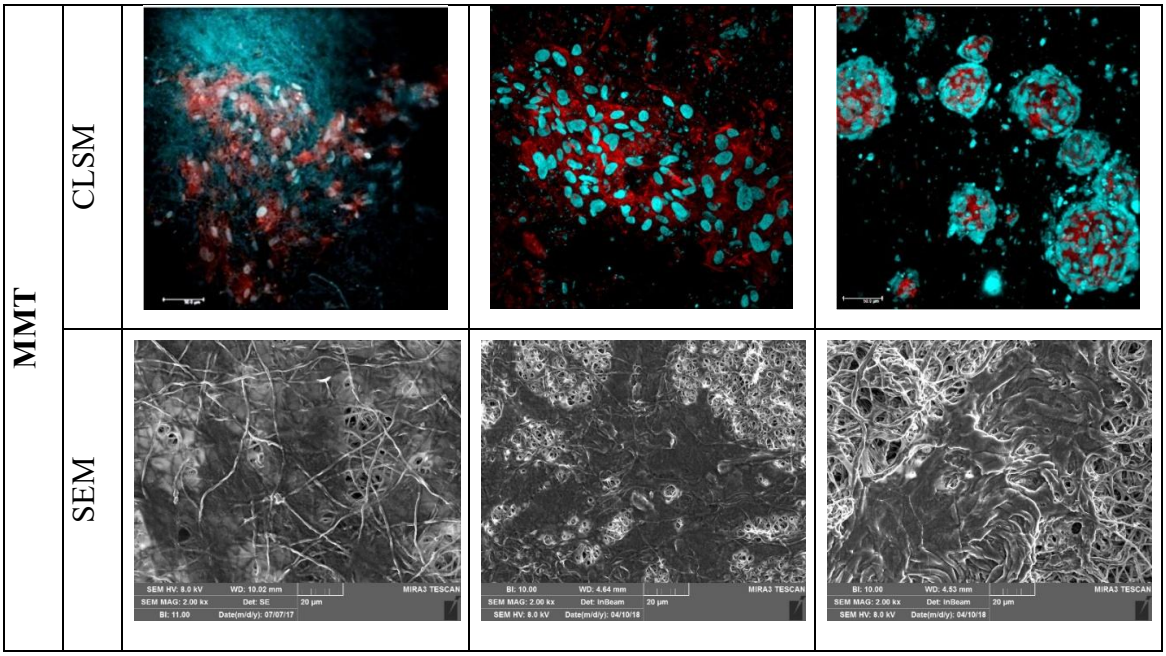

Figure 10. *CLSM (scale bar: 50 μm) and SEM (scale bar: 20 μm) representative images of fibroblasts grown for 6 days onto the scaffolds loaded with HNT or MMT at 1%, 2%, and 5% (CLSM: in blue: nuclei; in red: cytoskeleton). Cell proliferation pattern showed by the nuclear staining increased frequencies in the HNT and MMT.*

In a previous work [16], a blank scaffold was characterized for surface zeta potential by means of the measurements of a streaming current and streaming potential. Such a scaffold possessed 2.9 isoelectric point with a zeta potential plateau above pH 5, at about −13.8 mV, and this was related to the strong interaction between CS and the amino groups of CH. Moreover, the structural features at the mesoscale were characterized by means of SAXS analysis [16]. These evidenced that nanofibers in the scaffold were characterized by tubular structures and that the hydration caused polymer chains protruding and stretching out from the fibers surface. The scaffold swelling was due to the dilatation of the scaffold mesh rather than single fiber swelling [16]. In addition, the blank scaffold possessed a certain degree of antibacterial activity against *Staphylococcus aureus*, and this was attributable to chitosan that retained its antimicrobial properties although entangled in the scaffold structure. Furthermore, the blank scaffold demonstrated to be resorbed in vivo in a preclinical (burn excisional murine) model after the lesion healing [16]: the evaluation of the degradation pathway evidenced that lysozyme, continuously secreted by white cells (macrophages and neutrophils) during the inflammatory phase of wound healing, played a crucial role in scaffold degradation [30].

3.5. Cytocompatibility of macrophages and pro-inflammatory immune response

Cytocompatibility was carried out by means of MTT assessment, recorded as intensity profile,analysed and presented on the macrophages in response to the scaffold components (a), the exposure and interaction with scaffolds after 24 and 72 h time points (b), as shown in Figure 11a,b. Moreover, TNFα concentrations (pg/mL), secreted by the macrophages after the contact with the components or the scaffolds are reported, in parallel to the MTT intensity readouts, in response to the components (Figure 11c); and the scaffolds (Figure 11d). From the collective results, it emerges that for all the cell substrates exposed to the components of the scaffold prepared in solution and for the LPS, at higher concentration (used as proinflammatory control) presented a full biocompatibility range when considering the two time points 24 or 72 h of contact with the macrophages (Figure 11a). Both HNT and MMT showed comparable biocompatibility although the macrophages' cytocompatibility decreased with MMT concentrations probably due to their different degradation profile up to 72 h.

The scaffold cytocompatibility towards fibroblasts and their proinflammatory response were evaluated only in the case of 2% clay mineral loading. In fact, the results obtained from mechanical properties and cell adhesion and proliferation capacity suggest that 2% clay mineral conferred to the scaffolds suitable stiffness/elasticity combined with the capability to support cell homing. After 24 and 72 h of growth, the scaffolds loaded with either HNT or MMT at 2% allowed macrophage viability similarly to that of their negative controls (GM, cell growth in standard conditions) (close to 75% of viability) (Figure 11b). However, the blank scaffold showed 50% cell viability with respect to the GM. The increase in the exposure time at 72 h also shows a decreased viability of the macrophages, when compared to their negative controls (GM).

Interestingly when looking at cytokine secretion, TNFα was secreted in significantly lower amounts from the cells in exposed and in contact with scaffold components for 24 h, while after 72 h of contact, the TNFα secretions were similar to the negative control, GM. The LPS positive controls provided the evidence that the cells were responsive to stimuli (proinflammatory agent) (Figure 11c). Considering 24 h exposure, the scaffolds caused a TNFα secretion similar to that of the GM. The scaffold loaded with HNT induced the TNFα secretion similar to those obtained when LPS was at a lower concentration but significantly lower than those observed for LPS at a higher concentration (Figure 11d). After 72 h of exposure time, all the scaffolds were assessed in their TNFα secretions that

were not significantly different to the GM. This could be possibly also linked to the decrease in macrophage viability after 72 h in standard growth conditions. These results showed that HNT and MMT scaffolds did not show any significant proinflammatory activity compared to controls.

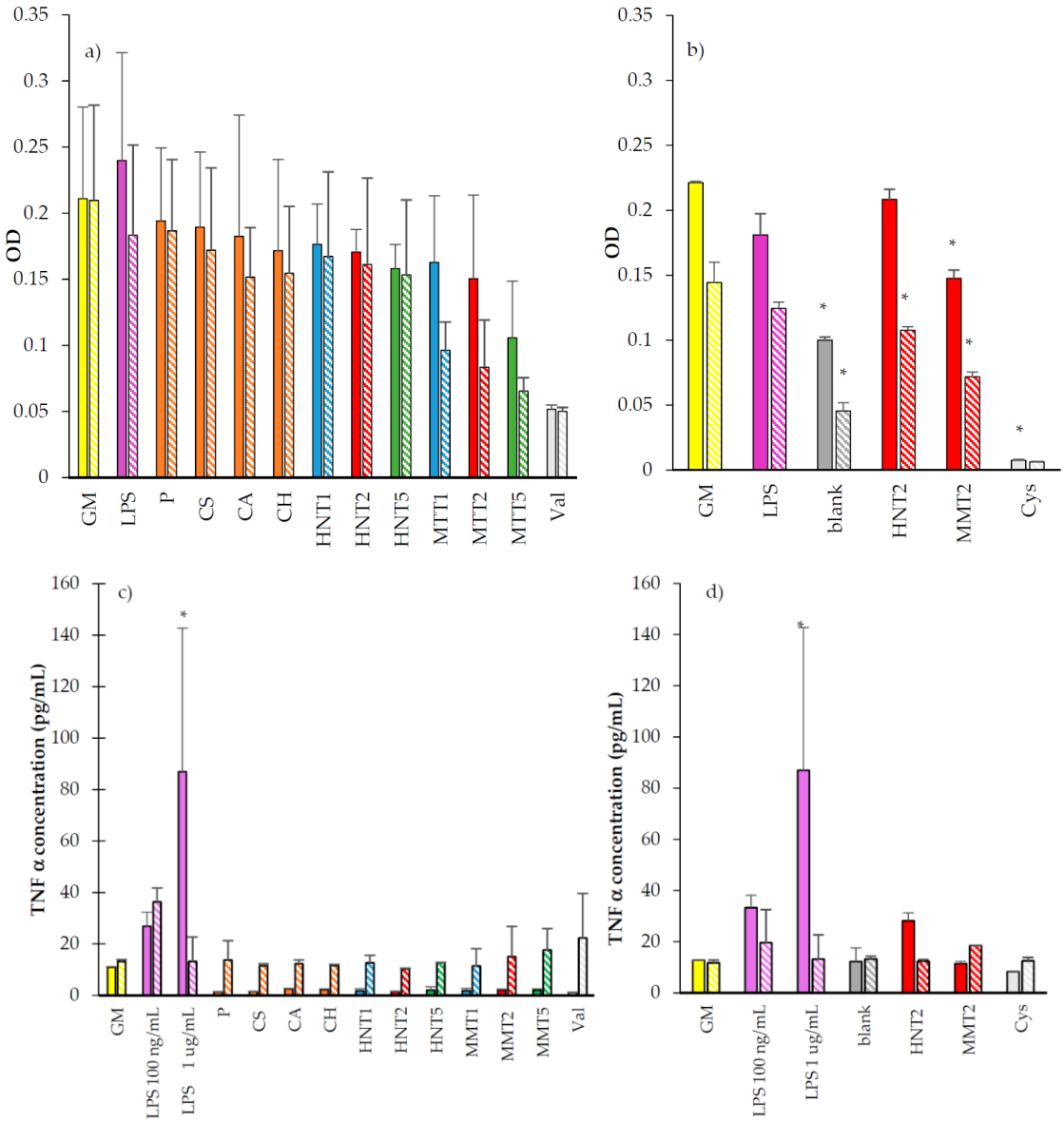

Figure 11. *Cytocompatibility of THP-1 macrophages of the scaffold components (**a**), and the scaffolds after 24 (plain color) and 72 h (oblique lines) of exposure and contact (**b**). TNFα cytokine expression and concentrations (pg/mL) for THP-1 cells exposed to components (**c**); and (**d**) scaffolds (mean values ± SD; n = 8) (GM: growth medium; LPS: lipopolysaccharide; P = pullulan; CS: chondroitin sulfate; CA: citric acid; CH: chitosan; HNT1: 1% w/w halloysite; HNT2: 2% w/w halloysite; HNT5: 5% w/w halloysite; MMT1: 1% w/w montmorillonite; MMT2: 2% w/w montmorillonite; MMT: 5% w/w montmorillonite; blank: unloaded scaffold; Val: valinomycin; Cys: cysplatinum) Statistics: * = Mann– Whitney (Wilcoxon) W test p < 0.05*

4. CONCLUSIONS

Halloysite or montmorillonite were loaded in an electrospun polysaccharidic scaffold in a one- pot process. Halloysite scaffolds were characterized by a fiber regular structure and smooth surface, and did not show any structural alterations when embedded in the polymeric matrix, probably due to the nanotubular structure of this clay mineral. MMT scaffolds were characterized by nanofiber portions with a regular, smooth surface, spaced out in broadened parts as knots with a scattered structure, possibly due to its structure. Moreover, MMT inclusion in the polymeric matrix of the scaffold caused interlayer space enlargement, causing the biopolymer intercalation into the MMT galleries, resulting in a deep interaction between the scaffold matrix and clay mineral. HNT or MMT (2% concentration) in the scaffolds were able to sustain homogeneous fibroblast spreading all over the scaffolds and their growth up to confluency, maintaining a cell fusiform structure and aligned and elongated cytoskeleton filaments. HNT and MMT (2% concentration) scaffolds. Due to their capability to support and enhance fibroblasts proliferation with negligible proinflammatory activity, these scaffolds are promising for applications in wound healing: Their capability to enable cell attachmnent and adhesion is probably due to their morphological 3D structure-assisted cell homing, and this could facilitate wound healing in vivo.

5. PATENTS

Sandri: G.: Bonferoni, M.C.; Rossi, S.; Ferrari, F. Electrospun nanofibers and membranes, PCT/IT2017/000160, 2017.

Author Contributions: Conceptualization, G.S., A.P.-M. (Cytocompatibility of Macrophages and Pro- inflammatory Immune Response); methodology, G.S.; A.P.-M. (Cytocompatibility of Macrophages and Pro- inflammatory Immune Response); software, F.F. and M.C.B.; validation, C.V.; investigation, M.L., A.F., D.M., M.R.; data curation, G.S., C.A. A.P.-M. (Cytocompatibility of Macrophages and Pro-inflammatory Immune Response); writing—original draft preparation, G.S., M.R., A.F.; writing—review and editing, G.S., A.P.-M. (Cytocompatibility of Macrophages and Pro-inflammatory Immune

Response); supervision, G.S., A.P.-M. (Cytocompatibility of Macrophages and Pro-inflammatory Immune Response); project administration, G.S.; funding acquisition, G.S., S.R., F.F., M.C.B., A.P.-M. (Cytocompatibility of Macrophages and Pro-inflammatory Immune Response). All authors have read and agreed to the published version of the manuscript.

Funding: This work was partially supported by Horizon 2020 Research and Innovation Programme under Grant Agreement No. 814607.

Acknowledgments: The authors wish to thank Giusto Faravelli SpA for supplying the polymers.

Conflicts of Interest: The authors declare no conflict of interest.

REFERENCE

1. Sorg, H.; Tilkorn, D.J.; Hager, S.; Hauser, J.; Mirastschijski, U. Skin Wound Healing: An Update on the Current Knowledge and Concepts. *Eur. Surg. Res.* **2017**, *58*, 81–94.
2. Järbrink, K.; Ni, G.; Sönnergren, H.; Schmidtchen, A.; Pang, C.; Bajpai, R.; Car, J. The humanistic and economic burden of chronic wounds: A protocol for a systematic review. *Syst. Rev.* **2017**, *6*, 15.
3. Sen, C.K. Human Wounds and Its Burden: An Updated Compendium of Estimates. *Adv. Wound Care* **2019**,*8*, 39–48.
4. Naumenko, E.A.; Guryanov, I.D.; Yendluri, R.; Lvov, Y.M.; Fakhrullin, R.F. Clay nanotube–biopolymer composite scaffolds for tissue engineering. *Nanoscale* **2016**, *8*, 7257–7271.
5. Dawson, J.I.; Oreffo, R.O.C. Clay: New Opportunities for Tissue Regeneration and Biomaterial Design. *Adv. Mater.* **2013**, *25*, 4069–4086.
6. Williams, L.B.; Metge, D.W.; Eberl, D.D.; Harvey, R.W.; Turner, A.G.; Prapaipong, P.; Poret-Peterson, A.T. What Makes a Natural Clay Antibacterial? *Environ. Sci. Technol.* **2011**, *45*, 3768–3773.
7. Sandri, G.; Bonferoni, M.C.; Rossi, S.; Ferrari, F.; Aguzzi, C.; Viseras, C.; Caramella, C. *Clay Minerals for Tissue Regeneration, Repair, and Engineering*; Ågren, M.S., Ed.; Elsevier: Amsterdam, The Netherlands, **2016**; pp. 385– 402.

8. Garcia-Villen, F.; Faccendini, A.; Aguzzi, C.; Cerezo, P.; Bonferoni, M.C.; Rossi, S.; Grisoli, P.; Ruggeri, M.; Ferrari, F.; Sandri, G.; et al. Montmorillonite-norfloxacin nanocomposite intended for healing of infected wounds. *Int. J. Nanomed.* **2019**, *14*, 5051–5060.
9. Sandri, G.; Aguzzi, C.; Rossi, S.; Bonferoni, M.C.; Bruni, G.; Boselli, C.; Cornaglia, A.I.; Riva, F.; Viseras, C.; Caramella, C.; et al. Halloysite and chitosan oligosaccharide nanocomposite for wound healing. *Acta Biomater.* **2017**, *57*, 216–224
10. Aguzzi, C.; Sandri, G.; Viseras, C.; Bonferoni, M.C.; Cerezo, P.; Rossi, S.; Ferrari, F.; Caramella, C. Solid state characterization of silver sulfadiazine loaded on montmorillonite/chitosan nanocomposite for wound healing. *Colloid Surf. B* **2014**, 113, 152–157.
11. Sandri, G.; Bonferoni, M.C.; Ferrari, F.; Rossi, S.; Aguzzi, C.; Mori, M.; Grisoli, P.; Cerezo, P.; Tenci, M.; Viseras, C.; et al. Montmorillonite-chitosan-silver sulfadiazine nanocomposites for topical treatment of chronic skin lesions: In vitro biocompatibility, antibacterial efficacy and gap closure cell motility properties. *Carbohyd. Polym.* **2014**, *102*, 970–977.
12. Gaharwar, A.K.; Cross, L.M.; Peak, C.W.; Gold, K.; Carrow, J.K.; Brokesh, A.; Singh, K.A. 2D Nanoclay for Biomedical Applications: Regenerative Medicine, Therapeutic Delivery, and Additive Manufacturing. *Adv. Mater.* **2019**, *31*, 1900332.
13. Mousa, M.; Evans, N.D.; Oreffo, R.O.C.; Dawson, J.I. Clay nanoparticles for regenerative medicine and biomaterial design: A review of clay bioactivity. *Biomaterials* **2018**, *159*, 204–214.
14. Vivekanandhan, S.; Schreiber, M.; Mohanty, A.K.; Misra, M. *Advanced Electrospun Nanofibers of Layered Silicate Nanocomposites: A Review of Processing, Properties, and Applications*; Pandey, J., Reddy, K., Mohanty, A., Misra, M., Eds.; Springer: Berlin/Heidelberg, Germany, 2014; pp. 361–388.
15. Lvov, Y.; Abdullayev, E. Functional polymer–clay nanotube composites with sustained release of chemical agents. *Prog. Polym. Sci.* **2013**, *38*, 1690–1719.
16. Sandri, G.; Rossi, S.; Bonferoni, M.C.; Miele, D.; Faccendini, A.; Del Favero, E.; Di Cola, E.; Icaro Cornaglia, A.; Boselli, C.; Luxbacher, T.; et al. Chitosan/glycosaminoglycan scaffolds for skin reparation. *Carbohydr. Polym.* **2019**, *220*, 219–227, doi:10.1016/j.carbpol.2019.05.069.

17. Kupiec, T.C.; Matthews, P.; Ahmad, R. Dry-heat sterilization of parenteral oil vehicles. *Int. J. Pharm. Compd*. **2000**, *4*, 223–224.
18. Malgarim Cordenonsi, L.; Faccendini, A.; Rossi, S.; Bonferoni, M.C.; Malavasi, L.; Raffin, R.; Scherman Schapoval, E.E.; Del Fante, C.; Vigani, B.; Miele, D.; et al. Platelet lysate loaded electrospun scaffolds: Effect of nanofiber types on wound healing. *Eur. J. Pharm. Biopharm.* **2019**, *142*, 247–257.
19. Saporito, F.; Sandri, G.; Bonferoni, M.C.; Rossi, S.; Malavasi, L.; Del Fante, C.; Vigani, B.; Black, L.; Ferrari, F. Electrospun gelatin-chondroitin sulfate scaffolds loaded with platelet lysate promote immature cardiomyocyte proliferation. *Polymers* **2018**, *10*, 208.
20. Cravero, F.; Churchman, G.J. The origin of spheroidal halloysites: A review of the literature. *Clay Miner.***2016**, *51*, 417–427.
21. Faccendini, A.; Ruggeri, M.; Rossi, S.; Bonferoni, M.C.; Aguzzi, C.; Grisoli, P.; Viseras, C.; Sandri, G.; Ferrari, F. Norfloxacin loaded electrospun scaffolds: Montmorillonite nanocomposite vs. free drug. *Pharmaceutics* **2020**, 12: 325
22. Habibi, S.; Saket, M.; Nazockdast, H.; Hajinasrollah, K. Fabrication and characterization of exfoliated chitosan–gelatin–montmorillonite nanocomposite nanofibers. *J. Text. I* **2019**, *110*, 1672–1677.
23. Sandri, G.; Rossi, S.; Bonferoni, M.C.; Caramella, Ferrari, F. Electrospinning Technologies in Wound Dressing Applications. *Ther. Dress. Wound Health Appl.* **2020**, *14*, 315–366.
24. Falcón, J.M.; Sawczen, T.; Aoki, I.V. Dodecylamine-Loaded Halloysite Nanocontainers for Active Anticorrosion Coatings. *Front. Mater.* **2015**, *2*, 69.
25. Darder, M.; Colilla, M.; Ruiz-Hitzky, E.; Biopolymer–clay nanocomposites based on chitosan intercalated in montmorillonite. *Chem. Mater.* **2003**, *15*, 3774–3780.
26. Deb Nath, S.; Abueva, C.; Kim, B.; Taek Lee, B. Chitosan–hyaluronic acid polyelectrolyte complex scaffold crosslinked with genipin for immobilization and controlled release of BMP-2. *Carbohydr. Polym*. **2015**, *115*, 160–169.
27. Sedghi, R.; Sayyari, N.; Shaabani, A.; Niknejad, H.; Tahereh, T. Novel biocompatible zinc-curcumin loaded coaxial nanofibers for bone tissue engineering application. *Polymers* **2018**, *142*, 244–255.

28. Drosou, C.; Krokida, M.; Biliaderis, C.G. Composite pullulan-whey protein nanofibers made by electrospinning: Impact of process parameters on fiber morphology and physical properties. *Food Hydrocoll.* **2017**, *17*, 726–735.
29. Islam, S.; Rahaman, S.; Yeum, J.H. Electrospun novel super-absorbent based on polysaccharide–polyvinyl alcohol–montmorillonite clay nanocomposites. *Carbohydr. Polym.* **2015**, *115*, 69–77
30. Sandri, G.; Miele, D.; Faccendini, A.; Bonferoni, M.C.; Rossi, S.; Grisoli, P.; Taglietti, A.; Ruggeri, M.; Bruni, G.; Vigani, B.; et al. Chitosan/Glycosaminoglycan Scaffolds: The Role of Silver Nanoparticles to Control Microbial Infections in Wound Healing. *Polymers* **2019**, *11*, 1207

CHAPTER 3

Norfloxacin-Loaded electrospun Scaffolds: Montmorillonite Nanocomposite *vs*. free drug

Angela Faccendini [1], Marco Ruggeri [1], Dalila Miele [1], Silvia Rossi [1], Maria Cristina Bonferoni [1], Carola Aguzzi [2], Pietro Grisoli [1], Cesar Viseras [2], Barbara Vigani [1], Giuseppina Sandri [1,*] and Franca Ferrari [1]

[1] *Department of Drug Sciences, University of Pavia, Viale Taramelli 12, 27100 Pavia, Italy;*
[2] *Department of Pharmacy and Pharmaceutical Technology, Faculty of Pharmacy, University of Granada, Campus of Cartuja, 18071 Granada, Spain;*
* *Corresponding author:*
Received: 24 February 2020; Accepted: 27 March 2020; Published: 4 April 2020

Abstract

Infections in nonhealing wounds remain one of the major challenges. Recently, nanomedicine approach seems a valid option to overcome the antibiotic resistance mechanisms. The aim of this study was the development of three types of polysaccharide-based scaffolds (chitosan-based (CH), chitosan/chondroitin sulfate-based (CH/CS), chitosan/hyaluronic acid-based (CH/HA)), as dermal substitutes, to be loaded with norfloxacin, intended for the treatment of infected wounds. The scaffolds have been loaded with norfloxacin as a free drug (N scaffolds) or in montmorillonite nanocomposite (H—hybrid-scaffolds). Chitosan/glycosaminoglycan (chondroitin sulfate or hyaluronic acid) scaffolds were prepared by means of electrospinning with a simple, one-step process. The scaffolds were characterized by 500 nm diameter fibers with homogeneous structures when norfloxacin was loaded as a free drug. On the contrary, the presence of nanocomposite caused a certain degree of surface roughness, with fibers having 1000 nm diameters. The presence of norfloxacin–montmorillonite nanocomposite (1%) caused higher deformability (90–120%) and lower elasticity (5–10 mN/cm2), decreasing the mechanical resistance of the systems. All the scaffolds were proven to be degraded via lysozyme (this should ensure scaffold resorption) and this sustained the drug release (from 50% to 100% in 3 days, depending on system composition), especially when the drug was loaded in the scaffolds as a nanocomposite. Moreover, the scaffolds were able to decrease the bioburden at least 100-fold, proving that drug loading in the scaffolds did not impair the antimicrobial activity of norfloxacin. Chondroitin sulfate and montmorillonite in the scaffolds are proven

to possess a synergic performance, enhancing the fibroblast proliferation without impairing norfloxacin's antimicrobial properties. The scaffold based on chondroitin sulfate, containing 1% norfloxacin in the nanocomposite, demonstrated adequate stiffness to sustain fibroblast proliferation and the capability to sustain antimicrobial properties to prevent/treat nonhealing wound infection during the healing process.

1. INTRODUCTION

The skin is the major protective barrier against the environment and the loss its integrity, as a result of injury or illness, may lead to morbidity or even death.

Wound healing is a complex event, based on overlapping but well-orchestrated cellular and molecular processes, to repair damaged tissue and restore skin function [1,2]. The process of healing proceeds through different phases (hemostasis, inflammatory, proliferative and remodeling) and involves extracellular matrix (ECM) molecules, soluble mediators, as cytokines and growth factors, various resident cells, and infiltrating leucocytes.

In nonhealing wounds, the healing process stops at the inflammatory state, and chronic wounds, such as venous leg ulcers, arterial ulcers, diabetic ulcers, and pressure ulcers, i.e., bed sores, fail to proceed through an orderly and timely process to restore skin anatomical and functional integrity [1,2]. Moreover, all of these wounds are contaminated by proliferating bacteria from the surrounding skin, the local environment, and the endogenous patient sources, resulting in wound colonization [3,4]. This could enhance or impair wound healing, depending on the bacterial load. In the absence of an effective immune response, impeded by underlying morbidity, as venous and arterial insufficiency, diabetes, or ageing, bacterial colonization becomes critical and an unavoidable transition towards infection occurs [3,4]. In fact, the exposed subcutaneous tissue provides a favorable substrate for the microbial growth of a wide variety of microorganisms. Moreover, a longer healing time could dramatically increase the possible occurrence of infection and biofilm formation [4,5].

Infections in nonhealing wounds remain one of the major challenges. Although appropriate systemic antibiotics are considered essential for the treatment of clinically infected wounds, topical antibiotics are not recommended since they could promote bacterial resistance.

Recently, a nanomedicine approach, creating antimicrobial nanotherapeutics, has appeared to be a valid option to eliminate bacterial infections, since nanomaterials can overcome antibiotic resistance mechanisms, owing to their unique and advantageous physico-chemical properties [6,7]. In fact, several studies report that nanosystems interact with microorganisms upon multiple mechanisms, including electrostatic attraction, hydrophobic and Van der Waals forces through surface interactions, and this makes them promising candidates to achieve enhanced therapeutic efficacy against multidrug resistant (MDR) infections [6,7]. Considering this evidence, in this work, a norfloxacin–montmorillonite nanocomposite (VHS-N), previously prepared by an intercalation solution procedure, was encapsulated in nanofibrous scaffolds, since it proved to increase drug potency against both Pseudomonas aeruginosa and Staphylococcus aureus (probably due to the high surface area to volume ratio, which increases the contact area with target organisms), maintaining cytocompatibility towards fibroblasts in vitro [8].

Given this premise, the aim of this study was the loading of montmorillonite norfloxacin nanocomposite (VHS-N) in three types of biopolymer–polysaccharide-based scaffolds (chitosan-based (CH), chitosan/chondroitin sulfate-based (CH/CS), chitosan/hyaluronic acid-based (CH/HA) (H hybrid scaffolds) to obtain dermal substitutes, intended for the treatment of wounds prone to infection, such as chronic ulcers (diabetic foot, venous leg ulcers) and burns.

The hybrid scaffolds were compared with scaffolds with the same compositions in polysaccharides, but loaded with norfloxacin as a free drug (N scaffolds).

The unloaded scaffolds were previously designed and developed [9,10]. Briefly, chitosan and chitosan/glycosaminoglycan electrospun scaffolds were manufactured using electrospinning by means of a simple/single-step process. Polymeric blends in water/acetic acid mixture were electrospun and the resulting random scaffolds were crosslinked by heating to obtain water resistant systems. The scaffolds proved their effectiveness in enhancing cell growth in vitro (fibroblasts and endothelial cells) and wound healing in vivo in a murine, burn/excisional model [9]. Moreover, lysozyme, normally secreted by macrophages and polymorphonuclear neutrophilis during the inflammatory phase of the healing process, proved to degrade the scaffolds in vitro [10].

Chitosan, glycosaminoglycans and pullulan were selected since they are polysaccharide biopolymers (organic molecules synthesized by the living organisms [11]), and biopolymers are recognized as the most promising materials in wound healing since they

are characterized by having many advantages over synthetic materials because of their biocompatibility, biodegradability, lower antigenicity and renewability [11]. Therefore, although there are some examples in the literature focused on the enhancement of wound healing using antimicrobial loaded electrospun scaffolds/ dressings [12–15], those were in large part based on synthetic polymers, as polycaprolactone [12–14] or polyethylene glycol [15], and produced using critical solvents such as formic acid [12], or chloroform [15].
Furthermore, biomaterial-based complex nanostructures developed by electrospinning could lead to great advancements in the drug delivery and bioengineering/biomedical panorama [16]. In fact, electrospinning is a robust and on-demand process with high-throughput capable of making available broadly used drugs, such as antibiotics/chemotherapeutics, and enhancing their activities thanks to the nanostructure. Moreover, the electrospun materials are characterized by high mimicry and mechanical properties capable of modulating biological processes and determining cell fate, as the case of biochemical signals [17].

2. MATERIALS AND METHODS

2.1. Materials

Chitosan (CH) (β-(1-4)-linked *D*-glucosamine and *N*-acetyl-d-glucosamine) with a low molecular weight of 251 kDa, deacetylation degree 98%, (ChitoClear, Giusto Faravelli, Milan, Italy); chondroitin sodium sulfate (CS) (β-1,4-linked d-glucuronic acid and β-1,3-linked N-acetyl galactosamine) bovine 100 EP, with a low molecular weight of 14 kDa, mixture of chondroitin A (chondroitin 4 sulfate) and chondroitin C (chondroitin 6 sulfate) (Bioiberica, Barcellona, Spain); hyaluronic acid (HA) (based on β -1,3-linked N-acetylglucosamine and β-(1,4)-d-glucuronic acid) with a low molecular weight of 212 kDa (Bioiberica, Barcellona, Spain); and pullulan (PUL) (based on maltotriose repeating units, linear α 1-4 and α 1-6 glucan, produced by *Aureobasidium pullulans*) with a low molecular weight of ~200–300 kDa (food grade, Hayashibara, Japan, Giusto Faravelli, Milan, Italy) were used for the scaffold preparations. Citric acid (CA) (monohydrated citric acid, European Pharmacopeia grade, Carlo Erba, Milan, Italy) was used as a crosslinking agent. Norfloxacin (N) (Sigma-Aldrich, Milan, Italy) was used as an antimicrobial drug.

2.2. Preparation of polymeric blends

All the polymeric blends were based on: PUL, CH and CA; PUL, CH and CA containing CS or HA. PUL solution was prepared in distilled water and CS or HA were added to PUL, thus preparing three different solutions: PUL; PUL/CS and PUL/HA. N, as a free drug, or loaded in a hybrid system (H) (nanocomposite based on VHS and N [8]), was mixed with PUL, PUL/CS or PUL/HA. Then, CH was hydrated in acetic acid and CA was added. Three different polymeric blends were prepared by mixing each PUL, PUL/CS, and PUL/HA with CH solution at 1:1 weight ratio and norfloxacin concentration was 0.15% or 0.30% w/w, respectively, corresponding to 1% or 2% w/w in dry systems, after electrospinning. The composition of the blends prepared is reported in Table 1.

Table 1. *Quali-quantitative composition of polymeric blends.*

% *w*/*w*	**PUL**	**CH**	**CA**	**CS**	**HA**	**N**	**VHS**	**H_2O/CH_3COOH**
CH-N1	10	2.5	2.5	–	–	0.15	–	55/45
CH-N2	10	2.5	2.5	–	–	0.30	–	55/45
CH-H1	10	2.5	2.5	–	–	0.15	0.94	55/45
CH-H2	10	2.5	2.5	–	–	0.30	1.88	55/45
CH/CS-N1	10	2.5	2.5	0.5	–	0.15	–	55/45
CH/CS-N2	10	2.5	2.5	0.5	-	0.30	-	55/45
CH/CS-H1	10	2.5	2.5	0.5	-	0.15	0.94	55/45
CH/CS-H2	10	2.5	2.5	0.5	-	0.30	1.88	55/45
CH/HA-N1	10	2.5	2.5	-	0.5	0.15	-	55/45
CH/HA-N2	10	2.5	2.5	-	0.5	0.30	-	55/45
CH/HA-H1	10	2.5	2.5	-	0.5	0.15	0.94	55/45
CH/HA-H2	10	2.5	2.5	-	0.5	0.30	1.88	55/45

2.3. Electrospinning process

The polymer blends were electrospun using an electrospinning apparatus (STKIT-40, Linari Engineering, Pisa, Italy), equipped with a high voltage generator (5–40 kV), a glass syringe of 10 mL with a stainless steel needle (0.8 mm), a volumetric pump (Razel R99-E) and a planar collector. The following parameters were used to obtain N loaded scaffolds: DV (voltage) = 22 kV, needle-to-collector distance = 24 cm, flow = 0.379 mL/h, to obtain H loaded scaffolds: DV (voltage) = 24 kV, needle-to-collector distance = 22 cm, flow = 0.379 mL/h, relative humidity: 40%, environmental temperature: 25 °C.

All the scaffolds were then crosslinked by heating at 150 ◦C for 1 h in a tight container protected from light; the process was also reported as being able to dry sterilize the products [18]. Preliminarily, N stability in the heating process was assessed using a diode array detector (DAD) HPLC (see Section 2.2.5.1). For this purpose, the active ingredient was subjected to the heating treatment in the same conditions as the scaffolds (150 ◦C for 1 h) (in a tight container protected from light). Chromatograms and UV/visible spectra (200–700 nm) at the maximum of the corresponding chromatographic peaks were compared.

2.4. Chemico-physical characterization

Scaffold morphology was analyzed using scanning electron microscopy (SEM, Tescan, Mira3XMU, Brno, Czechia, CISRIC, University of Pavia, Pavia, Italy) after graphite sputtering in a vacuum. Nanofiber diameters were measured (Image J, ICY, Institute Pasteur, Paris, France). The presence of nanocomposite (VHS-Ns) loaded into the hybrid scaffolds was investigated by ultra-high-resolution transmission electron microscope (HR-TEM, FEI Titan G2 60–300, Thermo Fisher, Barcellona, Spain), coupled with analytical electron microscopy (AEM), with a SUPER-X silicon-drift windowless energy-dispersive X-ray spectroscopy detector. X-ray chemical element maps were collected. The samples were directly deposited onto copper grids (300 mesh coated by formvar/carbon film, Agar Scientific, Rome, Italy).

X-ray powder diffraction (XRPD) analysis was carried out using a diffractometer (X-Pert Pro model, Malven Panalytical, Monza, Italy) equipped with a solid-state detector (X-Celerator) and a spinning sample holder. The diffractogram patterns were recorded using random oriented mounts with CuKα radiation, operating at 45 kV and 40 mA, in the range 4◦–60◦ 2θ. The diffraction data were analyzed using the XPOWDER® software (Version 2017).

Fourier transform infrared spectroscopy (FTIR) spectra of the samples were recorded using spectrophotometer (Spectrum BX FTIR, PerkinElmer, Milan, Italy). All analyses were performed from 400 to 4000 cm−1 with a resolution of 0.25 cm−1. The results were processed with a software package (Spectrum, Perkin Elmer, I). In the Supplementary Materials, the spectra of the pristine components are reported (Figure S1).

2.5. Mechanical properties

Mechanical properties were assessed using a texture analyzer (TA-XT plus, Stable Microsystems, Enco, Spinea, Italy) equipped with a 1 kg load cell and A/TG tensile grips [19]. Rectangular portions (3 × 1 cm) of each scaffold (thickness ~100 μm) were kept vertical by means of two grips, the lower one fixed and the upper one movable at a constant rate of 0.5 mm/s. Dry or hydrated scaffolds were stretched up to break and the force was recorded as a function of the movable grip displacement.

The force at break was recorded and elongation % was calculated as follows (Eq 1):

$$E\% = 100 \times (Lbreak - L0)/Lbreak, \quad (Eq.1)$$

where Lbreak = the distance of the two grips at scaffold breaking and L0 = the initial distance of the two grips. Moreover, the Young's modulus (mN/cm2) was calculated as the slope of the initial linear portion of force vs. grip displacement.

2.6. Norfloxacin release measurements

All the release measurements were performed in sink conditions to study drug liberation from the systems independent of the concentration of the drug released during the test [20]. Two different approaches were considered: in the first one, the drug release was studied using saline solution to simulate the lesion exudates, while in the second one, the effect of lysozyme on drug release was analyzed. Each scaffold was placed in 3 mL of dissolution medium to simulate the small number of exudates generally present in the wound, and the scaffold was completely dipped in the dissolution medium to simulate the implant of the system in the lesion bed. For this purpose, two different media were considered: saline solution (NaCl 0.9% w/v) or phosphate buffer 0.05 M (pH 6.2) containing 3.3 mg/mL of lysozyme (120.530 IU/mg, Sigma-Aldrich, Milan, Italy). As for saline solution, at prefixed times, 500 μL of dissolution medium was collected and replaced with fresh medium to keep the volume constant. The samples were analyzed by means of the DAD–HPLC method (Section 2.2.5.1) [21].

When lysozyme was present, the dissolution medium was totally collected and completely substituted with fresh medium every 24 h to avoid a loss of the enzyme activity over time. Each sample was divided in two aliquots. One aliquot was assayed to quantify the norfloxacin released from each scaffold (Section 2.2.5.1) and, for this purpose, each sample was pre-processed by diluting 1:1 with 1 N perchloric acid and by centrifugation (5000 rpm for 15 min), to precipitate the lysozyme in the solution. The second aliquot was assayed to quantify the glucosamine release, as product of lysozyme activity (Section

2.2.5.2). Moreover, the morphology of scaffolds subjected to lysozyme degradation (after 10 days) was analyzed using SEM as previously described.

2.7. Norfloxacin assay

Norfloxacin released from each scaffold was determined by DAD–HPLC (Series 200 system, PerkinElmer, Milan, Italy). A Zorbax Eclipse XDB-C8 column (4.6 mm × 150 mm, silica particle size 5 μm, Agilent, Milan, Italy) was used as the stationary phase. The mobile phase was based on acetonitrile/methanol/citric acid 0.4 M, 7:15:78 (% v/v) at a flow rate of 1.0 mL/min, using 275 nm wavelength detection [21,22]. The injection volume was 10 μL. Calibration curves were obtained using norfloxacin standard solution in the mobile phase, in saline solution or processed as the samples subjected to lysozyme degradation. In every case, the method was linear from 0.08 to 200 μg/mL with an R^2 value that was always higher than 0.995.

2.8. Glucosamine assay

Glucosamine released due to the lysozyme degradation of the scaffolds was quantified by means of ninhydrin assay [23].

All samples were diluted 1:1 ratio (v/v) with 400 μL of ninhydrin reagent (ninhydrin 2% w/v, hydrindantin 6.8 mg/L in 3:1 v/v dimethylsulfoxide: lithium acetate buffer 4 M, pH 5.2; Sigma-Aldrich, Milan, Italy) under a nitrogen blanket. Each sample was stirred at 100°C for 8 min, and vortexed until cooling, then the samples were diluted 1:10 (v/v) with a 1:1 ethanol:water mixture and quantified by a colorimetric test at L = 570 nm using an ELISA Plate Reader (iMARK Microplate Absorbance Reader, BioRad, Milan, Italy). The calibration curve (glucosamine in phosphate buffer 0.05 M at pH 6.2) was linear in the range from 0.0125 to 0.1 μg/mL with a R2 > 0.995.

2.9. Biopharmaceutical characterizations

Adhesion and proliferation assay was carried out using normal human dermal fibroblasts (NHDF) from juvenile foreskin (PromoCell, VWR, Milan, Italy) [9,10]. Fibroblasts were grown in the presence of 150 μL Dulbecco's modified Eagle medium (DMEM, Sigma-Aldrich, Milan, Italy) supplemented with 10% v/v fetal bovine serum (Euroclone, Milan, Italy), and with penicillin/streptomycin solution (pen/strep, 100 UI/100 μg/mL, Sigma-Aldrich, Merck, Milan, Italy), at 37 ◦C in a 5% CO_2 atmosphere with 95% relative

humidity. The 0.36 cm^2 circular portion scaffolds were placed at the bottom of the wells in a 96-well plate (flat bottom, Cellstar©, Greiner bio-one, Frickenhausen, Germany). Fibroblasts were seeded onto the scaffolds at a seeding density of 35,000 cells/well and grown for 3 or 6 days. The cell growth without scaffolds (35,000 cells/well) was considered the standard growth (growth medium (GM). After 3 or 6 days, the MTT [3-(4,5-dimethylthiazol-2-yl)-2,5-diphenyltetrazolium bromide] assays were performed. The fibroblasts that adhered and grew onto the scaffolds (growth for 6 days) were fixed for 2 h at 4 ◦C, using 3% w/v of glutaraldehyde in Dulbecco's phosphate buffered saline (PBS, Sigma-Aldrich, Milan, Italy) and analyzed by SEM and confocal laser scanning microscopy (CLSM), as described in the following paragraphs.

2.10. MTT assay

The biocompatibility was performed by MTT test (tetrazolium salt, [3-(4,5-dimethylthiazol-2-yl)- 2,5-diphenyltetrazolium bromide]; Sigma-Aldrich, Milan, Italy). Briefly, MTT was solubilized at 2.5 mg/mL in PBS (phosphate buffer solution, Sigma-Aldrich, Milan, Italy). At prefixed days, the medium in each well was removed and 50 µL of MTT solution plus 100 µL of PBS were added and subsequently put in contact with the cell substrates at 37 ◦C for 3 h in the incubator. Then, MTT solution was removed from each well and 100 µL of dimethylsulfoxide (DMSO, Sigma-Aldrich, Milan, Italy) was added. The absorbance was read using an ELISA Plate Reader at L = 570 nm (with reference L = 690 nm).

2.11. SEM analysis

The substrates were then washed three times with PBS and dehydrated with ethanol solutions at increasing concentrations (50–75–100% v/v). The scaffolds were then removed from culture wells, applied onto stubs, sputtered with graphite and analyzed by SEM, as previously described.

2.12. CLSM Analysis

The substrates were then washed three times with PBS. Then cell actin cytoskeleton was stained with phalloidin FITC Atto 488 (50 µL at 20 µg/mL in PBS in each well, contact time 30 min) (Sigma-Aldrich, Milan, Italy). Subsequently, after three PBS washes, the cell nuclei were stained with Hoechst 33258 (100 µL of solution at 1:10,000 dilution in PBS

per each well, contact time 10 min in the dark) (Sigma-Aldrich, Milan, Italy), for 10 min. After three further PBS washes, the scaffolds were mounted on glass slides, covered using coverslips and analyzed using CLSM (Leica TCS SP2, Leica Microsystems, Milan, Italy) at λex = 346 nm and λem = 460 nm for Hoechst 33258 and λex = 501 nm and λem = 523 nm for phalloidin FITC. The acquired images were processed by means of Leica software (Leica Microsystem, Milan, Italy).

2.13. In vitro antimicrobial assay

The antimicrobial activity of norfloxacin-loaded scaffolds, either as free drug, N, or in nanocomposite, H, was evaluated against two bacteria strains—Staphylococcus aureus ATCC 6538 and Pseudomonas aeruginosa ATCC 15442. In particular, killing time was determined as the exposure time required to kill a standardized microbial inoculum [8,10,23]. Bacteria used for killing time evaluation were grown overnight in Tryptone Soya Broth (Oxoid, Basingstoke, Hampshire, UK) at 37 ◦C. The bacteria cultures were centrifuged at 2000 rpm for 20 min to separate the cells from the broth and then suspended in phosphate buffer saline (PBS, pH 7.3). The suspension was diluted to adjust the number of cells to 107–108 CFU/mL (CFU = colony forming unit).

For each microorganism strain, a suspension was prepared in PBS without scaffolds and used as the control. Unloaded scaffolds were also tested for comparison. Bacterial suspensions were incubated at 37 ◦C. Viable microbial counts were evaluated after contact for 0, 5, and 24 h with scaffolds and in control suspensions; bacterial colonies were enumerated in Tryptone Soya Agar (Oxoid, Basingstoke, Hampshire, UK) after incubation at 37 ◦C for 24 h. The microbiocidal effect (ME value) was calculated for each test organism and contact times were calculated according to the following equation (Eq. 2):

$$ME = \log Nc - \log Nd, \qquad \text{(Eq. 2)}$$

where Nc is the number of CFUs in the control microbial suspension and Nd is the number of CFUs in the microbial suspension in the presence of the scaffold [10,23] .

2.14. Statistical analysis

Statistical differences were evaluated by means of a one-way ANOVA post-hoc Fisher's Least Significant Difference (LSD) or Mann–Whitney (Wilcoxon) W test (Statgraphics Centurion XV, Statistical Graphics Corporation, Statgraphics Technologies, Inc., The Plains, Virginia, USA). Differences were considered significant at $p < 0.05$.

3. RESULTS AND DISCUSSION

3.1. Chemico-physical characterization

Preliminarily, to scaffold preparation and cross-linking by heating, the drug stability in the heating process was assessed. For this purpose, the drug was subjected to a heating treatment in the same conditions used for the scaffold cross-linking (1 h at 150 ◦C). The heating treatment did not cause the drug degradation; in fact, after the process, the N content was 99.21% w/w (SD = 2.04) compared to the active ingredient in standard storage conditions. Figure 1 reports the UV spectra of N, and N subjected to the heating treatment at the maximum of the chromatographic peak (N retention time).

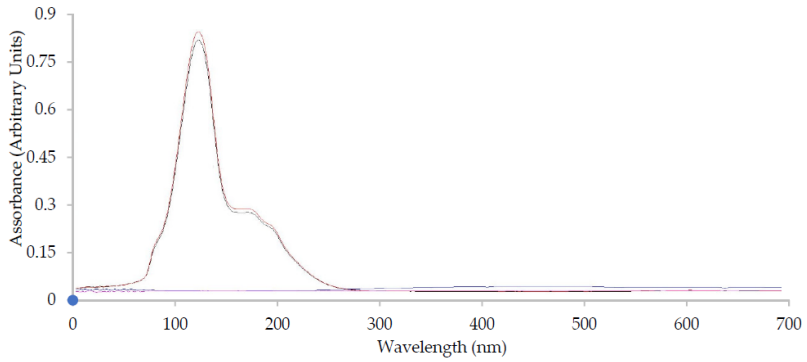

Figure 1. *UV spectra of N (red line) and N subjected to heat treatment (1 h at 150 ◦C) (black line) obtained from the HPLC analysis at N peak maximum.*

The complete overlapping of the spectra supported the stability of the drug in the heating treatment.

In a previous work [8], norfloxacin was loaded in montmorillonite, a phyllosilicate widely used in pharmaceutical field, to obtain a nanocomposite. This was prepared by means of the adsorption mechanism, as one single process, and the clay–drug adsorption isotherm was calculated. The solid-state analysis (XRPD, FTIR, thermal analysis—differential scanning calorimetry/ thermogravimetric analysis DSC/TGA, HRTEM) evidenced that protonated norfloxacin molecules interact with the active sites of montmorillonite located at its edges and within its interlayer space, thus forming a drug monolayer onto the clay mineral interlayer surface. Norfloxacin in the nanocomposite was proved in an amorphous

state, and its loading (16% w/w of total nanocomposite weight) is homogeneous and causes an expansion of montmorillonite interlayer spaces. Moreover, the nanocomposite causes a prolonged norfloxacin release over time. Moreover, the nanocomposite was characterized by good biocompatibility in vitro toward fibroblasts, and it was able to increase the antimicrobial potency of the free drug against P. aeruginosa and S. aureus, Gram-negative and Gram-positive bacteria, respectively, both of which are often concurrent causes of wound chronicization, leading to the possible impairment of the healing path and, finally, to nonhealing wounds. Montmorillonite norfloxacin nanocomposite was loaded into scaffolds and their performance was compared to those loaded with the free drug scaffolds. Figure 2 reports SEM microphotographs of CH, CH/CS or CH/HA scaffolds loaded with 1% or 2% norfloxacin, as a free drug (1% N or 2% N), or loaded with VHS-N nanocomposite (1% H or 2% H).

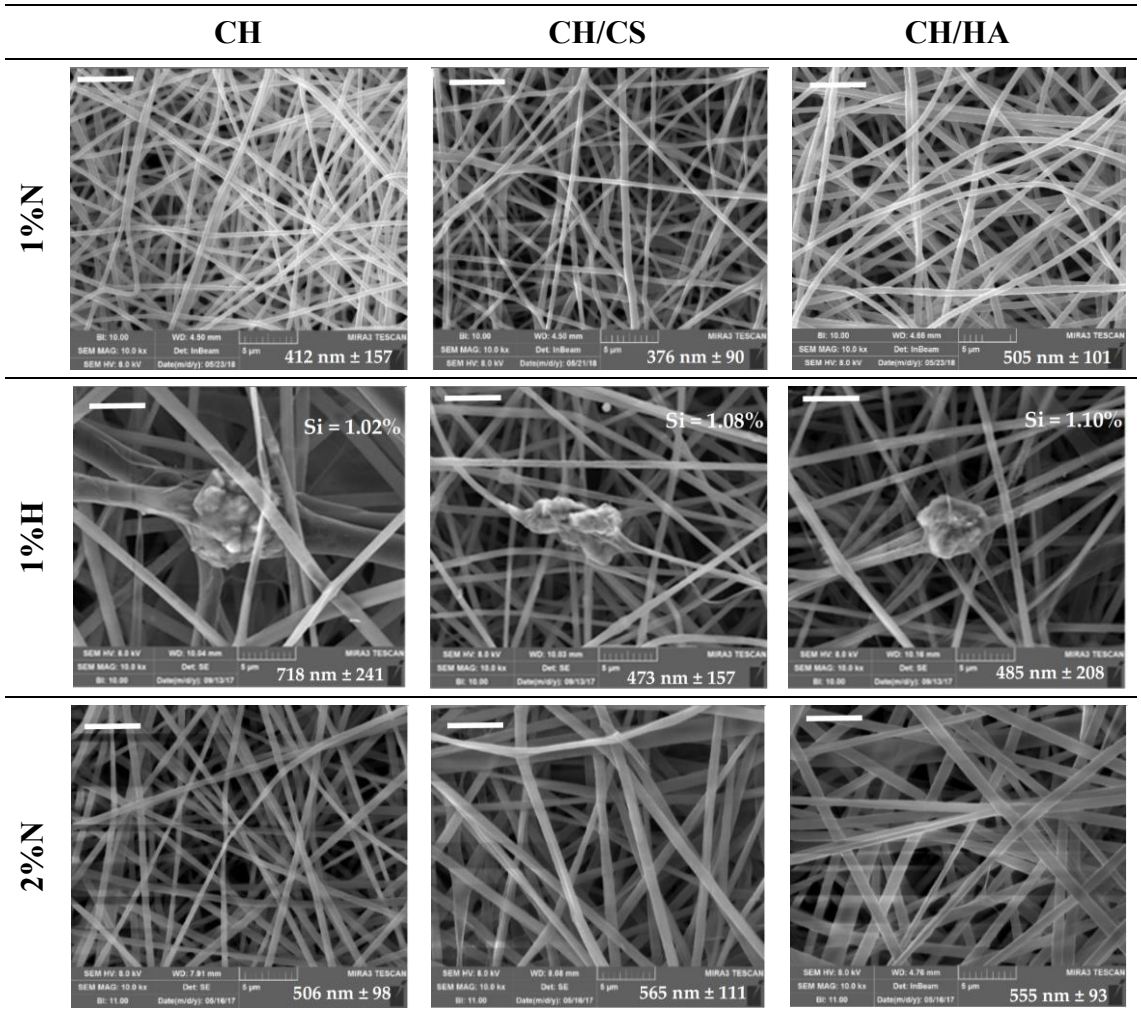

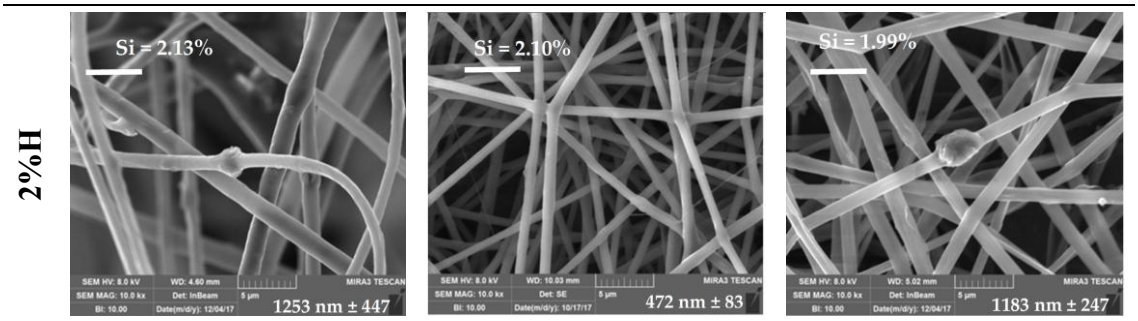

Figure 2. *SEM microphotographs of chitosan-based (CH), chitosan/chondroitin sulfate-based (CH/CS) and chitosan/hyaluronic acid-based (CH/HA) scaffolds loaded with 1% or 2% norfloxacin, as a free drug (1% N or 2% N), or in VHS-N nanocomposite. In each image, the nanofiber diameters (nm, mean values ± SD; n = 30) and Si content for hybrid scaffolds are reported. Statistics: Mann–Whitney (Wilcoxon) W test p < 0.05: CH2H vs. CH/CS2H; CH/CS2H vs. CH/HA2H; CH/HA1H vs. CH/HA2H; CH/HA2H vs.CH/HA2N (scale bar 5 µm).*

The N scaffolds, loaded with N as a free drug, were characterized by a regular structure with a smooth surface where no ribbon could be detected, independent of drug concentration. The H scaffolds, loaded with N in nanocomposite, presented nanofiber portions with a regular, smooth surface spaced out in broadened parts, with knots and a scattered structure. These conceivably could be related to the montmorillonite–norfloxacin (VHS-N) nanocomposite. Moreover, the presence of glycosaminoglycans (CS or HA) in the scaffolds caused a certain degree of surface roughness (probably due to chitosan and glycosaminoglycan interaction [9]) and this was more evident due to the increasing drug concentration in the fibers.

Nanofiber diameters were generally smaller when norfloxacin was loaded as a free drug (around 500 nm), independent of the drug concentration, although the differences were not statistically significant. On the contrary, H scaffolds were characterized by nanofibers with higher diameters (around 500 nm for 1% scaffold and around 1000 nm for 2% scaffolds) compared to those containing 1% of the drug, although this was significant only for the CH/HA scaffold; in this case, HA's high molecular weight was ten folds greater than that of CS and could cause the formation of fibers with greater diameters. On the contrary, H scaffold containing chondroitin sulfate and loaded with 2% of the drug showed similar nanofiber diameters to those loaded with the free drug. The content of Si, an element characteristic of montmorillonite, was consistent with the nanocomposite concentration in each scaffold [23].

The analysis of system viscosity previously performed on the blank systems [9], stated that chondroitin sulfate (negatively charged) conceivably interacted with chitosan (positively

charged) and this could be due to the high charge density of sulfate groups greater than those of the carboxylic moieties of hyaluronic acid. However, the presence of particles in suspension, as was the case in nanocomposite, could cause unbalanced particle charge density that generally increases the conductivity, influencing fiber diameter during electrospinning [24]. Moreover, the acid environment of the polymer blends, due to the 45% v/v acetic acid in the medium, conceivably prevented the interactions between the various moieties and drug precipitation [25,26].

Figure 3 reports the HR-TEM microphotographs and EDX spectra obtained for CH (A–C), CH/CS (G–I) and CH/HA (D–F) H scaffolds, loaded with N in the nanocomposite at 2%.

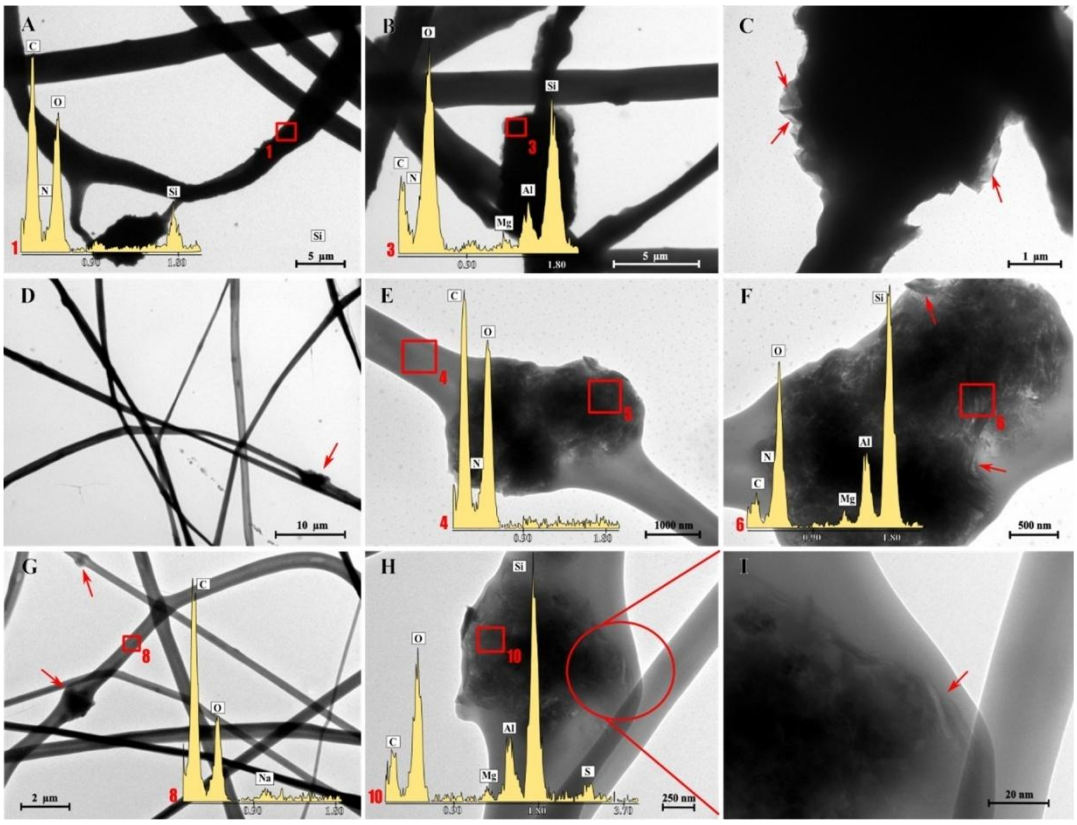

Figure 3. *Transmission electron microscope (TEM) microphotographs and EDX spectra for CH, CH/CS and CH/HA scaffolds loaded with 2% norfloxacin in nanocomposite CH (**A**–**C**), CH/CS (**G**–**I**) and CH/HA (**D**–**F**).*

The EDX analysis performed in the marked zone (red square) confirms that there was the presence of C, O and N (typical of organic elements) and characteristic elements of montmorillonite (Si, Al, Mg) in the broad, interwoven knots. This was observed for all the scaffolds, independent of their polymeric composition. At a higher magnification (Figure

3C,F,I), it was possible to identify the typical lamellar structure of montmorillonite (red arrows).

Figure 4 reports FTIR spectra evaluated for norfloxacin-loaded scaffolds (CH-N2, CH/CS-N2, CH/HA-N2) and VHS-N loaded scaffolds (CH-H2, CH/CS-H2, CH/HA-H2), both types containing 2% w/w norfloxacin.

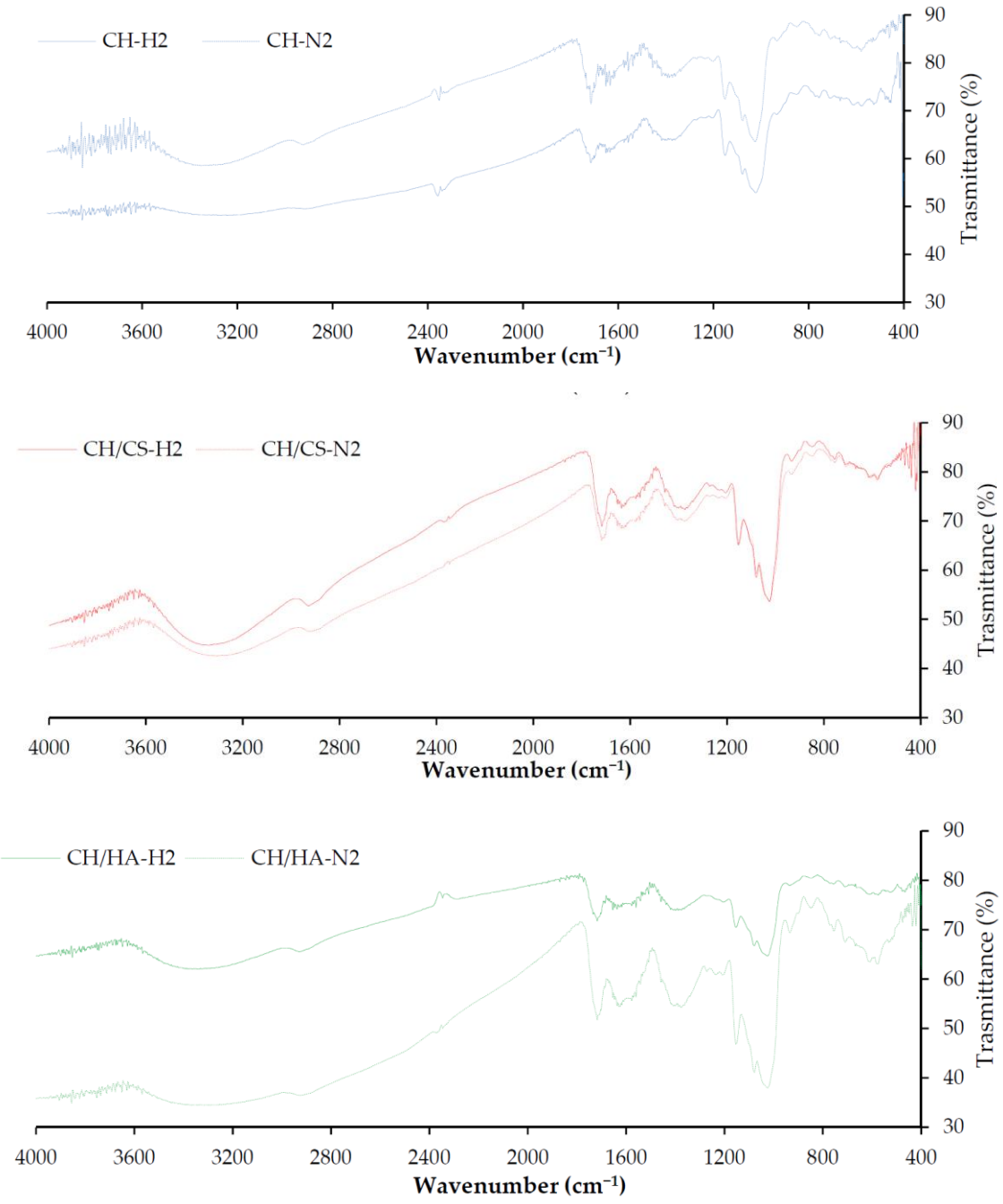

Figure 4. *Fourier transform infrared spectroscopy (FTIR) spectra evaluated for norfloxacin-loaded scaffolds (CH-N2, CH/CS-N2, CH/HA-N2) and VHS-N loaded scaffolds (CH-H2, CH/CS-*

H2, CH/HA-H2), both types containing 2% w/w norfloxacin in norfloxacin–montmorillonite nanocomposite (VHS-N).

Independent of the polysaccharide composition and loading type, either with N (free drug, norfloxacin) or H (VHS-N nanocomposite), the typical polysaccharide signals (hydrogen bonds of –OH and –NH2 groups) (pullulan: 3331 cm−1 and chitosan: 3355 cm−1) hid the drug and nanocomposite-related peaks [27]. In fact, the VHS spectrum should present a band around 1017 cm−1 due to the vibrational band of the silicates.
Figure 5 reports the XRPD patters of the scaffolds loaded with VHS-N nanocomposite containing norfloxacin at 2% compared to VHS-N, the nanocomposite and the unloaded CH scaffold.

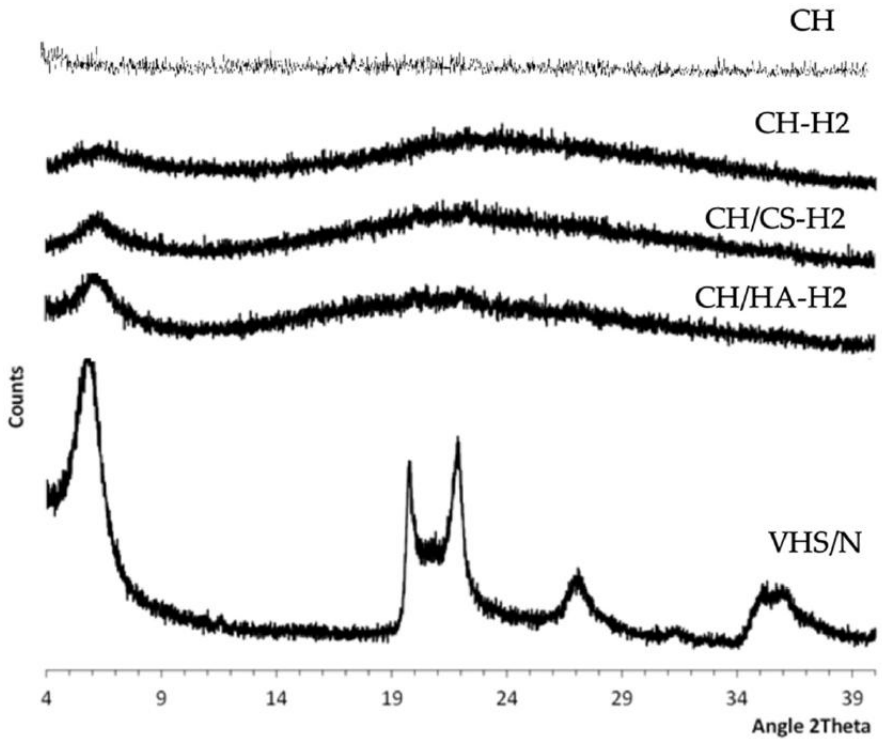

Figure 5. *X-ray powder diffraction (XRPD) diffractograms of the scaffolds loaded with VHS-N at 2% norfloxacin (CH-H2, CH/CS-H2, CH/HA-H2) compared to unloaded CH scaffolds (CH) and VHS-N.*

All the unloaded scaffolds were characterized by amorphous behavior (CH pattern is reported in Figure 5 as example) and no paracrystallinity could be detected. This was probably related to the electrospinning process. For all the scaffolds, the diffractograms were characterized by a hump between 20° and 29° 2θ, which was probably due to the

presence of the polysaccharides. The reflection peak centered at 6° 2θ, which was probably due to the nanocomposite (VHS-NF) since it coincided with the d001 of montmorillonite once NF located in the interlayer space (5.94° 2θ). Similar XRD results were obtained by Rabbani et al. (2016) [28]. Moreover, there was an absence of other intense peaks that could be attributable to the nanocomposite (VHS-N), probably due to the nanocomposite concentration in the scaffolds, which was too low.

3.2. Mechanical properties

Figure 6 reports the mechanical properties (force at break mN, a–b; elongation %, c–d; Young's modulus mN/cm^2, e–f) of scaffolds loaded with 1% or 2% of norfloxacin as a free drug (N) or as a nanocomposite (H), in dry (a, c, e) or wet (b, d, f) conditions.

In a dry state, the increase in N concentration in the scaffolds caused an increase in the force at break, except for the scaffold containing hyaluronic acid (Figure 3a). This was less evident when norfloxacin was loaded as a nanocomposite: it is conceivable that the effect of montmorillonite, which altered the entanglement of polymer chains in the scaffolds, causing lower resistance to break, prevailed over the effect attributable to the free drug, which seems to reinforce the structure. In this condition, the N scaffolds were less deformable than H scaffolds and the N concentration at 1% in H scaffolds was responsible for a higher deformability (Figure 3c). Moreover, the free drug seems to increase scaffold elasticity, especially for scaffolds containing chondroitin sulfate (Figure 3e). The hydration of the scaffolds, which simulates the application/implant in the lesion, dramatically changed the scaffold mechanical properties. N scaffolds, loaded with N as a free drug, were characterized by slightly higher resistance to break with respect to H scaffolds, confirming the behavior of the dry state (Figure 3b), while the scaffolds were simultaneously characterized by a higher degree of deformability (Figure 3d), which could be advantageous for wound bed application, and low elasticity (Figure 3f). The hydration caused a remarkable decrease in resistance to break, an increase in deformability and a loss of elasticity

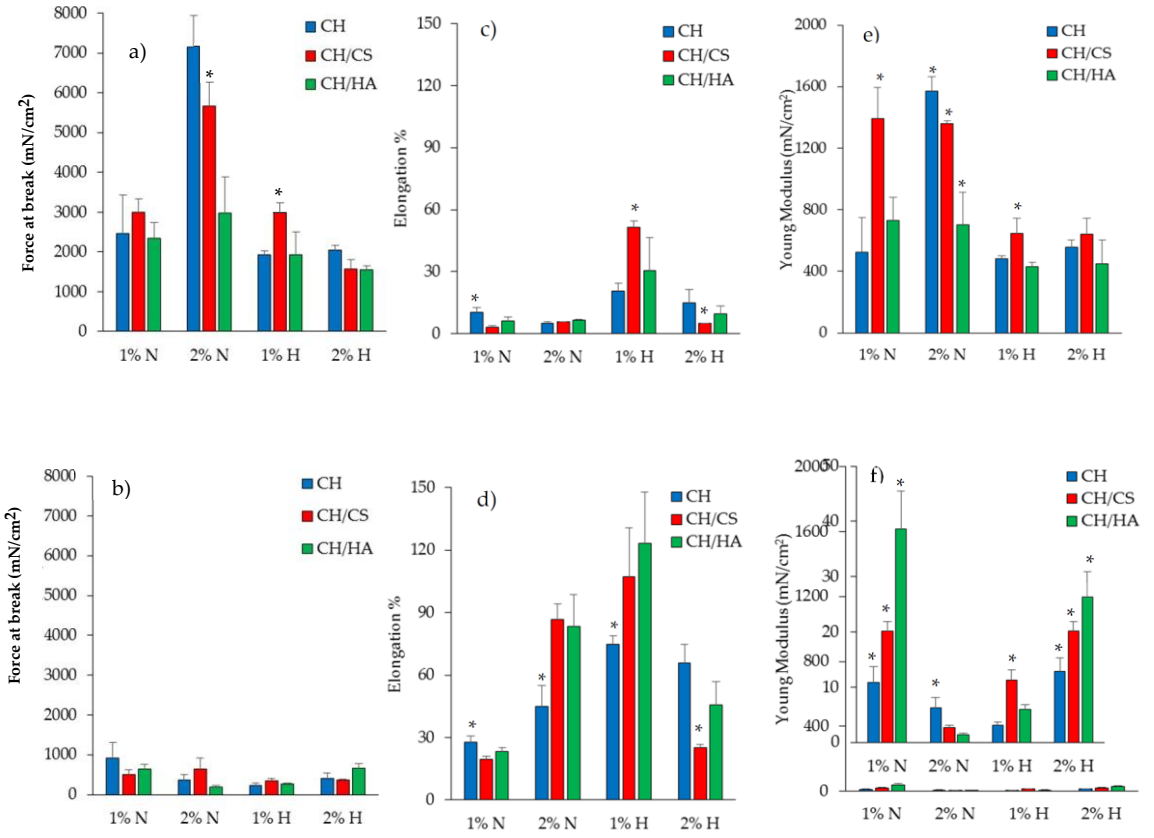

***Figure 6**. Mechanical properties (force at break mN, a-b; elongation %, **c-d**; Young's modulus mN.cm2, e-f) for dry (**a,c,e**) and wet (b,d,f) scaffolds loaded with 1% (**a**) or 2% (**b**) of norfloxacin as a free drug (N) or as nanocomposite (H) (mean values ± SD; n = 3). Statistics: * = Mann–Whitney (Wilcoxon) W test $p < 0.05$.*

The presence of montmorillonite in the hybrid scaffolds seems to weaken the scaffold structure, and this was probably due to the presence of particles embedded into the polymeric matrix that could disrupt the polymer chain entanglements, causing a significant decrease in the scaffold elasticity, and mechanical resistance, and a directly related increase in the deformability: this was more evident when 2% of drug in the nanocomposite was loaded in the scaffolds compared to scaffolds loaded with the free drug.

The mechanical properties are key features for the success of scaffold implants and their integration with the surrounding tissue. In fact, the native skin is characterized by tensile strength values approximately between 5.0 and 30.0 MPa (5000–30,000 mN/mm2), the Young's modulus in the range of 4.6–20.0 MPa (46–200 mN/cm2) and the elongation at break of about 35.0–115.0% [29]. Clearly, the ranges of the reference values are wide since the mechanical properties of the skin are strictly related to age and body lines (static lines,

as described by Langer, Kraissl's lines or Borge's lines) [30]. In particular, force at break (mechanical strength) is related to the scaffold's capability to maintain its integrity during implantation, which should occur in the dry state, while the elongation and the Young's modulus are mainly related to the scaffold performance upon implantation. The scaffolds developed in the present work were characterized by force at break in the dry state close to the skin, especially for CH and CH/CS scaffolds, when loaded with norfloxacin at 2% as a free drug. Moreover, upon hydration, all the scaffolds were characterized by elongation superimposable to that of native skin. Furthermore, as for the Young's modulus, the scaffolds were characterized by the stiffness/elasticity closest to that of the skin, both in dry and hydrated states. Moreover, there is evidence in the literature that correlates the fibroblast adhesion and proliferation to substrate stiffness [31]; stiff matrices with a 2 MPa Young's modulus enhanced fibroblast proliferation much more than an elastic substrate (0,042 MPa). In fact, in the literature, there is evidence that the fibroblasts of granulation tissue are proliferative and motile, while those of the dermis are in a quiescent and stationary state [32]. Moreover, stiff substrates were demonstrated to sustain cell spreading and to facilitate guiding the pro-angiogenic signaling of fibroblasts [33].

3.3. Norfloxacin release properties

Figure 7 reports the release profiles of norfloxacin in saline solution. As for H scaffolds (N loaded as nanocomposite), independent of the drug loading, the profiles reached plateau values at 20% of the drug released after 3 h.

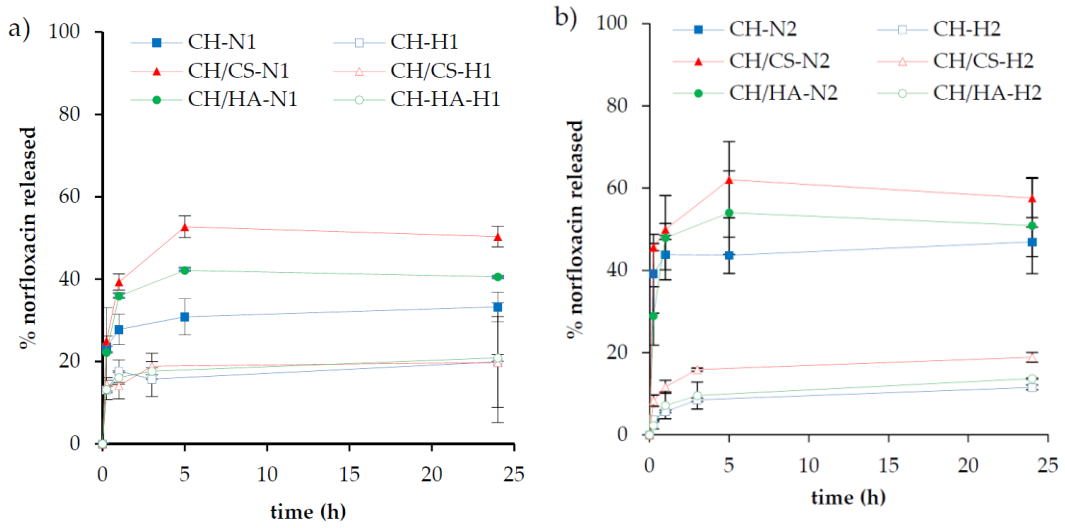

Figure 7. *Release profiles (%) of norfloxacin from the N or H scaffolds loaded with 1% (**a**) or 2% (**b**) as a free drug (N) or as nanocomposite (H), in saline solution (mean values ± SD; n = 3).*

As for N scaffolds (N loaded as a free drug), independent of the drug loading, the release profiles reached plateau values after 5 h; CH/CS scaffolds were characterized by their higher profile (50% and 57% for 1% and 2% N loading, respectively) followed by CH/HA scaffolds (about 40% and 50% for 1% and 2% N loading, respectively) and finally by CH scaffolds (33% and 50% for 1% and 2% N loading, respectively). When norfloxacin was loaded in the scaffolds as a nanocomposite (H scaffolds), the release was lower than when the scaffolds contained the free drug, and this seems to be independent of scaffold polymer composition. On the contrary, when norfloxacin was loaded as a free drug (N scaffolds), the presence of glycosaminoglycans markedly influenced norfloxacin release. This could be due to an interaction between anionic glycosaminoglycans and cationic chitosan forming a polyelectrolyte complex, which could make the fibrous structure less entangled and, therefore, more available to interact with the dissolution medium and to allow drug diffusion through the polymer matrix and, consequently, its release. In fact, scaffolds containing chondroitin sulfate, characterized by a charge density greater than hyaluronic acid, were characterized by a higher release profile. Chondroitin sulfate is characterized by the sulfate groups having an acid behavior greater than the carboxylic groups of hyaluronic acid. Consequently, the interaction between chondroitin sulfate and chitosan could cause a coiled structure less prone to polymer chain entanglements [34]. In any case, in the scaffolds loaded with higher concentrations of the drug, this difference was less evident with respect to those with lower drug loadings.

Figure 8 reports the norfloxacin release profiles (a and b) and glucosamine release profiles (c and d) of scaffolds subjected to lysozyme degradation

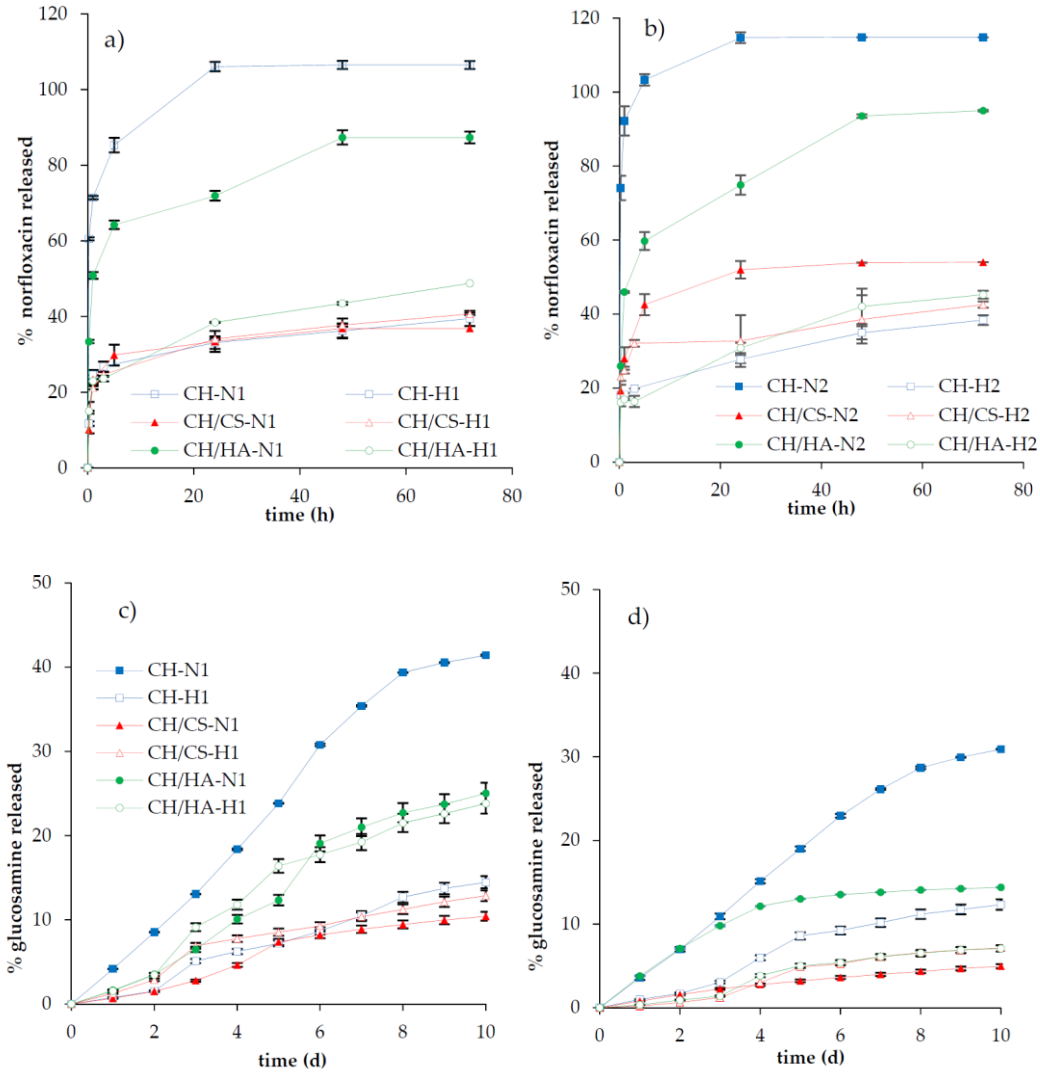

Figure 8. *Norfloxacin released (%) in lysozyme from the scaffolds loaded with 1% (**a**) or 2% (**b**) of norfloxacin as a free drug (N) or as nanocomposite (H) and glucosamine released (%) from the scaffolds loaded with 1% (**c**) or 2% (**d**) of norfloxacin as a free drug (N) or as nanocomposite (H) subjected to lysozyme activity (mean values ± SD; n = 3)*

Independent of norfloxacin concentration in the N scaffolds (free drug loading), the activity of lysozyme markedly increased the drug release: CH scaffolds containing chitosan, without glycosaminoglycans, showed higher release profiles, reaching, in almost 24 h, 100% of the drug being released; scaffolds based on CH/HA showed 80% of the drug being released in 48 h, while CH/CS scaffolds were characterized by a lower release close to 40–50% of the drug being released in 72 h, for 1% or 2% norfloxacin loading, and these profiles were similar to those obtained in saline solution. These behaviors could be explained considering the activity of lysozyme on the scaffold matrices:

CH scaffolds completely lost their nanofibrous structure in contact with lysozyme (Figure 9). On the contrary, after 10 days of lysozyme activity, the CH/CS scaffold and, mainly, the CH/HA scaffold showed a residual of nanofibrous structure, submerged in a non-structured material. It is conceivable that the interaction of chitosan amino groups (positively charged) with either sulfate groups of chondroitin sulfate or the carboxylic ones of hyaluronic acid (both negatively charged) conferred a higher resistance against enzyme degradation, probably hindering interaction with the substrate. Moreover, chitosan/glycosaminoglycan interactions could partially prevent the loss of the system morphology, decreasing drug release.

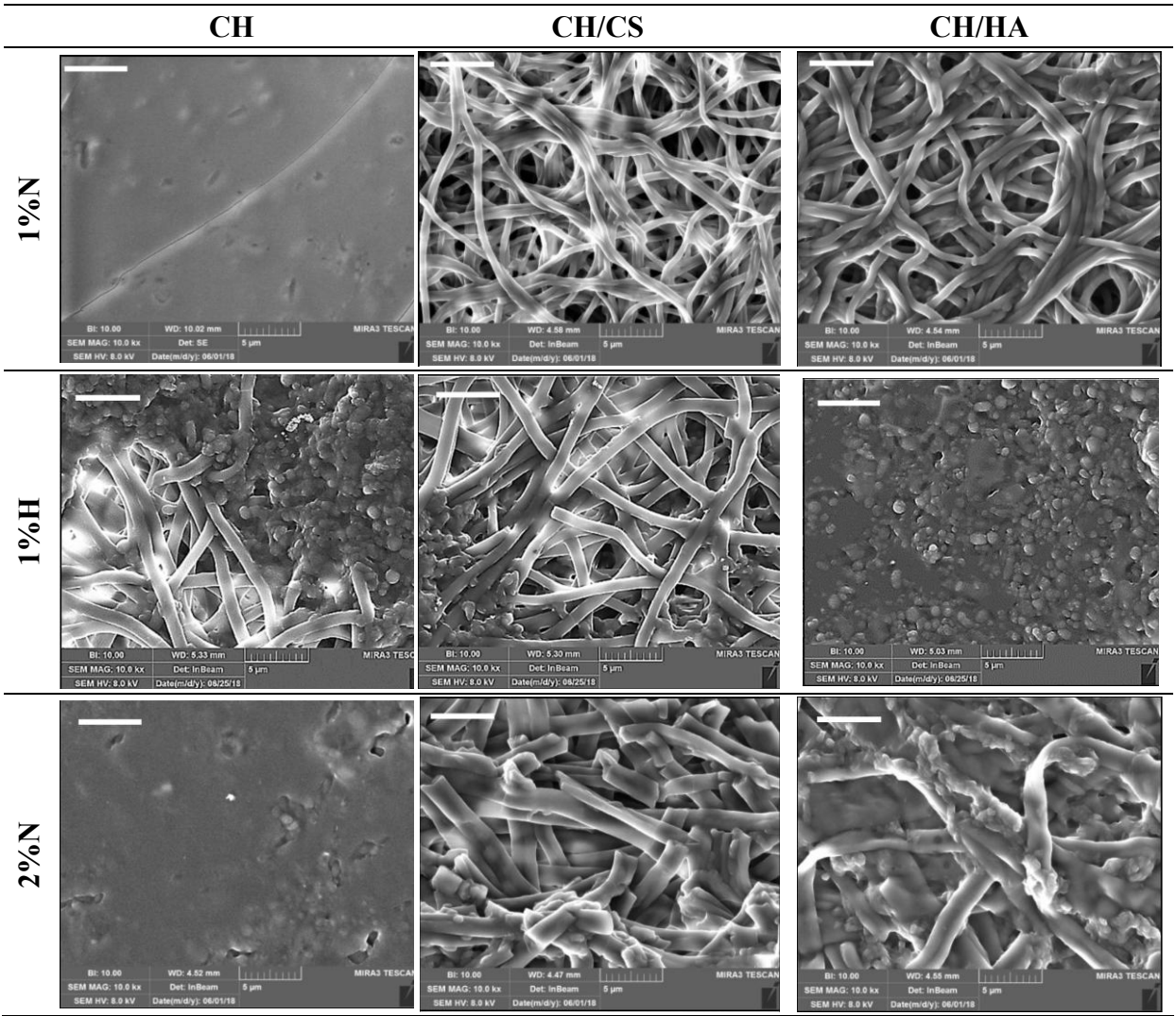

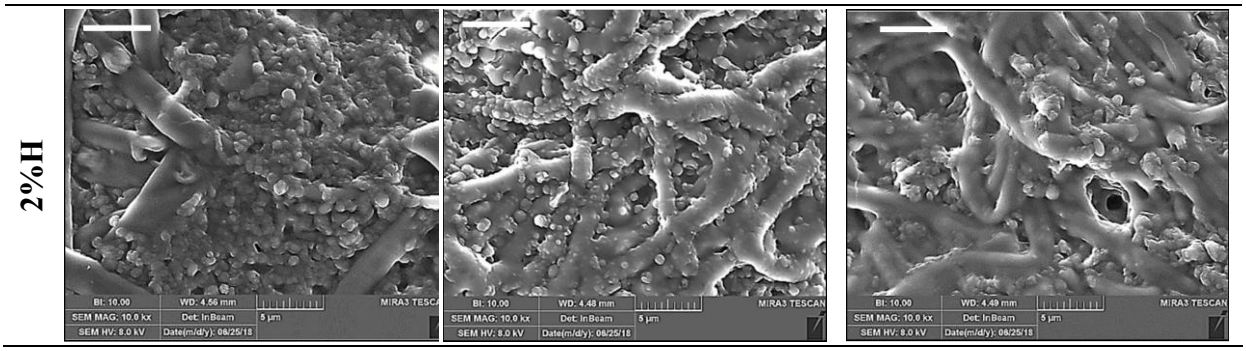

Figure 9. *SEM microphotographs of the scaffolds loaded with 1% or 2% of norfloxacin as a free drug (N) or as nanocomposite (H) subjected to lysozyme activity for 10 days (scale bar: 5 µm).*

In hybrid H scaffolds, loaded with norfloxacin in the montmorillonite nanocomposite, the profiles of norfloxacin released in the presence of the lysozyme were higher than those obtained in saline solution, although no difference could be evidenced, considering both the scaffold composition and the percentage of drug loaded, and all the scaffolds were characterized by release profiles reaching drug loading of 50% in 72 h.

However, in all cases, the glucosamine release profiles suggest that the enzymatic degradation of chitosan occurred, independent of system composition and percentage of drug loaded. CH scaffolds were characterized by their higher profiles, followed by H/HA scaffolds and CH/CS ones. Generally, the presence of norfloxacin–montmorillonite nanocomposite seems to decrease the lysozyme activity and the profiles of glucosamine (degradation product) were consistent with the norfloxacin release ones. Furthermore, the drug loading seems to have a negative impact on enzymatic activity and the glucosamine release profiles were higher in 1% loaded systems than in 2% ones. It is reported in the literature that lysozyme interacts with quinolones and this supports that there is a competition between norfloxacin and chitosan, as enzyme substrates, decreasing the enzymatic activity towards chitosan degradation when norfloxacin is at higher concentrations [35]. Moreover, the presence of montmorillonite in the scaffolds could impair lysozyme activity, probably due to a certain degree of interaction between montmorillonite and chitosan, which could prevent chitosan interaction with the enzyme. Furthermore, the interaction between chitosan and either chondroitin sulfate or hyaluronic acid could render chitosan, as lysozyme substrate, less prone to interaction with lysozyme, resulting in less efficient degradation activity towards chitosan [36].

Similar norfloxacin release profiles were observed by Dua et al. [37] for semisolid systems loaded with 1% norfloxacin. Dependent of the type of system, drug release ranged from

70% to 41% in 7 h. The highest drug release was observed for Carbopol-based gel (about 70%) followed by polyethylene glycol-based formulation (66%), HPMC-based gel (45%) and, finally, the slowest release was evidenced in the case of an ointment. Analogous behavior was observed by Denkbaş, et al. [38] and Mahmoud and Salama [21] for chitosan and chitosan collagen sponge-like dressings loaded with norfloxacin. In those cases, the norfloxacin release was mainly related to system swelling that controlled the drug diffusion for an extended time of up to 4 days.

However comparing the features of the nanofibrous scaffolds presented in this work with those of the systems in the literature, the capability of the scaffolds based on chitosan or glycosaminoglycan (either chondroitin sulfate or hyaluronic acid) associated with chitosan (CH, CH/CS and CH/HA) to possess minimal swelling (as shown by SEM images after 6 days of hydration in aqueous environment) and controlled norfloxacin release, tuned up by both the hydration and the activity of lysozyme (secreted during the inflammatory phase of wound healing), confer the ideal properties of these systems. Indeed, as soon as the systems can be implanted, norfloxacin release should occur due to the hydration of exudate from the lesions; subsequently, the inflammatory phase, preceding the proliferative one, should lead to a further release of the drug to support the whole healing process.

Figure 9 reports SEM microphotographs of all the scaffolds subjected to 10 days of enzymatic degradation by lysozyme. These images are in agreement with the glucosamine release profiles (Figure 8c,d). In fact, the higher degree of scaffold degradation (loss of nanofibrous structure) was associated with a higher glucosamine release profile. Independent of drug concentrations in CH scaffolds containing chitosan, without glycosaminoglycans, and loaded with norfloxacin as a free drug, the nanofibrous structure was no longer visible, while CH scaffolds loaded with norfloxacin in nanocomposite were characterized by a nanofibrous structure, partially covered by spherical particles, reported in the literature as lysozyme molecules attached to the biopolymer matrix [36]. The presence of glycosaminoglycans in the scaffolds determined a higher resistance against enzymatic activity. In some cases, as for the CH/CS-N2 scaffold, nanofibers were partially broken, swollen, and partially fused. Long-lasting scaffold degradation could be advantageous, especially in deep/cavity wounds, since this should allow the gradual replacement of the scaffold matrix with native tissue, due to the production of the extracellular matrix by fibroblasts.

3.4. Cytocompatibility: fibroblast adhesion and proliferation

Figure 10 reports the cytocompatibility (optical density (OD)) of the scaffolds towards fibroblasts after 3 or 6 days of growth. Fibroblast adhesion and proliferation onto the scaffolds were compared to those of the control (GM and cell growth in standard conditions).

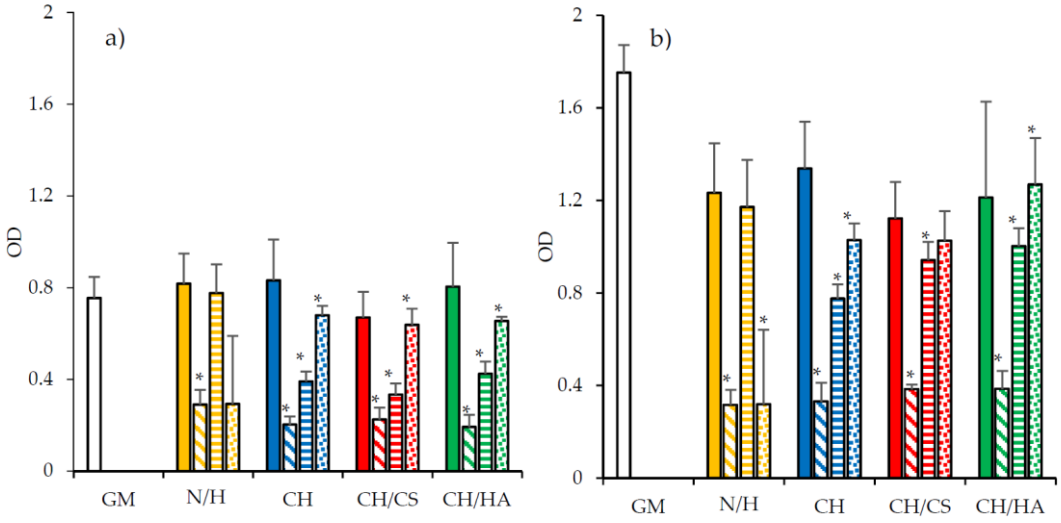

Figure 10. *Cytocompatibility (optical density (OD)) of fibroblasts grown for 3 days (**a**) and 6 days (**b**) onto CH (blue), CH/CS (red), CH/HA (green) loaded with norfloxacin at 1% (plain color) and 2% (oblique lines), and with norfloxacin–montmorillonite nanocomposite (N-VHS) at 1% (horizontal lines) and 2% (dots) in norfloxacin. N norfloxacin as a free drug and H (N-VHS nanocomposite) at the same concentrations of the scaffolds are evaluated (mean values ± SD; n = 8). Statistics: * = Mann–Whitney (Wilcoxon) W test $p < 0.05$.*

The cytocompatibility of the scaffolds loaded either with norfloxacin as a free drug or with the nanocomposite VHS-N at 1% or 2% were evaluated and N or H at the same concentrations as in the scaffolds were considered for comparison. After 6 days of growth, all the samples were characterized by higher OD than those after 3 days of growth, suggesting that the cells were in proliferation. Considering the scaffolds loaded with N as a free drug, the increase in drug concentration caused a significant decrease in cell viability with respect to the control. These results were similar to those obtained for N. This indicates that the decrease in cytocompatibility could be completely attributed to the drug and not to the scaffolds.

On the contrary, for the scaffolds loaded with the nanocomposite, the drug loading increased the cytocompatibility, suggesting that the nanocomposite in the scaffolds was able to prevent the negative effect of norfloxacin towards the fibroblasts (this was also

evident considering the cytocompatibility of the nanocomposite, which was higher for the 1% solution than the 2% solution). Such an increase in cytocompatibility could be due to montmorillonite, which was able to control the drug release and could enhance fibroblast proliferation [39].

Figures 11 and 12 report CLSM and SEM microphotographs of fibroblasts grown for 6 days onto CH, CH/CS, CH/HA loaded with norfloxacin at 1% or 2%, either as a free drug or in the nanocomposite. The complementary information from the SEM and CLSM analyses suggests that in the scaffolds loaded with N as a free drug, the fibroblasts were not homogeneously distributed on the scaffolds and mainly formed aggregates as cell clusters. This behavior was dramatically influenced by drug concentration, in agreement with the cytocompatibility. However, both the scaffolds containing glycosaminoglycans allowed the fibroblasts to maintain their fusiform structure and cytoskeletons based on aligned and elongated filaments. However, norfloxacin concentration did not alter nuclei morphology. In the hybrid scaffolds, loaded with norfloxacin nanocomposite, fibroblasts were spread out all over the scaffolds and, in some areas, confluence could be reached and, although all the scaffolds were effective to allow cell adhesion and proliferation, the scaffolds containing chondroitin sulfate were characterized by their better performance.

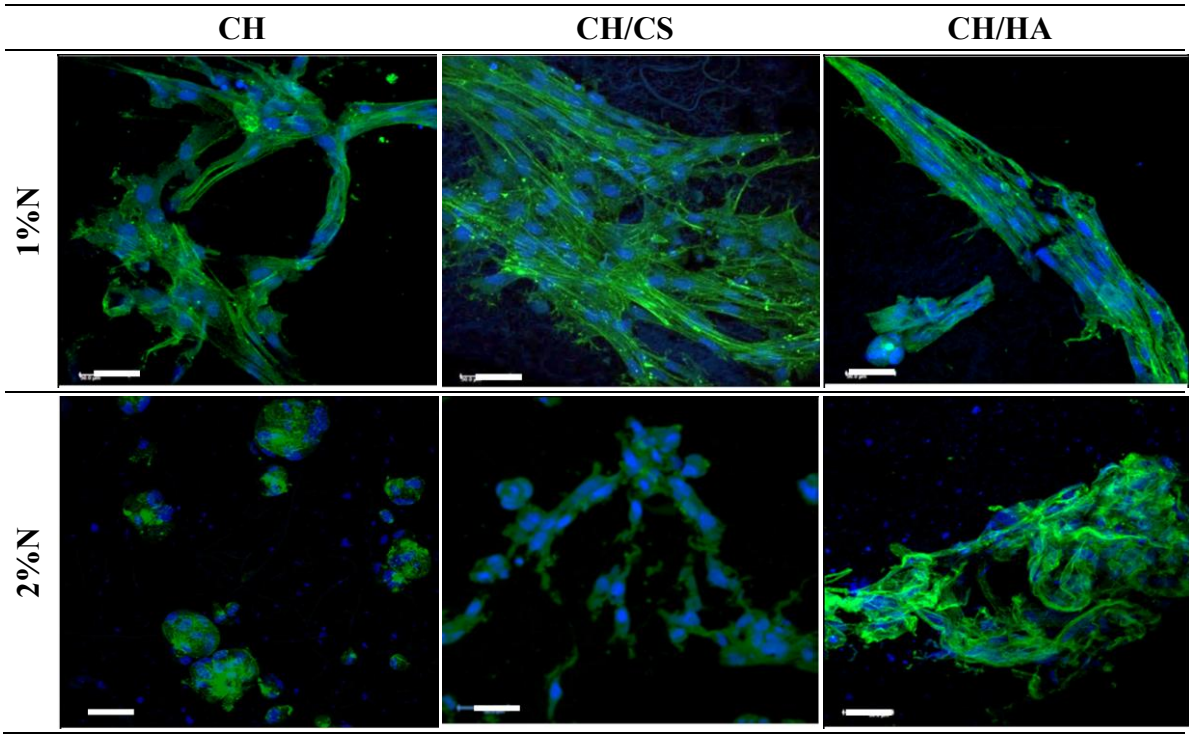

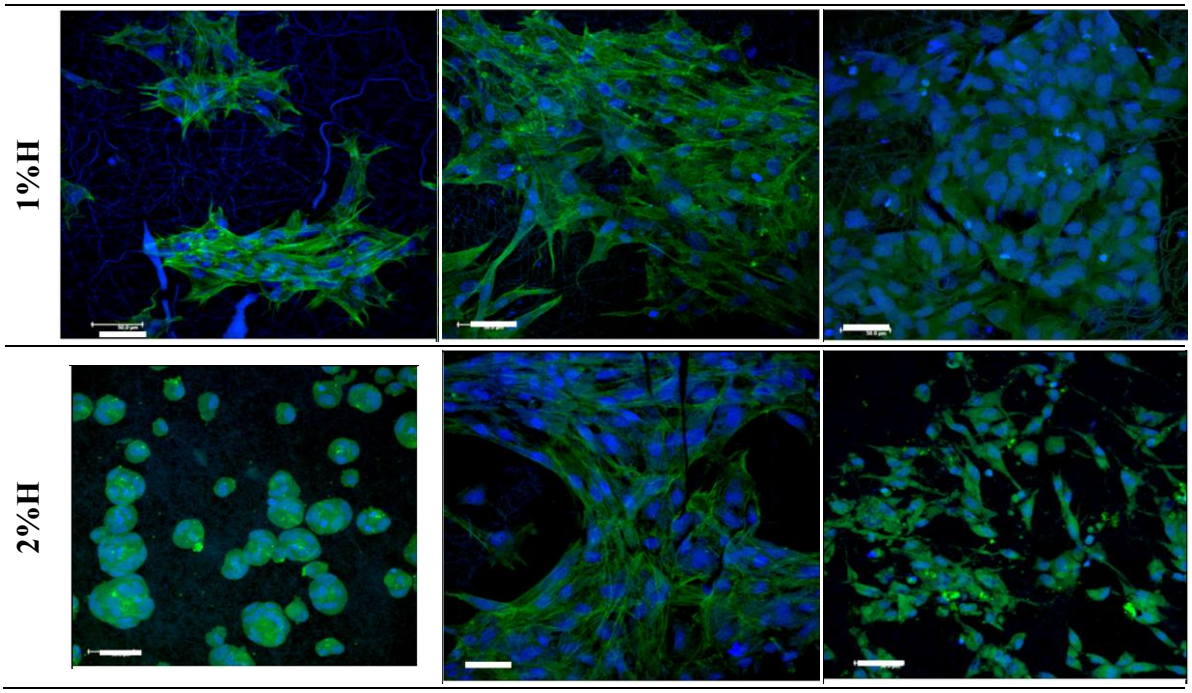

Figure 11. *Confocal laser scanning microscopy (CLSM) microphotographs of fibroblasts grown for 6 days onto CH, CH/CS, CH/HA loaded with norfloxacin as a free drug (N) or norfloxacin–montmorillonite nanocomposite (H, N-VHS) at 1% or 2% (in blue: nuclei; in green: cytoskeleton) (scale bar: 50 μm).*

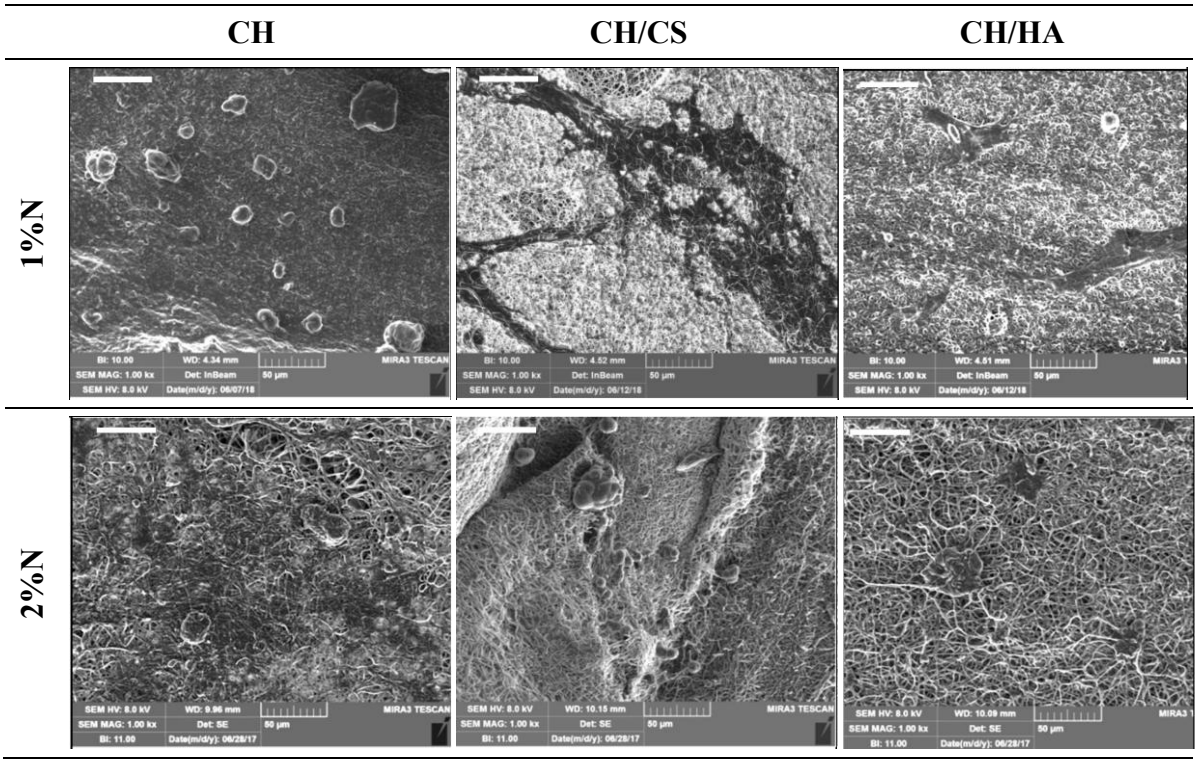

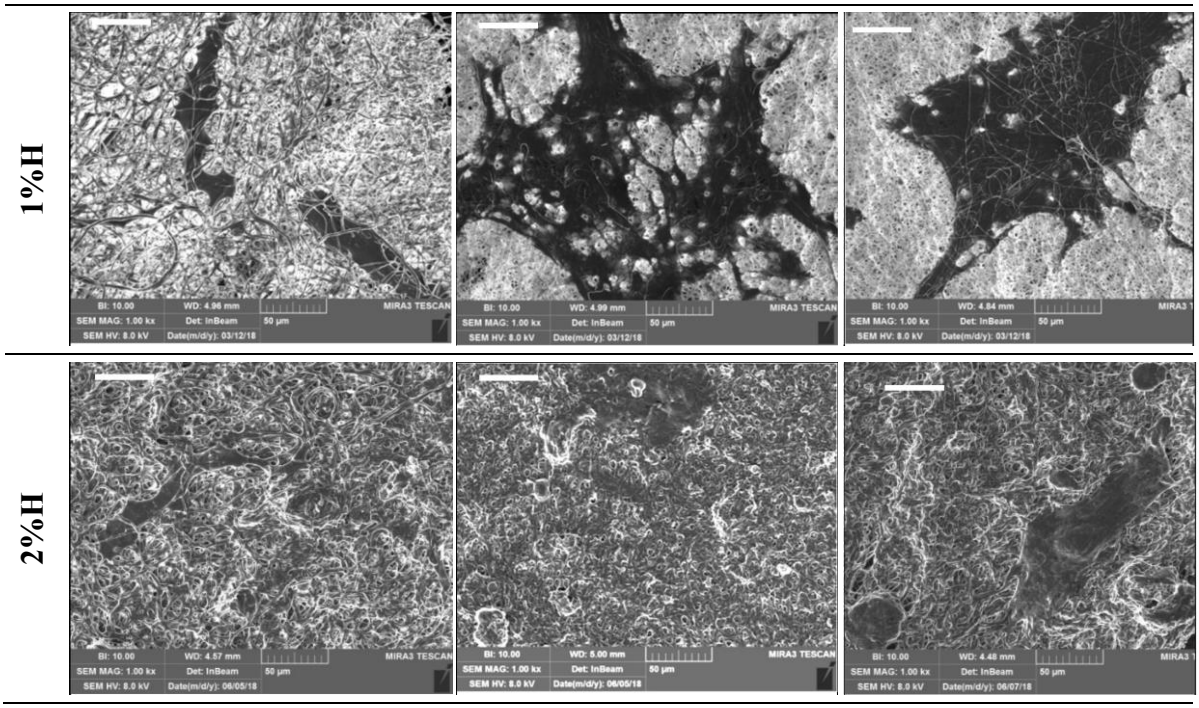

Figure 12. *SEM microphotographs of fibroblasts grown for 6 days onto CH, CH/CS, CH/HA loaded with norfloxacin as a free drug (N) or norfloxacin–montmorillonite nanocomposite (H, N-VHS) at 1% or 2% (scale bar: 50 µm).*

These results are in agreement with others in the literature stating the biocompatibility and the proliferation enhancement properties of montmorillonite and halloysite, both phyllosilicates with a planar and rolled structure, respectively [40–42]. Moreover, the polymer matrix of the scaffolds had a synergic effect with montmorillonite, leading to effectiveness in enhancing cell growth in the presence of norfloxacin [43].

Moreover, the mechanical properties combined with norfloxacin release could better support fibroblast adhesion, proliferation and spreading all over the scaffold when the norfloxacin is loaded in the scaffolds as a nanocomposite, at 1% concentration, and chondroitin sulfate or hyaluronic acid are present in the composition.

3.5. Antimicrobial properties

Figure 13 reports the microbicidal effect vs. time profiles evaluated for CH, CH/CS and CH/HA scaffolds loaded with norfloxacin as a free drug (a, c) and (b, d) as nanocomposite at 1% against Pseudomonas aeruginosa and Staphylococcus aureus.

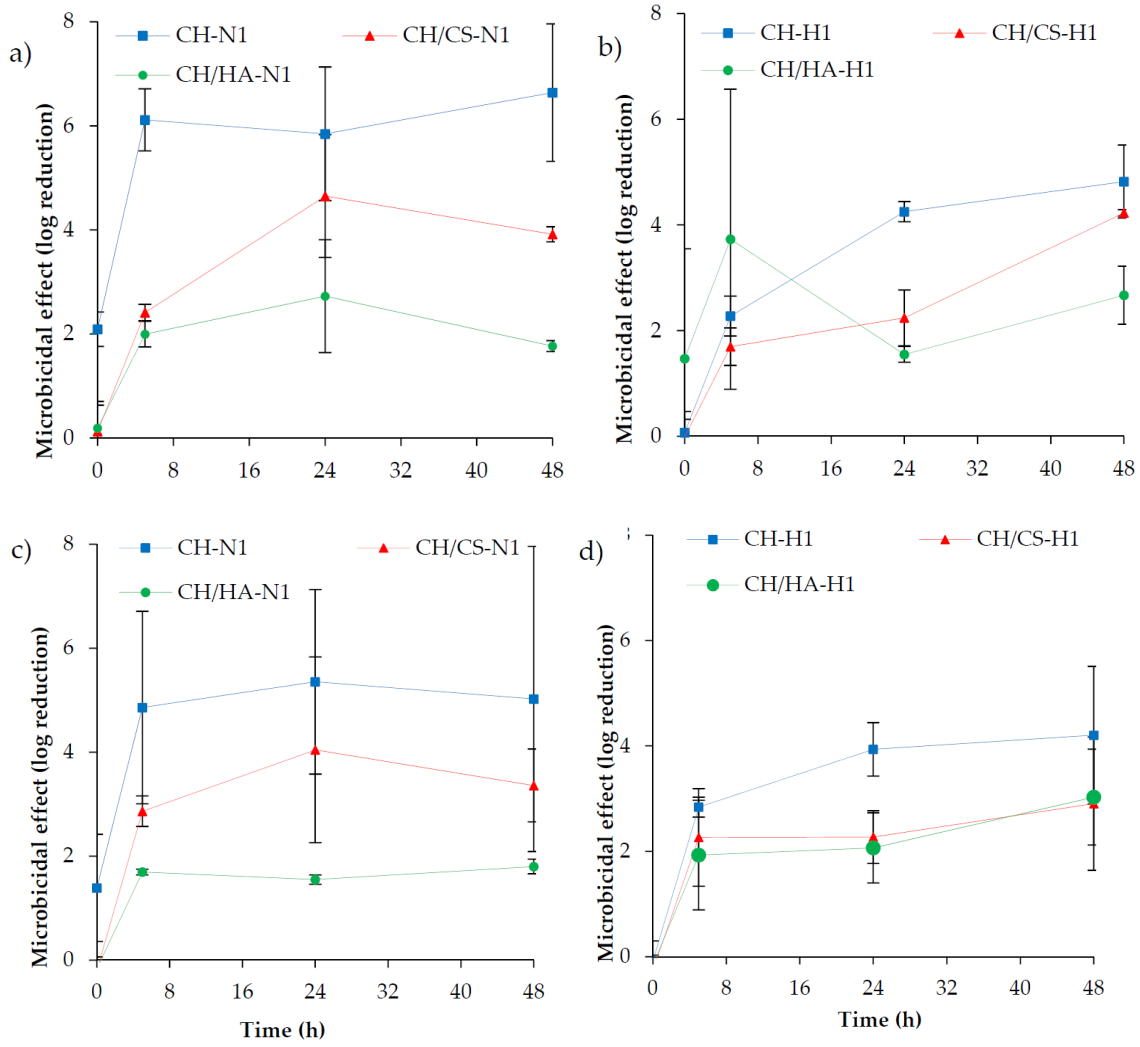

Figure 13. *Microbicidal effect evaluated for 1% norfloxacin as a free drug (**a**,**c**) and (**b**,**d**) as nanocomposite loaded into CH, CH/CS and CH/HA scaffolds against Pseudomonas aeruginosa (**a** and **b**) and Staphylococcus aureus (**c** and **d**), in comparison to norfloxacin as a free drug and as nanocomposite, with the same concentration as in the scaffolds (mean values ± SD; n = 3).*

Pseudomonas aeruginosa is a facultative Gram-negative anaerobe bacterium. It is recognized as a multidrug-resistant pathogen for its intrinsically advanced antibiotic resistance mechanisms since it causes infections of considerable medical importance, among them hospital-acquired infections such as sepsis syndromes. Staphylococcus aureus is facultative Gram-positive anaerobe bacterium. It is part of the skin microbiota; however, as an opportunistic pathogen, it could cause skin infections. Moreover, S. aureus could become resistant to antibiotics, and its methicillin-resistant strains are a worldwide emergency in clinical medicine. N is reported in the literature as being effective against

both P. aeruginosa and S. aureus, having a MIC (minimal inhibitory concentration) of 2 μg/mL in both cases [44].

Norfloxacin loaded in the scaffolds was characterized by a microbicidal effect slightly higher against P. aeruginosa than against S. aureus and, moreover, scaffolds loaded with the free drug seem to have an antimicrobial activity higher than those loaded with norfloxacin in the nanocomposite. These could be due to the slower drug release of hybrid scaffolds compared to those loaded with norfloxacin as a free drug. However, the antimicrobial activity was sustained for 48 h.

Although a certain margin of error could be evidenced by the high variability of the results, a significant antimicrobial effect was achieved since all the scaffolds were able to decrease the bioburden by at least 100-fold (a two-log reduction). This suggests that upon implant, the scaffolds were effective for controlling and decreasing bacteria proliferation.

4. CONCLUSIONS

Scaffolds entirely based on polysaccharides (pullulan and chitosan plus chondroitin sulfate or hyaluronic acid) were manufactured by means of electrospinning and norfloxacin was loaded as a free drug or as nanocomposite of montmorillonite. The scaffolds were characterized by their homogeneous structures, with fibers of 500 nm diameter when norfloxacin was loaded as a free drug, independent of drug concentration.

On the contrary, the presence of nanocomposite caused a certain degree of surface roughness of the fibers with 1000 nm diameters, dramatically influenced by drug concentration. Moreover, this altered entanglement of polymer chains in the scaffolds and caused higher deformability and lower elasticity, compared to the scaffolds loaded with norfloxacin as a free drug, and decreased the mechanical resistance of the systems. The hydration of the scaffolds changed their mechanical properties and the scaffolds were more prone to deformation. This is an advantageous feature, considering their implantation in lesions.

Moreover, scaffold degradation occurring via lysozyme secreted during the inflammatory phase of the healing process should ensure scaffold resorption and, simultaneously, drug release. All the scaffolds proved to be degraded via lysozyme and this sustained the drug release (from 50% to 100% in 3 days, depending on system composition), especially when

the drug was loaded in the scaffolds as a nanocomposite at 1%. Moreover, the scaffolds were able to decrease the bioburden by at least 100-fold, proving that drug loading in the scaffolds did not impair the antimicrobial activity of norfloxacin.

Chondroitin sulfate and montmorillonite in the scaffolds proved to possess a synergic performance in enhancing the fibroblast proliferation without impairing norfloxacin antimicrobial properties. The scaffold based on chondroitin sulfate and containing 1% norfloxacin in nanocomposite was demonstrated to possess adequate stiffness to support fibroblast proliferation and the capability to sustain antimicrobial properties to prevent/treat nonhealing wound infection during the healing process.

5. PATENTS

Sandri, G., Bonferoni, M.C., Rossi, S., Ferrari, F., electrospun nanofibers and membranes, PCT/ IT2017/000160, 2017.

Supplementary Materials: The following are available online at *http://www.mdpi.com/1999-4923/12/4/325/s1*, Figure S1: FTIR spectra of all the components of the scaffolds, Figure S2: XRPD spectra of the components of the scaffolds presenting signals, Figure S3: Thermal analysis (TGA and DSC) of the components and the scaffolds containing the nanocomposite.

Author Contributions: Conceptualization, G.S.; methodology, G.S.; software, F.F. and M.C.B.; validation, C.V.; investigation, P.G., A.F., M.R.; B.V.; D.M.; data curation, C.A., G.S.; writing—original draft preparation, G.S., M.R., A.F.; writing—review and editing, G.S.; supervision, G.S.; project administration, G.S.; funding acquisition, C.V., G.S., S.R., F.F., M.C.B. All authors have read and agreed to the published version of the manuscript.

Funding: This work was partially supported by Horizon 2020 Research and Innovation Programme under Grant Agreement No 814607.

Acknowledgments: The authors wish to thank Giusto Faravelli SpA for suppling the polymers.

Conflicts of Interest: The authors declare no conflict of interest

REFERENCE

1. Boateng, J.; Matthews, K.; Stevens, H.N.; Eccleston, G.M. Wound Healing Dressings and Drug Delivery Systems: A Review. *J. Pharm. Sci.* **2008**, *97*, 2892–2923.
2. Velnar, T.; Bailey, T.; Smrkolj, V. The Wound Healing Process: An Overview of the Cellular and Molecular Mechanisms. *J. Int. Med Res.* **2009**, *37*, 1528–1542.
3. Gupta, A.; Mumtaz, S.; Li, C.-H.; Hussain, I.; Rotello, V.M. Combatting antibiotic-resistant bacteria using nanomaterials. *Chem. Soc. Rev.* **2019**, *48*, 415–427.
4. Siddiqui, A.R.; Bernstein, J.M. Chronic wound infection: Facts and controversies. *Clin. Dermatol.* **2010**, *28*, 519–526.
5. Percival, S. Importance of biofilm formation in surgical infection. *BJS* **2017**, *104*, e85–e94.
6. Van Giau, V.; An, S.S.A.; Hulme, J. Recent advances in the treatment of pathogenic infections using antibiotics and nano-drug delivery vehicles. *Drug Des. Dev. Ther.* **2019**, *13*, 327–343.
7. Fulaz, S.; Vitale, S.; Quinn, L.; Casey, E. Nanoparticle-Biofilm Interactions: The Role of the EPS Matrix. *Trends Microbiol.* **2019**, *27*, 915–926.
8. García-Villén, F.; Faccendini, A.; Aguzzi, C.; Cerezo, P.; Bonferoni, M.C.; Rossi, S.; Grisoli, P.; Ruggeri, M.; Ferrari, F.; Sandri, G.; et al. Montmorillonite-norfloxacin nanocomposite intended for healing of infected wounds. *Int. J. Nanomed.* **2019**, *14*, 5051–5060.
9. Sandri, G.; Rossi, S.; Bonferoni, M.C.; Miele, D.; Faccendini, A.; Del Favero, E.; Di Cola, E.; Cornaglia, A.I.; Boselli, C.; Luxbacher, T.; et al. Chitosan/glycosaminoglycan scaffolds for skin reparation. *Carbohydr. Polym.* **2019**, *220*, 219–227.
10. Sandri, G.; Miele, D.; Faccendini, A.; Bonferoni, M.C.; Rossi, S.; Grisoli, P.; Taglietti, A.; Ruggeri, M.; Bruni, G.; Vigani, B.; et al. Chitosan/Glycosaminoglycan Scaffolds: The Role of Silver Nanoparticles to Control Microbial Infections in Wound Healing. *Polymers* **2019**, *11*, 1207
11. Sahana, T.G.; Rekha, P.D. Biopolymers: Applications in wound healing and skin tissue engineering. *Mol. Boil. Rep.* **2018**, *45*, 2857–2867.
12. Ajmal, G.; Bonde, G.V.; Thokala, S.; Mittal, P.; Khan, G.; Singh, J.; Pandey, V.K.; Mishra, B. Ciprofloxacin HCl and quercetin functionalized electrospun nanofiber

membrane: Fabrication and its evaluation in full thickness wound healing. *Artif. Cells Nanomedicine Biotechnol.* **2019**, *47*, 228–240.

13. Nejaddehbashi, F.; Hashemitabar, M.; Bayati, V.; Moghimipour, E.; Movaffagh, J.; Orazizadeh, M.;Abbaspour, M. Incorporation of Silver Sulfadiazine into An Electrospun Composite of Polycaprolactone as An Antibacterial Scaffold for Wound Healing in Rats. *Cell J.* **2019**, *21*, 379–390.
14. Grguric′, T.H.; Mijovic′, B.; Zdraveva, E.; Bajsic′, E.G.; Slivac, I.; Ujcˇic′, M.; Dekaris, I.; Trcin, M.T.; Vukovic′, A.; Kuzmic′, S.; et al. Electrospinning of PCL/CEFUROXIM®fibrous scaffolds on 3D printed collectors. *J. Text. Inst.* **2020**, 1–12.
15. Abdallah, O.; Jalali, F.; Zamani, S.; Isamil, H.I.; Ma, S.; Nasrallah, G.K.; Younes, H.M. Fabrication an Characterization of 3D electrospun biodegradable nanofibers for wound dressing, drug delivery and other tissue engineering applications. *Pharm. Nanotechnol.* **2016**, *4*, 191–201.
16. Mehta, P.; Zaman, A.; Smith, A.; Rasekh, M.; Haj-Ahmad, R.; Arshad, M.S.; Der Merwe, S.; Chang, M.-W.; Ahmad, Z.; Van Der Merwe, S. Broad Scale and Structure Fabrication of Healthcare Materials for Drug and Emerging Therapies via Electrohydrodynamic Techniques. *Adv. Ther.* **2018**, *2*, 1800024.
17. Chen, S.; Liu, B.; A Carlson, M.; Gombart, A.F.; A Reilly, D.; Xie, J. Recent advances in electrospun nanofibers for wound healing. *Nanomedicine* **2017**, *12*, 1335–1352.
18. Kupiec, T.C.; Matthews, P.; Ahmad, R. Dry-heat sterilization of parenteral oil vehicles. *Int. J. Pharm. Compd.* **2013**, *4*, 223–224.
19. Cordenonsi, L.M.; Faccendini, A.; Rossi, S.; Bonferoni, M.C.; Malavasi, L.; Raffin, R.; Schapoval, E.E.S.; Del Fante, C.; Vigani, B.; Miele, D.; et al. Platelet lysate loaded electrospun scaffolds: Effect of nanofiber types on wound healing. *Eur. J. Pharm. Biopharm.* **2019**, *142*, 247–257.
20. Pharmaceutical Quality/CMC. Transdermal and Topical Delivery Systems—Product Development and Quality Considerations, Guidance for Industry. In *U.S. Department of Health and Human Services*; Food and Drug Administration, Center for Drug Evaluation and Research (CDER), FDA: Rockville, MD, USA, November **2019**.

21. Mahmoud, A.A.; Salama, A. Norfloxacin-loaded collagen/chitosan scaffolds for skin reconstruction: Preparation, evaluation and in-vivo wound healing assessment. *Eur. J. Pharm. Sci.* **2016**, *83*, 155–165.
22. Samanidou, V.F.; Demetriou, C.E.; Papadoyannis, I.N. Direct determination of four fluoroquinolones, enoxacin, norfloxacin, ofloxacin, and ciprofloxacin, in pharmaceuticals and blood serum by HPLC. *Anal. Bioanal. Chem.* **2003**, *375*, 623–629.
23. Sandri, G.; Bonferoni, M.C.; Ferrari, F.; Rossi, S.; Aguzzi, C.; Mori, M.; Grisoli, P.; Cerezo, P.; Tenci, M.; Viseras, C.; et al. Montmorillonite–chitosan–silver sulfadiazine nanocomposites for topical treatment of chronic skin lesions: In vitro biocompatibility, antibacterial efficacy and gap closure cell motility properties. *Carbohydr. Polym.* **2014**, *102*, 970–977.
24. Huan, S.; Liu, G.; Han, G.; Cheng, W.; Fu, Z.; Wu, Q.; Wang, Q. Effect of Experimental Parameters on Morphological, Mechanical and Hydrophobic Properties of Electrospun Polystyrene Fibers. *Materials* **2015**, *8*, 2718–2734.
25. Yu, X.; Zipp, G.L.; Iii, G.W.R.D. The Effect of Temperature and pH on the Solubility of Quinolone Compounds: Estimation of Heat of Fusion. *Pharm. Res.* **1994**, *11*, 522–527. [CrossRef]
26. Irwin, N.; McCoy, C.P.; Carson, L. Effect of pH on the in vitro susceptibility of planktonic and biofilm-grown Proteus mirabilis to the quinolone antimicrobials. *J. Appl. Microbiol.* **2013**, *115*, 382–389.
27. Sandri, G.; Faccendini, A.; Longo, M.; Ruggeri, M.; Rossi, S.; Bonferoni, M.C.; Miele, D.; Prina-Mello, A.; Aguzzi, C.; Iborra, C.V.; et al. Halloysite- and Montmorillonite-Loaded Scaffolds as Enhancers of Chronic Wound Healing. *pharmaceutics* **2020**, *12*, 179.
28. Rabbani, M.; Bathaee, H.; Rahimi, R.; Maleki, A. Photocatalytic degradation of p - nitrophenol and methylene blue using Zn-TCPP/Ag doped mesoporous TiO 2 under UV and visible light irradiation. *Desalin. Water Treat.* **2016**, *57*, 1–9.
29. Tran, T.; Hamid, Z.; Cheong, K. A Review of Mechanical Properties of Scaffold in Tissue Engineering: Aloe Vera Composites. *J. Physics: Conf. Ser.* **2018**, *1082*, 012080.
30. Pawlaczyk, M.; Lelonkiewicz, M.; Wieczorowski, M. Age-dependent biomechanical properties of the skin. *Adv. Dermatol. Allergol.* **2013**, *30*, 302–306.

31. Hadjipanayi, E.; Mudera, V.; Brown, R.A. Close dependence of fibroblast proliferation on collagen scaffold matrix stiffness. *J. Tissue Eng. Regen. Med.* **2009**, *3*, 77–84.
32. Clark, R.A. Biology of Dermal Wound Repair. *Dermatol. Clin.* **1993**, *11*, 647–666.
33. El-Mohri, H.; Wu, Y.; Mohanty, S.; Ghosh, G. Impact of matrix stiffness on fibroblast function. *Mater. Sci. Eng. C* **2017**, *74*, 146–151.
34. Saporito, F.; Sandri, G.; Rossi, S.; Bonferoni, M.C.; Riva, F.; Malavasi, L.; Caramella, C.; Ferrari, F. Freeze dried chitosan acetate dressings with glycosaminoglycans and traxenamic acid. *Carbohydr. Polym.* **2018**, *184*, 408–417.
35. Perez, H.A.; Bustos, A.; Taranto, M.P.; Frias, M.; Ledesma, A.E. Effects of Lysozyme on the Activity of Ionic of Fluoroquinolone Species. *Molecules* **2018**, *23*, 741.
36. Islam, N.; Wang, H.; Maqbool, F.; Ferro, V. In Vitro Enzymatic Digestibility of Glutaraldehyde-Crosslinked Chitosan Nanoparticles in Lysozyme Solution and Their Applicability in Pulmonary Drug Delivery. *Molecules* **2019**, *24*, 1271
37. Dua, K.; Malipeddi, V.R.; Madan, J.R.; Gupta, G.; Chakravarthi, S.; Awasthi, R.; Kikuchi, I.S.; Pinto, T.D.J.A. Norfloxacin and metronidazole topical formulations for effective treatment of bacterial infections and burn wounds. *Interv. Med. Appl. Sci.* **2016**, *8*, 68–76.
38. Öztürk, E.; Agalar, C.; Öztürk, E. Norfloxacin-loaded Chitosan Sponges as Wound Dressing Material. *J. Biomater. Appl.* **2004**, *18*, 291–303.
39. Sandri, G.; Aguzzi, C.; Rossi, S.; Bonferoni, M.C.; Bruni, G.; Boselli, C.; Cornaglia, A.I.; Riva, F.; Viseras, C.; Caramella, C.; et al. Halloysite and chitosan oligosaccharide nanocomposite for wound healing. *Acta Biomater.* **2017**, *57*, 216–224.
40. Sandri, G.; Bonferoni, M.C.; Rossi, S.; Ferrari, F.; Aguzzi, C.; Iborra, C.V.; Caramella, C. Clay minerals for tissue regeneration, repair, and engineering. In *Wound Healing Biomaterials*, 2nd ed.; Ågren, S.M., Ed.; Elsevier BV: Sawston, Cambridge, UK, **2016**; Volume 2, pp. 385–402.
41. Sandri, G.; Bonferoni, M.C.; Rossi, S.; Ferrari, F.; Mori, M.; Cervio, M.; Riva, F.; Liakos, I.; Athanassiou, A.; Saporito, F.; et al. Platelet lysate embedded scaffolds for skin regeneration. *Expert Opin. Drug Deliv.* **2014**, *12*, 525–545.

42. Aguzzi, C.; Sandri, G.; Bonferoni, M.C.; Cerezo, P.; Rossi, S.; Ferrari, F.; Caramella, C.; Iborra, C.V. Solid state characterisation of silver sulfadiazine loaded on montmorillonite/chitosan nanocomposite for wound healing. *Colloids Surf. B Biointerfaces* **2014**, *113*, 152–157.
43. Rossi, S.; Marciello, M.; Sandri, G.; Ferrari, F.; Bonferoni, M.C.; Papetti, A.; Caramella, C.; Dacarro, C.; Grisoli, P. Wound Dressings Based on Chitosans and Hyaluronic Acid for the Release of Chlorhexidine Diacetate in Skin Ulcer Therapy. *Pharm. Dev. Technol.* **2007**, *12*, 415–422.
44. Norrby, S.R.; Jonsson, M. Antibacterial activity of norfloxacin. *Antimicrob. Agents Chemother.* **1983**, *23*, 15–18.

CHAPTER 4

Electrospun hybrid tubular scaffold designed to be extemporarily loaded with human platelet lysate, for tendon to bone regeneration.

Abstract

The spontaneous healing of a tendon-to-bone laceration, results in the formation of a scar tissue having lower functionality then the original one. To face this, several types of scaffolds have been developed using the tissue engineering approach. In this work, an electrospun hybrid tubular scaffold was designed to mimic the tissue fibrous arrangement and the extracellular matrix (ECM) composition, and to be extemporaneously loaded with human platelet lysate (PL) for leading toa fully functional regeneration of this tissue.

At this purpose Pullulan (PU)/Chitosan (CH) based polymer solutions, were enriched with nano-Hydroxyapatite (HP) and electrospun. The nanofibers were collected vertically along the length of the scaffold, for mimicking the fascicle direction of the original tissue. The scaffold obtained showed tendon-like mechanical performances, depending on HP content and tube size. The growth factors derived from PL, crossed the scaffold wall and *in vitro* studies, demonstrated that tenocytes and SAOS-2cells grown onto the scaffold in presence of PL. Moreover, both the cell types considerably expressed high metabolic activity, proliferation and ECM production. The presence of HP and PL resulted in a synergic effect towards the cell adhesion/proliferation in the scaffold. These results suggested that the hybrid tubular scaffold, extemporarily loaded with PL, could be an effective strategy to support a new tissue formation in the tendon-to bone regeneration.

1. INTRODUCTION

Laceration, contusion, and tensile overload are the main mechanisms of tendon injuries. Moreover, paratendinopathy, that causes local inflammation, most commonly occurs because of junction overuse. When tendon laceration is total, the surgery is required at tendon to bone insertion site.

Many studies have been focused on strategies to accelerate the healing process in the injured site, especially following surgical repair. Among them the growth factors (GFs),

especially in the early phases of healing process, show positive results. Since the tendon healing process is basically similar to that of coetaneous tissue, a lot of experimental findings, have verified the effectiveness of the GFs on the enhancement of tendon wound healing, such as TGF-β, EGF, PDGF-B, bFGF, VEGF, and HGF (Whals W.R et al. 2006).
The human platelet lysate (PL) has been widely used in the orthopaedic clinical treatment as growth factor source to treat tendon-related damage. Its efficacy to promote wound healing, have been strongly proved starting from the ’80s. During these decades different sources of PL have been studied in term of effect on musculoskeletal tissue healing, and the age of donors or the source (autologous or allogenic)were identified as crucial (Berger DR et al 2019). In any case, the autologous source of PL seems the best option(Klatte-Schulz F et al. 2018; MalgarimCordenonsi L - Faccendini A et al 2019).
The PL administration and ideal pharmacokinetics in the orthopaedic practices, have still poorly explored. Normally PL is injected in the injury side, however the fast local metabolism of growth factors decreases their regenerative effective. Currently many strategies for increasing PL efficacy, reported growth factors releases up to2 weeks through the PL inclusion in nanoparticles. This frame time, seemed to be the optimal for up-regulating stem cell proliferation and gene expression (Jooybar E et al 2020; Babo PS et al 2016; Santo et al 2012). A suitable PL vehicle should be compatible, should preserve the correct GF folding, should avoid technological processes, that could degrade the growth factor structures, and should control the biomolecule release, to prolong the effect.
Given this premises, the aim of this work was to develop a tubular scaffold as orthopaedic surgical support, in tendon or tendon to bone regeneration. The tubular scaffold was designed to be loaded extemporaneously with autologous PL for a local sustained release of endogenous and pooled growth factors. The tubular scaffold was built up by means of electrospinning, and the nanofibers were collected vertically along the tube length aiming to mimic the tendon matrix fascicle direction. The polymeric matrix of electrospun nanofibers was reinforced with hydroxyapatite nanoparticles (HP), by simple mixing HP with the polymeric materials before spinning in order to increasing scaffold mechanical properties and cellular graft.
The hybrid electrospun nanofibers were prepared with a continuous electrospinning manufacturing, started with the stretching out of the polymeric suspension from the needle tip directly in the electric field, up to collecting dry nanofibers onto the rotating mandrel

(Contreras-Cáceres R et al 2019, Zong H et al 2018;Malgarim Cordenonsi L - Faccendini A et al 2019).

The nanofibers were entirely based on polysaccharides, well known for their biocompatibility and biodegradability. Pullulan (PU) was chosen for its well spinnability (Sandri G. et al 2019; Faccendini A. et al 2020; Malgarim Cordenonsi L - Faccendini A et al 2019; Sandri G. et al 2020) chitosan (CH) was employed for its biocompatibility and reinforcing capacity, when combined with crosslinking agents.

Finally, hydroxyapatite nanoparticles (HP) were loaded in the polymeric matrix as reinforcing material, described in literature as enhancer of adhesion and migration of both tendon and bone like cells.

In fact HP has been recognized as an active agent capable to support tendon/bone reparation thanks to its biomimetic cue. Many researchers have been moved towards nano-bioceramic/polymer composites as new strategy to improve the interaction with the host tissue/cells. In this regard hybrid nanofiber based on bioceramics, mixed with biopolymer, have been proposed as potential tools in bio-engineering (Day RM et al 2004; Krishna L et al 2016). The presence of HP phase can tune fiber biodegradation, creating a smart composite biomaterial. The bioceramic degradation determines the formation of a hydroxyapatite layer on the fiber surface, which mimics the mineral bone composition and this allows the firm bonding with living cell (Rodriguez IA. Et al. 2012). These are able to enhance cell proliferation and possess osteogenic properties, antibacterial activities and angiogenic potential, considering their soft tissue application (Faccendini A. et al 2020;Whals W.R. et al 2006;Keshaw H. et al 2005;Rahaman MN et al 2011; Day RM et al 2004; García-Villén F et al 2019). Moreover the nanofiber geometry leads to cell migration and orientation, establishing the correct environment for the cell remodelling in the last phase of the healing process (Calejo I et al. 2019).

In this work HP crystals loaded in the nanofibrous structure, allows to manage the final scaffold porosity and strength as well as the intracellular signalling response (Ozdemir T et al 2006; Krishna L et al 2016).

The HP 0.1% based tubular scaffold was characterized in dry state by maximum tensile force up to 7.8 MPa, not far from the one expected in vivo, usually between 5-100 MPa. It presented values of elongation maxium between 4-10% and Young Modulus above 18 MPa (reference values between 20-1200 MPa).

The biological evaluation confirmed that system allowed to control PL release up to 14 days. The in vitro culture in presence of PL, was performed using tenocytes and SAOS-2 cell lines. They were amply employed in tissue engineering as relevant in vitro culture models, for studying tendon and bone tissue reparation respectively (Berger DR et al 2019;Klatte-Schulz F et al 2018). Especially due to the limited availability of primary human osteoblast cells, SAOS-2 cell, derived from human osteosarcoma, have been often applied in regenerative medicine, thanks to their matrix mineralisation capability, and growth factor sensitivity(Czekanska EM et al 2012).

The tubular scaffolds enhanced tenocytes and SAOS-2 cells adhesion and proliferation. Moreover GFs and HP presented a synergic effect for stimulating the biological response, derived from both soft and hard tissue, respectively. The morphology and the topography of the nanofibrous structure of the scaffolds were key elements for scaffold effectiveness.

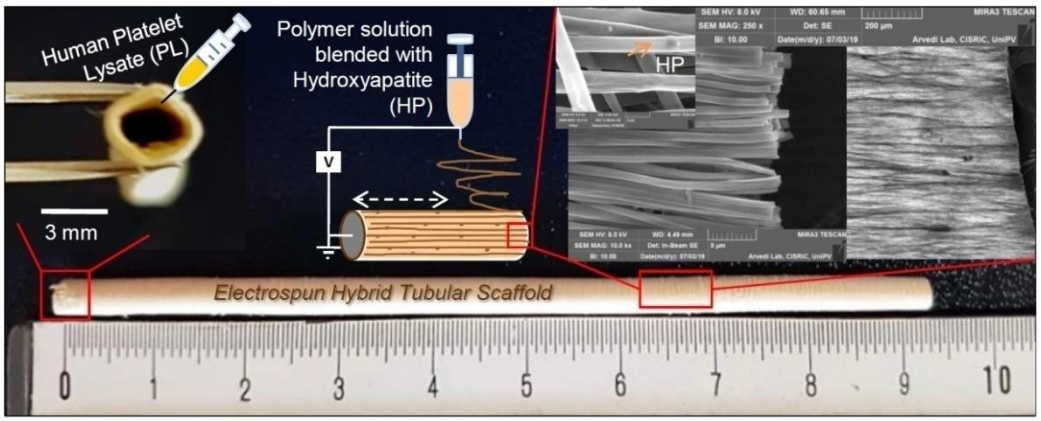

Figure 1 *Graphical abstract: of the electrospun hybrid scaffold developed*

2. MATERIALS AND METHODS

2.1. Material and reagents

Chitosan (CH), deacetylation degree 98%, MW 251000 Da, (ChitoClear, Siiiglufjordur-Iceland); Pullulan (PU), Food grade (Hayashibara, Okayama-Japan); Citric acid (CA) (Carlo Erba Reagents, Italy); Hydroxyapatite (HP), nanopowder≥ 97% synthetic (Sigma-Aldrich, USA); Acetic acid (AA) (Carlo Erba Reagents, Italy). Ultrapure water was obtained from a Milli-Q apparatus (Millipore®, Italy).

2.2. Platelet lysate (PL)

PL was obtained from the Apheresis Service of Immunohaematology and Transfusion Service Centre for transplant immunology, by employing a sterile connection technique. Aliquots of hyper-concentrate platelets (high platelet concentration in small plasma volume and minimal leukocyte contamination) were obtained from apheresis, carried out on regular blood donors (Immunohaematology And Transfusion Service, Apheresis and Cell Therapy Unit, Fondazione IRCCS Policlinico S. Matteo, Pavia, Italy). The platelet pool was frozen at −80 °C for 5 h, and subsequently unfrozen in a sterile water bath at 37 °C. An automated platelet count and tests for aerobic, anaerobic and fungi contamination were performed after saline dilution.

2.3. Hydroxyapatite characterization before electrospinning

The HP powder was suspended at 0.1% or 0,5% (w/w) in water (0.1%W; 0.5%W) or in acetic acid 45%v/v (0.1%; 0.5%A.A.). The colloidal blends were spread onto the stubs or slides and dried with hot source for 10 minutes. The samples were observed at SEM (Tescan, Mira3XMU, platinum sputtering) and analysed by X-RPD (Buker D8 Advance; copper cathode source). The X-rays radiated the sample overnight from 20° to 60 ° with a step size of 0.02° every 20 seconds.

The 0.1%W; 0.1%A.A were left 24 hours under stirring, and undergone to 5 min sonication. The mean HP particle size and polydispersity index were evaluated at room temperature by Particle Analyser (Litesizer 500 Anton Paar, Italy).

2.4. Preparation of the polymeric blend and characterizations

The polymeric blend was based on CH and pullulan PU polymers. HP was added in the final blend 1 h before electrospinning at 0.1% or 0,5% (w/w) concentrations. The solutions were prepared by mixing two polymeric solutions in a 1:1 ratio, under magnetic stirring at room temperature. The first solution was based on 20% (w/w) PU, in milliQ water, while the second one was based on 5% (w/w) CH in AA 90% or adding the 5% (w/w) CA (as also described in Sandri G. et al 2019). Finally, HP was added to the polymeric blend to obtain0,1% and 0,5% (w/w)final mineral concentrations(0.1HP and 0.5HP blends). A blank formulation (B) was obtained by mixing the same polymeric solutions without adding HP.

Every polymeric solution was characterized for consistency, using Texture Analyzer TA.XT plus (ENCO, Spinea, I), equipped with a cylindrical probe (Ø=20 mm P/20P, batch No. 11434). During the analysis the samples were placed in a thermostatically-controlled bath at 30°C (electrospinning work temperature). The following parameters were set as follows: pre-test speed: 1 mm/sec; test speed: 0,50 mm/sec; post-test speed: 10 mm/sec; trigger force: 0,10 mN.

The conductivity (FiveGo F3 - Mettler Toledo) was measured at 30°C (electrospinning work temperature). The surface tension of the polymeric blends was measured at 30°C. The automatic tensiometer (DY-300 Kyowa) was equipped with a platinum plate of 2,5cm x 1cm. The analysis was performed in a *time based mode*, with 3 s with immersion distances of 0,2 mm, 0,5 mm and 1 mm.

2.5. Preparation of electrospun scaffolds

Scaffolds were obtained from the B; 0.1HP and 0.5HP blends using an electrospinning apparatus (STKIT-40, Linari Engineering, I), equipped with a high-voltage power supply (Razel R99-E 40, kV), a 10 cc syringe with inox 21G needle and a volumetric pump (Razel R99-E). The process was carried out for 1 h at atmospheric pressure, at 25-35°C temperature range and at 25-35% relative humidity.

A static and flat collector, coated with aluminium foil, was used to obtain the random scaffolds, R-B, R-0.1HP and R-0.5HP. The aligned and tubular scaffolds, A-B, A-0.1HP and A-0.5HP, were collected in a tubular shape using a cylindrical rotating drum in inox steel, with two diameters, 0.8 or 3 x 150mm. The clockwise rotation of the drum around the axis, was regulated at 3000 rpm by a control unit (Easy Drum). In order to have vertically oriented nanofibers along the scaffold length (Figure 1), a longitudinal movement of the collector was simultaneously added to the drum clockwise rotation, and was fixed at 60 rpm constant speed. The spinning parameters were listed in the table 1.

***Table 1**: Spinning parameters*

scaffold	voltage (kV)	needle-to-collector distance (cm)	polymeric solution flux (cc/h)	Needle size
R-B	22	15	0.397	0.8 x 20 mm
R-0.1HP	20	15	0.397	0.7 x 20 mm
R-0.5HP	20	15	0.397	0.7 x 20 mm

A-B	22	15	0.397	0.8x20 mm
A-0.1HP	20	15	0.397	0.7x20 mm
A-0.5HP	20	15	0.397	0.7x20 mm

Finally, all the electrospun scaffolds were cross linked by means of dry heating treatment at 150°C for 1 h. This process is also reported as able to sterilize the products (Kupiec T.C. et al 2000)

2.6. Scaffold chemical-physical characterization

After electrospinning process, TEM analysis (JEOL JEM-1200 EX II microscope; CCD camera Olympus Mega View G2 with 1376 X 1032 pixel format) was performed to verify the HP inclusion in the electrospun nanofibrous structure (operating HV at 100 kV; magnifications: 15k, 25k, 50k). At this purpose, a thin layer of fibre was electrospun (R-0.1HP) directly onto the TEM grids, and cross-linked before the analysis.

Scaffold morphology was analysed after the crosslinking treatment, by means of SEM or EDX-SEM analysis, in order to quantify calcium and phosphorous content in the scaffold (Tescan, Mira3XMU, platinum sputtering). Electrospun nanofiber diameters and alignment were assessed by image analysis software (Image J, ICY, Institute Pasteur, F).

FT-IR analysis was carried out by means of Infrared Imaging Microscope (FT-IR, Spectrum BX, Perkin Elmer). The infrared spectra were acquired in the range 4000-400 cm^{-1} .The measurement was performed on the random crosslinked scaffolds, R-B, R-0.1HP, R-0.5HP, having test area of 5x5 mm^2 x 10 μm.

The wettability of the electrospun fibres was assessed with a Contact Angle Meter (DMe-211 Plus; FAMAS software). The droplet shape (0,4 μl of PBS) was captured through the CCD camera at 1 second after the droplet touching the scaffold interface.

2.7. Scaffold mechanical properties

Scaffolds were subjected to tensile measurements using a TA.XT plus apparatus (Stable Microsystems, ENCO, Italy), equipped with a measurement system A/TG (5kg loading cell),having two grips. The scaffolds were cut to obtain samples as described in Table 2. In the case of the aligned scaffold, the mechanical properties were evaluated in a close tubular conformation. Each sample was then fixed between the texture grips, so that the exposed area was constant (Table 2).

***Table 2**: Scaffold sizes prepared for the tensile test.*

Sample	Dimensions (cm^2)	Thickness (mm)	Area (cm^2)
Random scaffolds (R-B; R-0.1HP; R-0.5HP)	3 x 1	0.2-0.3	1 x 1
Tubular scaffolds (A-B; A-0.1HP; A-0.5HP)	2 x 0.5	0.4-0.5	1 x 0.5

The speed of the tensile test was set at 0,5 mm/sec. A trigger force was applied before the test, and the maximum distance reached from the grips was 30mm.

The maximum tensile force (Fmax,Pa) needed to break the scaffold, the load-to-failure, was normalized as a function of thickness and area exposed between the grips. The elongation values (E%, deformation) were obtained by dividing the final distance covered by the clamps (L_{fin}-L_{in}) for their initial distance (L_{in}), and expressed in percentage (Eq 1):

$$E\% = 100x(L_{fin}-L_{in})/L_{in}.(Eq\ 1).$$

Finally the Young Modulus (YM) was the slope of the linear region in the Fmax *vs* displacement curve. The mechanical properties were investigated in dry and hydrated state. The hydration was performed by spraying milliQ water, at 37°C on scaffold surface for 30 s before testing (MalgarimCordenonsi L - Faccendini A et al 2019; Sandri G. et al 2020).

2.8. Platelet lysate release from scaffold

The scaffolds A-B and A-01HP were cut into 2 cm^2 area diskettes (diameter of 5 mm), with 0,2 mm of thickness, to perfectly cover the bottom of the insert in a transwell chamber (96wells plate Corning Transwell Cell Culture Plate, Merck, Sigma Aldrich, 4,26 mm well diameter of the transwell and 3 μm membrane porosity).

A calibration curve using albumin was analysed (concentration range 0,131 - 1,4 mg/ml). The calibration curve was linear in the concentration range with R^2 greater than 0,994.The permeation test was performed putting the scaffold at the bottom of the insert chamber, and above each membrane 70 μl of pure HBSS (1x with $CaCl_2$ and $MgCl_2$, Gibco, Thermofisher) was added. 200 μl of Platelet Lysate (1:10 dilution in HBSS) was placed in the basal chamber of the well plate, and 70 μl HBSS (with $CaCl_2$ and $MgCl_2$, Gibco, Thermofisher) in the apical one. At fixed times apical phase samples were withdrawn and replaced with fresh HBSS. The growth factors passage through the scaffold was quantified,

by means of Bradford reaction (Breadford Reagent, Sigma Aldrich)at 595 nm -using ELISA plate reader (Biorad Milan, I).

2.9. SAOS-2 and TEN-1 cell cultures

The human osteogenic sarcoma (SAOS-2) cell line, derived from a primary osteosarcoma, were purchased by Sigma-Aldrich. The cells were seeded in polystyrene flasks (75 cm^2),using McCoy medium (McCoy's 5A Medium Modified, with L-Glutamine and sodium bicarbonate, Sigma-Aldrich, Milan, Italy) supplemented with 1% v/v of a penicillin-streptomycin-amphotericin 100x solution (pen/strep/ampho, Euroclone, Italy), and 10% v/v of a foetal bovine serum FBS (Fetal Bovine Serum, Euroclone).

The Human Tenocytes (TEN-1) (ZenBio, USA),at passages 1-5,wereseeded in polystyrene flasks (75 cm^2), previously coated with collagen (Rat Tail Collagen Coating Solution, Cell Applications) using Tenocyte Growth Medium, (ZenBio, USA).

Both the cell lines were handled under a vertical laminar flow hood (Ergosafe Space2, PBI International, Milan, Italy),and grown in an incubator (CO_2 Incubator, PBI International, Milan, Italy) at 37°C, with 95%relative humidity and 5% CO_2. Both the cell growth and morphology were evaluated using reverse optical microscope (Leica, DMI-3000B model). When the cells were in proliferative phase, they showed their typical shape.

2.10.Adhesion and proliferation of tenocytes or SAOS-2 cells onto the scaffolds

Scaffolds were cut to have 2 cm^2 area (5 mm diameter, 0.2 mm thickness) to cover the insertof 96 trans-well-plate (96 wells plate Corning Transwell Cell Culture Plate, Merck, Sigma Aldrich, 4,26 mm well diameter and 3 μm membrane porosity). The PL solution was prepared at 1:20 dilution in McCoy or TEN-1 culture medium, for SAOS-2 or TEN-1 culture, respectively.

TEN-1 or SAOS-2 cells were seeded on the scaffold in the apical chamber at $8 \cdot 10^4$ cells/cm^2seeding density. Cells seeded directly on the insert, were the controls (standard growth, SG) and 200 μl PL, diluted 1:20 in the specific media or growth media, were placed in the basolateral chambers (PL1:20).

After 3, 6 and 14 days, AlamarBlue test (AlamarBlueHS cell viability reagent, Invitrogen, Thermo Fisher, US) was performed to evaluate the metabolic activity (viability) of the cells. 10% (v/v) Alamar Blue wasdiluted in the respective media and added in both the apical(70 μl) and basolateral(200 μl) chambers of each well. After 3h incubation in dark at

37°C, the Alamar Blue solution was collected from both the chamber, and transferred in new flat wells. Each trans-well was refilled with the specific medium and left inculture again.

The Alamar Blue fluorescence was recorded using a microplate reader (Microplate Reader Biotek, Synergy/HT) at 530 nm excitation wavelength, and 590 nm emission wavelength. Triplicate measurements were performed for each sample. In each experiment the positive control was considered as cell viability grown in standard condition (SG) onto the insert, and without PL. A further control was the cell viability grown on the scaffolds without PL.

2.11. Immunofluorecence staining.

After 14 days of culture the scaffolds, subjected to the adhesion and proliferation test, were fixed using 3% glutaraldehyde (Glutaraldehyde 50%in PBS 1%) overnight at 4°C. Then the scaffolds were transferred in flat 96 well plate and washed twice using PBS. Subsequently, scaffolds were stained using Anti-Collagen I Rabbit Polyclonal Antibody (Thermofisher cod. PA126204) (100µl/sample) at the 10µg/ml concentration (dilution 1:100 inPBS 10%) (contact 24h at 4˚C), in order to immuno-labelled collagen I, released from tenocytes. Alternatively, bone sialoprotein antibody (Thermofisher cod. PA579425) was added (100µl/sample, at 1µg/ml of concentration, dilution 1:100 in PBS), for 24h at 4˚C to immune labelled sialoprotein, released by SAOS-2 cells.

The primary antibodies were stained with ATTO 488 goat Anti Rabbit IgG (Sigma Aldrich, Italy), as secondary antibody(10µg/ml concentration, 1:100 dilution in PBS), for 24h (100µl/sample). Cell cytoskeletons were stained in red with Phalloidin TRICT (Sigma Aldrich, Italy),(50 µl/ml concentration in PBS,50µl/sample) for 40 min. Finally, cell nuclei were stained in blue with Hoechst-332 (Sigma Aldrich, Italy, at $1:10^4$dilutionin in PBS) for 100µl/sample, and left in contact for 15 minutes. Each step was performed in dark at 4˚C.

The cell morphology and penetration in the scaffolds, were observed by Confocal Laser Scanning Microscopy (CLSM), using Leica TCS SP2 (Leica Microsystems, Milan, Italy) at 20x, 40x and 63x of magnification. Two replicates for samples were considered. The CLSM images were processed with ImageJ software considering the 3D projection of 10 to 15 staked slides with 2 to 7 microns of spacing.

2.12. Statistical analysis

Statistical analysis was performed using post-hoc Tukey HSD Test Calculator. One-way ANOVA followed by Scheffé, Bonferroni and Holm method, was considered. For the comparison of two groups, statistical significance was determined by using a two-tailed Student's t-test method. A p-value ≤0.05 was considered statistically significant.

3. RESULTS AND DISCUSSION

3.1. Hydroxyapatite characterization

A pre-evaluation on the bioavailability and the proliferation properties of HP nanoparticles, as a function of particles size, was performed. HP having different diameters (200, 400 or 600 nm) were selected (see annex A). 200 nm diameter HP was characterized by higher cell, with respect to the other particle sizes.

Figure 2 reports XRPD patterns of HP colloidal suspension, in water and acetic acid at 0.1 and 0.5%w/w concentrations (0.1% W, 0.1%A.A., 0.5% W, 0.5%A.A).The patterns were characterized by three characteristic peaks. Those were evident in HP powder or HP colloidal suspension in water, while the presence of acetic acid (A.A.) caused a significant decrease of the peaks, conceivably due to a partial solubilization of HP particles in acidic environments.

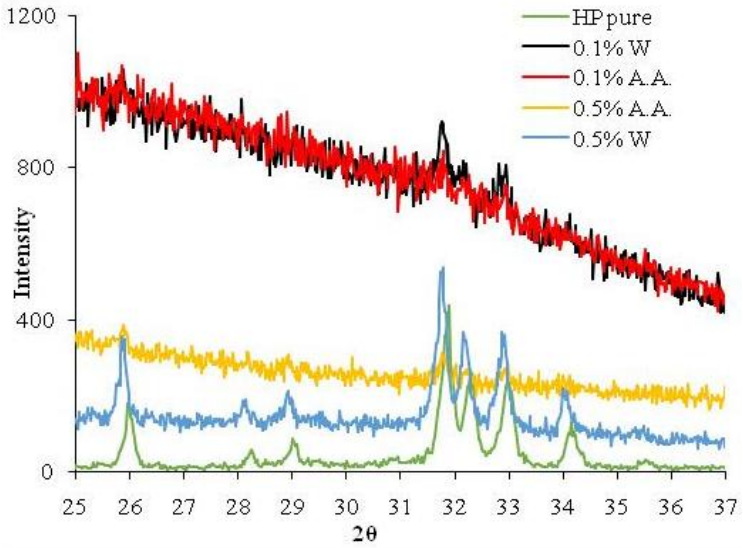

Figure 2 :*XRPD pattern of the pure commercial Hydroxyapatite (HP) powder and when in suspension in water (0.1%W) and in acetic acid 45%v/v at 0.1% w/w concentration (0.1%A.A.)*

HP colloidal suspensions in water or in acetic acid (0.1% W, 0.1%A.A., 0.5% W, 0.5%A.A) were subjected to a morphological analysis. The SEM images evidence that HP particles had a smooth surface and spherical structure. Moreover, particles in acetic acid were bigger than those in water (Figure 3 and 4), suggesting the complete solubilization of the smallest HP particles in acid.

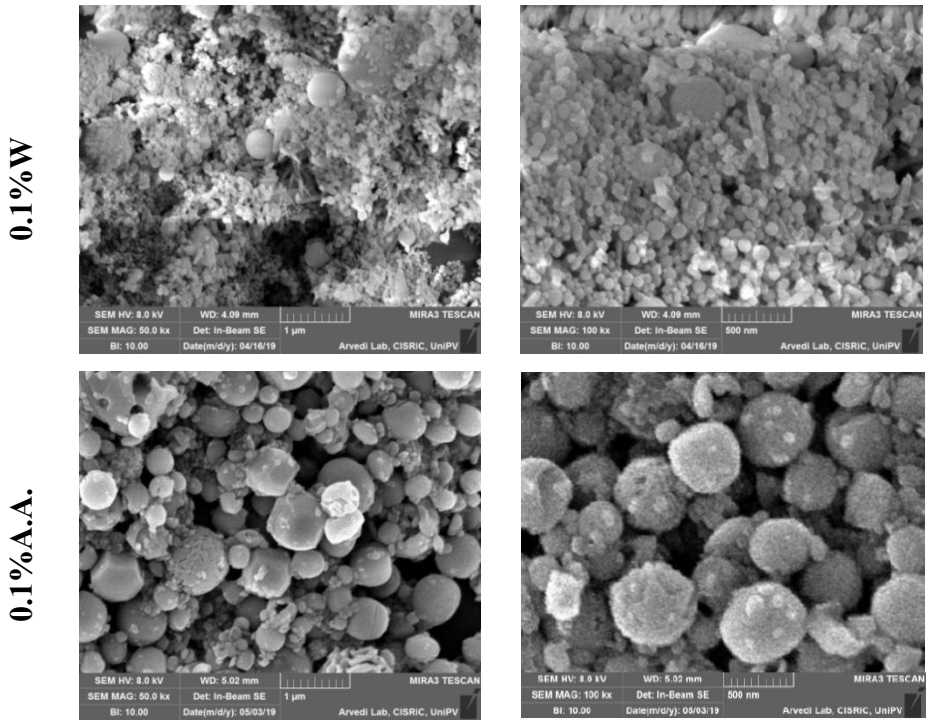

Figure 3:*SEM images of the Hydroxyapatite Sigma Aldrich (HP) suspension in water (0.1%W), in acetic acid 45% v/v (A.A.) at 0.1%w/w concentration (0.1%A.A.)(Two magnification at 500nm and 1 µm)*

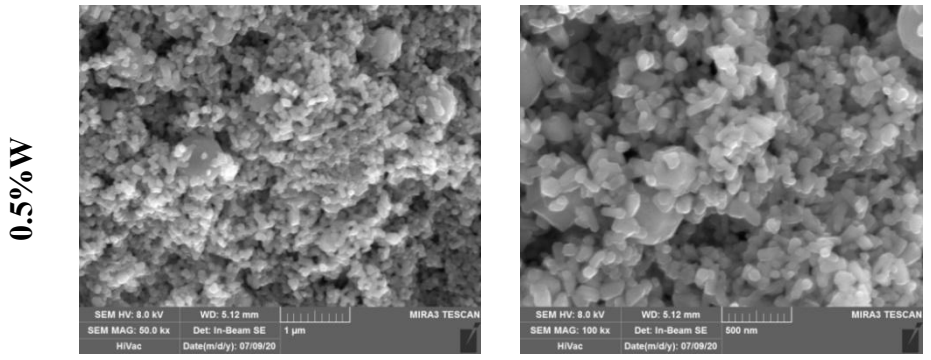

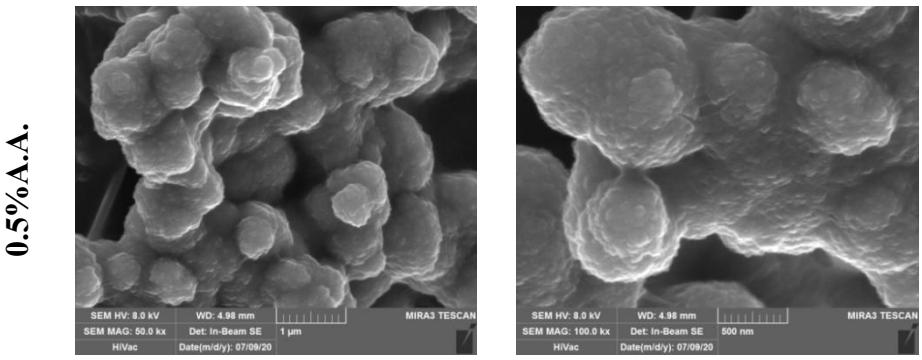

Figure 4:*SEM images of the Hydroxyapatite Sigma Aldrich (H) suspension in water (0.5%W), in acetic acid 45% v/v (A.A.) at 0.5%w/w concentration (0.5%A.A.) (Two magnification at 500nm and 1 µm)*

The particle size of water or acetic HP colloidal suspensions, measured by means of light dynamic scattering (DLS) (Figure 5), was higher than those observed in SEM images in figure 3, probably due the partial particle aggregation in suspension. HP particle size in acid was confirmed 5 folds lower than those in water (from 650nm to 1130nm, using DLS and form 100nm to 500nm using SEM analysis).

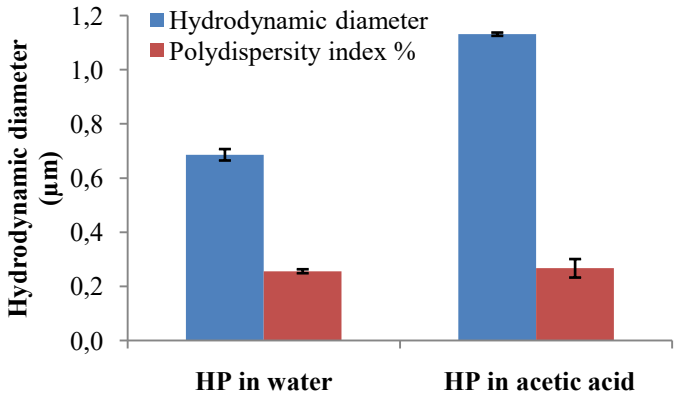

Figure 5 *Hydrodynamic diameter and polydispersity index of hydroxyapatite Sigma Aldrich (HP) measured in water or acetic acid 45% v/v at room temperature(mean value n=6; ±e.s.)*

3.2 HP loading and polymer blend characterization.

0.1% and 0.5% w/w HP (0.1HP and 0.5HP) was added to the polymeric blend, based on pullulan and chitosan, with citric acid, and the mixture was subjected to electrospinning. A polymeric blend without HP was also prepared (blank).

Table 1 reports the conductivity, consistency and surface tension of the polymer blends (blank, 0.1HP and 0.5HP). The presence of HP increased the conductivity. This

phenomenon could be attributed to the increase of electrolytes in solution, caused by the HP partial solubilisation. Moreover, the decrease of mixture consistency could be due to an interference of HP nanoparticles on polymer chain entanglement

	Conductivity (µS/cm)	Surface Tension (mN/m)	Consistency (mN*mm)
Blank	1215** (±7.37)	37.30** (±0.10)	38.58 **(±0.98)
0.1HP	1314** (±2.00)	40.38** (±0.13)	16.4 *(±0.89)
0.5HP	1746.3** (±26.60)	38.41** (±0.51)	17.56* (±0.88)

Table 3 *Conductivity, Surface Tension and Consistency of colloidal solutions at 0.5% (0.5H) and 0.1% (0.1HP) of hydroxyapatite (HP) and the Blank solution. Significant differences were reported between every samples for the conductivity and surface tension properties. The Blank solution was recorded significant different in consistency vs 0.1 and 0.5HP solutions (mean value, n=3; ±e.s.).*
** one time and** two times significantly different between the group of R-B, R-0.1HP, R-0.5HP*

3.2. Electrospun scaffold characterization

Figure 6 reports the TEM images of blank, 0.1HP and 0.5HP nanofibers. HP nanoparticles were embedded in the polymeric matrix (0.1HP and 0.5HP), and the nanofibers presented enlargement like a knot, due to the presence of inorganic particle (0.1HP and 0.5HP). Blank nanofibers presented a homogeneous structure(R-B) (Figure 6).

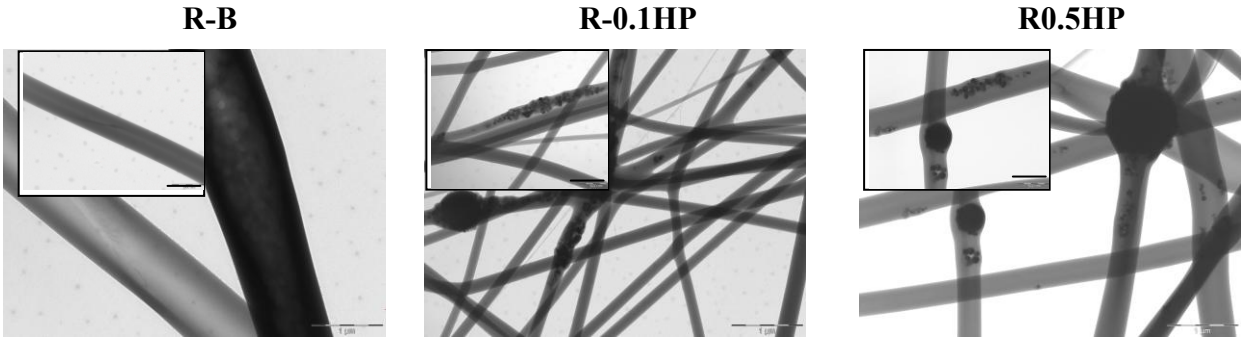

Figure 6*: TEM images of the electrospun scaffold loaded with 0.1% or 0.5% of HP (R-0.1HP;R-0.5HP) and the blank (R-B) collected in random(Two magnification at 500 nm and 1 µm)*

The nanofibers were collected randomly (R-B, R-0.1HP and R-0.5HP) or aligned (A-B, A-0.1HP and A-0.5HP) in a tubular structure. Figure 7 reports scaffold morphology in two

conditions: 1) after the crosslinking by heating; and 2) crosslinked and hydrated for 6 days in PBS(phosphate buffer solution).

SEM images evidence the presence of knots due to the HP inclusion in the scaffolds. Random (R-B) and aligned (A-B) blank scaffolds, presented similar dimensions (17% difference) in dry state. HP had a crucial role in scaffold hydration. The presence of HP in random scaffold (R-0.1HP; R-0.5HP)caused a significant decrease(40%) of the fiber diameters, in dry state, while HP caused a significant increase of nanofiber dimension, upon hydration, up to 70% swelling. In the aligned scaffold (A-B, A-0.1HP; A-0.5HP) the HP content significantly increased the fiber diameter (43%), and this was more pronounced after hydration.

Scaffold porosity (Figure 8) significantly increased, due to the nanofiber alignment and the presence HP. Nanofiber diameters and porosity were dramatically dependent to the collection. This caused a different fiber stretching, evident during the drying phase in the electrospinning process. The phenomena could be attributed to the electrostatic repulsion, started after the jet formation at the liquid drop. The longitudinal movement of the drum prevailed over the clockwise movement, and the flight of the fiber, during the deposition, could undergo minor oscillation and consequently minor stretching.

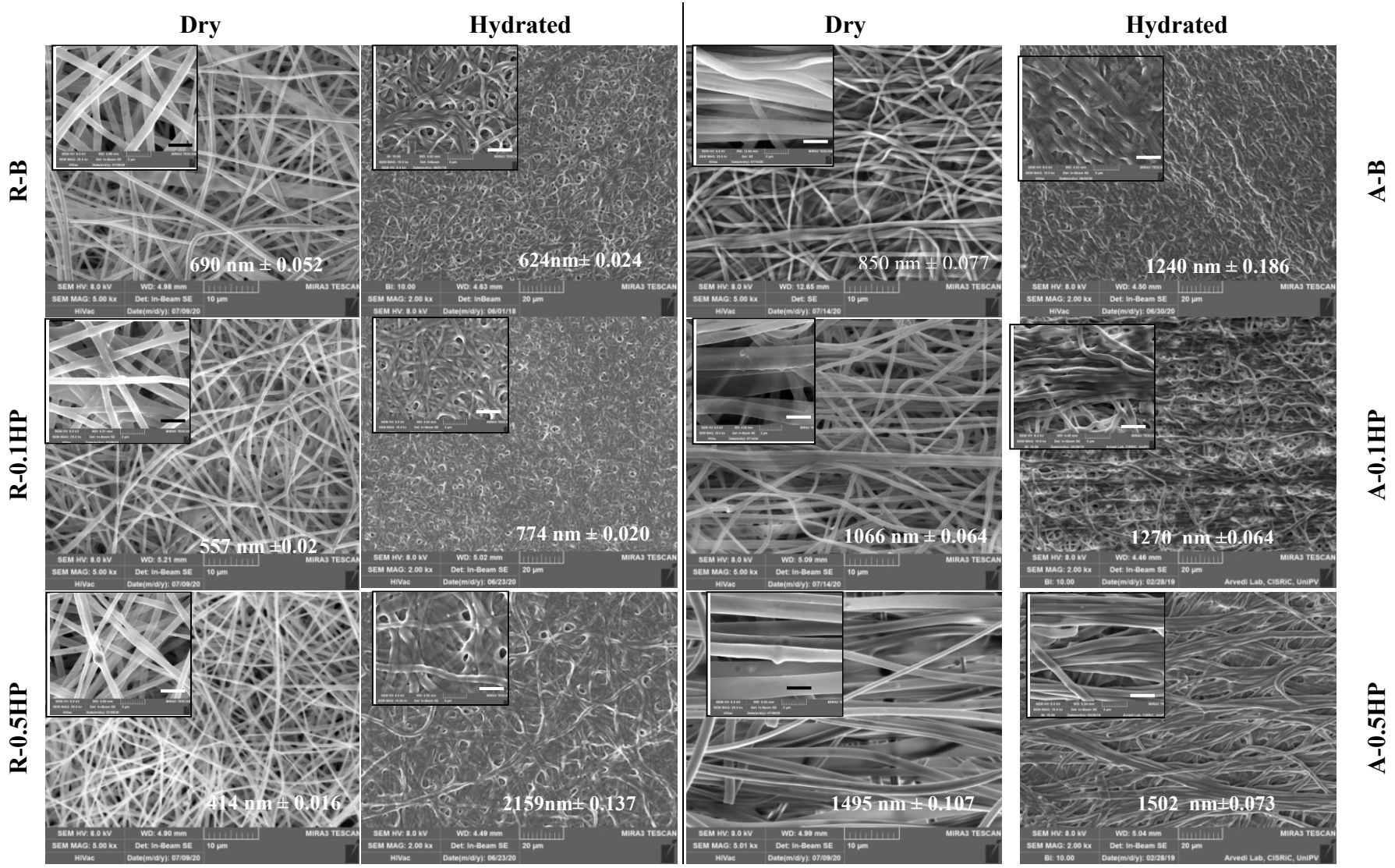
Dry
Hydrated
Dry
Hydrated
R-B
R-0.1HP
R-0.5HP
A-B
A-0.1HP
A-0.5HP
690 nm ± 0.052
624nm± 0.024
850 nm ± 0.077
1240 nm ± 0.186
557 nm ±0.02
774 nm ± 0.020
1066 nm ± 0.064
1270 nm ±0.064
414 nm ± 0.016
2159nm± 0.137
1495 nm ± 0.107
1502 nm±0.073

Figure 7 *SEM images (three magnifications 2 , 10 µm and 20) of the electrospun nanofibers collected random (R-B; R-0.1HP;R-0.5HP)and aligned (A-B; A-0.1HP;A-0.5HP) in dray and hydrated. Fiber diameters were reported. Significant differences of fiber diameter were recorded in the group of dried fibers for R-B vs R-05HP; R-B vs A-05HP; A-B vs R-01HP; A-B vs R0.5HP; A-B vs A-05HP; R-01HP vs A-05HP; A-0.1HP vs A-05HP; R-05HP vs A-05HP. Significant differences in fiber diameter were recorded in the group of hydrated fibers for R-B vs A-B; R-B vs R-05HP; R-B vs A-05HP; R-01HP vs R-05HP; R-01HP vs A-05HP. Significant difference were recorded for dried R-01HP; R-05HP; A-0.1HP; A-05HP comparing with the respective hydrated ones(mean value n=60; ±e.s)*

R-B	R-01HP	R-05HP
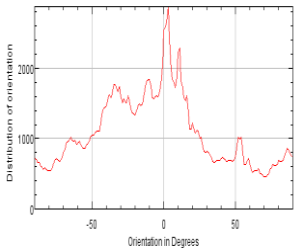	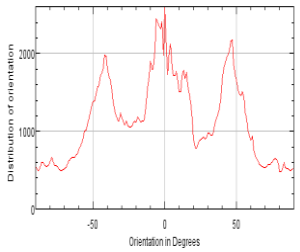	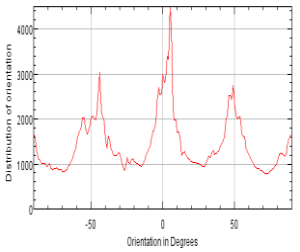
Mean Pore area (µm^2)	Mean Pore area (µm^2)	Mean Pore area (µm^2)
76.65 ±14.13	51.91 ±9.83	38.81 ±5.01
% porosity	% porosity	% porosity
0.37 ±0.05	0.41 ±0.09	0.33 ±0.04
A-B	**A-01HP**	**A-05HP**
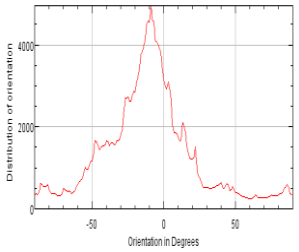	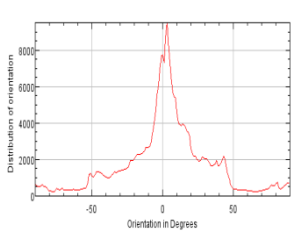	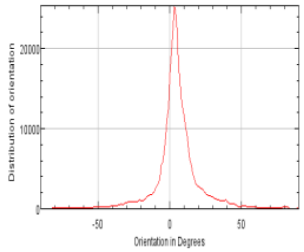
Mean Pore area (µm^2)	Mean Pore area (µm^2)	Mean Pore area (µm^2)
70.53 ±4.09	75.96 ±2.52	180.22 ±5.18
% porosity	% porosity	% porosity
0.421 ± 0.01	0.44 ±0.02	0.53 ±0.02

Figure 8 *Image J analysis of the scaffold collected random (R-B; R-0.1HP;R-0.5HP) and aligned (A-B; A-0.1HP;A-0.5HP) in dry. Degree of fiber orientation, percentage of porosity (%) and mean pore area (µm^2) were reported. Significant differences in the mean pore area were recorded between R-B vs R-0.5HP; R-B vs A-0.5HP; R-0.1HP vs A-0.5HP; R-0.5HP vs A-0.5HP;A-B vs A-0.5HP; A-0.1HP vs A-0.5HP (mean value n=10; ±e.s.)*

EDX-SEM analysis, confirmed the homogeneous calcium and phosphorous distribution. (Figure 9).

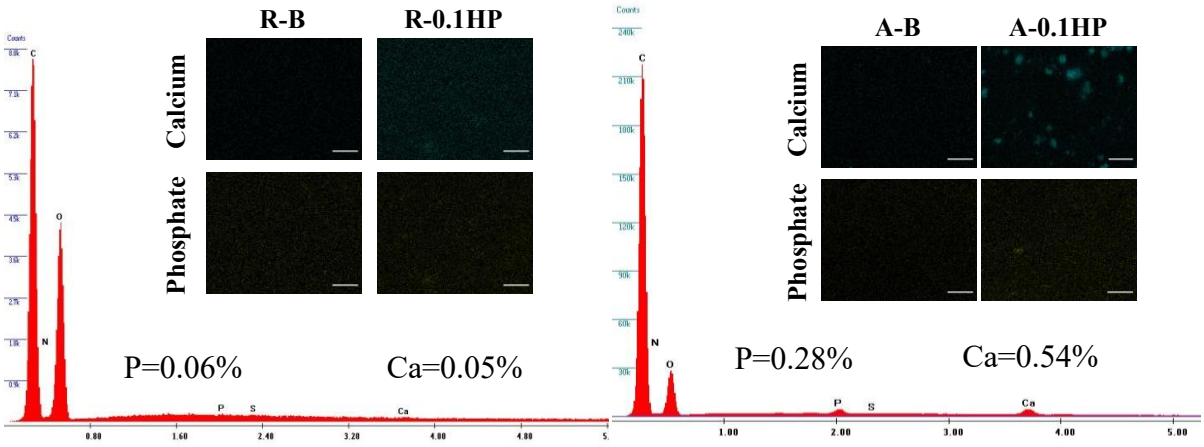

Figure 9 *SEM-EDX analysis for Calcium and Phosphate elements distribution and quantification in the scaffold. The blank (R-B and A-B) scaffold without hydroxyapatite was analysed as control)(magnification 5μ).*

In Figure 10 the scaffold wettability is reported. There were no significant differences among R-B; R-0.1HP; R-0.5HP samples, as well as among A-B, A-0.1HP; A-0.5HP. Both aligned and random scaffolds were characterized by hydrophilic surface, although, the aligned scaffolds presented a significantly higher contact angles: this was conceivably due to the surface morphology which prevented the water spreading onto scaffold surface.

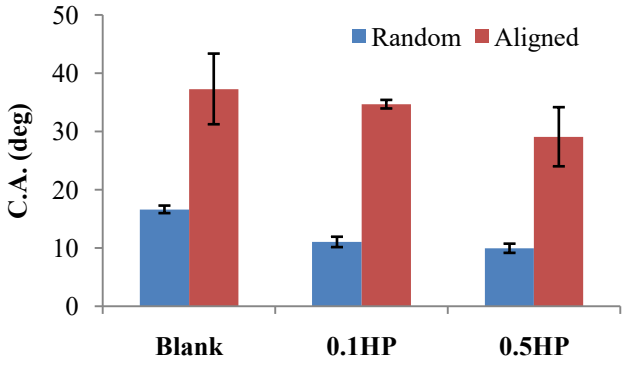

Figure 10 *Wettability for the random (R-B; R-0.1HP;R-0.5HP)and aligned (A-B; A-0.1HP;A-0.5HP). Not statistical differences were recorded in the group of aligned as well as in the random group.(mean value n=3; ±e.s).*

Figure 11 reports the FT-IR profiles of native and crosslinked scaffolds (R-B; R-0.1HP; R-0.5HP). The results confirmed identical bends, except for the characteristic vibration bends

at 601 cm^{-1},and 565 $cm^{-1}$for the HP phosphate groups in the scaffold, as reported in literature (Prasanna A.P.S et al 2018).

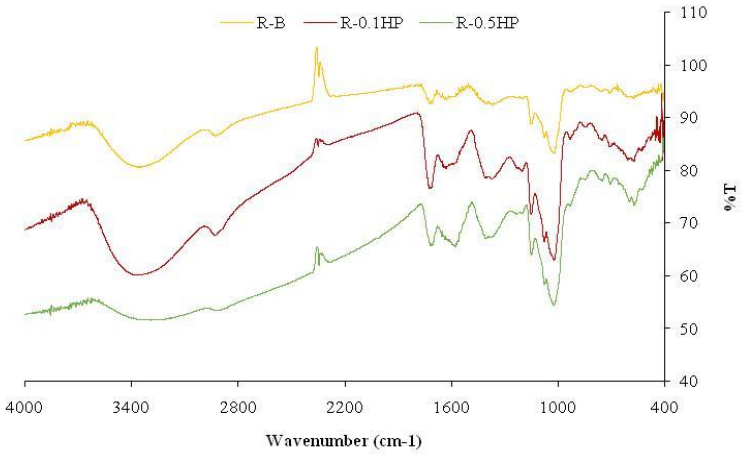

Figure 11 *FT-IR profiles for the scaffold blank (R-B) and loaded with HP (R-0.1HP and R-0.5HP)*

3.3. Scaffold mechanical properties

Random scaffolds were characterized by mechanical properties in dry state, not statistically different(Table 4.a). However, the hydration and the presence of HP, strongly affected scaffold mechanical properties, and R-0.1HPshowed higher mechanical performance thanR-0.5HP. This result suggests that HP influenced elasticity (Y.M), deformability (%E) and force at break (Fmax) of the scaffolds.

On contrary, 0.1% HP reinforced the structure of aligned tubular scaffolds, resulting in twofold higher force at break and elasticity (7.83 MPa and 18.55 MPa ultimate force and elasticity, respectively). However, 0.5 % HP concentration,caused a decrease of the mechanical properties (Table 2.B).

The mechanical results obtained for the A-0.1HP sample, were similar to the in vivo values, normally reported in literature between 5 – 100 MPa for the maximum tensile force, 20-1200 MPa for the Young Modulus and 4-10% for the elongation.

It was interesting to note that the tubular scaffold exhibited the typical sigmoid stress/strain curve, which the random one did not perform (Table 4b).Indeed the sigmoid curve is the typically viscoelastic behaviour recorded in the tendon when the tensile force is in line with the fiber direction and it is typical for the highly anisotropic tissue (Table 4b). In the sigmoid adamant, there was an initial “toe region”, between0-1%of strain, where the “crimp” structure of the tubular scaffold was stretched, and where the scaffold was totally

elastic. Above 2% of strain, the curve become linear with high slope value, where the Young Modulus was calculated (Table 4b).

A

	DRY STATE			HYDRATED STATE		
	Fmax (MPa)	**Y.M (MPa)**	**Elongation (%)**	**Fmax (MPa)**	**Y.M (MPa)**	**Elongation (%)**
R-B	**2.58** (±0.22)	**10.34** (±0.99)	**1.79** (±0.39)	**0.37*** (±0.03)	**0.28** (±0.05)	**20.89*** (±1.7)
R-0.1HP	**3.95** (±0.65)	**9.81** (±1.6)	**3.66** (±0.93)	**0.52*** (±0.06)	**0.31*** (±0.01)	**35.47**** (±1.48)
R-0.5HP	**2.47** (±0.87)	**11.35** (±4.84)	**1.96** (±0.65)	**0.06*** (±0.01)	**0.07**** (±0.02)	**17.83*** (±1.78)

** one time and** two times significantly different between the group of R-B, R-0.1HP, R-0.5HP*

B

3 mm Ø close	DRY STATE			HYDRATED STATE		
	Fmax (MPa)	**Y.M (MPa)**	**Elongation (%)**	**Fmax (MPa)**	**Y.M (MPa)**	**Elongation (%)**
A-B	**4.93** (±3.55)	**10.08** (±6.51)	**6.71** (±2.93)	**0.70** (±0.28)	**0.33** (±0.17)	**29.43** (±3.9)
A-0.1HP	**7.83**** (±1.74)	**18.55** (±5.71)	**9.13** (±1.55)	**0.79** (±0.22)	**0.48** (±0.14)	**30.08** (±2.88)
A-0.5HP	**3.75** (±1.85)	**6.97** (±4.40)	**8.91** (±2.20)	**0.26** (±0.12)	**0.15** (±0.07)	**30.10** (±5.22)

** one time and** two times significantly different between the group A-B, A-0.1HP, A-0.5HP*

Table 4a *Mechanical properties: maximum tensile force (FMax), Young module (YM) and elongation (%) performed for the scaffold collected random (R-B; R-0.1-HP; R-0.5-HP)(A), and aligned (A-B; A-0.1-HP; A-0.5-HP,) using 3 mm drum diameter (B). The scaffold collected aligned were measured in close conformation. (mean value n=4; ±e.s.)*

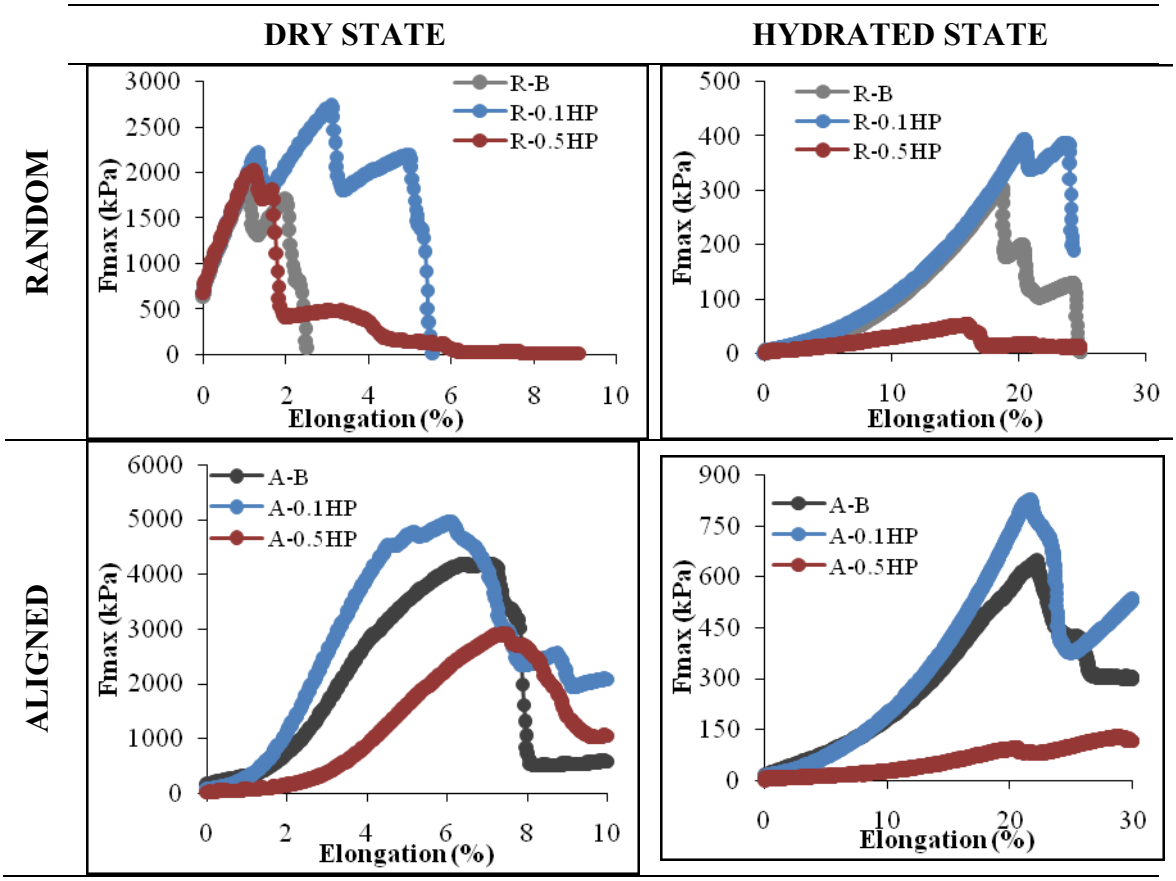

Table 4b *Tensile force (kPa) vs elongation (%) curve performed for the scaffold collected random (R-B; R-0.1-HP; R-0.5-HP), and aligned (A-B; A-0.1-HP; A-0.5-HP,) using 3 mm drum diameter (B). The curve of every sample is the mean of 4 curves replicated, for this reason they resulted to be different from the single average values of Fmax, YM or E% extracted by every single curve, and reported in Table 4a*

3.4. Release of Protein from Platelet Lysate loaded scaffold.

Figure 12shows the PL protein release profiles from aligned blank and HP loaded scaffolds. Protein release was sustained up to 14 days, reaching 60% proteins released, and 85% proteins released for A-0.1HP and A-B, respectively. A possible reason of these behaviours could be attributed to the nanofiber swelling and to the mineral phase which could prevent PL proteins diffusion.

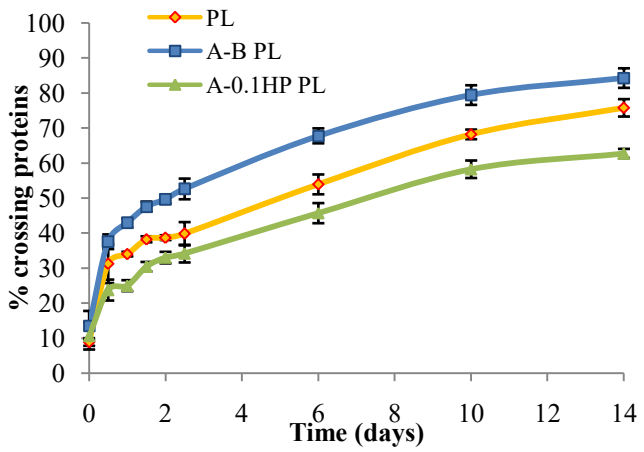

Figure 12. *% of protein crossing the scaffolds thickness in transwell system. Platelet Lysate (PL) diluted 1:20 in HBSS placed in the lower chamber. The A-B and A-0.1HP scaffold were place in the upper chamber. (mean value n=4; ± e.s.)*

3.5. Biocompatibility

Figure 13 a-b and 14 a-b report the metabolic activity of SAOS-2cellsand tenocytes, respectively, grown onto the blank and HP loaded aligned scaffolds. PL significantly increased cell bioavailability up to 14 days, while the cell growth reached a plateau value, or a viability decrease after 6 days, if PL was not present. These suggest that PL associated to the scaffolds was able to further sustain and enhance cell adhesion and proliferation onto the scaffolds.

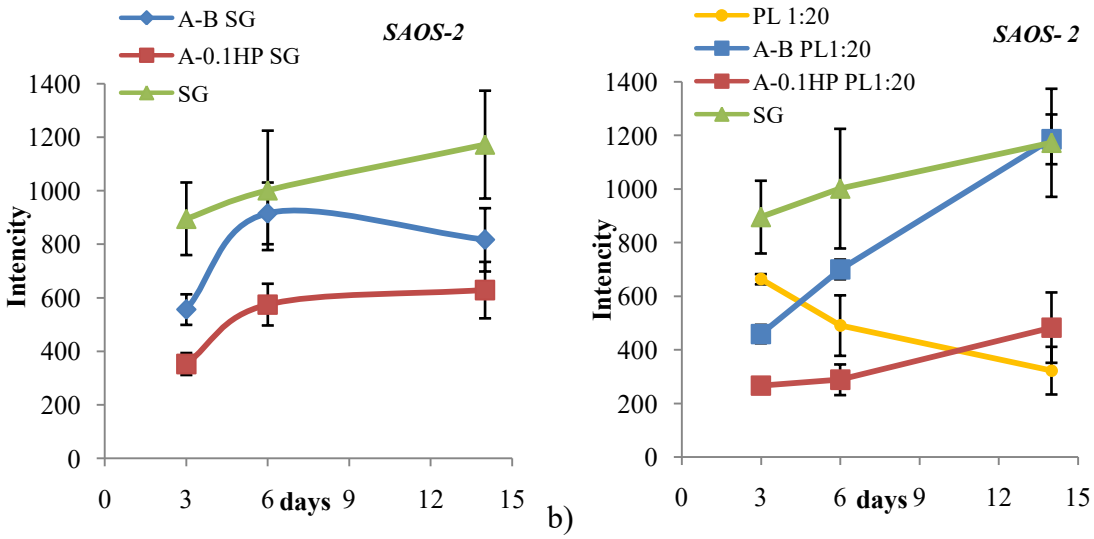

Figure 13.*Metabolic activity by Alamar Blue assay performed for SAOS cell grown (from 3 to 14 days) onto the scaffold placed in the upper chamber of trans-well plate. a) The cells were cultured in standard growth on to the transwell membrane (SG) or onto the scaffolds (A-B SG and A-01HP*

SG). b) SAOS were cultured in presence of 1:20 diluted platelet lysate (PL 1:20) onto the transwell membrane or onto the scaffolds (A-B PL1:20 and A-01HP PL1:20). PL solution was diluted at 1:20 in full medium and placed in the lower chamber. (mean value n=8; ±e.s.)

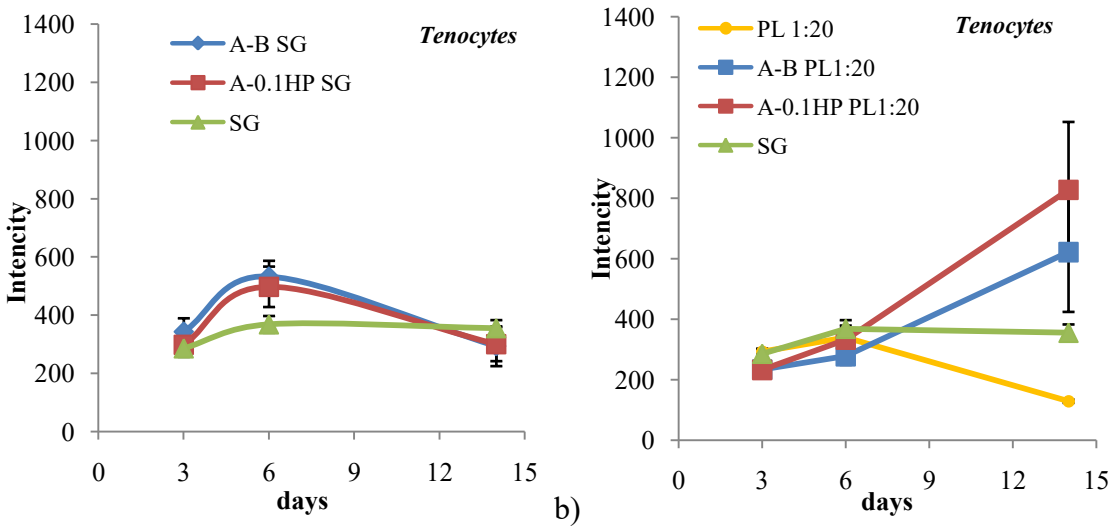

Figure 14.*Metabolic activity by Alamar Blue assay performed for Tenocytes cell grown (from 3 to 14 days) onto the scaffold placed in the upper chamber of trans-well plate. a) The cell were cultured in standard growth on to the transwell membrane (SG) or onto the scaffolds (A-B SG and A-01HP SG). b) Tenocytes were cultured in presence of 1:20 diluted platelet lysate (PL 1:20) onto the transwell membrane or onto the scaffolds (A-B PL1:20 and A-01HP PL1:20). PL solution was diluted at 1:20 in full medium and placed in the lower chamber. (mean value n=8; ±e.s.)*

3.6. Cell morphology

Figure 15 and 16 report the CLSM images of tenocytes and SAOS-2 cells grown onto the scaffolds. Tenocytes presented a cluster growth, when cultured onto the A-B scaffold, while they had a normal fusiform shape, when grown onto the hybrid scaffold (A-0.1HP). PL also enhanced the tenocytes proliferation and adhesion onto the fibrous scaffold and higher levels of collagen type I were found in the extracellular matrix produced by the tenocytes grown with PL (Figure 15). Analogously SAOS-2 cells grown onto the A-B and A-0.1HP scaffolds, in presence of PL, presented higher proliferation and higher production of sialoproteins in the extracellular matrix (Figure 16). Interestingly both tenocytes and SAOS-2 cells(Figure 17 and 18, respectively), demonstrated to deeply penetrate into the tubular scaffold wall, and this behaviour was dramatically higher in presence of PL.

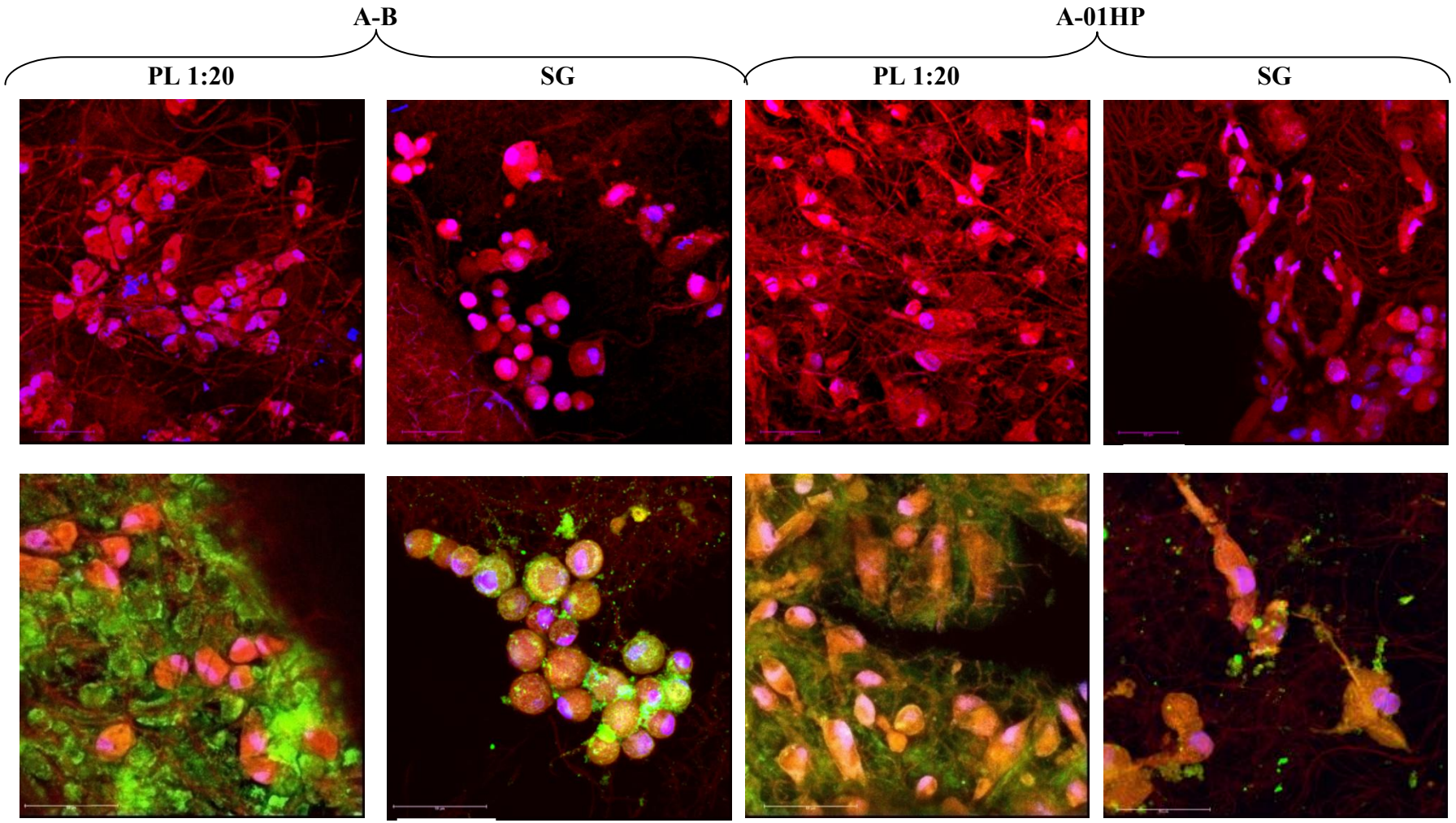

Figure 15 *CLSM images of tenocytes grown onto the aligned scaffold (A-B and A-0.1HP) after 14 days with or without platelet lysate (PL) (PL 1:20 dilution in full medium). Actin stained in red, , nuclei stained in blue and collagen I stained in green (tow magnifications at 50 µm were reported: 40x or 63x)*

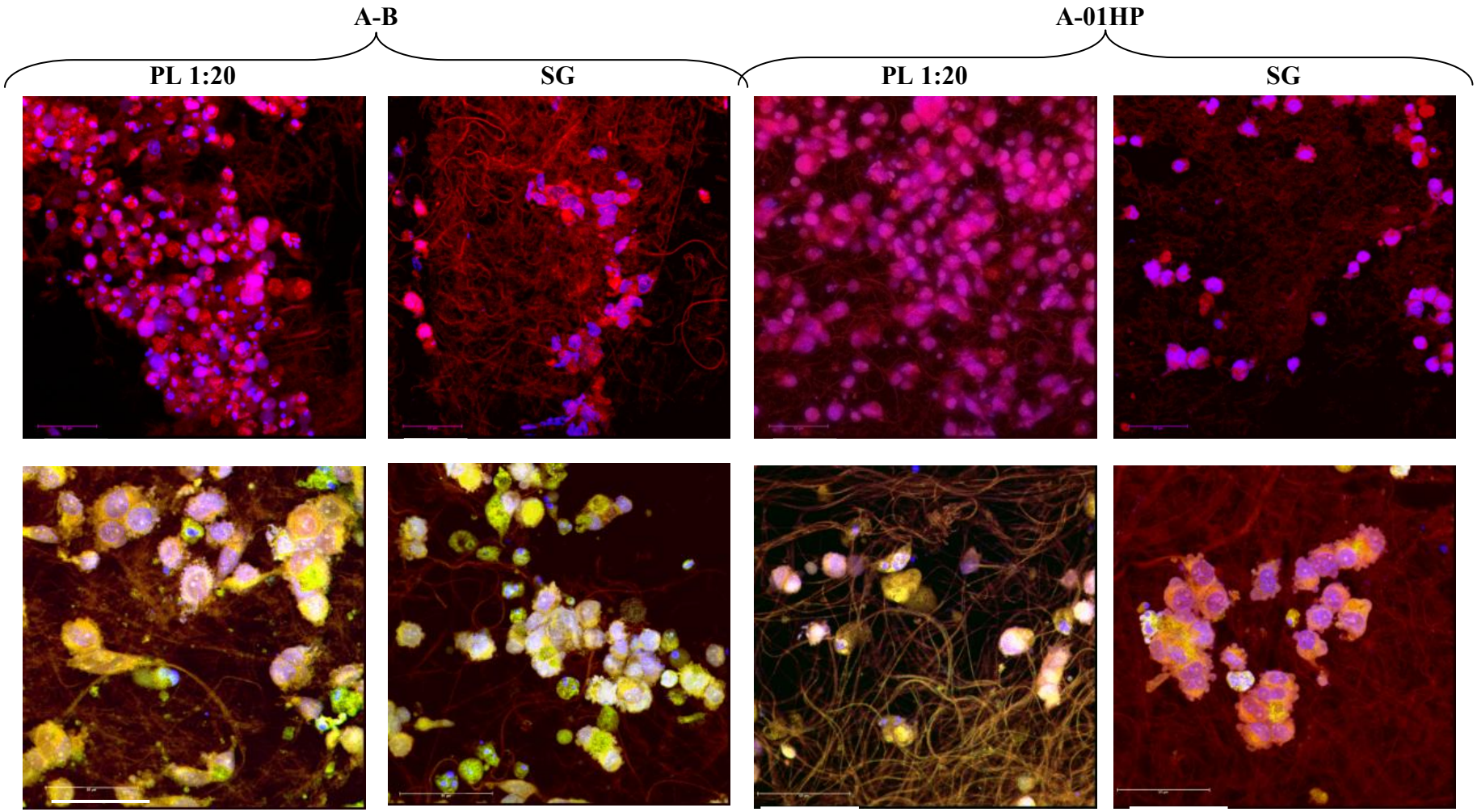

Figure 16 *CLSM images of SAOS grown onto the aligned scaffold (A-B and A-0.1HP) after 14 days with or without platelet lysate (PL) (PL 1:20 dilution in full medium). Actin stained in red, , nuclei stained in blue and collagen I stained in green (tow magnifications at 50 µm were reported: 40x or 63x)*

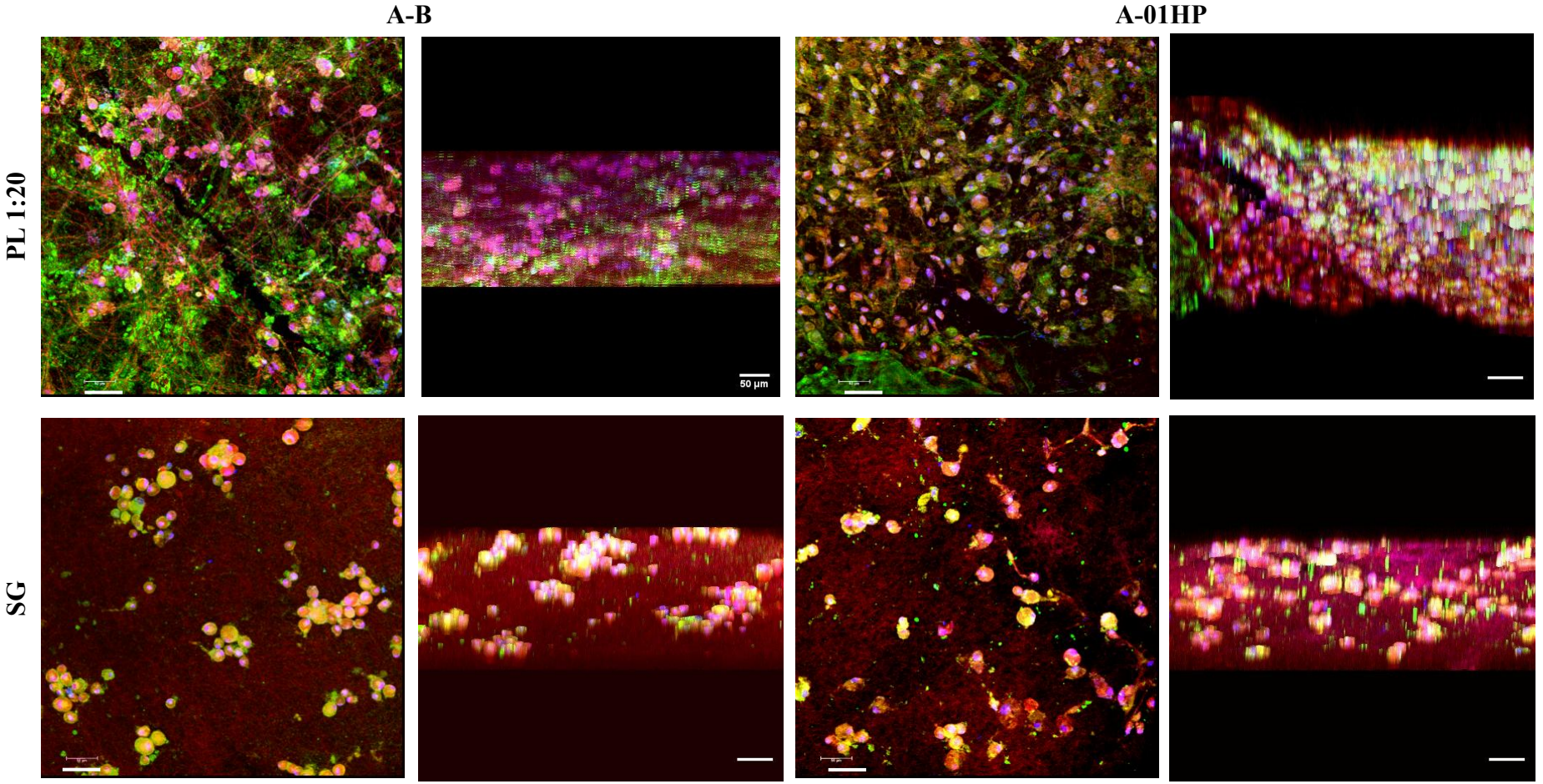

Figure 17*. CLSM images of tenocytes grown onto the aligned scaffold (A-B and A-0.1HP) after 14 days with or without platelet lysate (PL) (PL 1:20 dilution in full medium). Actin stained in red, , nuclei stained in blue and collagen I stained in green (one magnifications at 50 µm was reported at 20x in 2D or 3D projection)*

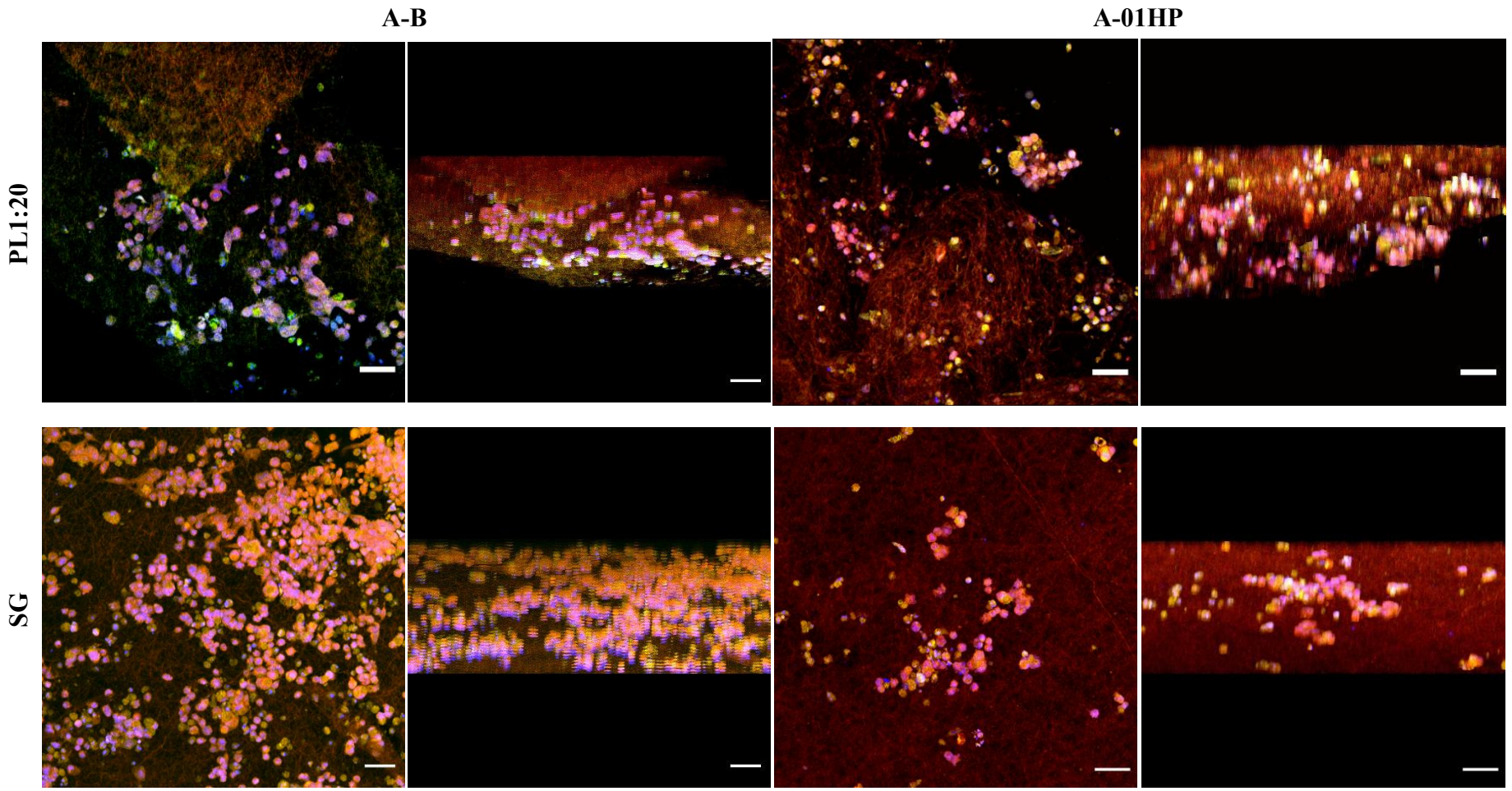

Figure 18. *CLSM images of tenocytes grown onto the aligned scaffold (A-B and A-0.1HP) after 14 days with or without platelet lysate (PL) (PL 1:20 dilution in full medium). Actin stained in red, , nuclei stained in blue and collagen I stained in green (one magnifications at 50 µm was reported at 20x in 2D or 3D projection)*

4. CONCLUSIONS

In the first part of the work, the cytotoxicity was assessed, as a function of hydroxyapatite (HP)particle size. It was already proved in literature that HP particle size and crystal shape, could cause cellular inflammatory response. In particular, it was reported in literature, that HP needle-shape nanoparticles induced stronger inflammatory response, in comparison with the smooth spherical particles (Lebre F et al 2017).

In this study 200 nm HP nanoparticles proved to be more biocompatible and to enhance tenocytes and SAOS–2cells proliferation, suggesting that nano-biocermics morphology directly affected cellular viability.

The novelty of the study was to load HP nanoparticles in pullulan and chitosan blend, and electrospun to form a unique tubular scaffold topography, made up of nanofibers aligned along the tube length. HP nanoparticles were preserved upon electrospinning, despite the acid pH of the polymer solution, and confirmed by electron microscopies (SEM and TEM), and spectroscopies (XRPD and FTIR).Moreover, they were embedded into the polymer matrix.

The presence of HP also influenced the mechanical behaviour of the scaffolds. 0.1% HP was found as the characteristic mineral concentration inducing a reinforcement of the scaffold structure, while 0.5 % decreased the mechanical properties. It is conceivable that the mineral phase and the polymer matrix deeply interacted up to a critical concentration. Further increase of HP concentration probably caused particle aggregation, which formed discontinuity points and weakened the 3D structure. The nanofiber alignment resulted in an anisotropic assembly, strongly influenced by the direction of the tensile force applied as it was possible to observe in the typical sigmoid curve resulted. The tubular construct preserved its mechanical properties, also upon hydration when 0.1 % HP was present. Although the mechanical properties of a single tubular scaffold did not satisfy totally the broad mechanical range of a native tendon, but it could be possible argued that the assembling of several tubular scaffolds, to form braids, could accomplish similar *in vivo* values.

Moreover the presence of HP in the scaffold played a role in preventing the PL local release up to 14 days. The PL after 14 days of culture, favoured tenocytes and SAOS-2 (adhesion and proliferation. The tenocytes, when cultured onto the aligned HP loaded scaffold, were characterized by elongated and spindle shape, suggesting that HP particles

played an important role in cell engraftment and in the activation of the focal adhesion points, and this could be favoured by the topography/ morphology of the scaffold and in particular by stiffness, and roughness.

HP tubular scaffolds also promoted the cell migration into the scaffold structure and extracellular matrix deposition. The presence of PL supported a stronger collagen I production, thanks to the growth factors, which have a crucial role in cell adhesion and proliferation.

These findings confirm that the innovative structure here designed and developed, based on hybrid tubular scaffold extemporarily loaded with PL, could be a power tool to accelerate new tissue formation, by remodelling and byre-establishing the tissue functionality.

Acknowledgements

This research did not receive any specific grant from funding agencies in the public, commercial, or not-for-profit sectors.

REFERENCE

1. Babo PS, Santo VE, Gomes ME, Reis RL. Development of an Injectable Calcium Phosphate/Hyaluronic Acid Microparticles System for Platelet Lysate Sustained Delivery Aiming Bone Regeneration. Macromol Biosci. 11 (2016) 1662-1677.
2. Berger DR, Centeno CJ, Steinmetz NJ. Platelet lysates from aged donors promote human tenocyte proliferation and migration in a concentration-dependent manner, Bone Joint Res. 2 (2019) 32-40.
3. Calejo I, Costa-Almeida R, Reis RL, Gomes ME., A textile platform using continuous aligned and textured composite microfibers to engineer tendon-to-bone interface gradient scaffolds. Adv Health Mater. 15 (2019) 1900200
4. Contreras-Cáceres R, Cabeza L, Perazzoli G, Díaz A, López-Romero JM, Melguizo C, Prados J., Electrospun nanofibers: recent applications in drug delivery and cancer therapy. Nanomaterials (Basel). 24 (2019) 656
5. Czekanska EM, Stoddart MJ, Richards RG, Hayes JS. In search of an osteoblast cell model for in vitro research. Eur Cell Mater. 9 (2012) 24:1-17

6. Day RM, Boccaccini AR, Shurey S, Roether JA, Forbes A, Hench LL, Assessment of poly(glycolic acid) mesh and bioactive glass for soft tissue engineering scaffolds, Biomaterials. 25 (2004) 5857–5866.
7. Faccendini A, Ruggeri M, Miele D, Rossi S, Bonferoni MC, Aguzzi C, Grisoli P, Viseras C, Vigani B, Sandri G, Ferrari F., norfloxacin-loadedelectrospun scaffolds: Montmorillonite nanocomposite vs. Free drug, Pharmaceutics. 4 (2020) 12-325
8. García-Villén F, Faccendini A, Aguzzi C, Cerezo P, Bonferoni MC, Rossi S, Grisoli P, Ruggeri M, Ferrari F, Sandri G, Viseras C., Montmorillonite-norfloxacin nanocomposite intended for healing of infected wounds, Int J Nanomedicine 14. (2019) 5051-5060.
9. Jooybar E, Abdekhodaie MJ, Karperien M, Mousavi A, Alvi M, Dijkstra PJ. Developing hyaluronic acid microgels for sustained delivery of platelet lysate for tissue engineering applications. Int J Biol Macromol. 144 (2020) 837-846
10. Keshaw H, Forbes A, Day RM. Release of angiogenic growth factors from cells encapsulated in alginate beads with bioactive glass. Biomaterials. 26 (2005) 4171–4179.
11. Klatte-Schulz F, Schmidt T, Uckert M, Scheffler S, Kalus U, Rojewski M, Schrezenmeier H, Pruss A, Wildemann B, Comparative analysis of different platelet lysates and platelet rich preparations to stimulate tendon cell biology: An in vitro study, Int J Mol Sci. 10 (2018) 212.
12. Krishna L, Dhamodaran K, Jayadev C, Chatterjee K, Shetty R, Khora SS, Das D., Nanostructured scaffold as a determinant of stem cell fate, Stem Cell Res Ther. 7 (2016) 188.
13. Kupiec, T.C.; Matthews, P.; Ahmad, R., Dry-heat sterilization of parenteral oil vehicles, Int. J. Pharm. Compd.4 (2000) 223–224.
14. Lebre F, Sridharan R, Sawkins MJ, Kelly DJ, O'Brien FJ, Lavelle EC. The shape and size of hydroxyapatite particles dictate inflammatory responses following implantation. Sci Rep. 7 (2017) 2922.
15. MalgarimCordenonsi L, Faccendini A, Rossi S, Bonferoni MC, Malavasi L, Raffin R, SchermanSchapoval EE, Del Fante C, Vigani B, Miele D, Sandri G, Ferrari F., Platelet lysate loaded electrospun scaffolds: Effect of nanofiber types on wound healing, Eur J Pharm Biopharm. 142 (2019) 247-257

16. Ozdemir T., Xu LC, Siedlecki C, Brown JL., Substrate curvature sensing through Myosin IIa upregulates early osteogenesis. Integr Biol (Camb). 5 (2013) 1407-16.
17. Prasanna A.P.S., DevanandVenkatasubbu G., Sustained release of amoxicillin from hydroxyapatite nanocomposite for bone infections, Process in Biomaterials. 7 (2018) 289-296
18. Rahaman MN, Day DE, Bal BS, Fu Q, Jung SB, Bonewald LF, Tomsia AP., Bioactive glass in tissue engineering. Acta Biomater. 7 (2011) 2355-73.
19. Rodriguez IA.; Madurantakam PA.; McCool JM.; Sell SA.; Yang H.; Moon PC.; Bowlin GL.; Mineralization potential of electrospunpdo-hydroxyapatite-fibrinogen blended scaffolds, Int J. Biomater 2012 (2012) 1-13
20. Sandri G, Faccendini A, Longo M, Ruggeri M, Rossi S, Bonferoni MC, Miele D, Prina-Mello A, Aguzzi C, Viseras C, Ferrari F., halloysite- and montmorillonite-loaded scaffolds as enhancers of chronic wound healing. Pharmaceutics. 12 (2020) 179.
21. Sandri G, Rossi S, Bonferoni MC, Miele D, Faccendini A, Del Favero E, Di Cola E, Icaro Cornaglia A, Boselli C, Luxbacher T, Malavasi L, Cantu' L, Ferrari F. Chitosan/glycosaminoglycan scaffolds for skinreparation. CarbohydrPolym. 15 (2019) 219-227.
22. Santo VE, Gomes ME, Mano JF, Reis RL. Chitosan-chondroitin sulphate nanoparticles for controlled delivery of platelet lysates in bone regenerative medicine. J Tissue Eng Regen Med. 3 (2012) 47-59
23. Savelyeva M S,Abalymov A A, Lyubun G P, Vidyasheva I V,YashchenokAM, Douglas T.E.L , Gorin D A,Parakhonskiy B. Vaterite V, Coatings on electrospun polymeric fibers for biomedical applications, J Biomed Mater Res A. 105 (2017) 94-103
24. Whals W.R. Repair and regeneration of ligaments, tendons, and joint capsule, Orthopedic Biology and Medicine (2006). pp 1-324
25. Zong H, X Xia, Y Liang, S Dai, A. Alsaedi, T. Hayat, F. Kong, J. H. Pan, Designing function-oriented artificial nanomaterials and membranes via electrospinning and electrospraying techniques Mater. Sci. Eng. C. 92 (2018) 1075–91

ANNEX A

1. MATERIALS AND METHODS

1.1. Materials

Calcium nitrate tetrahydrate (98%; $Ca(NO_3)_2 \cdot 4H_2O$; Sigma-Aldrich); ammonium hydrogen phosphate (99%; $(NH_4)_2HPO_4$; Merck), etilendiammine-tetra-acetic acid (EDTA, ≥ 98% Fluka) and urea (98% ; Sigma-Aldrich) Ammonia (Sigma-Aldrich).

1.2. Hydroxyapatite synthesis

Hydroxyapatite was synthesized using the sol-gel technique reported by Bezzi G. et al 2003.13,93 g of calcium nitrate tetrahydrate , 4,26 g of ammonium hydrogen phosphate, were solubilised in 62,75 ml of distilled water containing ammonia (7% v/v), the molar ratio of Ca/P was maintained up to1.7. As gelling agents 19,28 g of EDTA and 4,82 g of urea, were added. The ions exchange happened passing throughout a transparent sol-phase into a white gel-phase formation. The sol-gel transition end, was obtained by stirring and heating (90-120°C) for 2 hours.

The homogeneous and consistent gel obtained was dried in air at 340°C. After that, the material was grounded. The black powder obtained in the mortar, was fired at 800°C for 2 hours, to have higher hydroxyapatite particle size (HP800), or at 700°C for 2 h, to have lower hydroxyapatite particle size (HP700). The white powder formed in this first step, was impure hydroxyapatite, because still blended with a portion of CaO. Infact, CaO is the thermal decomposed product of calcite at 650-700°C as reported in literature (Mostafa N.Y & Brown P.W2007; Jay A.H. & Andrews K.W 1944) .TheX-ray pattern of the impure hydroxyapatite was carried out by Buker D8 Advance (copper cathode source) and confirmed the presence CaO in the powder (Figure. 1)(Jay A.H. & Andrews K.W. et al 1944) .

In the second step, the hydroxyapatite purification was achieved by lowering the Ca/P ratio to 1.667. At this purpose the impure hydroxyapatite was suspended in distilled water at 90°C for 1 hour, and the right amount of diammonium hydrogen phosphate was added.

Around 5 g of pure hydroxyapatite was resulted after draying at 120°C for 2 h, as confirmed by XRPD analysis (Figure 2) (Mostafa N.Y et al 2007).

1.3. Particle size evaluation

The X-ray diffraction was carried out by Buker D8 Advance diffractometer, operating at 40 mA, equipped with copper cathode, source 40 kV, with λ=1.54 Å, in the 2θ range from 20-60°, with step size 0.02°, counting time 20 s/step.

For SEM imaging (Tescan, Mira3XMU), the powder was placed on stubs and spattered with platinum.

The mean particle size and polydispersion index were evaluated at room temperature by a photon correlation spectroscopy (PCS) equipment (N5 Beckman Coulter, Instrumentation Laboratory, Milan, Italy). Each sample was suspended in ultrapure water in concentration according to the operating procedure. The suspensions were subjected to ultrasound for 5 minutes before analysis. Three hydroxyapatite powder types were compared: the first one resulted from 800°C of firing, and the second one from 700°C, and lastly the commercial type by Sigma Aldrich (particle size tabulated ≥ 200nm), (Figure 3, 4 and 5).

1.4. In vitro hydroxyapatite cytotoxicity assay on SAOS-2 and TEN-1 cell

The HP content in suspension was chosen in the same range used for the developed scaffolds: from 150 to 600 µg/ml. Commercial HP (Sigma-Aldrich), HP800 (HP fired at 800°C) and HP700 (HP fired at 700°C) were considered in the cytotoxicity assay.

The SAOS-2or TEN-1 cells were cultured in 96 well-plate with a density of $8 \cdot 10^4$ cells/cm^2, and left to spread for 4 h. After this time, the HP powder was suspended in the complete culture medium at the fixed concentrations, and added in the culture wells for 24 h. The cell metabolic activity was performed by MTT assay. At this purpose tetrazolium salt, [3-(4,5-dimethylthiazol-2-yl)-2,5-diphenyltetrazoliummbromide], (Sigma-Aldrich, Milan, I),MTT was solubilised in DMEM (Dulbecco's Modification of Eagle's Medium with 4,5 g/L glucose & sodium pyruvate without L-glutamine & phenol red), at a concentration of 2,5 mg/ml per well. The solution obtained was sterilised under a vertical laminar flow hood (Ergosafe Space2, PBI International, Milan, Italy), through a sterilizing filter (Minisart® single use filter unit, non-pyrogenic, hydrophilic, Sartorius Stedim Biotech GmbH, Goettingen, DE) with 0,22 µm of porosity.

To test the viability, 50 µl of the MTT solution and 100 µl of DMEM, were dispensed in each well and then placed in an incubator at 37°C for 3 hours in dark. After the aspiration of the MTT solution from the wells, 100 µl of dimethylsulfoxide were dispensed to solubilise the formazan resulting from the reduction of MTT by the cells.
The absorbance of the solution formed, was considered the level of cell viability, and was detected by Spectrophotometric ELISA Plate Reader (iMARK Microplate Absorbance Reader, BioRad, Milan, Italy) at a wavelength of 570 nm with a reference wavelength of 690 nm.

2. RESULTS AND DISCUSSION

In Figure A1 was reported the XRPD pattern of the Hydroxyapatite obtained at lower temperature (HP700), before and after purification step. The CaO impurity from the calcite decomposition, as reported in literature (Jay A.H. & Andrews K.W 1944; Mostafa N.Y et al 2007), presented the typical peak at 37.5 degree, which was signed by the blue bar in figure A1. After the purification process the HP700 pattern showed the characteristic hexagonal crystal profile (figure A1).

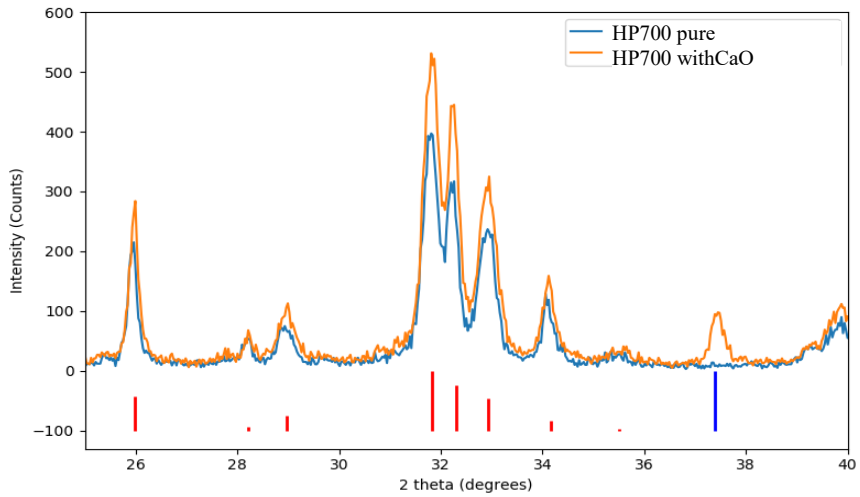

***Figure A.1**. Hydroxyapatite (HP700) before and post cleaning. Line blue show CaO peak impurity. Line red HP700 peak*

The comparison between the HP700 and HP800 patterns, confirmed the creation of the same crystal structure. The HP800 profile exhibited thinner peaks, with FWHM values

lower than the HP700 one. Lower FWHM values in HP800 suggested smaller crystals size formed (figure A.2).

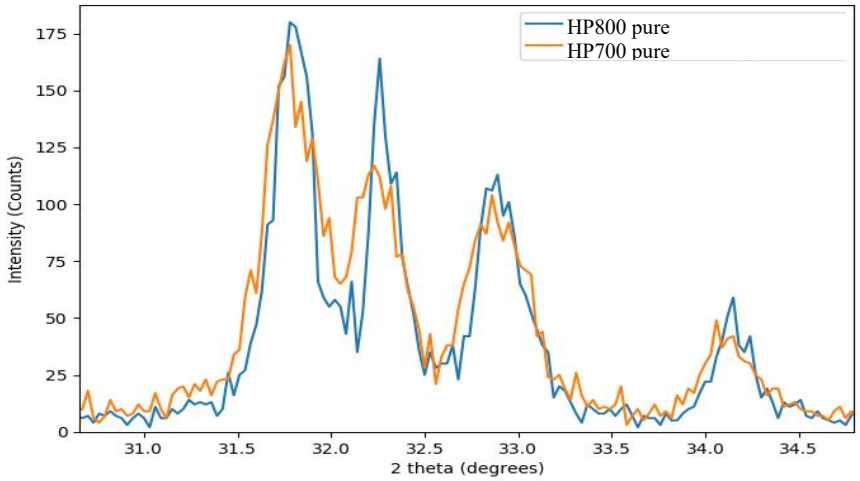

***Figure A.2**. Pure Hydroxyapatite fired at 700°C (HP700) and the one firing at 800°C (HP800) pattern and Full Width at Half Maximum (FWHM)*

From the SEM images of HP700 and HP800, both the samples showed particles with irregular shape and polyhedral structure. They were different from the spherical particles, which were found in the commercial HP type (Chapter 4, Figure 3 and 4). However the dimensional differences between the particles, were not easy to note at SEM analysis.

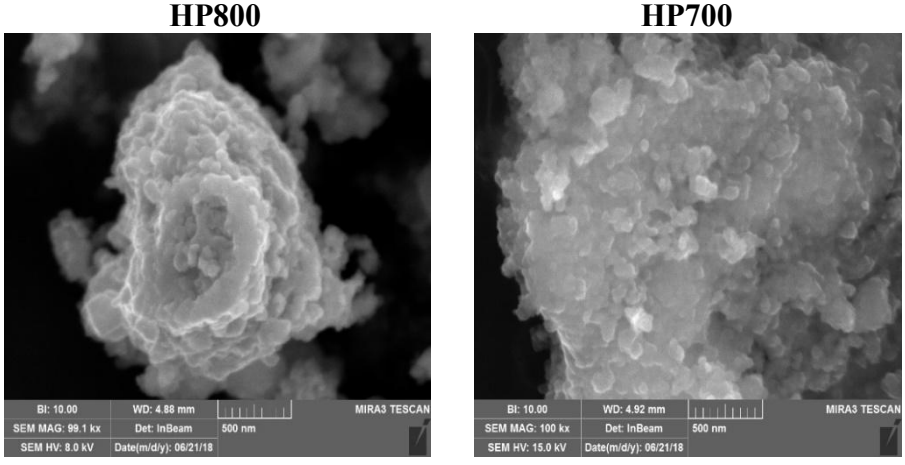

***Figure A.3** SEM images of Pure Hydroxyapatite fired at 700°C (HP700) and the one firing at 800°C (HP800)*

The HP700 and HP800 types of hydroxyapatite, were characterized by PCS analysis. As suggested from XRPD pattern, the HP800 type possessed greater particle dimension around 900nm, while the HP700 type was around 500nm in water suspension. But high values of PI (polydispersity index) for both the suspensions leaded to suppose a partial phenomena of aggregation in water.

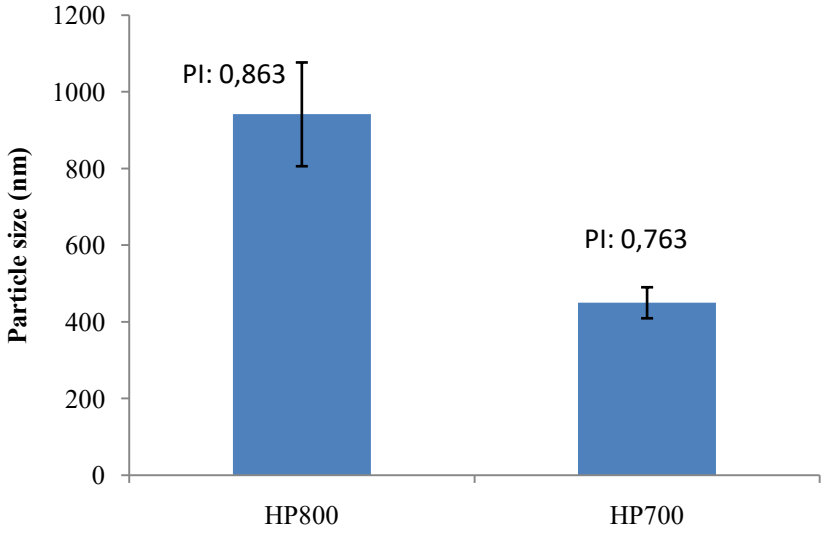

Figure A.4 *Mean particle Size for HP800 and HP700 and the respective polydispersity index*

The preliminarily biological evaluation of the powder cytotoxicity was carried out on tenocytes and SAOS-2cells. The HP800 and HP700 powder were compared with the commercial type (HP, Sigma-Aldrich). All the powders possessed good biocompatibility, since the cell viability was kept above the 50% of the control (SG). However, HP commercial was the only one with super-imposable availability, compared to the control.

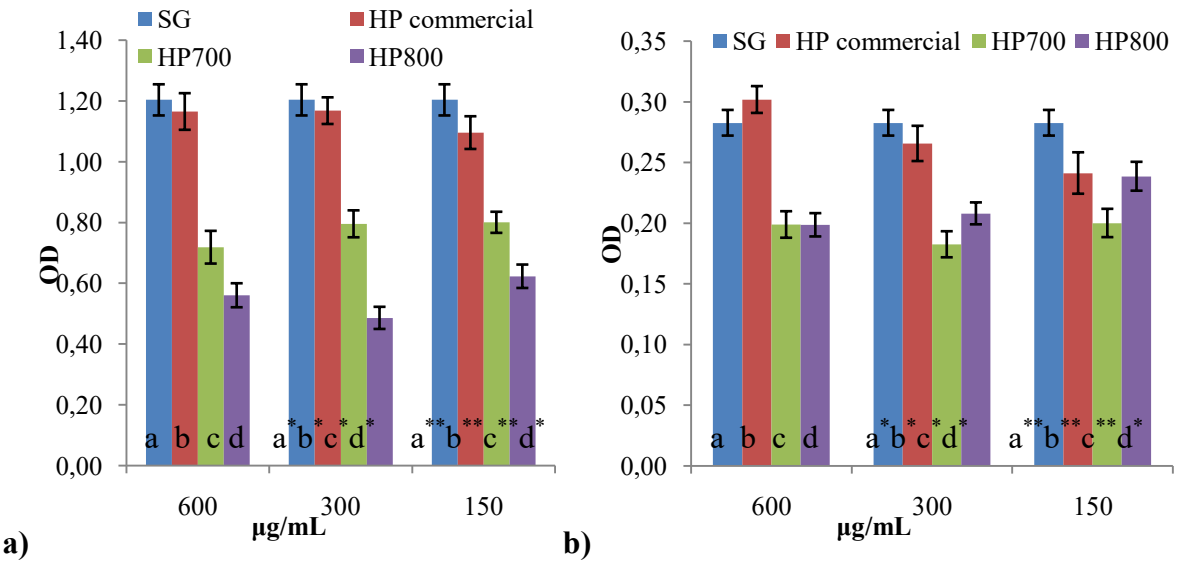

Figure A 5 *Tenocytes (a) and SAOS-2 (b) viability test (MTT test) performed after 24 hours of culture. HP commercial,HP800 and HP700were suspended in the complete growth medium (at 600-300-150 µg/mL) and were added 4 hours later the cell seeding (mean value n=8; ±e.s.). In figure* ***1.a*** *not significant differences were recorded for a vs b; c vs d; a^{*} vs b^{*}; a^{**} vs b^{**}. In figure* ***1.b*** *not significant differences were recorded for a vs b, c vs d; a^{*} vs b^{*}; c^{*} vs d;* b^{**} vs c^{**}; b^{**} vs d^{**} c^{**} vs d^{**})*

3. CONCLUSIONS

It was possible synthesised pure hydroxyapatite with two particle sizes. Both the particle size and crystal shape proved to have a crucial role in the cellular interaction. HP having smaller particles size, rounded and smooth particles, determined higher viability towards both tenocytes and SAOS-2 cells.

REFERENCE OF ANNEX A

1. Bezzi G., Celotti G,. Landi E,. La Torretta T.M.G,.Sopyan I,. Tampieri A ., A novel sol–gel technique for hydroxyapatite preparation, Materials Chemistry and Physics . 78 (2003) 816–824
2. Jay A.H. & Andrews K.W., Constitution of some Binary Oxide System, Nature, 154 (1944).11
3. Mostafa N.Y & Brown P.W., Computer simulation of stoichiometric hydroxyapatite: Structure and substitutions, Journal of Physics and Chemistry of Solids 68 (2007) 431-437

CHAPTER 5

Electrospun biphasic tubular scaffold with topographical and compositional gradient, for *enthesis* regeneration

Abstract

The tendon-to-bone interface (TBI) is an extremely specific region named enthesis, made ofahybrid connection of fibrocartilage with bone minerals. The direct enthesis is commonly subjectedto full laceration, due to the stiffness gradient between the soft tissue of the tendon and the hard tissue of the bone. Due to its peculiar structure enthesis is complicated to be surgically reconstructed.

For mimicking the mineralized fibrocartilage at TBI site, a tubular scaffold based on Pullulan (PU)/Chitosan(CH) polymers was designed with a topographical gradient of electrospun nanofiber and hydroxyapatite (HP) along the tubular length. The tubular shape of the scaffold wasdesigned to be extemporaneously loaded with functional bio-molecules, and in particularchondroitinsulfate (CS), before the surgery, to enhance wound healing. The end-zone of the scaffold, to be anchored to the bone,was based on electrospun hybrid nanofibers, randomly collected and loaded with hydroxyapatite, while the part to be anchored to the tendon, was made ofelectrospunaligned nanofibers, without inorganic component.

The scaffold was characterized by a continuous gradient in HP, without interruptions as observed by micro CT analysis. The random part of the scaffold was characterized by low porosity, that increased gradually along scaffold length, up to the aligned part of the scaffold. The gradient of nanofiber arrangement was observed by SEM, and this was preserved upon hydration.

In vitro studies demonstrated that human adipose stem cell (hASCs) grown onto both scaffold ends, expressed the typical ECM of tendon or bone tissue.

3% w/w of CS solution was loaded in the scaffold, and CS proved synergistic effect with scaffold morphology and topography, towardsthe adhesion/proliferation on the scaffold surface. These results suggestthatthe tubular scaffold loaded with CS and populated with hASCs, should represent a powerfulsystemfor the tendon laceration surgery at enthesis site.

1. INTRODUCTION

The enthesis is an elevated specific region localized in the tendon-to-bone interface (TBI). In this type of hybrid tissue, the fibrocartilage derived from the tendon part, is gradually reinforced with hydroxyapatite, and becomes gradually harder until the transition in bone tissue.

In anatomical sites more subjected to recurring loading forces (for example Cruciate ligament, Rotator cuff and Achilles tendon), the enthesis tissue is directly connected with the bone, which presents discontinuous periosteoum at the fixation site. The direct enthesis possesses 4 gradient zones: 1) the tendon zone, characterized by aligned fibers and type I collagen;2) the fibrocartilage zone (made of type II and IIIcollagen);3) the mineralized fibrocartilage (type II collagen and hydroxyapatite in gradient) and 4) lastly the bone (type I collagen and minerals). The TBI between fibrocartilaginous and mineralized fibrocartilaginous tissues, creates the stiffness gradient throughout the soft tendon and the hard bone, during joint movement. This connection is poorly vascularised and often subjected to mechanical stress, causing frequently issue due to scratch or complete laceration.

In the orthopaedic treatment the native tendon, surgically inserted in the bone, is not able to recreate the native direct enthesis, but forms scar tissue covering the periostium surface with inferior biomechanical properties (Morais et al 2015).The tissue engineering research, is going to answers to this specific issue, following two approaches: the biological one, based on stem cell therapy, growth factors and magnetic stimulation, which are locally injected into the injury site, or the second one based on bio-mimetic scaffolds linking the tendon-to-bone gap, by supporting the mechanical loading at the implanted site (Morais et al 2015).

However, in the first approach, the direct injection of biological modulators at injured site is limited by their high solubility and instability, also aggravated by the inflammatory scenario. Therefore, they need to be loaded in suitable delivery system. While in the second approach, the scaffold alone could not be enough effective for controlling all the healing phases.

Given this premises the aim of this study was the development of a biphasic tubular scaffold to be in plant at TBI site. The tubular shape of the scaffold was designed to obtain

double functions: the loading biological modulators, and in particular human-adipose stem cells (hASCs), as supporter for native cell growth.

The tubular scaffold was manufactured by means of electrospinning to obtain a topographical and mineral gradient in order to mimic the structure of the enthesis. The end zone of the scaffold, to be anchored to the bone, was based on electrospun hybrid nanofibers randomly collected and loaded with hydroxyapatite(R-HP), while the part to be anchored to the torn tendon, was made of electrospun aligned nanofibers without inorganic component(A-B).

Finally, Chondroitin Sulfate was selected as a biomimetic component to enhance wound healing. hASCs were seeded in the scaffolds to act as biological modulator and enhance tissue reparation. Osteogenic and tenogenic properties of the scaffold were also evaluated. In literature the hASCs stem cells (ASCs) therapy is amply used for clinical regenerative applications, since they are reported to release growth factors and cytokines, and to promote neo-vascularization in vivo (Kosaraju R et al 2016; Costa-Almeida R et al 2019).

hASCs are referred as able to modulate the tendon microenvironment in co-culture experiments, by increasing metalloproteinase activity, and promoting type III collagen deposition(Costa-Almeida R et al 2019). Other studied confirmed in vivo bone regeneration potential of hASCs. Several hASCs subcutaneous implants in vivo caused abundant osteo-calcin deposition, osteoclast proliferation and blood vessel infiltration.

Among many materials used as carriers for in vivo transplant, pullulan was successfully employed as hydrogel for loading living ASCs (Kosaraju R et al 2016) in skin wounds and chitosan/chondroitin sulfate lyophilized scaffold, enriched with hydroxyapatite, was employed as biomimetic component for releasing living hASCs in bone, resulting in new bone formation (Zubillaga V et al 2018; Fan et al 2014).

The biphasic tubular scaffold made of pullulan/chitosan nanofibers and mineralized with HP, should be a promising tool for supporting the specific reparation of the enthesis. Thanks to stem cell adhered and proliferated in the biphasic tubular scaffold, this should restore TBI, replacing a full functionality of the native tissue.

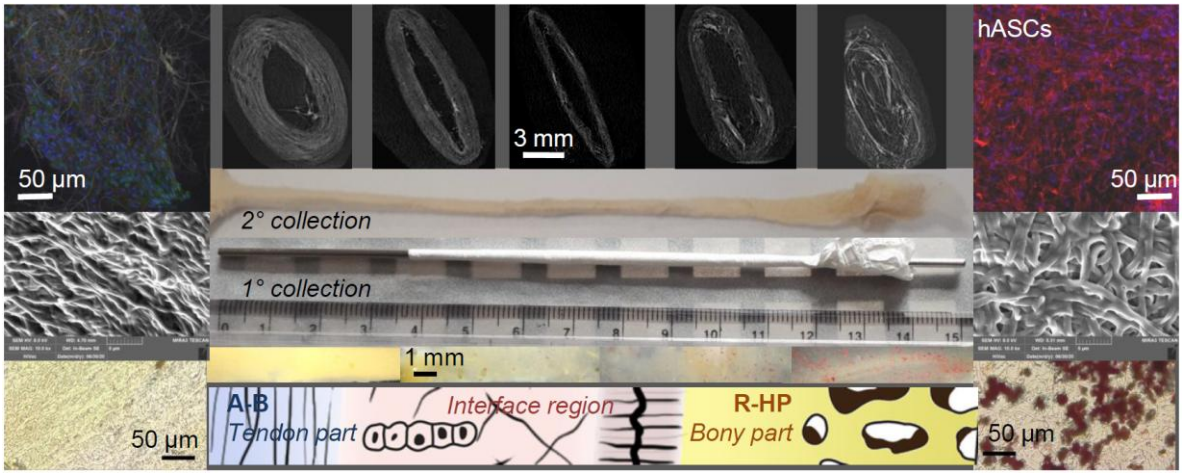

***Graphical Abstract**: schematic representation of the electrospun hybrid scaffold developed.*

2. MATERIALS AND METHODS

2.1. Materials:

Chitosan (CH), deacetylation degree 98%, MW 251000 Da, (ChitoClear, Siiglufjordur-Iceland); Pullulan (PL), Food grade (Hayashibara, Okayama-Japan);Chondroitin sodium sulfate (CS) (β-1,4-linked D-glucuronic acid and β-1,3-linked N-acetyl galactosamine) bovine 100 EP, low MW 14 kDa, and a mixture of chondroitin A (chondroitin 4 sulfate) and chondroitin C (chondroitin 6 sulfate) (Bioiberica, Italy); Citric acid (CA) (Carlo Erba Reagents, Italy); Hydroxyapatite (HP), nanopowder ≥ 97% synthetic (Sigma-Aldrich, USA); Solvent: Acetic acid (AA) (Carlo Erba Reagents, Italy).

2.2. Methods:

2.2.1. Preparation of the polymeric blend and characterizations

The polymeric blend was based on CH citrate and PL polymers. Lastly 0.1 %HP was added in the final blend 1 h before electrospinnig. HP and polymers mixture was prepared with the same method mentioned in Chapter 4, paragraph 2.2 (Sandri et 2019). R-HP part of the scaffold was prepared by collecting the HP loaded polymer nanofibers and this was the bone part of the scaffold, while A-B part was prepared by collecting polymer nanofibers without HP and this was the tendon part.

2.2.2. Electrospinning of the bi-phasic scaffold

Scaffold was obtained using an electrospinning apparatus (STKIT-40, Linari Engineering, I), equipped with a high-voltage power supply (Razel R99-E 40, kV)(20-22 kV voltage), a 10 cc syringe with inox 21G needle (0.7-0.8x20 mm spinneret size), and a volumetric pump (Razel R99-E),(0.397 cc/h flux),and a rotating drum(3mm diameter x 15cm), set at 15 cm needle tip to collector distance. The process was carried out for 1 h at atmospheric pressure, at 25-35°C temperature range, and at 25-35% relative humidity.

R-HP nanofibers, the bone part of the scaffold, were randomly collected in a tubular shape, using a cylindrical rotating drum in inox steel, under slow clockwise rotation at 2000 rpm (Easy Drum) for 1 h..A-B nanofibers, the tendon part of the scaffold, were collected using a 3000 rpm clockwise rotation of the drum around the axis, and a simultaneous longitudinal movement of the collector at 60 rpm constant speed, in order to have vertically oriented nanofibers along the scaffold length (aligned part). The two ends(A-B and R-HP) were collected layer by layer, for obtaining a unique and continuous tubular scaffold.

Finally, the unique tubular scaffold obtained with biphasic ends, was crosslinked by dry heating at 150°C for 1 h(as reported in Sandri et al 2019). The heating process was considered able to sterilize the scaffold (Kupiec et al., 2000).

2.2.3. HP gradient evaluation by Alizarin Red test

Alizarin red solution (Merk, Germany) was diluted in deionised water at 2% w/v and the pH adjusted at 4.1 with 10% w/w ammonium hydroxide. The scaffold was cut in 3 segments of 4 cm in length along the scaffold. Two samples were cut in the A-B and R-HP ends for having tendon and bone part, respectively. They were washed with deionised water before staining. The Alizarin red solution was added to cover all the scaffold pieces and left 5 -10 min up to the complete reaction visible at microscope. The calcium deposits in orange-red colour, were evident after washing with deionised water. The images were recorded using a stereo-microscope (Stereo Microscope+Lamp, Schott KL200) (low magnification) or direct microscope (Leica Microsystem MS, 4fach Obj. rev.) (high magnification).

2.2.4. Biphasic scaffold morphology after hydration by SEM analysis

The bi-phasic tubular scaffold was immersed in PBS for 6 days. Then it was treated for 5 min with ethanol gradient from 50:50 (etanol:water) to 100 %. Ethanol. It was cut at three zones: the R-HP, the A-B and the interface region, to obtained a sample length of 1 cm, suitable for the SEM analysis. The sample morphology was analysed by means of SEM (Tescan, Mira3XMU, platinum sputtering).

2.2.5. Scaffold characterization by Micro CT analysis

In order to evaluate the scaffold 3Dmicrostructure, 5 cm tubular scaffold was analysed by X-rays micro-computed tomography (micro-CT), using a high-resolution X-ray microtomography system: Skyscan 1 scanner (Skyscan 1272; Bruker, Billerica, MA, USA). The acquisition of X-ray images, was performed with a pixel size of 10 μm, a rotation step of 0.4° over 360°, and a smoothing averaging of every three images. The X-ray source was fixed at 50 keV and 200 μA, of voltage and current, respectively. After the acquisition, the grey-scale images were reconstructed, using the NRecon software (version 1.7.1.0, Bruker, Billerica, MA, USA). Moreover, the tubular scaffold was vertically aligned for the longitudinal analysis of the scaffold thickness, using the DataViewer software (version 1.5.3.6, Bruker, Billerica, MA, USA). Qualitative visualization of the 3D morphology, and the different phases of polymeric matrix and hydroxyapatite was performed, using CT-Vox software (version 3.3.0, Bruker, Billerica, MA,USA). Finally, the quantitative analysis was evaluated after converting the regions of interest into binary images, usinga dynamic threshold (30–255—polymeric phase; 80–255 ceramic phase). The binary images were used for morphometric examination (CT Analyzer v1.12.0.0, SkyScan, Kontich, Belgium) of porosity amount and their interconnectivity (Calejo et al 2019).

2.2.6. Human-adipose derived cells

Human-adipose derived cells (hASCs) were provided by Hospital da Prelada (Porto, Portugal) under established protocols (Calejo et al 2019) and were used at passage 1, to evaluate the biological performance of the scaffold. The hASCs were cultured in sterilized (with 0,22 μm pore size) basal α-MEM medium supplemented with 10% FBS (Fetal bovine serum), 0,22% Bicarbonate, 1% Antibiotic/Antifungal. Before the seeding, the scaffold portions were placed in wells in a 96-well plate and sterilized under UV irradiation for 10 min. Then they were immersed in 1% antibiotic D-PBS solution. The

scaffolds were left overnight in full medium, then the medium was removed, and the samples washed again. The tubular scaffolds were cut at both the A-B and R-HP extremities to have 2 cm^2 area portions(5 mm diameter) with 0.2 - 0.4 mm thickness.
The hASCs were seeded onto the scaffold surfaces ($4*10^5$/well seeding density) in a 48 well plate. 100µL cell suspension in basal α-MEM, was carefully dropped onto each scaffold and left in incubator (37 °C, 5% CO_2) for 30 min. Therefore, the culture basal α-MEM medium without additional supplementation, was added up to 0.2 mL. hASCs were grown onto the scaffolds until 14 days before staining their extracellular matrix.

2.2.7. Determination of cytotoxicity:

The scaffolds were left for 10min under UV irradiation and washed with 1% antibiotic D-PBS solution two folds.The scaffolds were left in supplemented α-MEMmedium for 2 days. Separately in another 48 well plate, hASCs were seeded at $65*10^3$/well/cells density, and grown for 24 hours. The supernatant medium derived from the 2 days scaffold incubation, was collected and put in contact with the cells for 3 days. The cytotoxicity was evaluated by performing Alamar Blue assay after 3 days of contact between cells and supernatant medium. Cell morphology was investigated at the fixed time (inverted microscope Axio Vert.A1, Zeiss). The cell grown in standard conditions(SG) with DMEM without the addition of supernatant was considered as positive control. The cells grown in presence of DMSO 10% v/v were cultured as negative control.

2.2.8. Immuno-staining

After prefixed time the samples were washed with D-PBS. Then the samples with the cells were fixed with 10%v/v of Neutral Buffered formalin (Bio-optical Milano, Italy) and left overnight at 4°C.Phosphate buffered saline solution (PBS) was prepared by dissolving phosphate saline tablet (2 tablets Sigma, Aldrich) in 400mL of milli-Q water. Separately 0,25% (v/v) of Triton X-100 (Alfa Aesar) was diluted in PBS solution. Separately 1% (w/v) of bovine serum albumin (BSA) (Sigma Aldrich) was diluted in PBS. Both the mixtures were hydrated for 3 hours. Finally, cells were stained using anti-scleraxin (SCXA, Abcam, Portugal) antibody(1:100 in 1% BSA solution) and secondary antibody (Alexa Fluor 488, donkey anti-rabbit IgG, Invitrogen, Thermofisher) (1:1000 dilution in 1%, green staining). The cytoskeleton and the nuclei were stained using phalloidin

fluorescein isothiocyanate(Sigma Aldrich) (1:200 in PBS, red staining) and DAPI (1:1000 in PBS, blue staining) (Biotium, Portugal), respectively.

The scaffold previously fixed, was washed with PBS for 3 h to remove any residual formalin. Then the scaffolds were treated with Triton X-100 solution for 10 min, 1% BSA solution for 20 min, scleraxin (SCXA) antibody mixture overnight at 4°C, the secondary antibody mixture for 1h at room temperature. Finally, the Phalloidin and DAPI mixtures, was added together for 20 min at room temperature. Between every passage, the samples were washed two folds with PBS for 5 min, and protected by the light. The samples were analysed by confocal laser scanning microscopy (Leica TCS SP8, Microsystems, Wetzlar, Germany).

2.2.9. hASCs culture in presence of Chondroitin sulfate

Scaffolds A-B and R-HP were cut, in order to have a 2 cm^2 area(5 mm diameter, 0,2 mm thickness). These were placed onto an insert in a well in a 96 trans-well-plate (96 wells plate Corning Transwell Cell Culture Plate, Merck, Sigma Aldrich, 4,26 mm well diameter and 3 μm pore size). hASCs cells were seeded on scaffolds at 8•104 cells/$cm^2$by dropping 70μlcell suspension, above each scaffold. In the case of sample without scaffold, the cells were dropped directly on the insert. In the lower chamber, 200 μl of 3%CS in α-MEM(after sterilized by filtration using 0,22 μm pore)was placed.

After 3, 6 and 14 days, Alamar Blue (AlamarBlue HS cell viability reagent, Invitrogen, Thermo Fisher, US) was performed to evaluate the metabolic activity (viability) of the cells (chapter 2.2.11).

2.2.10. Determination of cell Metabolic Activity by Alamar Blue Assay:

After 3, 7, and 14 days in culture in transwell system AlamarBlue test (AlamarBlue HS cell viability reagent, Invitrogen, Thermo Fisher, US) was performed to evaluate the metabolic activity (viability) of the cells.

10% (v/v) Alamar Blue was diluted in the respective media and added in both the apical (70 μl) and basolateral (200 μl) chambers of each well. After 3h incubation in dark at 37°C, the Alamar Blue solution was collected from both the chamber and transferred in new flat wells. Each trans-well was refilled with the specific medium and left in culture again.

The Alamar Blue fluorescence was recorded using a microplate reader (Microplate Reader Biotek, Synergy/HT) at 530 nm excitation wavelength, and 590 nm emission wavelength. Triplicate measurements were performed for each sample.
In each experiment the positive control was considered as cell viability in standard condition (SG).

2.2.11. Statistical analysis

Statistical analysis was performed using post-hoc Tukey HSD Test Calculator. One-way ANOVA followed by Scheffé, Bonferroni and Holm method, was considered. For the comparison of two groups, statistical significance was determined by using a two-tailed Student's t-test method. A p-value ≤ 0.05 was considered statistically significant.

3. RESULTS AND DISCUSSION

3.1. Electrospun hybrid scaffold characterization

Figure 1 reports the images of the bi-phasic tubular scaffold stained using Alizarin Red, in order to evaluate the mineral gradient along the scaffold. The treatment left red-brown residual particles in the R-HP end, the randomly collected scaffolds, to be implanted in the bone, suggesting the presence of HP particles, while the A-B end did not show any particles. This proves the HP gradient along the scaffold: HP particles gradually decreased along scaffold length up to their disappearance.
Figure 2reports SEM images of the biphasic tubular scaffold after hydration. The nanofibers appeared swelled, with topographical gradient from aligned (A-B) to random structure (R-HP), passing through an interfacial region with minor alignment.

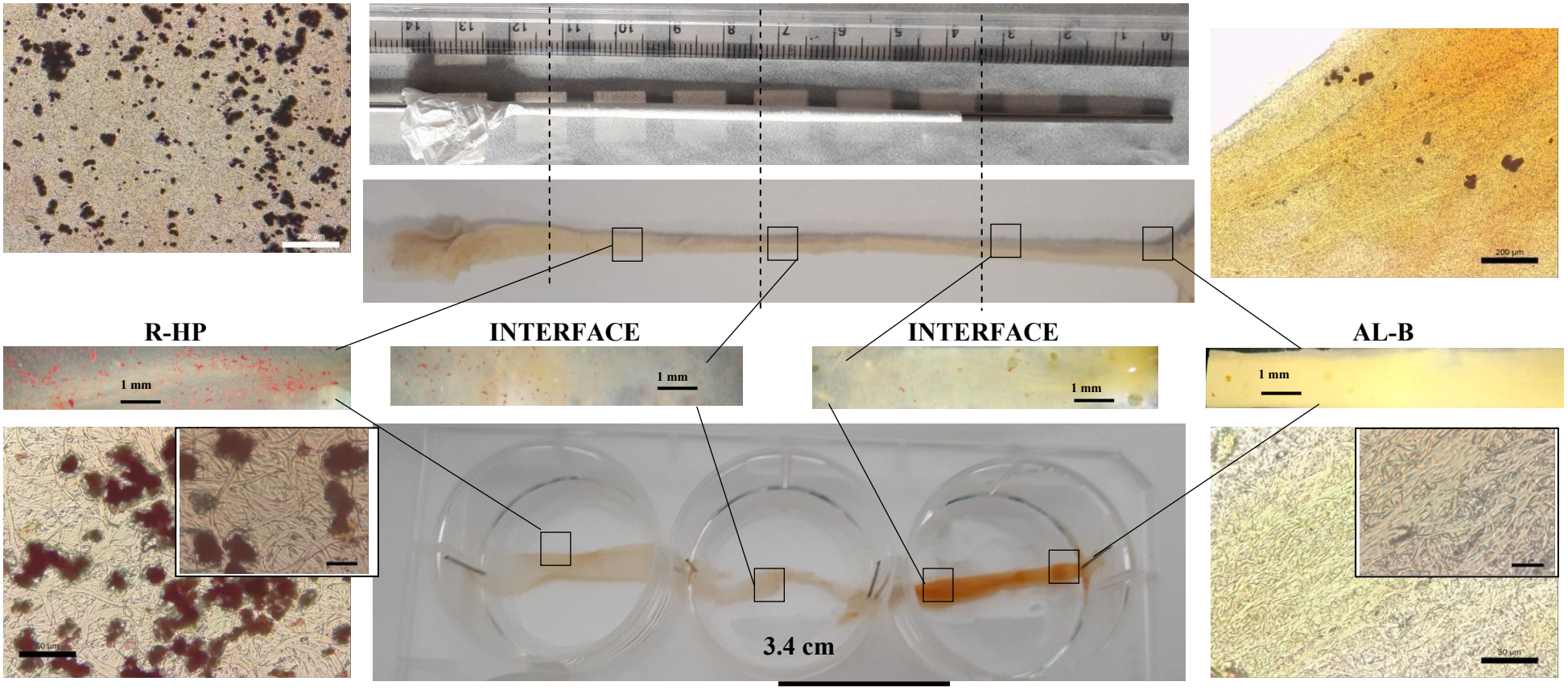

Figure 1. *Optical images of Alizarin Red staining along the tubular scaffold collected with the tendon zone (without hydroxyapatite, A-B) and bony zone (with 0.1% hydroxyapatite R-HP).*

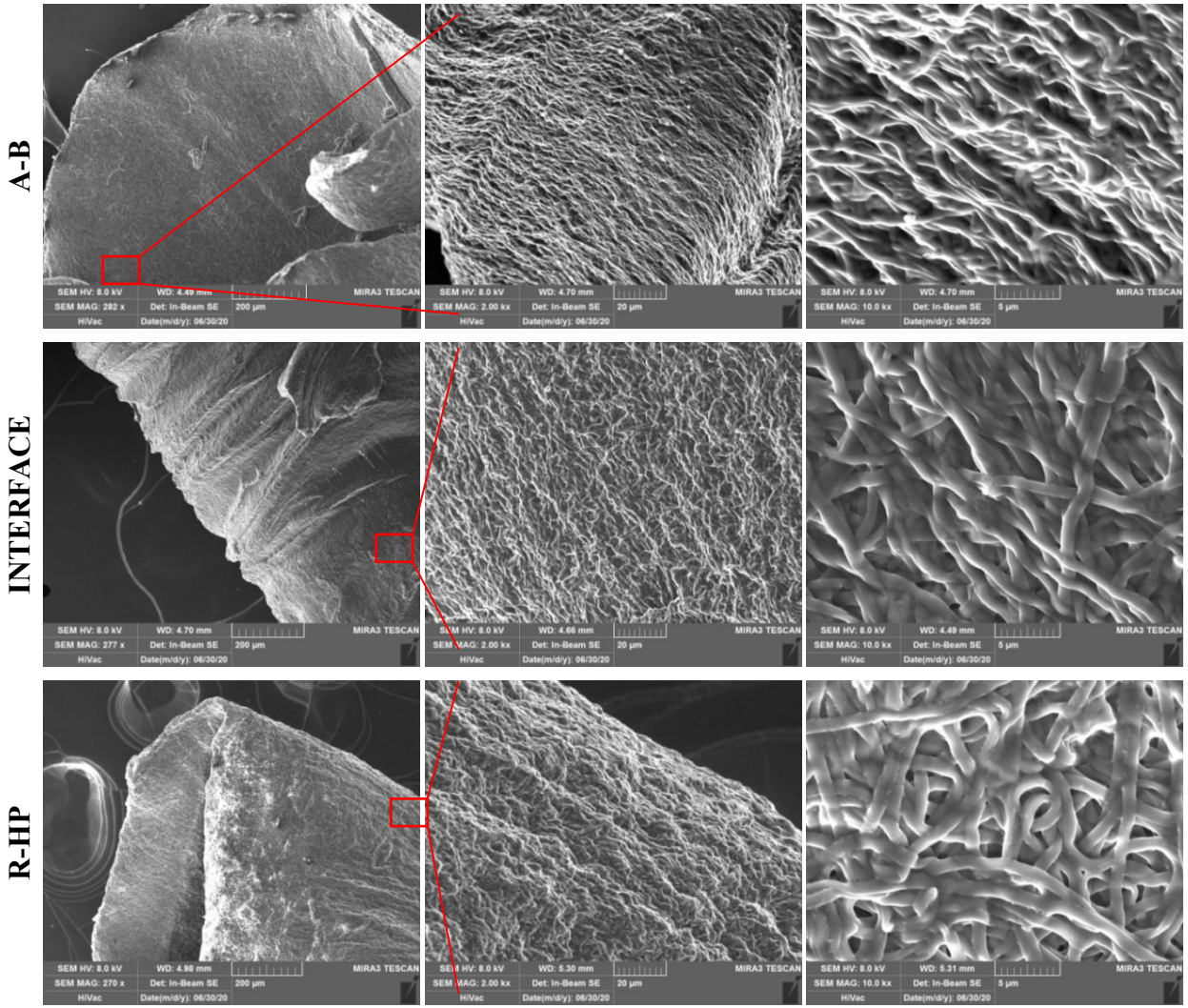

Figure 2 *SEM images of the biphasic tubular scaffold after hydration in PBS for 6 days. The tendon A-B and bony R-HP zones were captured at three magnifications*

The microCT analysis (Figure 3 and 4) confirmed the biphasic scaffold structure without interruptions. This was also visible in the 3D reconstruction (Figure 4a).The X-ray images of the longitudinal section of the scaffold, revealed the gradient of the mineral phase. The HP included in the fiber, gave a denser signal at 2D and 3D microCT images, while the fibrous polymeric phase was visible in the inter-spaces between the fibers, which highlighting their arrangement in the entire thickness of the scaffold (Figure 3 and 4a).

The length of the tubular scaffold analysedwas5 cm, however shorter or longer scaffold could be developed as a function of the tendon size.

The 2D microCT images reported in figure 3, shows the cross section of the scaffold at 5 stop-points, along the tubular length. Two of these sections are the R-HP (at 450 μm) and A-B (at 44˙000 μm) ends, corresponding to the randomly collected scaffold (R-HP) and the aligned one (B-A), respectively. Between them, it was possible distinguished the interface region (from 14˙070 μm to 28˙820 μm) which was characterised by two types of arrangements. The interface region closer to the R-HP end (14˙070 μm), was characterized by fully mineralized nanofibers, having a more orderly direction. The interface region closer to the A-B end (28˙820 μm) was characterized by very low mineralised nanofibers fully aligned (Figure 3).

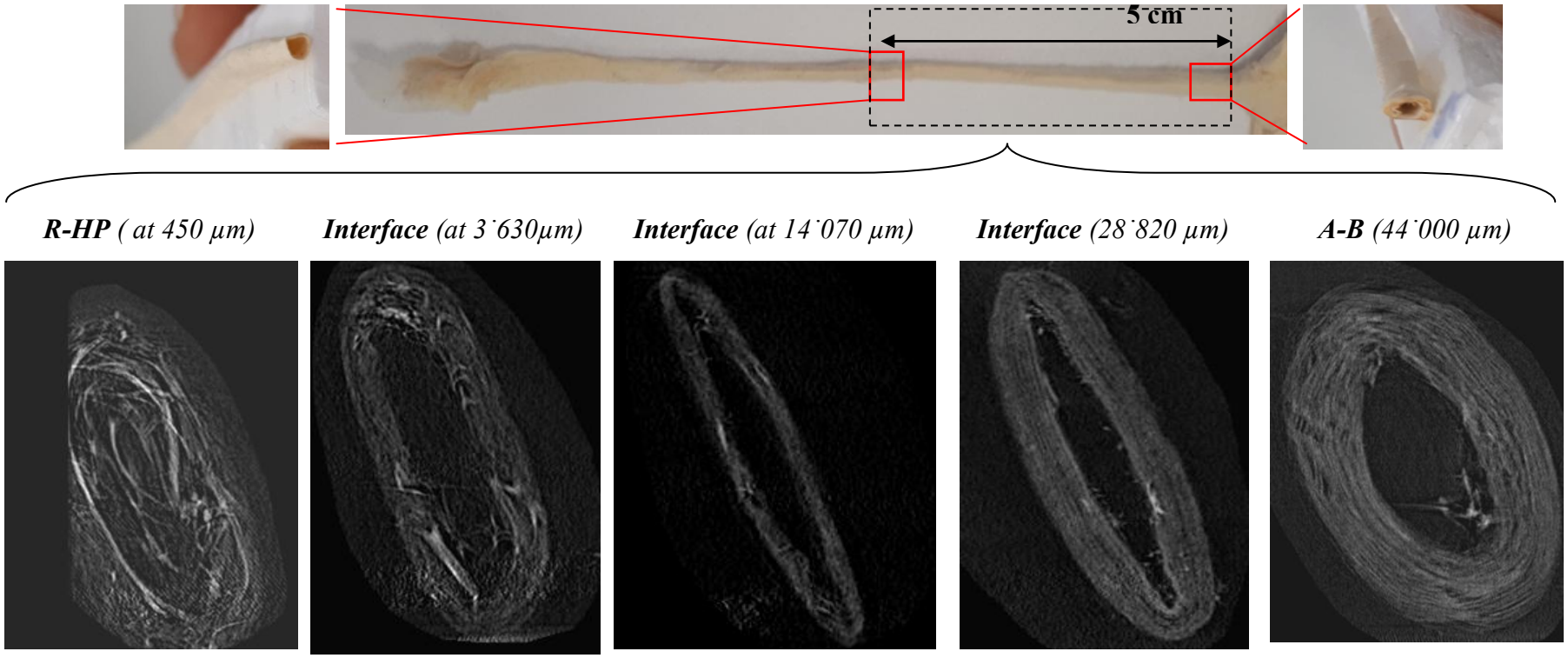

Figure 3. *Micro CT images of the cross sections acquired along the length of tubular scaffold from the bony (B-HP) to the tendon part (A-B) throughout the interface area*

The quantitative analysis of the scaffold composition was further performed. In Figure 4b, the topographical gradient along the scaffold section, was quantified in terms of % porosity and inter-fiber thickness. The line blue in the graph (Figure 4b),was the increase of porosity (%), by increasing the nanofiber alignment. The scaffold porosity was the minimum in the R-HP region, in the interface region the porosity profile has an oscillating trend, probably due to the coexisting of ordered and not ordered fibers, with few HP particles trapped in the fibrous matrix. Finally, the porosity strongly increased at the A-B end, due to the nanofiber alignment.

On the contrary, the inter-fiber thickness gradually decreased from the R-HP to the A-B end. This value indicates that the thickness occupied by each fiber, was higher when they were randomly oriented, and lower when they were aligned (Figure 4b).

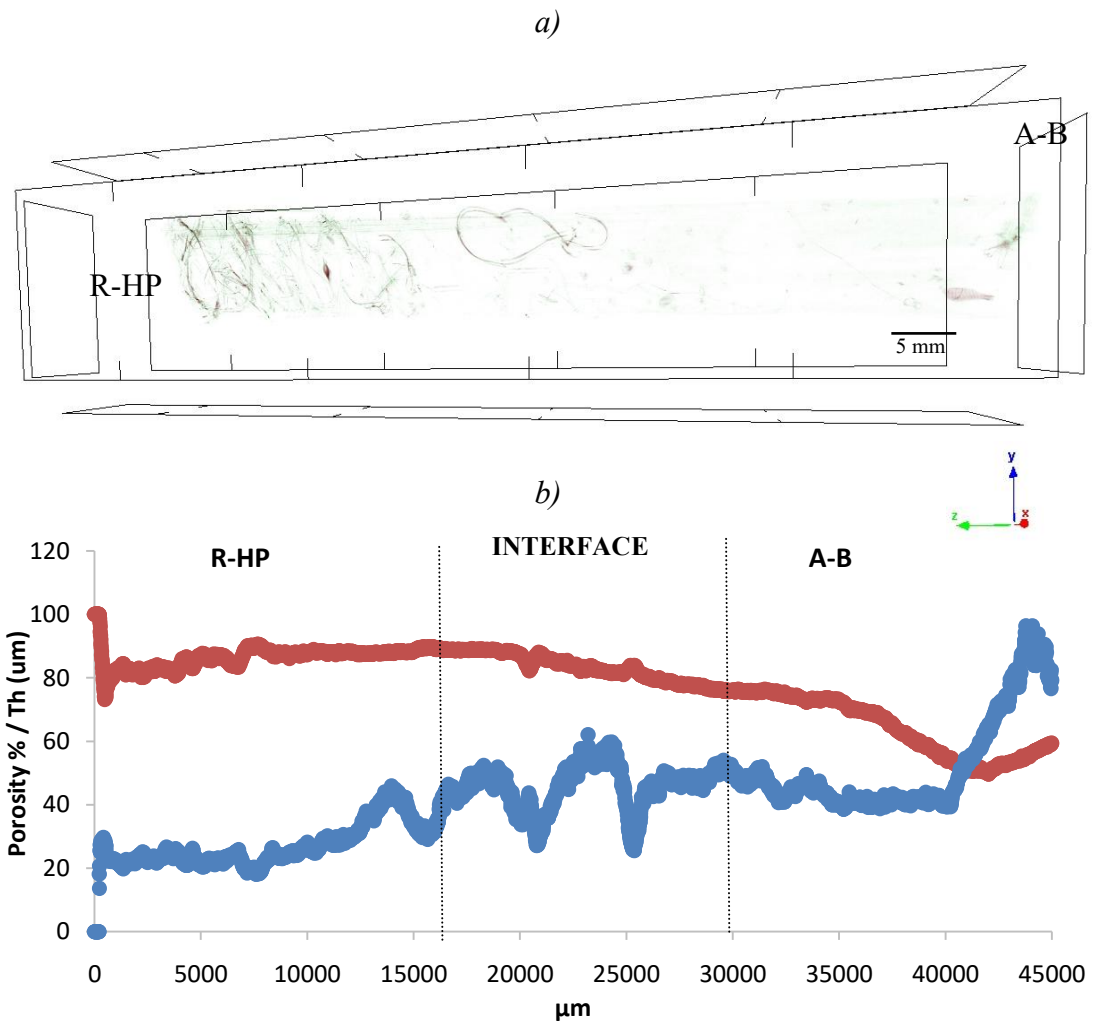

***Figure 4**. (a) Micro CT 3D image of the whole scaffold and (b) porosity/thickness values of tubular scaffold measured along the length from the bony (B-HP) to the tendon part (A-B)*

3.2. Biological evaluation

Preliminarily the cytotoxicity of the scaffold components was performed towards hASCs.

In Figure 5 the metabolic activity of hASCs cells is reported. Scaffold extract was highly biocompatible and determined higher cell viability, with respect to standard growth conditions, suggesting that the metabolic activity of stem cells was stimulated by the components of the extract.

What was the major component in the scaffold extract affecting the stem cell viability still remains unclear, few studies were reported about the chitosan and pullulan properties to enhance the hASCs proliferation and differentiation after implantation (Zubillaga V et al 2018; Kosaraju R et al 2016).

HP nanoparticles were recognized as a material effective to promote hASCs differentiation and proliferation in the early days of culture (Pulyala P et al 2017). In fact, the R-HP extract, which was enriched with hydroxyapatite, showed the highest value of hASCs viability. One hypothesis could be that the mineral content or the polysaccharides residual chains in the culture medium, were enough for activating the early phase of stem cell differentiation, and that this phenomenon could be associated with an increase of cell metabolic activity (Figure 5).

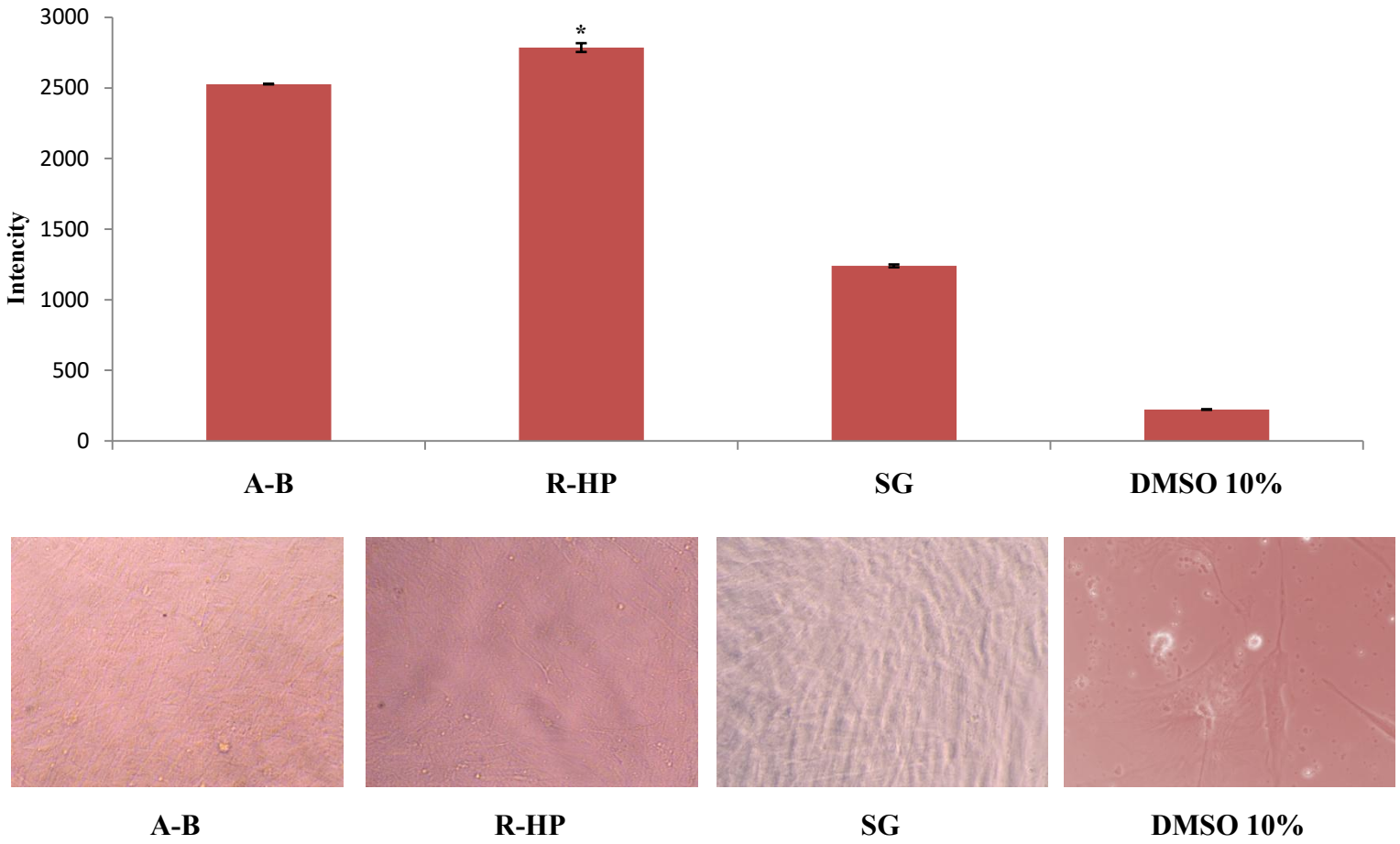

Figure 5. *Optical microscope images of human adipose stem cells (hASCs) growth after 3 days in presence of the supernatant derived from the scaffold (submerged in basic DMEM medium 48 hours). Metabolic activity was measured by Alamar Blue assay (graph) after 3 days of contact with the supernatant of the scaffold, the basic DMEM (SG) and 10% DMSO (negative control).The differences were statistically significant between every samples.*

In order to evaluate the osteogenic effect of the mineralized scaffold (R-HP), towards hASCs, the extracellular calcium production was evaluated by Alizarin Red staining (Figure 6). As reported in literature, the mineral deposition is the in vitro model of a possible bone production in vivo, by living osteoblasts. Recent studies clarified the synthesis reaction of hydroxyapatite (HP) formed by osteoblasts in vivo, here reported (Eq1).

$$6HPO_4^{-2} + 2H_2O + 10\ Ca^{+2} \leftrightarrow Ca_{10}(PO_4)_6(OH)_2 + 8H^+$$

(Eq 1; Blair et al 2017)

The equilibrium of HP synthesis involves phosphates and calcium ions, water and acid protons. In vivo the crucial mechanisms which lead to the bone formation, involve the chloride-hydrogen channels (ClCs) activity, at the apical membrane of osteoblasts. The ClCs channels uptake the H+ protons, and transfer acids in the basolateral membranes. This ionic equilibrium supports the complete conversion of phosphate and calcium, to hydroxyapatite crystals. This context suggests that the complete osteogenic differentiation of the stem cell in vitro, could reflect in part the transport processes in the osteoblasts, leading to the in vivo mineralization.

In literature it was widely proved as the calcium phosphate ceramics, added in stem cell culture, had bone-inducing effect. These bio-mimetic materials lead to the formation of fully differentiate cells, ready for the in vivo transplant resulting in a full bone grafts (Wang et al 2014).

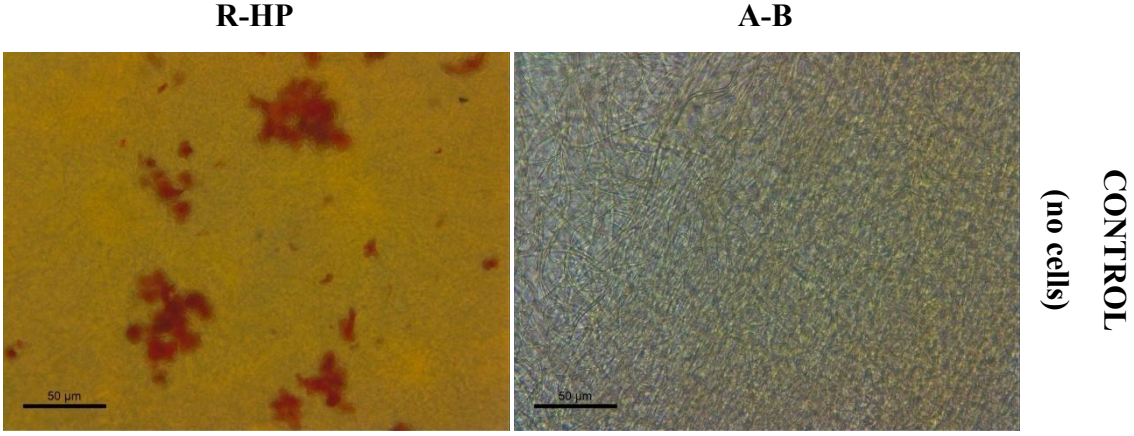

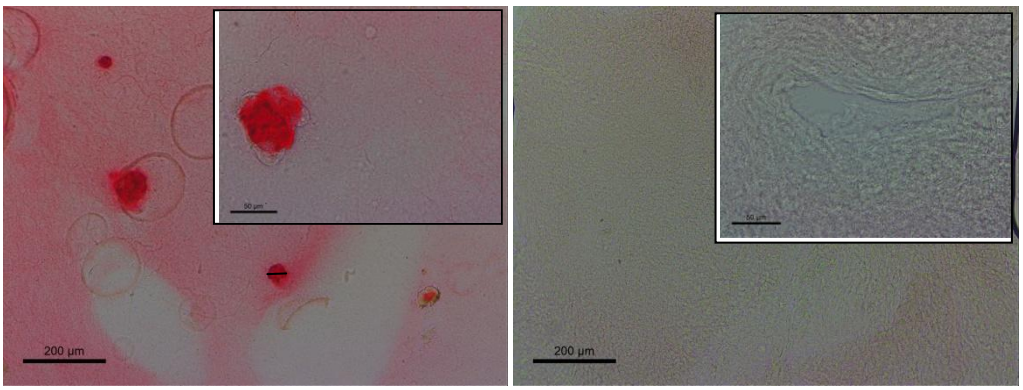

Figure 6. *Alizarin Red staining for the mineralized matrix produced by hASCs after 14 days growing onto the scaffold A-B and R-HP. Scaffolds without cells was stained with the same protocol*

In the optical images acquired (Figure 6) the red stained calcium deposition was visible, as a dense clot. The HP particle loaded in the scaffold formula, were even stained as control. The HP particles used for the scaffold formulation, without cell, exhibited spherical shape between 2- 10 µm size. While the HP deposition after cell incubation, showed clot with 30-50 µm size, suggesting the formation of bigger and denser agglomerates after 14 days of culture, without any osteogenic-inductive medium supplementation. It could be assumed that the HP particles were enlarged by the further HP nucleation, and eventually by the clotting effect produced by protein deposition. However the quantitative evaluation for the red intensity, should be analysed for better understanding the significant difference between the substrate and the control. It is interesting to note that any mineral deposition was observed in the cell substrate covering the A-B scaffold. (Figure 6).

The hASCs cultured for 14 day on R-HP and A-B scaffold were studied at CLSM analysis, for their morphology and capability to produce tendon like extracellular matrix. (Figure 7). The most relevant proteins related to tendon and generally stained for the in vitro evaluation are: collagen, tenascin, decorin, tenomodulin, versican, scleraxis. They were studied by several authors for understanding the tendon health, development and functionality. Scleraxis (SCXA) isfound in the early stage of the progenitor cell differentiation in tendon, and this is employed by embryonic development for forming tendon and blood vessels. It remains also highly expressed in all the adult connective tissue, and is thought to play a role in the tendon-to-bone attachment. (Schweitzer et al 2001; Killian et al 2016).The gene expression of SCXA seemed to be down-regulated by bone morphogenic proteins (BMPs) in the embryonic growth.

Given the essential role of SCXA in tendon differentiation and in the development of enthesis tissue, the SCXA produced by hASCs cultured without any supplements, onto the scaffold, was evaluated. The CLSM images in Figure 7 suggest a partial anisotropic behaviour of the hASCs. The actin, stained in red, showed a random organisation of the cell cytoskeletons, also highlighted by nuclei enlarged and orderly orientated (stained in blue). The green signal was not present in the substrate R-HP, indicating no production of SCXA protein from the cells.

On the A-B scaffold, the hASCs grew aligned, as it is evident from the nuclei elongation and alignment. The SCXA proteins marked in green, were synthesized by the stem cells only for direct contact with the scaffold surface. The SCXA proteins were localized especially in the cell cytosol, probably due to the early stage of differentiation, which arrives at fully expression at least after 21 days. These preliminarily results suggested that A-B scaffold provided the suitable environment for a new tendon promotion, while the opposite R-HP extremity caused a mineralized bone–like matrix. Further studies will be assessed for considering PCR analysis to fully evaluate the gene expression of the cells in both the ends.

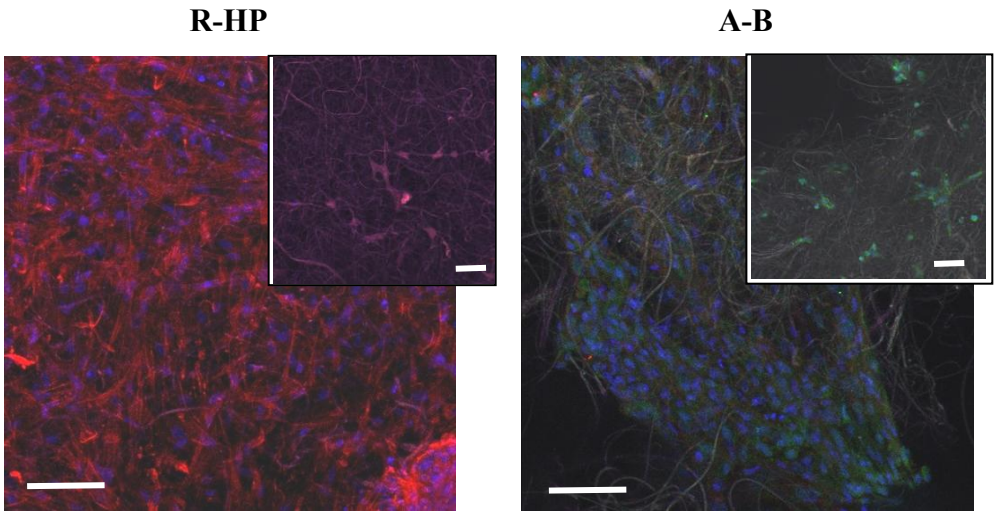

Table 7. *SCXA(scleraxin) immune-staining (green) performed on hASCs cells grown for 7 days onto R-HP and A-B scaffolds. Actin stained in red and nucleus in blue (magnification 50 µm)*

Finally the metabolic activity was performed, after 3 to 14 days by the hASCs grown onto the scaffold surfaces (Figure 8 a-b). The high Alalmar Blue intensity indicated high metabolic activity related to cell viability.

In this preliminarily evaluation, it was not possible to assess the effect of chondroitin sulfate on the stem cell differentiation. At this stage it was interesting to evaluate if CS addition could affect stem cell proliferation, when growing in adhesion to the scaffold.

The results show that the stem cells grown onto the scaffold surface, showed increasing viability up to the 6th day. Prolonged time caused a significant decrease of their viability. Moreover, when the cells were grown onto the transwell membrane in SG condition, their viability showed decreasing trend, with significantly lower value after 6 days (Figure 8a). The outcome confirmed the supporting capacity of both the scaffold for stem cell proliferation, however their gradual decreasing growth, could suggest the need of a3D substrate, for enhancing a further cell differentiation and proliferation.

In the second panel, in Figure 8b, the stem cells viability in presence of CS supplemented medium, was reported. The viability profile of the cell onto the R-HP and A-B scaffold, remained not statistically different during the 14 days, and overall high for all the culture time. The results proved that CS was a suitable niche for cell growth and a possible carrier component, for loading hASCs in the tubular scaffold before implant.

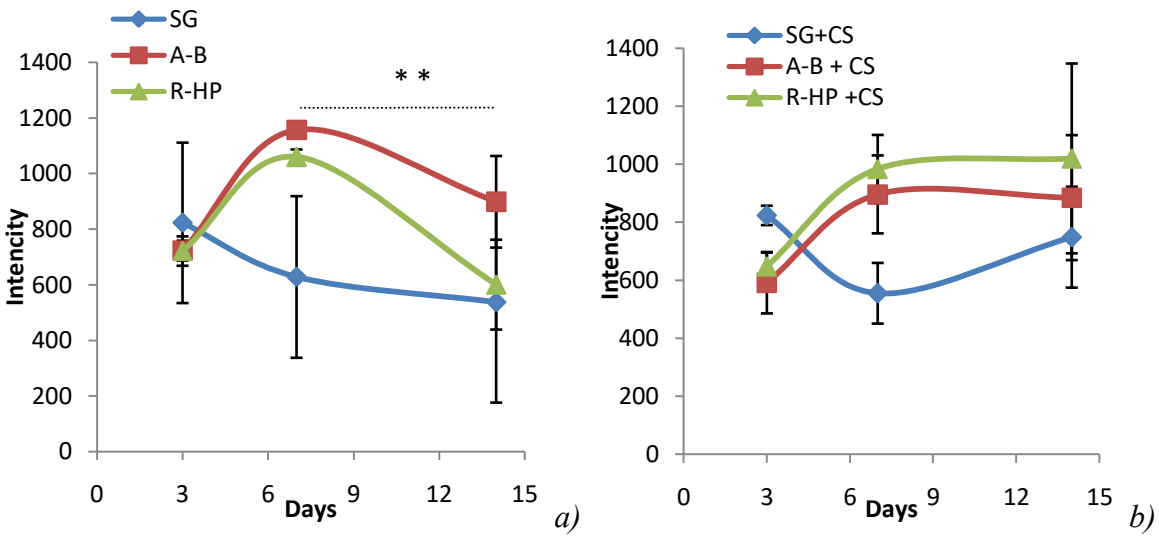

Figure 8. *Metabolic activity measured by Alamar Blue for human adipose stamina cells (hASCs) growth onto A-B and R-HP zones performed after 3-7 and 14 days. a)in full α-MEM and b) with CS 3%wt full α-MEM. Statistical differences were obtained in the A-B and R-HP substrates between respectively the 6th and 14th day of not-supplemented growth (a). In the 6thday of standard growth (SG) the values were significantly lower than the A-B and R-HP substrates in both the CS-supplemented and not supplemented medium (a-b).*

4. CONCLUSIONS

It was possible to develop a tubular scaffold based on pullulan/chitosan, designed with a tendon and bone part to be implanted in the TBI enthesis site. The scaffold developed showed a topography gradient in the electrospun nanofiber orientation, from random (R-HP) to aligned (A-B) direction, along the tubular length. This bi-polar structure represented the bone and tendon part, respectively. The tubular scaffold was also increasingly mineralized by including hydroxyapatite (HP) in the fiber matrix. The biphasic scaffold presented a continuous structure with an interface region, where the fiber alignment and mineral content gradually change from one to the other end.

hASCs were used as cell model for studying their possible inclusion in the tubular scaffold. They started an early osteogenic and tenogenic differentiation, when cultured onto the R-HP or A-B part, respectively, without additional supplements. Their viability was also well supported when chondroitin sulfate (CS) was added to the cell culture. The biphasic tubular scaffold showed promising outcomes for its employment as multi functional surgical support, in the complex enthesis tissue reparation.

REFERENCE

1. Blair HC, Larrouture QC, Li Y, Lin H, Beer-Stoltz D, Liu L, Tuan RS, Robinson LJ, Schlesinger PH, Nelson DJ. Osteoblast Differentiation and Bone Matrix Formation In Vivo and In Vitro. Tissue Eng Part B Rev. 23 (2017): 268-280
2. Calejo I, Costa-Almeida R, Reis RL, Gomes ME., A textile platform using continuous aligned and textured composite microfibers to engineer tendon-to-bone interface gradient scaffolds. Adv Health Mater. 15 (2019)
3. Costa-Almeida R, Calejo I, Gomes ME. Mesenchymal Stem Cells Empowering Tendon Regenerative Therapies. Int J Mol Sci. 20 (2019) : 3002
4. Fan J, Park H, Lee MK, Bezouglaia O, Fartash A, Kim J, Aghaloo T, Lee M. Adipose-derived stem cells and BMP-2 delivery in chitosan-based 3D constructs to enhance bone regeneration in a rat mandibular defect model. Tissue Eng Part A. 15-16 (2014) :2169-79.
5. Killian ML, Thomopoulos S. Scleraxis is required for the development of a functional tendon enthesis. FASEB J. 1 (2016): 301-11
6. Kosaraju R, Rennert RC, Maan ZN, Duscher D, Barrera J, Whittam AJ, Januszyk M, Rajadas J, Rodrigues M, Gurtner GC. Adipose-Derived Stem Cell-Seeded Hydrogels Increase Endogenous Progenitor Cell Recruitment and Neovascularization in Wounds. Tissue Eng Part A. 22. (2016):295-305
7. Kupiec T.C.; Matthews P.; Ahmad, R., Dry-heat sterilization of parenteral oil vehicles, Int. J. Pharm. Compd.4 (2000) 223–224.
8. Morais DS, Torres J, Guedes RM, Lopes MA. Current Approaches and Future Trends to Promote Tendon Repair. Ann Biomed Eng. 43 (2015):2025-35
9. Pulyala P, Singh A, Dias-Netipanyj MF, Cogo SC, Santos LS, Soares P, Gopal V, Suganthan V, Manivasagam G, Popat KC. In-vitro cell adhesion and proliferation of adipose derived stem cell on hydroxyapatite composite surfaces. Mater Sci Eng C Mater Biol Appl. 75 (2017):1305-1316
10. Sandri G., Rossi S., Bonferoni M.C., Miele D., Faccendini A., Del Favero E., Di Cola E., Icaro Cornaglia A., Boselli C.,Luxbacher T., Malavasi L., Cantu' L., Ferrari F. Chitosan/glycosaminoglycan scaffolds for skinreparation. CarbohydrPolym. 15 (2019) 219-227.

11. Schweitzer R, Chyung JH, Murtaugh LC, Brent AE, Rosen V, Olson EN, Lassar A, Tabin CJ. Analysis of the tendon cell fate using Scleraxis, a specific marker for tendons and ligaments. Development. 19 (2001) :3855-66
12. Wang P, Zhao L, Liu J, Weir MD, Zhou X, Xu HH. Bone tissue engineering via nanostructured calcium phosphate biomaterials and stem cells. Bone Res.30 (2014):14017
13. Weiss-Bilka HE, Meagher MJ, Gargac JA, Niebur GL, Roeder RK, Wagner DR. Mineral deposition and vascular invasion of hydroxyapatite reinforced collagen scaffolds seeded with human adipose-derived stem cells. Biomater Res. 17 (2019) 23:15
14. Zubillaga V, Salaberria AM, Palomares T, Alonso-Varona A, Kootala S, Labidi J, Fernandes SCM. Chitin Nanoforms Provide Mechanical and Topological Cues to Support Growth of Human Adipose Stem Cells in Chitosan Matrices. Biomacromolecules. 7 (2018): 3000-3012

GENERAL CONCLUSIONS

Electrospun nanofibers enriched with inorganic fillers, is a technique that allows to develop hybrid medical devices with superior properties. Recently these have found many applications in the field of regenerative medicine, for soft as well as hard tissue engineering.

In the development of hybrid electrospun scaffold for skin application, the nano-clay components were effective from the technological point of view, as well as from their biological one. The mechanisms of interaction between the hybrid fibers and the cells, still remain partially unknown although some evidence can be argued.

The drug profile obtained from the hybrid scaffold loaded with the nanocomposite confirmed the capability of the nanofiber to control the drug release, especially in presence of glycosaminoglycans components. This result suggested how biopolymers could be emerging tools even in advanced drug-delivery systems.

The tubular scaffolds intended to be use as surgical support in orthopaedic treatments, were designed with innovative morphology and composition. They showed an original capability to control the passage of proteins derivative from PL until two weeks. While the biomimetic topography and anisotropy of the tubular system, possessed mechanical behaviour close to in vivo values.

The advanced combination of biopolymers with HP particles created nanofibers able to support cell spreading, migration as well as, adipose stem cell differentiation. The cytoskeleton actin arrangement in the cells, via focal adhesion site activation, was controlled through roughness in scaffolds surface. Moreover, the extracellular matrix production was enhanced, due to topographical and compositional surface.

In this scenario, some steps have been made for employing suitable inorganic components combined with different bio-polymers and biological modulators, although further studies have to be done for better understand the new potentiality of these systems in controlling the specific tissue functionality.

INDEX

AIM AND SUMMARY 1

CHAPTER 1: Hybrid electrospun fiber in tissue engineering 5

CHAPTER 2: Halloysite and Montmorillonite loaded scaffolds as enhancers of chronic wound healing 53

CHAPTER 3: Norfloxacin-Loaded electrospun Scaffolds: Montmorillonite Nanocomposite vs. free drug 83

CHAPTER 4: Electrospun hybrid tubular scaffold designed to be extemporarily loaded with human platelet lysate, for tendon to bone regeneration 120

ANNEX A : 152

CHAPTER 5: Electrospun biphasic tubular scaffold with topographical and compositional gradient, for enthesis regeneration 158

GENERAL CONCLUSIONS 182